SAKARYA ÜNİVERSİTESİ

FEN BİLİMLERİ ENSTİTÜSÜ
DERGİSİ

Sakarya University Journal of Science (SAUJS)

SAKARYA
ÜNİVERSİTESİ
e-issn: 2147-835X

SAÜ Fen Bil Der/SAUJS

Cilt/Volume: 24

Sayı/Issue: 6

Aralık/December 2020

Sakarya Üniversitesi Fen Bilimleri Enstitüsü Dergisi
(Sakarya University Journal of Science)
Cilt/Volume: 24 No/ Issue: 6 Aralık/December 2020

Editör Kurulu/Editorial Boards

Editor-in-Chief

Davut Avcı, Pyhsics, Sakarya University (Turkey)

Editors

Alparslan Serhat Demir, Industrial Engineering, Sakarya University (Turkey)
Aysun Eğrisöğüt Tiryaki, Mechanical Engineering, Sakarya University (Turkey)
Ertan Bol, Civil Engineering, Sakarya University (Turkey)
Hüseyin Aksoy, Biology, Sakarya University (Turkey)
M. Hilmi Nişancı, Electrical and Electronics Engineering, Sakarya University (Turkey)
Mehmet İşleyen, Environmental Engineering, Bursa Technical University (Turkey)
Mehmet Nebioğlu, Chemistry, Sakarya University (Turkey)
Mehmet UYSAL, Metallurgical and Materials Engineering, Sakarya University (Turkey)
Mustafa Gülfen, Chemistry, Sakarya University (Turkey)
Muhammed Fatih Adak, Computer Engineering, Sakarya University (Turkey)
Murat Güzeltepe, Mathematics, Sakarya University (Turkey)
Nezaket Parlak, Mechanical Engineering, Sakarya University (Turkey)
Ömer Tamer, Physics, Sakarya University (Turkey)

Editorial Board

Aliye Suna Erses Yay, Environmental Engineering, Sakarya University (Turkey)
Aslı Uçar, Faculty of Health Sciences, Nutrition and dietetics, Ankara University (Turkey)
Aykut Astam, Physics, Erzincan Binali Yıldırım University (Turkey)
Burak Erkayman, Industrial Engineering, Atatürk University (Turkey)
Cansu Akbulut, Biology, Sakarya University (Turkey)
Caner Erden, Industrial Engineering, Sakarya University (Turkey)
Can Serkan Keskin, Chemistry, Sakarya University (Turkey)
Elif Büyük Öğüt, Mechanical and Metal Technologies, Kocaeli University (Turkey)
Emrah Bulut, Chemistry, Sakarya University (Turkey)
Emre Dil, Energy Systems Engineering, Beyket University (Turkey)
Emre Tabar, Physics, Sakarya University (Turkey)
Faruk Fırat Çalım, Civil Engineering, Alparslan Türkeş University (Turkey)
Gülnur Arabacı, Chemistry, Sakarya University (Turkey)

İrfan Yazıcı, Electrical and Electronics Engineering, Sakarya University (Turkey)
İsmail Hakkı Demir, Architecture, Sakarya University (Turkey)
Latif Kelebekli, Chemistry, Ordu University (Turkey)
Mahmud Tokur, Metallurgical and Materials Engineering, Sakarya University (Turkey)
Mevlüt Sami Aköz, Civil Engineering, Çukurova University (Turkey)
Miraç Alaf, Metallurgical and Materials Engineering, Bilecik Şeyh Edebali University (Turkey)
Muhammed Maruf Öztürk, Computer Engineering, Süleyman Demirel University (Turkey)
Murat Sarduvan, Mathematics, Sakarya University (Turkey)
Murat Tuna, Chemistry, Sakarya University (Turkey)
Murat Utkucu, Geophysical Engineering , Sakarya University (Turkey)
Mustafa Akpınar, Software Engineering, Sakarya University (Turkey)
Nazan Deniz Yön Ertuğ, Biology, Sakarya University (Turkey)
Nükhet Sazak, Electrical and Electronics Engineering, Sakarya University (Turkey)
Osman Kırtel, Civil Engineering, Sakarya University of Applied Sciences (Turkey)
Özer Uygun, Industrial Engineering, Sakarya University (Turkey)
Öznur Özkan Kılıç, Mathematics, Başkent University (Turkey)
Rıfkı Terzioğlu, Electrical and Electronics Engineering, Bolu Abant İzzet Baysal University, (Turkey)
Sibel Güneş, Mechanical Engineering, Erciyes University (Turkey)
Soley Ersoy, Mathematics, Sakarya University (Turkey)
Soydan Serttaş, Computer Engineering, Dumlupınar University (Turkey)
Tuğrul Çetinkaya, Metallurgical and Materials Engineering, Sakarya University (Turkey)
Turgay Şişman, Biology, Atatürk University (Turkey)

English Language Editor

Ömer Tamer, Physics, Sakarya University (Turkey)

SAKARYA ÜNİVERSİTESİ FEN BİLİMLERİ ENSTİTÜSÜ DERGİSİ
(SAKARYA UNIVERSITY JOURNAL OF SCIENCE)
İÇİNDEKİLER/CONTENTS

Cilt/Volume: 24 – No/Issue: 6 (ARALIK/DECEMBER 2020)

RESEARCH ARTICLES

SAKARYA ÜNİVERSİTESİ
FEN BİLİMLERİ ENSTİTÜSÜ
DERGİSİ

Sakarya University Journal of Science
SAUJS

e-ISSN 2147-835X | Period Bimonthly | Founded: 1997 | Publisher Sakarya University |
http://www.saujs.sakarya.edu.tr/en/

Title: Structural Design and Stress Analysis of a Helical Vertical Axis Wind Turbine Blade

Authors: Özer ÖĞÜÇLÜ

Recieved: 2020-04-13 12:38:20

Accepted: 2020-08-04 14:17:12

Article Type: Research Article

Volume: 24
Issue: 6
Month: December
Year: 2020
Pages: 1151-1161

How to cite
Özer ÖĞÜÇLÜ; (2020), Structural Design and Stress Analysis of a Helical Vertical Axis Wind Turbine Blade. Sakarya University Journal of Science, 24(6), 1151-1161, DOI: https://doi.org/10.16984/saufenbilder.719223
Access link
http://www.saujs.sakarya.edu.tr/en/pub/issue/57766/719223

Sakarya University Journal of Science 24(6), 1151-1161, 2020

Structural Design and Stress Analysis of a Helical Vertical Axis Wind Turbine Blade

Özer ÖĞÜÇLÜ*[1]

Abstract

In this study, a Computational Fluid Dynamics (CFD) model is designed to investigate the structural analysis of a helical Vertical Axis Wind Turbine (VAWT) blade which is using National Advisory Committee for Aeronautics (NACA) 0018 airfoil and numerical calculations are conducted by using Comsol Multiphysics. The main objective of this study is to determine that the strength of the turbine blade against bending caused by increased wind speeds is sufficient for the selected turbine blade material. This paper presents also an investigation of the effects of different wind speeds on the structure of a helical VAWT blade that is fixed to the support arm which is attached to the VAWT's main shaft. In this study, a turbine blade which is placed in an air flow field is subjected to approaching strong wind with different velocities. The model solves for the flow around the blade and the structural displacement due to the fluid load. This investigation consists of two main parts: Solving for the fluid flow around the turbine blade with a free stream velocities of 1, 3, 5, 7, and 9 m/s, and Studying the deformation of the turbine blade caused by the fluid load. The risk of failure according to the von Mises criterion for the ductile materials such as aluminum is also investigated.

Keywords: CFD model, airfoil, helical, Vertical Axis Wind Turbine, turbine blade, von Mises

1. INTRODUCTION

Wind turbine is one of the renewable energy sources whose importance is increasing. Therefore, the analysis, design and production of wind turbines is very important for the world's power generation industry. The most critical components of a wind turbine are turbine blades. The turbine blade, the first link in the energy conversion chain, is an important issue in wind turbine design.

The kinetic energy in the wind should be transferred to the turbine blades without any loss. This significantly affects the yield to be achieved. For this reason, the turbine blades must be designed in such a way that they can capture the maximum energy from the wind. In the production of wind turbine rotors, the strength of the turbine blades at high wind speeds is an important consideration. If this issue is not taken into account sufficiently, the results can be very harmful. If no action is taken, resistance problems may arise in the turbine tower and especially the blades at high wind speeds.

As a result, the turbine elements may be deformed or even broken. The load that forces the tower is due to the wind force acting on the tower and especially the turbine blades. Turbine blades have to withstand wind, gravity and centrifugal loads, because they produce electricity by rotation. The blades are affected by the tangential and normal

---

*Corresponding Author: ozer.oguclu@ege.edu.tr

[1] Ege University, ORCID: https://orcid.org/0000-0002-6293-7742

components of the inertia forces resulting from both the wind force and the rotation of the blades. These forces cause bending stresses and normal stresses in towers and blades. If these stresses exceed the safe stress limit specific to the material used, they cause damage to the turbine tower and blades. Thus the structure of a turbine blade requires it to be made of strong materials.

Turbine rotor blades are exposed to different cyclic loads such as aerodynamics, centrifugal and gravitational forces during life of a wind turbine. Then the fatigue life of the wind turbine blades becomes the first step in design procedure to estimate the effectiveness of a wind turbine. The turbine blades must be strength and stiff. When the strength and stiffness of blades is considered, the weight of turbine blades becomes very important to determine the cost and to avoid the fatigue failure. In order to minimize total weight of a wind turbine system, a stiff and light material is generally required. The key of design a reliable wind turbine blade under complicated loading conditions is the correct fatigue life prediction. Sutherland presented a long record of the researches about wind turbine rotor blade material fatigue [1]. Winterstein and Veers defined the fatigue stress in terms of the root mean square of the instantaneous stress, which was regarded as an exponential function of wind speed [2]. Cox and Echtermeyer has designed a Horizontal Axis Wind Turbine (HAWT) with the 70 meter long blade were to use in a location where wind speeds are high [3]. They designed a blade which was made of a hybrid composite structure was subjected to Finite Element Analysis (FEA) researches to show its capability to resist excessive loading conditions according to the international open sea wind standards. Furthermore their results verified that the design to have sufficient capacity in point of tip deflection, maximum and minimum strains, and critical buckling load. In their paper, they presented detailed definitions of the turbine structural components with the results of maximum and minimum strains and deflections. Yeh and Wang evaluated the stress and deformation analyses of the National Renewable Energy Laboratory (NREL) turbine composite blade with FEA [4]. The stress distribution and deformation of the wind turbine blades under various loads was analyzed, and the effect of changing the stacking angle in composites and the thickness variation of the blade structure on the simulation results was discussed in their study. The increases in the size and flexibility of large wind turbine blades produces remarkable aeroelastic impacts which are produced by Fluid Structure Interaction (FSI). Correct FSI modeling of wind turbine blades is very important in the improving of large wind turbines. Wang et al. [5] established a wind turbine blade FSI model at full scale. They calculated the aerodynamic loads with a CFD model performed in ANSYS FLUENT and determined the blade structural responses with a FEA model applied in ANSYS Static Structural module. Wind turbine blades are tested for new structural improvements. Fagan et al. [6] developed and tested a special turbine blade. In their study, experimental tests on a wind turbine with long composite blades were presented. They used the results of the tests to calibrate FEA models. At last of this study, they implemented a design optimisation work with a genetic algorithm. To reduce the wind turbine blade's weight is an important subject for engineers. To improve the efficiency of power generating, wind turbines changed bigger in size. Turbine blades have also extended to capture more wind energy. A wind turbine blade made of fabric-based material can reduce the blade weight. To verify structural capability, Choi et al. [7] developed a 10 kW wind turbine with small fabric-covered turbine blades. They designed the cross section of turbine blades by using Variational Asymptotic Beam Sectional analysis (VABS), then they implemented structural analysis. Static structural tests and modal tests were completed. At last, they compared the analysis results with the test results in their study.

Firstly, wind turbines were used as windmills whose blades convert the kinetic energy they obtain from the wind into mechanical energy. These windmills have shafts that are spinning and moving the lever of pocket. Wind turbines are rotated by the movement of air that propels the blades or rotors of the turbine, which are generally named as airfoils. The airfoils are designed to react with wind and take the rotational power that is converted to energy. The shape of the airfoils has a great effect because it causes the pressure on one surface higher than the pressure on the other surface of the blade. These uneven pressure values make the blade rotate.

Small wind turbines are manufactured with a horizontal or vertical axis. Especially vertical axis wind turbines are interesting for building applications. Usual horizontal axis wind turbines must always be oriented to the wind destination. In contrast, the vertical axis wind turbines can catch incoming wind from any direction via the helical blade profile or the arms. Therefore, vertical axis wind turbines do not need to be steered, they can also benefit from turbulences [8].

The HAWT's axis is parallel to the wind flow whereas the VAWT's rotor is positioned vertically. The HAWTs are mounted on a large tower and has generally two or three blades. The difference in wind speeds on the top and bottom surfaces of the blade results a pressure difference between the blade surfaces. This pressure difference produces an aerodynamic lift and the rotation of the blade starts. On the other hand, there is a drag force perpendicular to the lift force which opposes the rotation of the blade. VAWTs has advantages when they operate at low wind speeds.

VAWTs are wind turbines that rotate about a vertical axis that is perpendicular to the wind direction. In modern designs, VAWT's center axis is a vertical shaft that is connected to a gearbox which increases turbine speed. The gearbox's output shaft drives a generator that converts the mechanical torque of the turbine rotor to electrical power [9]. Fig.1 shows typical designs of basic VAWT Configurations. The two main types of VAWTs are the Savonius and the Darrieus turbines.

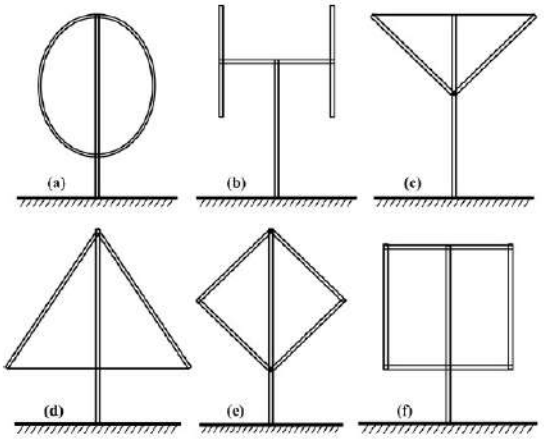

Figure 1 Basic VAWT Configurations: (a) Darrieus, (b) H, (c) V, (d) Delta, (e) Diamond and (f) Gyromill [9]

Though vertical axis wind turbines are manufactured in various shapes, they are classified into two basic categories as Savonius and Darrieus turbines. The Savonius turbines mainly work on the drag principle. These vertical axis turbines generally have low efficiency but they are very suitable for areas with turbulent winds. On the other hand, Darrieus turbines work on the lifting principle. The Darrieus vertical axis wind turbines require a motor to start their motion. They are also well suited for places with turbulent winds where they can have high efficiencies. Now, there are innovative models on the market that take advantage of the features of both Savonius and Darrieus turbines. A Savonius turbine is widely used in many places that require high reliability, such as ventilation and anemometers. They are less efficient than general HAWT since they are drag type turbines. Savonius turbines are perfect for turbulent wind fields and they have the feature of self-start at low wind speeds. Nowadays Darrieus wind turbines are manufactured with great efficiency. However they can cause much torque fluctuations and cyclical stress on the shaft. This results in bad reliability [8]. There is a helical bladed design, which is a more efficient development and called Gorlov turbine after its inventor. Fig.2 shows different types of Vertical Axis Wind Turbines.

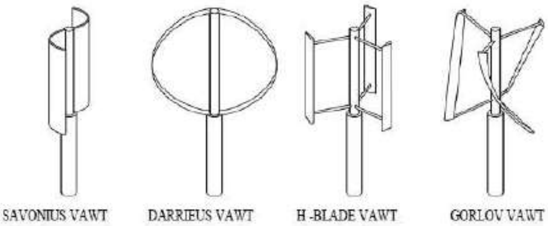

Figure 2 Different types of VAWTs [8]

Many research institutions and universities achieved wide research activities and improved a plenty of designs about many aerodynamic CFD vertical axis wind turbine models. Engineers used these important models for searching the performance of vertical axis wind turbine and achieving the best design parameters before manufacturing vertical axis wind turbine models [10]. Blade design aim is finding the right blade geometry that generates the most rotary action. Thus, blade design considers the wind turbine parameters which are: angle of attack, power coefficient, lift coefficient, drag coefficient, tip speed ratio, blade chord length, and number of blades.

2. TURBINE DESIGN

In this study, the helical VAWT turbine, also known as the Gorlov turbine, with three blades is investigated [11]. VAWTs with helical blades can yield a less noise emission and better aerodynamic performance compared with VAWTs which have straight blades [12]. Recently CFD models are often applied to VAWT turbines and give results that can express real flow events. In this study, the dimensions of the turbine as 0.3 m height and 0.3 m diameter are chosen, because they are convenient for a small-scale wind turbine.

Solidworks design software is used for drawing of three dimensional vertical axis wind turbine blade. Then blade drawing is imported into Comsol Multiphysics from Solidworks using Import command in the Comsol Model Builder.

In this study, due to its symmetrical structure, NACA 0018 airfoil profile is used [13]. The NACA 0018 airfoil profile coordinates required for drawing the three-dimensional blade geometry are taken from airfoiltools.com website. This site retrieves wing profile coordinate values from the University of Illinois at Urbana–Champaign (UIUC) – Airfoil Coordinates Database, which contains approximately 1600 aircraft airfoil coordinates [14].

For the improving of wind turbine blades, a great deal of airfoil types are designed in wind energy systems technology. The small wind turbine blade airfoils could be used already at the low attack angles where drag coefficient must be lower than lift coefficient. NACA series airfoils are generally used to design the turbine blade geometry. A significant part of the NACA airfoils, originally designed for aircraft, were later used in wind turbines. Early NACA airfoil series were composed with analytical equations that define camber of geometric center line of airfoil cross section with the cross section thickness distribution over the length of airfoil. NACA airfoil cross section is shaped from a camber line and a thickness distribution which is plotted vertical to camber line. A camber line equation is separated into sections both side of the point of maximum camber position. The gradient of camber line is also needed to calculate the position of final airfoil envelope. The first family of airfoils is known as NACA four digit series which were designed using this approach. NACA four digit airfoil series specification is defined by four numbers which describe camber, position of maximum camber and thickness. The first number states the maximum camber in percentage of airfoil chord length. The second number shows the position of maximum camber in tenths of chord length. And the last two numbers express maximum thickness of airfoil in percentage of chord length [14]. If the first two numbers of an airfoil of NACA four digit series are 00, it means that this airfoil is in symmetrical structure and has not a camber geometry [13]. Fig.3 shows a normal NACA airfoil's profile geometry.

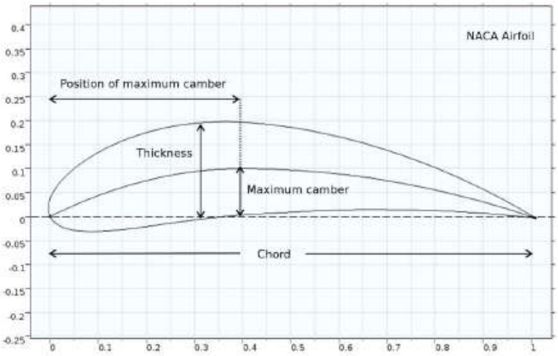

Figure 3 NACA airfoil profile geometry

NACA0018 airfoil has maximum thickness 18% at 30% chord length and maximum camber 0% at 0% chord length [14]. In this study, the chord length is chosen as 0.05 m.

First, airfoil profile is drawn using the NACA 0018 airfoil profile coordinates which are taken airfoiltools.com website. For this purpose, Solidworks design software uses the Curves Through XYZ Points command on the Curves Toolbar, which is used to generate three-dimensional curves from solid or surface forms. This command is used to create a curve according to the coordinate values entered in the table. Since only two dimensional drawing will be made, Z coordinates are given as zero in this table. Fig.4 shows the NACA 0018 airfoil profile drawing in design software.

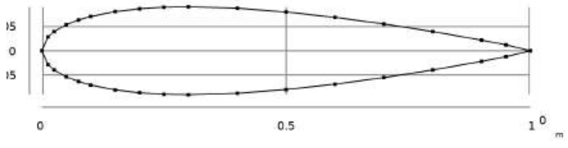

Figure 4 Blade airfoil drawing

The coordinates of point M(x, y, z) on the Gorlov turbine blade helical curve at height L and radius R are calculated by the following geometric correlation formulas [11];

$$x = R\cos\varphi \tag{1}$$

$$y = R\sin\varphi \tag{2}$$

$$z = R\varphi\tan\delta \tag{3}$$

where φ; is the helical rotation angle and δ; is the helix angle of rise. Using these geometric correlation formulas in Microsoft Excel or LibreOffice Calc, we can multiply the coordinates of the helical curve of the airfoil profile, which we have previously drawn in Solidworks, to form the three-dimensional turbine blade drawing. By using these helix curve coordinates, the helix curve that we will use to draw the three-dimensional turbine blade drawing from the airfoil profile, we have previously drawn in Solidworks design software, is drawn using the Helix/Spiral draw command of the Solidworks design software. With the Variable Step Helix draw option in the menu, the coordinates of the helix curve we want to draw are entered into the Solidworks as a table and the curve is drawn. This plotting process is shown in Fig.5.

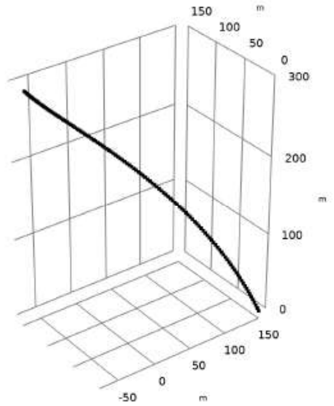

Figure 5 Blade Helix curve drawing

After completing the airfoil profile and helix curve drawings in the Solidworks design software, a three-dimensional blade model is drawn using the Sweep command in the Solidworks. For this, in the Profile and Path selection boxes in the command menu, the airfoil profile curve we have drawn as Profile and the helix curve that we have previously drawn as Path are selected. After setting the other start and end states, our solid blade model is completed by running the Sweep command. Since our vertical axis wind turbine model, which we designed, has three blades, the other blades are copied from our first drawing and two solid bottom and upper cylindrical blade connection elements are drawn and our solid model is finalized [15]. Fig.6 shows the final version of the Gorlov Turbine design.

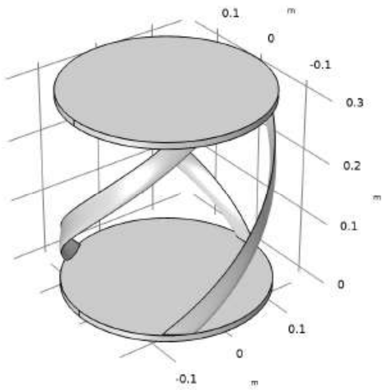

Figure 6 Gorlov Turbine design drawing

In this study, wind is considered a homogeneous mass without dust, steam or other particles. Therefore, the model is based on single-phase flow at low wind velocities. In Comsol Multiphysics, single-phase flow is modeled by Navier-Stokes fluid flow equations. The Re number is calculated as 16.7×10^3, at the conditions which are air density $\rho = 1.2$ kg/m^3, wind speed U = 5 m/s, airfoil chord length c = 0.05 m, and air dynamic viscosity $\mu = 1.8\times10^{-5}$ kg/(m.s) for NACA0018 airfoil used in this model.

$$\mathrm{Re} = \frac{\rho U c}{\mu} = \frac{1.2x5x0.05}{1.8x10^{-5}} = 16.7x10^3$$

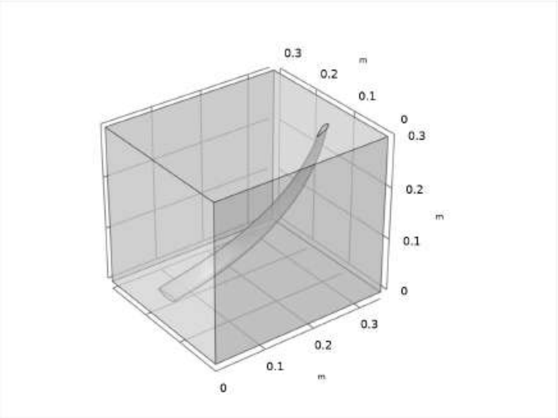

Figure 7 Model geometry

For simplicity, model geometry is reduced to a single blade as shown in Fig.7. The blade is free to move along all axis and is subjected to only the fluid forces. In Comsol, the fluid forces are automatically applied when using the Fluid-Structure Interaction multiphysics coupling. The blade is attached to the turbine body which is assumed to be rigid. The rigidity is enforced by applying a Fixed Constraint to the both blade ends. The turbine blade is then placed in a cubic volume of 0.3 m long, 0.3 m wide and 0.3 m high, which represents a part of a wind tunnel. The lateral, upper and lower walls of this cube and the surface of the turbine blades are determined as the wall boundary condition. At the same time, the right and left walls of this cube are set as the inlet and outlet where the wind flows evenly along the horizontal direction.

Fluid-Structure Interaction is a common class of multiphysics problems in which structural response and surrounding fluid flow are coupled. The interaction between the fluid flow and structural deformation is in general bidirectional. The fluid exerts an external load on the structure, leading to deformation of structural components. Conversely, the motion or deformation of structural components changes the direction of fluid flow. Depending upon the type of interaction between fluid and solid objects, Fluid-Structure Interaction problems can be categorized into either one-way coupled or two-way coupled problems [16].

In the general design of the Fluid-Structure interaction problem, the elastic solid object is immersed in a channel where the fluid flows [17]. The interaction between the fluid and the structural mechanism is specified through the interface boundaries between the two domains. The two identity pairs between the fluid and solid domains are selected in the Fluid-Structure Interaction to incorporate the multiphysics coupling between the two physics. Thus, in the Multiphysics section, Coupling Type is selected as Fluid loading on structure in Comsol Multiphysics [16].

In this study, mesh independency is conducted to assure that the number of the mesh is adequate for estimating the maximum velocity around blade for wind speed U = 1 m/s. Four different number of mesh is generated for model as shown in Fig.8. The number of domain elements is varied from 94.2 thousands to 5.35 millions.

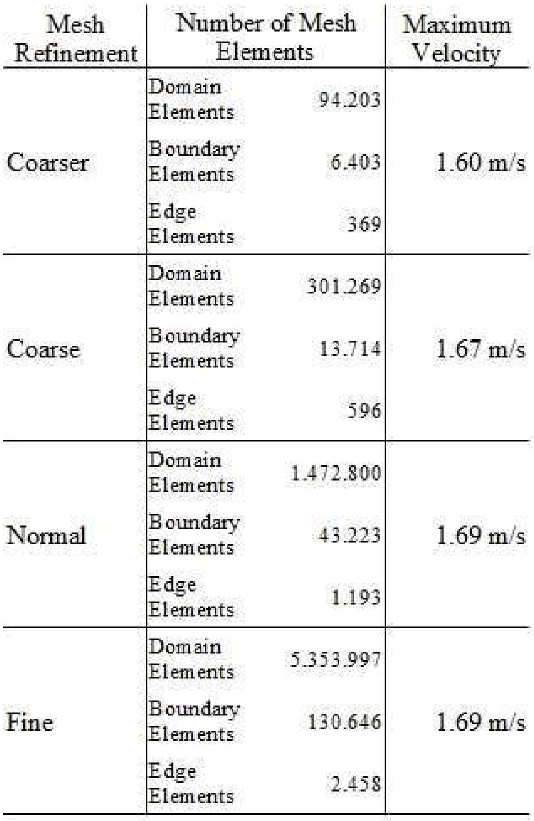

Mesh Refinement	Number of Mesh Elements		Maximum Velocity
Coarser	Domain Elements	94.203	1.60 m/s
	Boundary Elements	6.403	
	Edge Elements	369	
Coarse	Domain Elements	301.269	1.67 m/s
	Boundary Elements	13.714	
	Edge Elements	596	
Normal	Domain Elements	1.472.800	1.69 m/s
	Boundary Elements	43.223	
	Edge Elements	1.193	
Fine	Domain Elements	5.353.997	1.69 m/s
	Boundary Elements	130.646	
	Edge Elements	2.458	

Figure 8 The number of elements for the three-dimensional mesh

Thus, Physics-controlled mesh with Fine element size is selected and the final model meshing is shown in Fig.9. The mesh used to discretize the fluid domain and the turbine blade is characterized by tetrahedral elements. The maximum element size for the entire domain is set to 0.0276 m, whereas the minimum element size is 0.00345 m. The mesh is configured to be tightest around the blade, in order to resolve the stress within the bending blade.

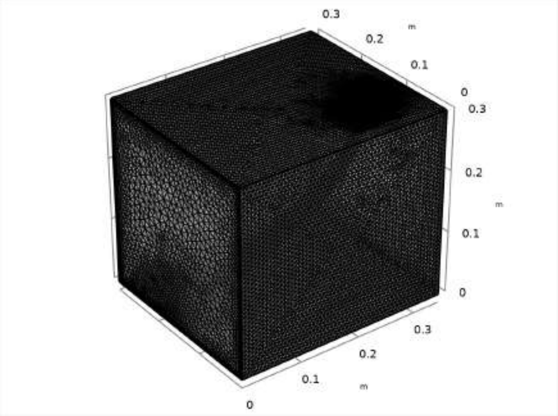

Figure 9 Model geometry meshing

Low number mesh distribution may produce computation with large error but high number mesh may increase computational time. Therefore high concentrated mesh distribution is applied close to the blade surface. The maximum element size for the blade surface is set to 0.00692 m, whereas the minimum element size is 0.00045 m. Mesh distribution around NACA 0018 airfoil is presented in Fig.10.

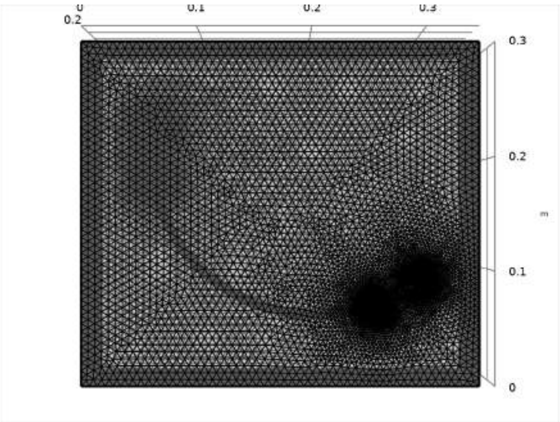

Figure 10 Model airfoil meshing

In this study, the turbine blades and body are made of Aluminum ASTM 5083 alloy which is used in marine, auto and aircraft applications [18]. The material properties of Aluminum ASTM 5083 alloy are Density; ρ = 2.66 g/cm^3 at 20 ºC, Tensile Strength; 290 MPa, Yield Strength; 145 MPa, Young’s modulus; E = 70.3 GPa, and Poisson’s ratio; μ = 0.33.

In this study, the simulation is set up by using a Turbulent Flow, k-ω interface with a stationary study type to analyze the interaction of the blade and the fluid. Turbulence is modeled with the k-ω model instead the k-ε turbulence model. The k-ω turbulence model is a widely used model for CFD simulations in the near-wall region with good performance for swirling flows. Although the k-ω model is better suited for these types of flows, it takes longer to converge than the k-ε model due to the strong non-linearity in the turbulence coefficients [16]. The model solves for the flow around the blade and the structural displacement due to the fluid load for flow inlet velocities of 1, 3, 5, 7, and 9 m/s. Then model investigates the deformation of the turbine blade caused by the fluid load. The outlet is set as a pressure outlet, keeping the pressure constant equal to 101325 Pa.

The lateral, upper and lower walls and the surface of the blade are set as No-slip wall boundary condition.

3. RESULTS

Fig.11 shows the fluid velocity magnitude around the blade of the turbine for inlet velocity 5 m/s. The maximum velocity is about 8.49 m/s and the main flow path and the recirculation flow around blade are clearly visible.

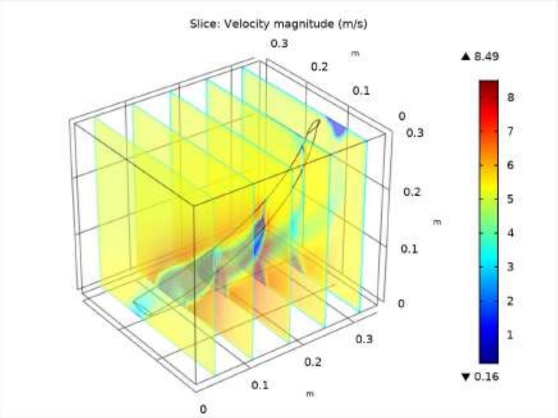

Figure 11 Velocity magnitude around blade

Fig.12 presents fluid pressure around blade due to the surrounding flow. The maximum relative pressure, about 33.3 Pa, occurs on the nearest point to the bottom rigid blade end.

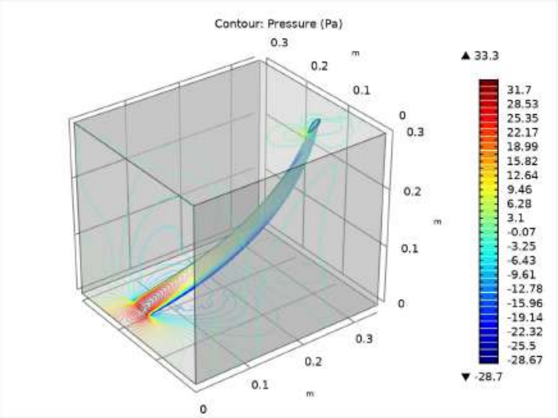

Figure 12 Fluid pressure around blade

Fig.13 shows the von Mises stress in the solid blade. Because of fluid pressure, the original structure of turbine blade bends. The deformed shape of the blade due to fluid load is seen clearly from Fig.13.

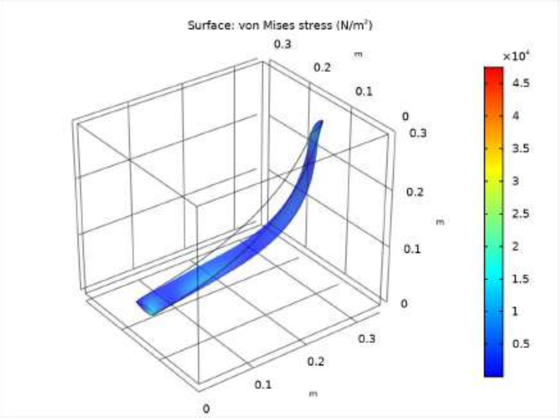

Figure 13 von Mises stress in blade

The largest displacement occurs in the middle part of the blade between both rigid ends. It is seen in Fig.14. However, the maximum displacement is small, about 1.05x10^{-7} m. This indicates that the strength of the blade effectively protect the blade from wind flow. The fluid load on the structure at the current flow velocity is not significant enough to affect the design of the blade. The yield strength for the Aliminum 5083 Alloy is large enough to consider that the blade is far from failure.

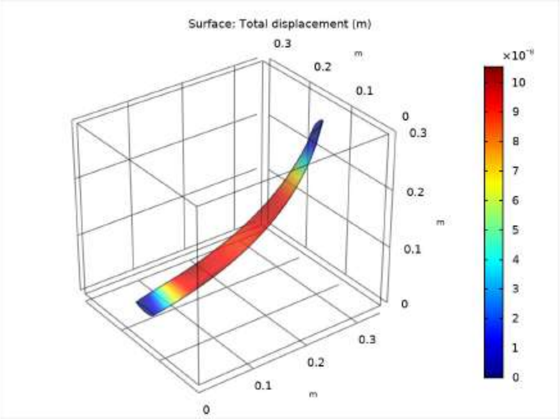

Figure 14 Total displacement of blade

The maximum von Mises stress in the blade is formed on the nearest point to the rigid blade end. It is seen clearly in Fig.15.

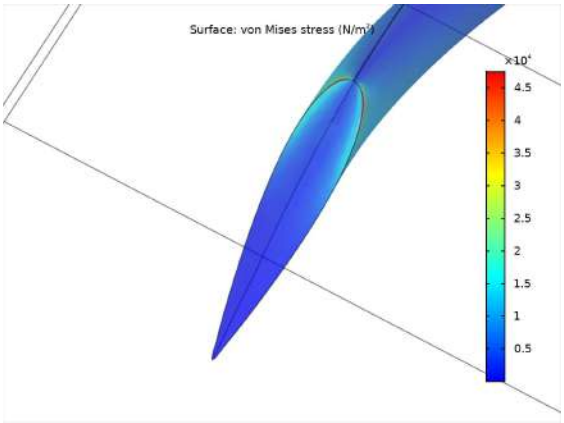

Figure 15 Maximum von Mises stress in blade

The von Mises yield criterion is formulated in terms of von Mises stress in material science and engineering. The von Mises stress is a value which is used to determine whether a ductile material will yield or fracture. A given ductile material starts to yield when its von Mises stress exceeds a critical value named the yield strength.

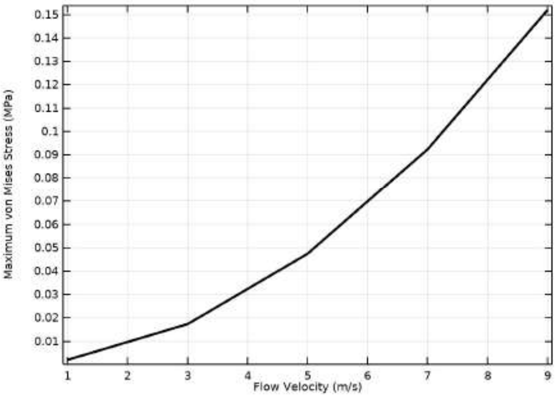

Figure 16 Relationship between flow velocity and maximum von Mises stress of blade

Fig.16 shows the relation with the maximum von Mises stresses and different air flow velocities. Obviously, with increase of flow velocity, the maximum von Mises stress value of the blade increases. Additionally the maximum von Mises stress rapidly increases from the velocity 5 m/s to the velocity 9 m/s. A ductile structural material is safe as long as the maximum value of the von Mises stress in that material remains smaller than the yield strength of the same material.

4. CONCLUSION

This model presents the structural analysis of a helical vertical axis wind turbine blade made of Aluminum 5083 Alloy which is placed in an air flow field. First, a CFD analysis is solved for the fluid flow around the turbine blade to calculate the velocity magnitude and the pressure distribution around the blade.

Second, a stress analysis is carried out in which the blade is exposed to a strong wind at different velocities. At all points on the blade, the total displacement and maximum von Mises stress values are calculated for different wind velocities. At last, the relation with the maximum von Mises stresses and different air flow velocities is calculated and represented.

Because of fluid pressure, the original structure of turbine blade bends. The largest displacement occurs in the middle part of the blade between both rigid ends.

The maximum displacement is small, this indicates that the strength of the blade effectively protect the blade from wind flow.

The maximum stress in the blade occurs on the nearest point to the rigid blade end. The yield strength for the blade’s material is large enough to consider that the blade is far from failure.

With increase of flow velocity, von Mises stress in the blade increases. The fluid load on the structure at the current flow velocities are not significant enough to affect the design of the blade.

The model developed in this study can be used to decide the best material for the wind turbine blades among different materials under different loading conditions. Also it can be used to examine the strength and stiffness of the turbine blades made of selected materials for different wind velocities. In future works, turbine design parameters such as turbine height and diameter, blade chord length, and number of blades can be changed and this model can be used easily.

Acknowledgements

The author would like to thank the SAUJS editors and reviewers who reviewed the study.

Funding

The author received no financial support for the research, authorship, and/or publication of this paper.

The Declaration of Conflict of Interest/ Common Interest

No conflict of interest or common interest has been declared by the author.

The Declaration of Ethics Committee Approval

The author declares that this document does not require an ethics committee approval or any special permission.

The Declaration of Research and Publicatıon Ethics

The author of the paper declares that he complies with the scientific, ethical and quotation rules of SAUJS in all processes of the article and that he does not make any falsification on the data collected. In addition, he declares that Sakarya University Journal of Science and its editorial board have no responsibility for any ethical violations that may be encountered, and that this study has not been evaluated in any academic publication environment other than Sakarya University Journal of Science.

REFERENCES

[1] H. J. Sutherland, “On the fatigue analysis of wind turbines,” Sandia National Laboratories Report, 1999.

[2] S. R. Winterstein and P. S. Veers, “A numerical analysis of the fatigue and reliability of wind turbine components,” Sandia National Laboratories Report, 2000.

[3] K. Cox and A. Echtermeyer, “Structural design and analysis of a 10 MW wind turbine blade,” Energy Procedia, vol. 24, pp. 194–201, 2012.

[4] M. Yeh and C. Wang, “Stress analysis of composite wind turbine blade by finite element method,” ACMME 2017 5th Asia Conference on Mechanical and Materials Engineering, vol. 241, pp. 12–15, 2017.

[5] L. Wang, R. Quant and A. Kolios, “Fluid structure interaction modeling of horizontal axis wind turbine blades based on CFD and FEA,” Journal of Wind Engineering and Industrial Aerodynamics, vol.158, pp. 11-25, 2016.

[6] E. M. Fagan, M. Flanagan, S. B. Leen, T. Flanagan, A. Doyle and J. Goggins, “Physical Experimental Static Testing and Structural Design Optimisation for a Composite Wind Turbine Blade,” Composite Structures, 2016.

[7] D. K. Choi, B. D. Pyeon, S. Y. Lee, H. G. Lee and J. S. Bae, “Structural Design, Analysis, and Testing of a 10 kW Fabric-Covered Wind Turbine Blade,” Energies, vol.13, pp. 3276, 2020.

[8] M. Casini, “Small Vertical Axis Wind Turbines for Energy Efficiency of Buildings,” Journal of Clean Energy Technologies, vol. 4, no. 1, pp. 56–65, 2016.

[9] H. J. Sutherland, D. E. Berg, and T. D. Ashwill, “A Retrospective of VAWT Technology,” Sandia National Laboratories Report, 2012.

[10] M. Islam, D. King, and A. Fartaj , “Aerodynamic models for Darrieus-type straight-bladed vertical axis wind turbines,” Renewable and Sustainable Energy Reviews, vol. 12, no. 4, pp. 1087–1109, 2008.

[11] A. M. Gorlov, “Development of the helical reaction hydraulic turbine. Final Technical

Report," The US Department of Energy, 1998.

[12] Q. Cheng, X. Liu, H. S. Ji, K. C. Kim, and B. Yang, "Aerodynamic Analysis of a Helical Vertical Axis Wind Turbine," Energies, vol. 10, no. 4, pp. 575–592, 2017.

[13] NACA Report No. 824. http://naca.central.cranfield.ac.uk/reports/1945/naca-report-824.pdf.

[14] Airfoil Tools. http://airfoiltools.com/airfoil/details?airfoil=naca0018-il.

[15] A. Özekes, "Helisel Dikey Eksen Bir Rüzgar Türbininin Belirli Tasarım Kriterleri Altında Performansının İncelenmesi," MSc, Manisa Celal Bayar Üniversitesi, 2019.

[16] Comsol Multiphysics, CFD Module Users Guide, 2018.

[17] S. Turek and J. Hron, "Proposal for numerical benchmarking of fluid-structure interaction between an elastic object and laminar incompressible flow, H. J. Bungartz HJ, M. Schäfer, editors. Fluid-Structure Interaction; Modelling, Simulation, Optimisation," Springer, pp. 371–385, 2007.

[18] ASM Handbook Committee, "ASM Handbook Volume 2: Properties and Selection: Nonferrous Alloys and Special-Purpose Materials," pp. 62–122, 1990.

SAKARYA ÜNİVERSİTESİ
FEN BİLİMLERİ ENSTİTÜSÜ
DERGİSİ

Sakarya University Journal of Science
SAUJS

e-ISSN 2147-835X | Period Bimonthly | Founded: 1997 | Publisher Sakarya University |
http://www.saujs.sakarya.edu.tr/en/

Title: The Relation Between Chebyshev Polynomials and Jacobsthal and Jacobsthal Lucas Sequences

Authors: Şükran UYGUN

Recieved: 2020-02-11 12:18:20

Accepted: 2020-08-29 10:08:44

Article Type: Research Article

Volume: 24
Issue: 6
Month: December
Year: 2020
Pages: 1162-1170

How to cite
Şükran UYGUN; (2020), The Relation Between Chebyshev Polynomials and Jacobsthal and Jacobsthal Lucas Sequences . Sakarya University Journal of Science, 24(6), 1162-1170, DOI: https://doi.org/10.16984/saufenbilder.687708
Access link
http://www.saujs.sakarya.edu.tr/en/pub/issue/57766/687708

Sakarya University Journal of Science 24(6), 1162-1170, 2020

The Relation Between Chebyshev Polynomials and Jacobsthal and Jacobsthal Lucas Sequences

Şükran UYGUN*[1]

Abstract

In this paper Jacobsthal, Jacobsthal Lucas and generalized Jacobsthal sequences are denoted by aid of first or second type of Chebyshev polynomials by different equalities. Then using these equalities a relation is obtained between Jacobsthal and generalized Jacobsthal numbers. Moreever, the nth powers of some special matrices are found by using Jacobsthal numbers or Chebyshev polynomials. Some connections among Jacobsthal, Jacobsthal Lucas are revealed by using the determinant of the power of some special matrices. Then, the properties of Jacobsthal, Jacobsthal Lucas numbers are obtained by using the identities of Chebyshev polynomials.

Keywords: Chebhshev polynomials, Jacobsthal Sequences, Jacobsthal Lucas Sequences

1. INTRODUCTION

For any $n \geq 2$ integers, $a, b; p, q$ are integers, Horadam sequence was defined by Horadam in 1965, denoted by $\{W_n\}_{n>0}$, by the following recursive relation

$$W_n = W_n(a, b; p, q) = pW_{n-1} - qW_{n-2},$$

$$W_0 = a, \;\; W_1 = b.$$

where $p^2 - 4q \neq 0$. For special choices of $a, b; p, q$, special integer sequences are obtained. For example,

$W_n(0,1; 1, -1) = F_n$ classic Fibonacci sequence

$W_n(2,1; 1, -1) = L_n$ classic Lucas sequence

$W_n(0,1; p, -q) = \widetilde{F_n}$ generalized Fibonacci sequence

$W_n(0,1; 1, -2) = j_n$ classic Jacobsthal sequence

$W_n(a, b; 1, -2) = J_n$ generalized Jacobsthal sequence

$W_n(2,1; 1, -2) = c_n$ classic Jacobsthal Lucas sequence

$W_n(0,1; 2, -1) = P_n$ classic Pell sequence

---

* Corresponding Author: suygun@gantep.edu.tr

[1] Gaziantep University, Department of Mathematics, ORCID: https://orcid.org/0000-0002-7878-2175

$W_n(2,2;2,-1) = Q_n$ classic Pell Lucas sequence

$W_n(1,x;2x,1) = T_n$ first kind Chebyshev polynomials

$W_n(1,2x;2x,1) = U_n$ second kind Chebyshev polynomials.

The humankind encountered special integer sequences with Fibonacci in 1202. The importance of Fibonacci sequence was not understood in that century. But now, because of applications of special sequences, there are too many studies on it. For example, the Golden Ratio, the ratio of two consecutive Fibonacci numbers is used in Physics, Art, Architecture, Engineering. We can also encounter Golden Ratio so many areas in nature, human body. Horadam sequence is very important since we can obtain almost most of other special integer sequences by using Horadam sequence. Horadam sequence was studied by Horadam, Carlitz, Riordan and other some mathematicians. Horadam intended to write the first paper which contains the properties of Horadam sequences in [1,2]. In 1969, the relations between Chebyshev functions and Horadam sequences were investigated in [3]. In [6], Udrea found important relations with Horadam sequence and Chebyshev polynomials. In [7], Mansour found a formula for the generating functions of powers of Horadam sequence. Horzum and Koçer studied the properties of Horadam polynomial sequences in [8]. The authors established identities involving sums of products of binomial coefficients that satisfy the general second order linear recurrence in [9]. In [10], the authors obtained Horadam numbers with positive and negative indices by using determinants of some special tridiagonal matrices. In [11], the authors established formulas for odd and even sums of generalized Fibonacci numbers by matrix methods. In [12], some properties of the generalized Fibonacci sequence were obtained by matrix methods. One of important special integer sequences is Jacobsthal sequence because of its application in computer science. In [4,13,14,15], you can find some properties and generalizations of Jacobsthal sequence.

2. MAIN RESULTS

Definition 1. Let $n \geq 2$ integer, the Jacobsthal $\{j_n\}_{n>0}$, the Jacobsthal Lucas $\{c_n\}_{n>0}$ and generalized Jacobsthal $\{J_n\}_{n>0}$ sequences are defined by

$$j_n = j_{n-1} + 2j_{n-2}, \quad j_0 = 0, \ \ j_1 = 1,$$

$$c_n = c_{n-1} + 2c_{n-2}, \quad c_0 = 2, \ \ c_1 = 1,$$

$$J_n = J_{n-1} + 2J_{n-2}, \quad J_0 = a, \ \ J_1 = b.$$

respectively.

Definition 2. Let $n \geq 2$ integer, the first kind $\{T_n\}_{n>0}$, and second kind $\{U_n\}_{n>0}$, Chebyshev polynomial sequences are defined by the following recurrence relations

$$T_n = 2xT_{n-1} - T_{n-2}, \quad T_0 = 1, \ \ T_1 = x,$$

$$U_n = 2xU_{n-1} - U_{n-2}, \quad U_0 = 1, \ \ U_1 = 2x,$$

respectively.

The Binet formula for the Horadam sequence is given by

$$W_n = \frac{Xr_1^n - Yr_2^n}{r_1 - r_2},$$

where $X = b - ar_2$, $Y = b - ar_1$; r_1, r_2 being the roots of the associated characteristic equation of the Horadam sequence $\{W_n\}_{n>0}$. It is obtained the quadratic characteristic equation for $\{W_n\}_{n>0}$, as $r^2 - pr + q = 0$, with roots r_1, r_2 defined by

$$r_1 = \frac{p+\sqrt{p^2-4q}}{2}, \ r_2 = \frac{p-\sqrt{p^2-4q}}{2}.$$

The summation, difference and product of the roots are given as

$$r_1 + r_2 = p, \ \ r_1 - r_2 = \sqrt{p^2 - 4q}, \ \ r_1 r_2 = q.$$

The Binet formulas for the Jacobsthal, Jacobsthal Lucas and generalized Jacobsthal sequences are given by respectively

$$j_n = \frac{2^n - (-1)^n}{3},$$

$c_n = 2^n + (-1)^n$,

$J_n = \frac{A2^n - B(-1)^n}{3}$,

where $A = b + a, \quad B = b - 2a$.

We define $E_w = -XY = pab - qa^2 - b^2$ for Horadam sequence $\{W_n\}_{n>0}$. Similarly, for the first kind Chebyshev polynomials $E_T = -XY = pab - qa^2 - b^2 = x^2 - 1$, and for the second kind Chebyshev polynomials $E_U = -1$. For the Jacobsthal, Jacobsthal Lucas, generalized Jacobsthal numbers, we have $E_J = ab + 2a^2 - b^2$, $E_j = -1$, $E_c = 9$.

Chebyshev polynomials are also defined by

$$T_n(cos\varphi) = cosn\varphi, \ \ U_n(cos\varphi) = \frac{sinn\varphi}{sin\varphi},$$

$n \in Z^+, sin\varphi \neq 0$.

Proposition 3. Jacobsthal, Jacobsthal Lucas, generalized Jacobsthal numbers are obtained by using Chebyshev polynomials as

$$j_n = (2i^2)^{\frac{n-1}{2}} U_{n-1}\left(\frac{1}{2\sqrt{2}i}\right),$$

$$c_n = 2(2i^2)^{\frac{n}{2}} T_n\left(\frac{1}{2\sqrt{2}i}\right),$$

$$\begin{aligned} J_n &= a(2i^2)^{\frac{n}{2}} T_n\left(\frac{1}{2\sqrt{2}i}\right) \\ &+ \frac{(2b-a)(2i^2)^{\frac{n-1}{2}}}{2} U_{n-1}\left(\frac{1}{2\sqrt{2}i}\right) \\ &= (2i^2)^{\frac{n}{2}}\left[\frac{b}{\sqrt{2}i} U_{n-1}\left(\frac{1}{2\sqrt{2}i}\right) - aU_{n-2}\left(\frac{1}{2\sqrt{2}i}\right)\right]. \end{aligned}$$

Proof: The roots of characteristic equation for Horadam sequence are $r_1 = \frac{p+\sqrt{p^2-4q}}{2}$, $r_2 = \frac{p-\sqrt{p^2-4q}}{2}$ are demonstrated by

$$\begin{aligned} r_1, r_2 &= \sqrt{q}\left(\frac{p}{2\sqrt{q}} \pm \sqrt{\left(\frac{p}{2\sqrt{q}}\right)^2 - 1}\right) \\ &= \sqrt{q}(cos\theta \pm isin\theta) \end{aligned}$$

where $cos\theta = \frac{p}{2\sqrt{q}}$. By De Moivre formula it is obtained that

$$r_1^n = q^{\frac{n}{2}}(cosn\theta + isinn\theta),$$

$$r_2^n = q^{\frac{n}{2}}(cosn\theta - isinn\theta).$$

We know that for *p=1, q=-2,* Horadam sequence turns out Jacobsthal and Jacobsthal Lucas sequences. Hence

$$W_n(0,1;1,-2) = j_n = \frac{r_1^n - r_2^n}{r_1 - r_2}$$

$$\begin{aligned} &= \frac{q^{\frac{n}{2}}[(cos\theta + isin\theta)^n - (cos\theta - isin\theta)^n]}{2\sqrt{q}isin\theta} \\ &= \sqrt{2i^2}^{n-1} \frac{sinn\theta}{sin\theta} \\ &= \sqrt{2i^2}^{n-1} U_{n-1}(cos\theta) \\ &= \sqrt{2i^2}^{n-1} U_{n-1}\left(\frac{1}{2\sqrt{2i}}\right). \end{aligned}$$

$$W_n(2,1;1,-2) = c_n = r_1^n + r_2^n$$

$$\begin{aligned} &= \sqrt{2i^2}^n 2cosn\theta = 2\sqrt{2i^2}^n T_n(cos\theta) \\ &= 2\sqrt{2i^2}^n T_n\left(\frac{1}{2\sqrt{2i}}\right). \end{aligned}$$

By $A = b + a, \quad B = b - 2a$, we have

$W_n(a,b;1,-2) = J_n = \frac{Ar_1^n - Br_2^n}{r_1 - r_2} == \frac{q^{\frac{n}{2}}[A(cos\theta+isin\theta)^n - B(cos\theta - isin\theta)^n]}{2\sqrt{q}isin\theta} = \frac{q^{\frac{n}{2}}[cosn\theta(A-B)+isinn\theta(A+B)]}{2\sqrt{q}isin\theta} = \frac{q^{\frac{n}{2}}cosn\theta(A-B)}{3} + \frac{q^{\frac{n-1}{2}}sinn\theta(A+B)}{2sin\theta} = a(2i^2)^{\frac{n}{2}}T_n(cos\theta) + \frac{(2b-a)(2i^2)^{\frac{n-1}{2}}U_{n-1}(cos\theta)}{2} = a(2i^2)^{\frac{n}{2}}T_n\left(\frac{1}{2\sqrt{2}i}\right) + \frac{(2b-a)(2i^2)^{\frac{n-1}{2}}}{2}U_{n-1}\left(\frac{1}{2\sqrt{2}i}\right)$.

By using the well- known property of Chebyshev polynomials as $T_n(x) = xU_{n-1}(x) - U_{n-2}(x)$, it is easily seen that

$$\begin{aligned} J_n = (2i^2)^{\frac{n}{2}} \Bigg[a\frac{1}{2\sqrt{2}i} U_{n-1}\left(\frac{1}{2\sqrt{2}i}\right) \\ - aU_{n-2}\left(\frac{1}{2\sqrt{2}i}\right) \\ + \frac{2b-a}{2\sqrt{2}i} U_{n-1}\left(\frac{1}{2\sqrt{2}i}\right)\Bigg] \\ = (2i^2)^{\frac{n}{2}} \Bigg[\frac{b}{\sqrt{2}i} U_{n-1}\left(\frac{1}{2\sqrt{2}i}\right) \\ - aU_{n-2}\left(\frac{1}{2\sqrt{2}i}\right)\Bigg]. \end{aligned}$$

Corollary 4. Jacobsthal, Jacobsthal Lucas, generalized Jacobsthal numbers can also be demonstrated by using Chebyshev polynomials as

$$j_{n+1} = 2^{\frac{n}{2}} i^{3n} U_n\left(\frac{i}{2\sqrt{2}}\right),$$

$$c_n = 2^{\frac{n+2}{2}} i^{3n} T_n\left(\frac{i}{2\sqrt{2}}\right),$$

$$J_n = i^n \left[\frac{a2^{\frac{n}{2}}}{3} T_n\left(\frac{-i}{2\sqrt{2}}\right) + \frac{(2b-a)2^{\frac{n-1}{2}}}{2i} U_{n-1}\left(\frac{-i}{2\sqrt{2}}\right)\right].$$

Proof:

$$\begin{aligned} j_n = (2i^2)^{\frac{n-1}{2}} U_{n-1}\left(\frac{1}{2\sqrt{2}i}\right) \\ = 2^{\frac{n-1}{2}} i^{n-1} U_{n-1}\left(\frac{-i}{2\sqrt{2}}\right) \\ = 2^{\frac{n-1}{2}} i^{3n-3} U_{n-1}\left(\frac{i}{2\sqrt{2}}\right) \end{aligned}$$

$$\begin{aligned} c_n = (2i^2)^{\frac{n}{2}} T_n\left(\frac{1}{2\sqrt{2}i}\right) = 2^{\frac{n+2}{2}} i^n T_n\left(\frac{-i}{2\sqrt{2}}\right) \\ = 2^{\frac{n+2}{2}} i^{3n} T_n\left(\frac{i}{2\sqrt{2}}\right) \end{aligned}$$

$$\begin{aligned} J_n = i^n \left[\frac{a2^{\frac{n}{2}}}{3} T_n\left(\frac{1}{2\sqrt{2}i}\right) + \\ \frac{(2b-a)2^{\frac{n-1}{2}}}{2i} U_{n-1}\left(\frac{1}{2\sqrt{2}i}\right)\right] = \\ i^n \left[\frac{a2^{\frac{n}{2}}(-1)^n}{3} T_n\left(\frac{i}{2\sqrt{2}}\right) + \\ \frac{(2b-a)2^{\frac{n-1}{2}}(-1)^n}{2i} U_{n-1}\left(\frac{i}{2\sqrt{2}}\right)\right] = i^n \left[\frac{a2^{\frac{n}{2}}}{3} T_n\left(\frac{-i}{2\sqrt{2}}\right) + \\ \frac{(2b-a)2^{\frac{n-1}{2}}}{2i} U_{n-1}\left(\frac{-i}{2\sqrt{2}}\right)\right]. \end{aligned}$$

Theorem 5. Generalized Jacobsthal numbers are denoted by using the first kind Chebyshev polynomials as

$$J_n = \frac{2\sqrt{E_J}(2i^2)^{\frac{n}{2}}}{3} T_n\left(cos\left(\theta - \frac{\varphi}{n}\right)\right),$$

where $cos\varphi = \frac{X-Y}{2\sqrt{E}.}$.

Proof: It is easily seen that $\sqrt{(X-Y)^2 + (i(X+Y))^2} = 2\sqrt{E_J}.$ By using this equality and the third part of the proof of Proposition 3, it is obtained that

$$\begin{aligned} J_n = \frac{(2i^2)^{\frac{n}{2}}}{r_1 - r_2}.[(X-Y)cosn\theta + i(X+Y)sinn\theta] \\ = \frac{(2i^2)^{\frac{n}{2}}}{3}.\left[\frac{(X-Y)cosn\theta}{\sqrt{(X-Y)^2 + \big(i(X+Y)\big)^2}} \\ + \frac{i(X+Y)sinn\theta}{\sqrt{(X-Y)^2 + \big(i(X+Y)\big)^2}}\right] \\ \cdot \sqrt{(X-Y)^2 + \big(i(X+Y)\big)^2} \end{aligned}$$

$$= \frac{(2i^2)^{\frac{n}{2}}2\sqrt{E}}{3} . \left[\frac{(X-Y)cosn\theta}{2\sqrt{E}} + \frac{i(X+Y)sinn\theta}{2\sqrt{E}}\right]$$

$$= \frac{(2i^2)^{\frac{n}{2}}2\sqrt{E}}{3} . [cos\varphi cosn\theta + i(X+Y)sin\varphi sinn\theta]$$

$$= \frac{(2i^2)^{\frac{n}{2}}2\sqrt{E}}{3} \cos(n\theta-\varphi).$$

Theorem 6. Let $n, r, s \in N$. The following relation between generalized Jacobsthal numbers and Jacobsthal numbers is satisfied

$$J_nJ_{n+r+s} - J_{n+r}J_{n+s} = -(-2)^{2n}j_rj_s.$$

Proof: By using Theorem 5, it is obtained that

$$J_nJ_{n+r+s} = \frac{2\sqrt{E_J}(2i^2)^{\frac{n}{2}}}{3}\cos(n\theta - \varphi)\frac{2\sqrt{E_J}(2i^2)^{\frac{n+r+s}{2}}}{3}\cos((n+r+s)\theta-\varphi)$$

$$J_{n+r}J_{n+s} = \frac{4E_J(2i^2)^{\frac{2n+r+s}{2}}}{9}\cos((n+r)\theta-\varphi)\cos((n+s)\theta-\varphi)$$

By substracting the equalities,

$$J_nJ_{n+r+s} - J_{n+r}J_{n+s} = \frac{4E_J(2i^2)^{\frac{2n+r+s}{2}}}{9}.$$

$$\left[\frac{cos\big((2n+r+s)\theta-2\varphi\big) + \cos(r+s)\theta - \cos((2n+r+s)\theta-2\varphi) - \cos(r-s)\theta}{2}\right]$$

$$= \frac{4E_J(2i^2)^{\frac{2n+r+s}{2}}}{9}\left[\frac{\cos(r+s)\theta - \cos(r-s)\theta}{2}\right]$$

$$= -\frac{4E_J(2i^2)^{\frac{2n+r+s}{2}}}{9}[\operatorname{sinr}\theta\sin s\theta]$$

$$= -sin^2\theta\frac{4E_J(2i^2)^{\frac{2n+r+s}{2}}}{9}\left[\frac{\operatorname{sinr}\theta\sin s\theta}{\sin\theta\sin\theta}\right]$$

$$= -sin^2\theta\frac{4E_J(2i^2)^{\frac{2n+r+s}{2}}}{9}\frac{\operatorname{sinr}\theta\sin s\theta}{\sin\theta\sin\theta} =$$

$$= (cos^2\theta - 1)\frac{4E_J(2i^2)^{\frac{2n+r+s}{2}}}{9}U_{r-1}(cos\theta)U_{s-1}(cos\theta)$$

$$= \left[\left(\frac{1}{2\sqrt{2}i}\right)^2 - 1\right]\frac{4E_J(2i^2)^{\frac{2n+r+s}{2}}}{9}U_{r-1}\left(\frac{1}{2\sqrt{2}i}\right)U_{s-1}\left(\frac{1}{2\sqrt{2}i}\right)$$

$$= E_J(2i^2)^{\frac{2n+r+s-2}{2}}U_{r-1}\left(\frac{1}{2\sqrt{2}i}\right)U_{s-1}\left(\frac{1}{2\sqrt{2}i}\right).$$

For the other side of the equality, from Proposition 3, it is obtained that

$$E_J(2i^2)^{2n}j_rj_s = E_J(2i^2)^{2n}(2i^2)^{\frac{r-1}{2}}U_{r-1}\left(\frac{1}{2\sqrt{2}i}\right) \cdot (2i^2)^{\frac{s-1}{2}}U_{s-1}\left(\frac{1}{2\sqrt{2}i}\right).$$

The equality of the results is proved the theorem.

The applications of Theorem 6 for Jacobsthal sequence

$$j_nj_{n+r+s} - j_{n+r}j_{n+s} = -(-2)^{\frac{2n+r+s-2}{2}}U_{r-1}\left(\frac{1}{2\sqrt{2}i}\right)U_{s-1}\left(\frac{1}{2\sqrt{2}i}\right) = -(-)^{2n}j_rj_s$$

The applications of theorem for Jacobsthal Lucas sequence

$$c_nc_{n+r+s} - c_{n+r}c_{n+s} = 9(-2)^{\frac{2n+r+s-2}{2}}U_{r-1}\left(\frac{1}{2\sqrt{2}i}\right)U_{s-1}\left(\frac{1}{2\sqrt{2}i}\right) = 9(-)^{2n}j_rj_s$$

Lemma 7. It is well-known that if

$A = \begin{bmatrix} a & b \\ c & d \end{bmatrix} \in M_2(C)$, then

$$A^n = \begin{cases} \frac{x_1^n - x_2^n}{x_1 - x_2}A - \det(A)\frac{x_1^{n-1} - x_2^{n-1}}{x_1 - x_2}I_2, & x_1 \neq x_2 \\ nx_1^{n-1}A - (n-1)\det(A)x_1^{n-2}I_2, & x_1 = x_2 \end{cases}$$

x_1 and x_2 being the roots of the associated characteristic equation of the matrix A:

$$x^2-(a+d)x+\det(A)=0.$$

Corollary 8. If $A=\begin{bmatrix} a & b \\ c & d \end{bmatrix}\in M_2(C)$ whose trace is $a+d=1$ and determinant is $\det(A)=-2$, then

$$A^n=j_nA-j_{n-1}I_2\ .$$

Proof: We know that the quadratic characteristic equation for the Jacobsthal sequence is $r^2-r-2=0$ with roots $x_1=2,\ x_2=-1$. If a $2x2$ square matrix is chosen whose trace is $a+d=1$ and determinant is $\det(A)=-2$, then we will get

$$\begin{aligned} A^n &= \frac{x_1^n-x_2^n}{x_1-x_2}A-\det(A)\frac{x_1^{n-1}-x_2^{n-1}}{x_1-x_2}I_2 \\ &= j_nA-j_{n-1}I_2 \end{aligned}$$

Because the determinant of the matrix is equal the product of the eigenvalues of the matrix. The trace is equal the sum of the eigenvalues.

Theorem 9. If $A=\begin{bmatrix} a & b \\ c & d \end{bmatrix}\in M_2(C)$ whose trace is $a+d=1$ and determinant is $\det(A)=-2$, then another relation with Jacobsthal sequence and Chebyshev polynomials is established by using the matrix of A as

$$\begin{aligned} A^n = (2i^2)^{\frac{n-1}{2}}\Big[& U_{n-1}\left(\frac{1}{2\sqrt{2}i}\right)A \\ & -\frac{1}{\sqrt{2}i}U_{n-2}\left(\frac{1}{2\sqrt{2}i}\right)I_2\Big] \end{aligned}$$

$$\begin{aligned} A^n = (2i^2)^{\frac{n-1}{2}}\Big[& U_{n-1}\left(\frac{1}{2\sqrt{2}i}\right)\left(A-\frac{1}{\sqrt{2}i}I_2\right) \\ & +\frac{1}{\sqrt{2}i}T_n\left(\frac{1}{2\sqrt{2}i}\right)I_2\Big]. \end{aligned}$$

Proof: We know that

$$\begin{aligned} W_n(0,1;1,-2)=j_n &= \frac{r_1^n-r_2^n}{r_1-r_2} \\ &= (2i^2)^{\frac{n-1}{2}}U_{n-1}\left(\frac{1}{2\sqrt{2}i}\right). \end{aligned}$$

By Corollary 8,

$$A^n=j_nA-j_{n-1}I_2=(2i^2)^{\frac{n-1}{2}}\left[U_{n-1}\left(\tfrac{1}{2\sqrt{2}i}\right)A-\tfrac{1}{\sqrt{2}i}U_{n-2}\left(\tfrac{1}{2\sqrt{2}i}\right)I_2\right].$$

By using the property between Chebyshev polynomials

$T_n(x)=xU_{n-1}(x)-U_{n-2}(x)$, it is obtained that

$$\begin{aligned} A^n = (2i^2)^{\frac{n-1}{2}}\Bigg[& U_{n-1}\left(\frac{1}{2\sqrt{2}i}\right)A \\ & -\frac{1}{\sqrt{2}i}\Bigg(\frac{1}{2\sqrt{2}i}U_{n-1}\left(\frac{1}{2\sqrt{2}i}\right)I_2 \\ & -T_n\left(\frac{1}{2\sqrt{2}i}\right)I_2\Bigg)\Bigg] \end{aligned}$$

$$\begin{aligned} A^n = (2i^2)^{\frac{n-1}{2}}\Big[& U_{n-1}\left(\frac{1}{2\sqrt{2}i}\right)\left(A-\frac{1}{\sqrt{2}i}I_2\right) \\ & +\frac{1}{\sqrt{2}i}T_n\left(\frac{1}{2\sqrt{2}i}\right)I_2\Big]. \end{aligned}$$

Example 10. Let $A=\begin{bmatrix} 1/2 & 3/2 \\ 3/2 & 1/2 \end{bmatrix}$, then

$$\begin{bmatrix} \frac{1}{2} & \frac{3}{2} \\ \frac{3}{2} & \frac{1}{2} \end{bmatrix}^n = j_n\begin{bmatrix} \frac{1}{2} & \frac{3}{2} \\ \frac{3}{2} & \frac{1}{2} \end{bmatrix}-j_{n-1}\begin{bmatrix} 1 & 0 \\ 0 & 1 \end{bmatrix}= \begin{bmatrix} \frac{j_n}{2}-j_{n-1} & \frac{3j_n}{2} \\ \frac{3j_n}{2} & \frac{j_n}{2}-j_{n-1} \end{bmatrix}$$

By the equality of the determinant of matrices, we get a property of Jacobsthal sequence

$$(-2)^n=-2j_n^2+j_{n-1}^2-j_nj_{n-1}.$$

Example 11. Let $A=\begin{bmatrix} 0 & 1 \\ 2 & 1 \end{bmatrix}$, then

$$\begin{aligned} \begin{bmatrix} 0 & 1 \\ 2 & 1 \end{bmatrix}^n = j_n\begin{bmatrix} 0 & 1 \\ 2 & 1 \end{bmatrix}-j_{n-1}\begin{bmatrix} 1 & 0 \\ 0 & 1 \end{bmatrix} \\ = \begin{bmatrix} -j_{n-1} & j_n \\ 2j_n & 2j_{n-2} \end{bmatrix}. \end{aligned}$$

By the equality of the determinant of matrices, we get

$$(-2)^{n-1}=j_n^2+j_{n-2}j_{n-1}.$$

Example 12. Let $A = \begin{bmatrix} 1 & 1 \\ 2 & 0 \end{bmatrix}$, then

$$\begin{aligned}\begin{bmatrix} 1 & 1 \\ 2 & 0 \end{bmatrix}^n &= j_n \begin{bmatrix} 1 & 1 \\ 2 & 0 \end{bmatrix} - j_{n-1} \begin{bmatrix} 1 & 0 \\ 0 & 1 \end{bmatrix} \\ &= \begin{bmatrix} 2j_{n-2} & j_n \\ 2j_n & -j_{n-1} \end{bmatrix}.\end{aligned}$$

By the equality of the determinant of matrices, we get the same result with the previous example.

Theorem 13. By using the properties of Chebyshev polynomials in [16], we get some properties of Jacobsthal and Jacobsthal Lucas sequences as

a) $c_{m+n} + (-2)^n c_{m-n} = c_m c_n,$

b)$j_{n+1} j_{n+2r+1} + (-2)^{n+1} j_r^2 = j_{n+r+1}^2$

c) $c_n c_{n+2r} = (-2)^r [2c_{n+r}^2 - 9j_r^2],$

d) $\frac{j_{nk}}{j_k (-2)^{k(n-1)/2}} = \frac{sinn(cos^{-1}\left(\frac{c_n}{(-2)^{n/2}}\right)}{sin(cos^{-1}\left(\frac{c_n}{(-2)^{n/2}}\right)},$

e) $c_n^2 = 2(-2)^n + c_{2n},$

f) $c_n^2 - c_{n-1} c_{n+1} = -9(-2)^{n-1},$

g) $c_n^2 - 9j_r^2 = (-2)^{n+2}$.

Proof: a) Let $x = \frac{1}{2\sqrt{2}i}$. By using this property

$$j_n = (2i^2)^{\frac{n-1}{2}} U_{n-1}\left(\frac{1}{2\sqrt{2}i}\right),$$

$$c_n = 2(2i^2)^{\frac{n}{2}} T_n\left(\frac{1}{2\sqrt{2}i}\right),$$

it is obtained that

$$T_{m+n} + T_{m-n} = 2T_m T_n$$

$$\frac{c_{m+n}}{2(2i^2)^{\frac{m+n}{2}}} + \frac{c_{m-n}}{2(2i^2)^{\frac{m-n}{2}}} = 2\frac{c_m}{2(2i^2)^{\frac{m}{2}}} \frac{c_n}{2(2i^2)^{\frac{n}{2}}}$$

$$\frac{(2i^2)^{\frac{m-n}{2}} c_{m+n} + (2i^2)^{\frac{m+n}{2}} c_{m-n}}{(2i^2)^m} = \frac{c_m c_n}{(2i^2)^{\frac{m+n}{2}}}$$

$$c_{m+n} + (-2)^n c_{m-n} = c_m c_n$$

b) Similarly

$$U_n U_{n+2r} + U_{r-1}^2 = U_{n+r}^2$$

$$\frac{j_{n+1}}{(-2)^{n/2}} \frac{j_{n+2r+1}}{(-2)^{(n+2r)/2}} + \frac{j_r^2}{(-2)^{(r-1)}} = \frac{j_{n+r+1}^2}{(-2)^{n+r}}$$

$$j_{n+1} j_{n+2r+1} + (-2)^{n+1} j_r^2 = j_{n+r+1}^2$$

c) $T_n T_{n+2r} - (x^2 - 1) U_{r-1}^2 = T_{n+r}^2$

$$\begin{aligned}T_n\left(\frac{1}{2\sqrt{2}i}\right) T_{n+2r}\left(\frac{1}{2\sqrt{2}i}\right) - (\frac{-1}{8} \\ - 1) U_{r-1}^2\left(\frac{1}{2\sqrt{2}i}\right) = T_{n+r}^2\left(\frac{1}{2\sqrt{2}i}\right)\end{aligned}$$

$$\frac{c_n c_{n+2r}}{2(2i^2)^{\frac{n}{2}} 2(2i^2)^{\frac{n+2r}{2}}} + \frac{9j_r^2}{8(2i^2)^{n-1}} = \frac{c_{n+r}^2}{2(2i^2)^n}$$

$$\frac{c_n c_{n+2r}}{4(2i^2)^r} + \frac{9j_r^2}{4} = \frac{c_{n+r}^2}{2}$$

d) By using this property $U_{n-1}(T_k(x)) = \frac{U_{nk-1}(x)}{U_{k-1}(x)}$ and the equality of the results we prove the statement. For the first part of the equality, we get

$$\begin{aligned}U_{n-1}(T_k(x)) &= U_{n-1}\left(\frac{c_n}{2(-2)^{n/2}}\right) \\ &= \frac{sinn(cos^{-1}\left(\frac{c_n}{(-2)^{n/2}}\right)}{sin(cos^{-1}\left(\frac{c_n}{(-2)^{n/2}}\right)}\end{aligned}$$

And for the second part of the equality, we get

$$\frac{U_{nk-1}(x)}{U_{k-1}(x)} = \frac{\left(\frac{j_{nk}}{(-2)^{\frac{nk-1}{2}}}\right)}{\left(\frac{j_k}{(-2)^{\frac{k-1}{2}}}\right)} = \frac{j_{nk}}{j_k (-2)^{\frac{k(n-1)}{2}}}.$$

e) $2T_n^2 = 1 + T_{2n}$

$$2\left(\frac{c_n}{2(-2)^{n/2}}\right)^2 = 1 + \frac{c_{2n}}{2(-2)^n}$$

$$c_n^2 = 2(-2)^n + c_{2n}$$

f) $T_n^2 - T_{n+1} T_{n-1} = 1 - x^2$

$$\left(\frac{c_n}{2(-2)^{n/2}}\right)^2 - \frac{c_{n+1}}{2(-2)^{\frac{n+1}{2}}}\frac{c_{n-1}}{2(-2)^{\frac{n-1}{2}}} = 1 - \left(-\frac{1}{8}\right)$$

$$c_n^2 - c_{n-1}c_{n+1} = -9(-2)^{n-1}$$

g) $T_n^2 - (x^2 - 1)U_{n-1}^2 = 1$

$$\left(\frac{c_n}{2(-2)^{n/2}}\right)^2 - \left(-\frac{1}{8} - 1\right)\frac{j_n^2}{(-2)^{n-1}} = 1$$

$$c_n^2 - 9j_r^2 = (-2)^{n+2}.$$

3. CONCLUSION

In this study, it is aimed to develop some properties of Jacobsthal and Jacobsthal Lucas sequences by using Chebyshev polynomials. It is denoted that the entries of nth power of some special matrices are the elements of Jacobsthal numbers. Jacobsthal, Jacobsthal Lucas, generalized Jacobsthal numbers are obtained by using Chebyshev polynomials.

Acknowledgements

The author would like to thank the anonymous referees for necessary comments which have improved the presentation of the paper.

Funding

The author received no financial support for the research, authorship or publication of this study.

The Declaration of Conflict of Interest/ Common Interest

No conflict of interest or common interest has been declared by the author.

The Declaration of Ethics Committee Approval

The author declares that this document does not require an ethics committee approval or any special permission.

The Declaration of Research and Publication Ethics

The author of the paper declares that she complies with the scientific, ethical and quotation rules of SAUJS in all processes of the paper and that she does not make any falsification on the data collected. In addition, she declares that Sakarya University Journal of Science and its editorial board have no responsibility for any ethical violations that may be encountered, and that this study has not been evaluated in any academic publication environment other than Sakarya University Journal of Science.

REFERENCES

[1] A. F. Horadam, “Basic Properties of a certain generalized Squence of Numbers”, Fibonacci Quarterly, pp. 161-176, 1965.

[2] A. F. Horadam, “Special Properties of the Sequence {Wn(a,b;p,q)}”, Fibonacci Quarterly, vol. 5, pp. 424-434, 1967.

[3] A. F. Horadam, “Tschebyscheff and Other Functions Associated with the Sequence”, Fibonacci Quarterly, vol. 7, no. 1, pp. 14-22, 1969.

[4] A. F. Horadam, “Jacobsthal representation numbers”, The Fibonacci Quarterly, vol. 37, no. 2, pp. 40-54, 1996.

[5] T. Koshy, “Fibonacci and Lucas Numbers with Applications”, John Wiley and Sons Inc., NY 2001.

[6] G. Udrea, “A note on Sequence of A. F. Horadam,” Portugalia Mathematica, vol. 53, no. 24, pp. 143-144, 1996.

[7] T. Mansour, “A formula for the generating functions of powers of Horadam sequence”, Australasian Journal of Combinatorics, vol. 30, pp, 207-212, 2004.

[8] T. Horzum and E. G. Kocer, “On Some Properties of Horadam Polynomials”, Int

math. Forum, vol. 4, no. 25-28, pp. 1243-1252, 2009.

[9] E. Kilic and E Tan, “On Binomial Sums for the General Second Order Linear Recurrence”, Integers Electronic Journal of Combnatorial Number Theory, vol. 10, pp. 801-806, 2010.

[10] N. Taskara, K.Uslu, Y. Yazlık and N. Yılmaz “The Construction of Horadam Numbers in Terms of the Determinant of Tridioganal Matrices”, Numerical Analysis and Applied Mathematics, AIP Conference Proceedings, vol. 1389, pp. 367-370, 2011.

[11] C. K. Ho and C. Y. Chong, “Odd and even sums of generalized Fibonacci numbers by matrix methods”. Am. Inst. Phys. Conf. Ser., vol. 1602, pp. 1026-1032, 2014.

[12] S. P. Jun and K. H. Choi, “Some properties of the Generalized Fibonacci Sequence by Matrix Methods”, Korean J. Math, vol. 24, no. 4, pp. 681-691, 2016.

[13] S. Uygun, “The (s,t)-Jacobsthal and (s,t)-Jacobsthal Lucas sequences”, Applied Mathematical Sciences, vol. 9, no. 7, pp. 3467-3476, 2015.

[14] S. Uygun, “The Combinatorial Representation of Jacobsthal and Jacobsthal Lucas Matrix Sequences”, Ars Combinatoria, vol. 135, pp. 83-92, 2017.

[15] S. Uygun, “A New Generalization for Jacobsthal and Jacobsthal Lucas Sequences”, Asian Journal of Mathematics and Physics, vol. 2, no. 1, pp. 14-21, 2018.

[16] G. Udrea, “A Problem of Diophantos-Fermat and Chebyshev polynomials of the second kind”, Portugalia Mathematica, vol. 52, pp. 301-304, 1995.

SAKARYA ÜNİVERSİTESİ

FEN BİLİMLERİ ENSTİTÜSÜ
DERGİSİ

Sakarya University Journal of Science
SAUJS

e-ISSN 2147-835X | Period Bimonthly | Founded: 1997 | Publisher Sakarya University |
http://www.saujs.sakarya.edu.tr/en/

Title: Clustering Entrepreneurial and Innovative Universities in Turkey According to Their Relevance to Industry 4.0

Authors: Türkay DERELİ, Özge VAR, Alptekin DURMUŞOĞLU

Recieved: 2020-01-31 12:56:40

Accepted: 2020-08-31 16:03:30

Article Type: Research Article

Volume: 24
Issue: 6
Month: December
Year: 2020
Pages: 1171-1184

How to cite
Türkay DERELİ, Özge VAR, Alptekin DURMUŞOĞLU; (2020), Clustering Entrepreneurial and Innovative Universities in Turkey According to Their Relevance to Industry 4.0 . Sakarya University Journal of Science, 24(6), 1171-1184, DOI: https://doi.org/10.16984/saufenbilder.682459
Access link
http://www.saujs.sakarya.edu.tr/en/pub/issue/57766/682459

Sakarya University Journal of Science 24(6), 1171-1184, 2020

Clustering Entrepreneurial and Innovative Universities in Turkey According to Their Relevance to Industry 4.0

Türkay DERELİ[1], Özge VAR[*2] and Alptekin DURMUŞOĞLU[2]

Abstract

Industry 4.0 differentiates production and business models through connecting embedded system, production technologies, and smart production processes. Preparing the young generation to this change is a challenge for higher education. In this study, the adaptation of the entrepreneurial and innovative universities in Turkey to Industry 4.0 is linked with their relevance level to Industry 4.0. To represent the relevance level of universities, a cluster analysis is put forward. Three criteria, named as the number of academic publications related to Industry 4.0, the number of physical structures that facilitate the adaptation to Industry 4.0, and the number of events organized by the universities within the Industry 4.0 concept, were selected for the clustering analysis. To access the number of academic publications of universities, ISI Web of Science database was used. "Industry 4.0" and its components were used as keywords. Both the websites of the each university and Google search results were used to access the values of remaining two criteria. The obtained data were used for K-means clustering analysis. The optimal number of cluster was determined as five with the elbow method. It is thought that the results of the study could be used as an indicator for universities to determine their Industry 4.0 road maps.

Keywords: Industry 4.0, Elbow method, K-means algorithm.

1. INTRODUCTION

The fourth industrial revolution-also named as Industry 4.0- has been the agenda of both businesses and academicians. It considers gathering data in real time, analyzing them, providing quality, faster, cheaper, and useful information about the system [2]. It allows monitoring physical processes with cyber physical systems. The robots can be work collaboratively with the people and communicate with each other. With the entering of smart

---

[1] Hasan Kalyoncu University, Office of President, Gaziantep, Turkey
E-Mail: turkay.dereli@hku.edu.tr ORCID: https://orcid.org/0000-0002-2130-5503
[*] Corresponding Author: ozgevar@gantep.edu.tr ORCID: https://orcid.org/0000-0003-0519-0694
[2] Gaziantep University, Department of Industrial Engineering, Gaziantep, Turkey.
E-Mail:durmusoglu@gantep.edu.tr ORCID: https://orcid.org/0000-0001-9800-5747

production processes, connecting embedded systems, the production and business models have been changed. These changes have also leaded to differentiation in the ways of people works. The study of Janis and Alias [3] is a good example of this point. They defined the workforce needs, and competencies that are required by the Industry 4.0 with using systematic literature survey. The findings have shown that the tasks of low skilled, semi-skilled, and high skilled workers will differentiate with the introduction of the human-machine interface, advanced computation and digitalization. For the high skilled workers, the non- technical competencies such as problem solving and decision-making will come to the forefront especially.

It is expected that, qualified employees will be able to control work environments, which will radically transform. In this case, the education systems play a major role in raising qualified young generations. Especially, the adaptation of the higher education to this technological change is important. Dostal and Wang [4] emphasized this necessity in their study. The potential risks and possible benefits associated with the digital transformation were presented. Preparing the young generation for the threats of technological change in reality has been defined as a challenge. The inclusion of technological change in teaching is evaluated as critic.

Baygın et al. [5], Carutasu and Carutasu [6], and Lensing and Friedhoff [7] support adaptations of the curriculums to Industry 4.0. Baygın et al [5] suggested taking into consideration to the concept and principles of the Industry 4.0 in the curriculums. The laboratory practices were also presented as necessary activities. Carutasu and Carutasu [6] represented the advantages of using digital laboratories. By using ERP and Office 365, enterprise activities and internal workflow of companies were simulated and the professional and soft skills of graduates were measured. It is concluded that, these simulated or digital laboratories provide experiencing the real world business activities without fear of failure. Lensing and Friedhoff [7] focused on the mechanical engineering curricula. The conceptual design for the Internet of Things Laboratory is constructed which attract high school students, undergraduates, and graduates. The importance of working in interdisciplinary is also emphasized. This didactic design provides excellent conditions and options for the setting.

The study of Coskun et al. [8] is an important part of this literature for our research. The methodology of this study helps the selection of the criteria in our analysis. They focused on the adaptation of the engineering education to the requirements of Industry 4.0 vision. For this purpose, the road map was presented. It included three pillars which describe the changes to be conducted in the areas of curriculum development, laboratory concept and student club activities. The other important point of this study is the implementation of this framework in Turkish- German University. It is found feasible to adapt the engineering education to Industry 4.0 vision. Since the Industry 4.0 was introduced in the Hannover Fair by the Germans, it is meaningful to use the framework presented and implemented by Turkish- German University as a reference study.

This review shows that the emerging technologies have huge effect on the education programs. To overcome the new requirements of Industry 4.0, higher education programs should be viewed. This study aims to present the relevance to Industry 4.0 of entrepreneurial and innovative universities in Turkey with using K- means clustering algorithm. These universities are clustered according to three criteria. For defining these criteria, the approach in the study of Coskun et al. [8] is used. The remaining parts of this study are constructed as follows. Section 2 gives the methodology, materials, and methods of the study. The experimental results will be presented in Section 3. The summary of the results, limitations and the suggestions for the future works will be discussed in last section.

2. MATERIALS AND METHODS

There are 207 universities in Turkey. Following the new technological trends and the adaptation to requirements of the new industrial revolution are already important for all of them. However, to evaluate the relevance to Industry 4.0 of all universities is not the focus of this paper. When the list of universities is evaluated, it can easily be seen that some of them is newly established. For this reason, the availabilities of the selected criteria for these universities are impossible. Other challenge is related to the number of criteria in this study. Only three criteria were selected for clustering the universities. It cannot be very comprehensive for the comparison of all universities. Therefore, the focus of this study is limited with the Entrepreneurial and Innovative Universities in Turkey.

The list of Entrepreneurial and Innovative Universities in Turkey has been released by Turkey Scientific and Technological Research Institution (TUBITAK) annually since 2012. This list includes the first fifty universities, which assessed within five dimensions. These dimensions are “Scientific and Technological Research Competence”, “Intellectual Property Pool”, ”Cooperation and Interaction”, “Entrepreneurship and Innovation Culture”, and “Economic Contribution and Commercialization”. With using these five dimensions, entrepreneurship and innovation index is constructed. The aim of this index is measuring the performance of universities regarding the entrepreneurship and innovation. It also contributes to the development of entrepreneurship and innovation indirectly.

In this study, the 50 universities which are in the list of entrepreneurial and innovative universities index in 2018 [9], are evaluated. It is expected that, each university in this list notice the adaptation to requirement of new industrial revolution. The university which takes place near the top, has high relevance towards Industry 4.0.

Figure 1 represents the methodology of this study. It begins with data gathering for clustering. For this process, ISI Web of Science, Google search results and the websites of each university are used as data sources. The scores of universities for each criterion are obtained in this step. The definitions of the criteria and the searching processes are given in the following title.

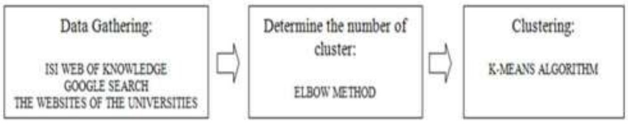

Figure 1 Methodology of this study

In Step 2, the number of clusters is determined with using elbow method. The “K” states the number of clusters for K-means algorithm. Since the success of the clustering algorithm depends on this user defined parameter, determination of the number of clusters is required systematic approach. With the elbow method, the performances of the clustering algorithm for different number of clusters are evaluated. The within- cluster sum of squares is used as a performance indicator of clustering for this method.

The last step of our analysis is clustering the 50 universities according to selected criteria and the determined number of clusters. For this purpose, K- means algorithm is used. It constructs the clusters with the principle of greater similarity within a cluster and greater difference between clusters. The steps of the algorithm are given in the following title. The constructed clusters are named as the relevance level to Industry 4.0. The relevance levels and the entrepreneurial and innovative index number of the universities are compared.

2.1. Inputs of the Clustering Analysis

The three inputs – in other words criteria- are selected for our analysis. These criteria are determined with the help of the study of Coskun et al. [8]. They presented a road map, consisted three pillars, for adaptation of the engineering education to the requirement of Industry 4.0. These three pillars describe the changes in the areas of curriculum development, laboratory concept, and student club activities.

The first pillar is related to the changes in the curriculum. It helps the application and improvement of Industry 4.0 concept in numerous areas. The second pillar, which is named as the changes in laboratory concepts, is presented for understanding the application of the Industry 4.0.

The last pillar represents the changes in the student club activities. These activities are key actors for disseminating the Industry 4.0 vision.

In our study, three criteria are associated with the three pillars of the Coskun et al. [8]. The first pillar in the roadmap, which is named as the changes in the curriculum, is represented as the number of academic publications of universities. To access the curriculums of the all programs in the universities is found a time consuming process. For this reason, the number of academic publications is used to reveal the contribution of universities to improvement of Industry 4.0 concept. ISI Web of Science database is selected to access the number of academic publications of universities. The list of keywords included “Industry 4.0”, “Fourth industrial revolution”, and the paradigms related to Industry 4.0 named as “Big Data”, “Internet of Things”, “Cyber security”, “System Integration”, “Autonomous Robots”, “Cloud Computing”, “Augmented Reality”, and “Additive Manufacturing”. These components pointed out that Industry 4.0 is a value added information processing process [2]. Therefore, they are added the list of keywords.

The Industry 4.0 was first introduced at the Hannover Fair in 2011. For this reason, only time is restricted from 2011 to 2019 during the searching process. The search results are refined by using the affiliation information on the database and the number of publications of each university is accessed. These results are divided by the number of academic member of universities to eliminate the effect of inequality in personal resources. It is assumed that the higher number of publications shows the high relevance towards Industry 4.0.

The second pillar of the roadmap is associated with the number of physical structures in this study. In roadmap, this pillar only represents the laboratories activities. It shows that the quality of education is not only depending on the personal content, but also related to the quality of the educational environment and tools [10]. The technology transfer offices, incubation centers, and techno parks are the important part of this environment. They facilitate the collaboration between university and industry and commercialization of the design of the academicians and students. This provides keeping pace with new technological changes for universities. Therefore, the content of the second pillar of the roadmap is extended for our study and the number of techno parks and technology transfer offices are also evaluated during our analysis. The values of the number of physical structures are obtained by searching the websites of each university. It is expected that the universities, which have the opportunity to access these types of foundations, adapt the new technological era easily. Therefore, they show the high relevance towards Industry 4.0.

The number of events organized by universities within the Industry 4.0 concept is the last criterion of this study, which is associated with the change in the student club activities in roadmap. The content of this pillar is also extended. The number of conferences, seminars, workshops, trainings, and meetings related to Industry 4.0 concept are evaluated. It is assumed that the student clubs related to Industry 4.0 support or held these types of organizations. The values of this criterion are accessed by searching the websites of each university and Google. It is expected that, the university, which organizes an event related to Industry 4.0 concept, attract the students. This facilitates realizing the importance of technological changes, attendance to the event and communicating with experts. Therefore, the high number of events related to Industry 4.0 shows the high relevance towards Industry 4.0.

2.2. Clustering Analysis: Integration K- Means Clustering and Elbow Method

Clustering analysis is a form of unsupervised classification. It partitions or groups a given set of data into disjoint clusters [11]. The goal is that the objects within a group be similar (or related) to one another and different from (or unrelated) to objects in other groups. The greater similarity within a group and the greater difference between groups mean the better clustering [12].

K- means clustering algorithm is the most commonly used one of the partitional clustering techniques [13]. The general logic of this algorithm is to divide a data set consisting of n data objects into a user-specified number of clusters (K) [13], [14].

The steps of the algorithm, which follow a simple way to cluster a given data set, can be summarized as follows [15]:

1. The algorithm starts with the choosing of initial centroids.
2. Each object is assigned to the closest centroid. Each collection of these objects, assigned to a centroid, is a cluster.
3. When all objects have been assigned, the centroid of each cluster updated based on the objects assigned to the cluster.
4. The assignment is repeated until no object changes its cluster.

The quality of clustering is measured by total sum of squares error (total SSE). It measures the total deviation of the response values. The smallest values for SSE mean that the centroids of clustering are a better representation of the points in their cluster. R- square can also be used for the evaluation of the performance of K-means clustering. It shows how successful the fit is in explaining the variation of the data. Therefore, the R-square value closer to 1 indicates that a greater proportion of variance is accounted by the model.

The advantages of this clustering algorithm are its low memory consumption, ease of implementation and high computational efficiency. However, the quality of the resulting clusters depends on the choice of the initial centroids. For this reason, determining the number of clusters is a fundamental issue for K-means clustering. Elbow method is a popular method to determine the optimal value of K. Its basic idea is that with the increasing of the clustering number of K, the total within-cluster sum of squares (WSS) is decreasing [16]. The WSS values of the clustering algorithm are calculated for alternative values of K in increments of one. If increasing the number of K does not contribute significantly to decrease of WSS value, this number should be an optimal number of clusters.

3. EMPIRICAL RESULTS

Before given the results of clustering algorithm, the performances of universities are discussed for each criterion. The scores of the universities for each criterion and the references of the criteria for four universities are presented in Table 1 (in Appendix 1) and Table 2[3] (in Appendix 2) respectively. Considering the number of academic publications related to Industry 4.0 for period between 2011 and 2019, “Middle East Technical University”, “İstanbul Technical University” and “İhsan Doğramacı Bilkent University” are the first three universities with the 93 publications, 88 publications and 52 publications respectively.

When the number of physical structures is reviewed, the results show that each university in the list has at least one of the technology transfer office, techno park or incubation center. For this criterion, the programs and departments related to Industry 4.0 are also evaluated. “Istanbul Technical University” and “Dokuz Eylül University” have Industry 4.0 and Digital Transformation Certification Program. “Sakarya University” establishes Industry 4.0 Coordination Office in the faculty of computer and information science. “Bahçeşehir University” and “Yeditepe University” offer M.Sc. programs related to Industry 4.0. “Düzce University” is uniting with open campus policy and beginning open courses. These situations are added the universities scores for the number of physical structures criterion. The result of this search shows that only “Dokuz Eylül University” has the strategic plan about the Industry 4.0. Coordination Office of Industry 4.0 is established by the university to coordinate this plan.

When universities are ranked according to the number of events related to Industry 4.0 concept, “Yıldız Technical University”, “İstanbul

---

[3] This table is limited to four universities due to space unavailability. We can provide the full table upon request by e-mail.

Technical University", and "Sakarya University" are placed among the first three. The existing platforms related to Industry 4.0 and its components are also evaluated for this criterion. While, "Ankara University" has the Community of Industry 4.0, Industry 4.0 platforms are constructed in "Boğaziçi University", "Gaziantep University", and "Middle East Technical University".

For clustering the universities according to these three parameters, K- means algorithm is performed. The number of clusters is determined by using elbow algorithm. The determination of K value with elbow method is choosing the number of clusters which contributes the significant decreasing in WSS value. The WSS values of clustering algorithm for different number of cluster number can be seen in Figure 2.

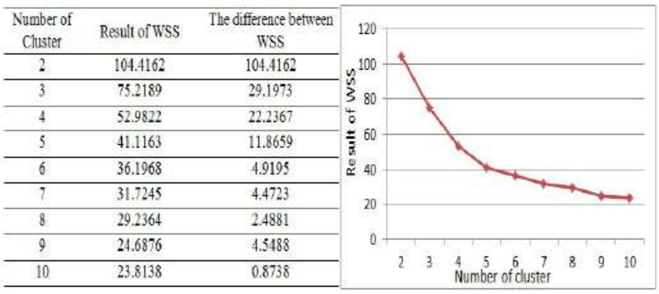

Number of Cluster	Result of WSS	The difference between WSS
2	104.4162	104.4162
3	75.2189	29.1973
4	52.9822	22.2367
5	41.1163	11.8659
6	36.1968	4.9195
7	31.7245	4.4723
8	29.2364	2.4881
9	24.6876	4.5488
10	23.8138	0.8738

Figure 2 Number of clusters and WSS values

Through observations, when the K value is greater than five, the decreasing range of WSS tends to be flat. This means that adding another cluster does not improve the total WSS. According to the elbow method, the optimal number of clusters is determined as five.

When the clustering performance is examined, the total SSE is found 150. The fit explains 72.59% of the total variation in the clustering. Figure 3 shows the averages of each criterion for each cluster. While the horizontal axis represents the clusters, vertical axis represents the averages of each criterion. The average of the number of academic publications increases from cluster 1 to cluster 2, and then decreases from cluster 2 to cluster 5. The average of the number of physical structures increases from cluster 1 to cluster 4. However, the average of this criterion decreases from cluster 4 to cluster 5. The average of the number of events does not show gradually increasing or gradually decreasing from cluster 1 to cluster 5.

It is assumed that getting the higher averages for each criterion means the higher relevance to Industry 4.0. However, the cluster, which has the high averages for all criteria, does not existed in our analysis, or vice versa. For this reason, the averages of each criterion in clusters compare with the total averages of the each criterion in data set.

Cluster 3 has the high averages for all criteria while the cluster 5 has low averages for all. Therefore, the cluster 3 presents the universities, which shows "very high relevance to Industry 4.0" and the cluster 5 represents the universities which shows "very low relevance to Industry 4.0". When evaluating the average of other clusters, Cluster 2, cluster 4 and cluster 1 link to the "high relevance to Industry 4.0", "medium relevance to Industry 4.0 and "low relevance to Industry 4.0" respectively.

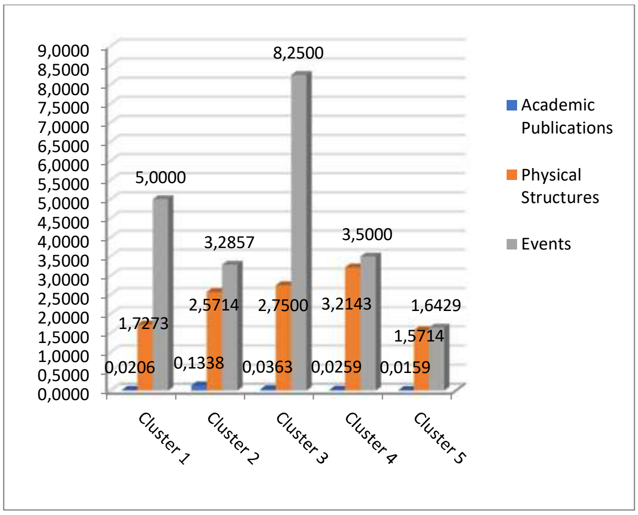

Figure 3 Comparison of averages of criteria in clusters

Clustering results are illustrated in Table 3. The sequence number of universities in entrepreneurial and innovative universities index is also given in the table to compare with the relevance level. The cluster sizes showed that, 14 out of 50 universities have been labeled as "very low relevance to Industry 4.0". It includes 4 foundation and 10 state universities. These 14 universities have low averages for three criteria. "Selçuk University" points out in this cluster. Its ranking in the index is better than the half of the universities. Especially, its low performance in the number of publications causes the assignment to very low relevance cluster.

The cluster of “low relevance to Industry 4.0” includes 9 state and 2 foundation universities. While “Gebze Technical University” and “Izmir Institute of Technology” are at the top 10 in entrepreneurial and innovative universities index ranking, they show low relevance to Industry 4.0. These situations result from their low performance in the number of events and the number of physical structures.

The cluster of “medium relevance to Industry 4.0” includes 14 universities. 10 state and 4 foundation universities exist in this cluster. While “Boğaziçi University” and “Hacettepe University” have high rankings in the index, they are assigned to the medium relevance to Industry 4.0 cluster. Their low performances in the number of events criterion cause these results. The performance of “Başkent University” also points out in this cluster. Its ranking is in the last positions in the index. Because of the advantages of its physical structures, it takes part in this cluster.

When the cluster of “high relevance to Industry 4.0” is evaluated, it is seen that one state university and 6 foundation universities fall into this cluster. “Middle East University” is the only state university in this cluster. Because of its ranking in entrepreneurial and innovative universities index, it is expected to show very high relevance to Industry 4.0. This situation is also in question for “Sabancı University” and “İhsan Doğramacı Bilkent University”. The reason for existing in high relevance to Industry 4.0 cluster is their low performance in the number of events criterion. “Istanbul Şehir University” shows good performance. While it is ranked as a last in the index, it falls into high relevance cluster. The number of publications related to Industry 4.0 supports its relevance level.

Finally, the cluster of “very high relevance to Industry 4.0” is evaluated. Only four universities fall into this cluster and all of them are state universities. The averages of all criteria in this cluster are higher than the total averages. The “İstanbul Technical University” and “Yıldız Technical University” are assigned to this cluster. It is the expected results, because of their high rankings in the index. “Dokuz Eylül University” and “Sakarya University” are also in this cluster. Especially, their good performances in the number of events criterion provide to exist in this cluster.

Table 3
The result of clustering

Sequence number in the index	University	Relevance to Industry 4.0	Sequence number in the index	University	Relevance to Industry 4.0
19	SELÇUK UNIVERSITY	Very Low	5	BOĞAZİÇİ UNIVERSITY	Medium
28	ABDULLAH GÜL UNIVERSITY	Very Low	8	HACETTEPE UNIVERSITY	Medium
29	MEDİPOL UNIVERSITY-İSTANBUL	Very Low	10	EGE UNIVERSITY	Medium
33	MARMARA UNIVERSITY	Very Low	13	GAZİ UNIVERSITY	Medium
35	KARADENİZ TECHNICAL UNIVERSITY	Very Low	18	ANKARA UNIVERSITY	Medium
36	FIRAT UNIVERSITY	Very Low	20	ANADOLU UNIVERSITY	Medium
37	İZMİR UNIVERSITY OF ECONOMY	Very Low	22	BURSA ULUDAĞ UNIVERSITY	Medium
40	MERSİN UNIVERSITY	Very Low	23	GAZİANTEP UNIVERSITY	Medium
42	HASAN KALYONCU UNIVERSITY	Very Low	24	AKDENİZ UNIVERSITY	Medium
43	NİĞDE ÖMER HALİSDEMİR UNIVERSITY	Very Low	25	KOCAELİ UNIVERSITY	Medium
45	ACIBADEM MEHMET ALİ AYDINLAR UNIVERSITY	Very Low	26	ATILIM UNIVERSITY	Medium
47	DÜZCE UNIVERSITY	Very Low	38	YAŞAR UNIVERSITY	Medium
48	ÇANAKKALE ONSEKİZ MART UNIVERSITY	Very Low	39	ÇANKAYA UNIVERSITY	Medium
49	TEKİRDAĞ NAMIK KEMAL UNIVERSITY	Very Low	46	BAŞKENT UNIVERSITY	Medium
7	GEBZE TECHNICAL UNIVERSITY	Low	1	MIDDLE EAST TECHNICAL UNIVERSITY	High
9	İZMİR INSTITUTE OF TECHNOLOGY	Low	3	SABANCI UNIVERSITY	High
12	İSTANBUL UNIVERSITY	Low	4	İHSAN DOĞRAMACI BİLKENT UNIVERSITY	High
17	ERCİYES UNIVERSITY	Low	11	KOÇ UNIVERSITY	High
27	ÇUKUROVA UNIVERSITY	Low	14	ÖZYEĞİN UNIVERSITY	High
30	SÜLEYMAN DEMİREL UNIVERSITY	Low	15	TOBB UNIVERSITY ECONOMICS AND TECHNOLOGY	High
31	YEDİTEPE UNIVERSITY	Low	50	İSTANBUL ŞEHİR UNIVERSITY	High
32	PAMUKKALE UNIVERSITY	Low	2	İSTANBUL TECHNICAL UNIVERSITY	Very High
34	ATATÜRK UNIVERSITY	Low	6	YILDIZ TECHNICAL UNIVERSITY	Very High
41	ESKİŞEHİR OSMANGAZİ UNIVERSITY	Low	16	DOKUZ EYLÜL UNIVERSITY	Very High
44	BAHÇEŞEHİR UNIVERSITY	Low	21	SAKARYA UNIVERSITY	Very High

4. CONCLUSION

Industry 4.0 comes into view with the need for new concepts, skills, and qualifications. To equip the students with these new requirements of industry, the universities are the key actors. The purpose of universities is not only providing proficiencies and skills according to major; but also promoting their students for independent search for getting new knowledge and practical techniques. Their efforts during the adaptation of new technological era ensure knowledge and development of competencies.

In this study, the level of relevance towards Industry 4.0 of the entrepreneurial and innovative universities in TUBITAK list (the first 50 universities) is presented. For this purpose, three criteria are selected. They are named as the number of academic publications, the number of physical structures, and the number of events organized by the university. The optimum number of cluster for the K- means clustering algorithm is determined as five with using elbow algorithm. For this reason, universities are divided to five clusters, which are labeled from “very high relevance” to “very low relevance”.

The results show that the half of the universities shows very low or low relevance towards Industry 4.0. Only, “Dokuz Eylül University” has the strategic plan for this new era. The number of constructed programs, platforms, and centers related to Industry 4.0 are incapable. However, providing basis knowledge and infrastructure for the applied training and preparing the students to the opportunities and threats of the real world should be the major role of universities.

When the number of universities in high relevance and very high relevance clusters are considered, 11 universities are assigned to them. The 5 state and 6 foundation universities exist in these clusters. It means that there is no difference between the state and foundation universities relevance to the Industry 4.0.

It can be also seen that, the number of events organized by the universities has an important role during the clustering. The universities, which have high performance for this criterion, show high relevance to the new era. This result reminds the importance of the promoting the willingness of students for getting new knowledge, research methods and practical techniques with the congress and conferences.

The limitations of this study are summarized in two fold. The first one related to the number of criteria. According to the study of Coskun et al. [8], the number of academics publications, physical structures and events are used for this research. Different parameters, which show the relevance towards Industry 4.0 such as curriculum development, can also be added. The second limitation is related to the contents of the criteria. Only the quantitative aspects of the each criterion are evaluated for this study. However, the qualitative aspects have also important role. For the number of academic publications, the number of citations to the studies can be considered to show the quality of the paper. For the number of physical structures criterion, the number of projects conducted in these centers, the number of collaborations with the industry and the number of technological firms in techno parks can be evaluated. They are very good indicators to show the performances of these structures. The impacts of the events related to Industry 4.0 can be used to represent the quality of the number of events criteria. The number of attendance, the number of keynote speakers and the number of workshops given during the organizations can be good indicators to consider this impact.

As a future work, the qualitative aspects of the indicators will be taken into account. The content of the study can also be broadened with using alternative keywords during the web search and using alternative databases such as Science Direct, ULAKBİM, and Scopus. If the number of criteria is increased and the content of the study is broadened, all universities in the Turkey will be clustered according to their relevance to Industry 4.0.

Appendix 1

Table 1

Industry 4.0 related statistics of universities

#	University	The number of academic member	The number of academic publications	The number of physical structures	The number of events organized within the Industry 4.0 concept
1	MIDDLE EAST TECHNICAL UNIVERSITY	829	93	3	4
2	İSTANBUL TECHNICAL UNIVERSITY	1109	88	3	8
3	SABANCI UNIVERSITY	203	33	3	4
4	İHSAN DOĞRAMACI BİLKENT UNIVERSITY	352	52	2	4
5	BOĞAZİÇİ UNIVERSITY	465	39	4	5
6	YILDIZ TECHNICAL UNIVERSITY	897	30	3	10
7	GEBZE TECHNICAL UNIVERSITY	272	10	1	6
8	HACETTEPE UNIVERSITY	1807	10	3	3
9	İZMİR INSTITUTE OF TECHNOLOGY	189	12	2	5
10	EGE UNIVERSITY	1668	15	3	3
11	KOÇ UNIVERSITY	393	49	2	2
12	İSTANBUL UNIVERSITY	1882	40	2	5
13	GAZİ UNIVERSITY	1439	51	3	4
14	ÖZYEĞİN UNIVERSITY	197	35	2	4
15	TOBB UNIVERSITY ECONOMICS AND TECHNOLOGY	218	24	3	3
16	DOKUZ EYLÜL UNIVERSITY	1629	24	3	7
17	ERCİYES UNIVERSITY	1074	10	2	4
18	ANKARA UNIVERSITY	1767	16	4	4
19	SELÇUK UNIVERSITY	1101	5	2	2
20	ANADOLU UNIVERSITY	730	20	4	5
21	SAKARYA UNIVERSITY	842	15	2	8
22	BURSA ULUDAĞ UNIVERSITY	1117	4	3	3
23	GAZİANTEP UNIVERSITY	672	12	3	5
24	AKDENİZ UNIVERSITY	1299	11	3	2
25	KOCAELİ UNIVERSITY	957	20	3	5

Table 1
Industry 4.0 related statistics of universities (cont.)

#	University	The number of academic member	The number of academic publications	The number of physical structures	The number of events organized within the Industry 4.0 concept
26	ATILIM UNIVERSITY	231	13	3	1
27	ÇUKUROVA UNIVERSITY	1021	3	2	4
28	ABDULLAH GÜL UNIVERSITY	82	8	1	1
29	MEDİPOL UNIVERSITY-İSTANBUL	646	7	1	1
30	SÜLEYMAN DEMİREL UNIVERSITY	859	11	2	5
31	YEDİTEPE UNIVERSITY	540	9	1	5
32	PAMUKKALE UNIVERSITY	974	6	2	5
33	MARMARA UNIVERSITY	1675	16	1	3
34	ATATÜRK UNIVERSITY	1532	15	2	4
35	KARADENİZ TECHNICAL UNIVERSITY	941	19	2	2
36	FIRAT UNIVERSITY	960	33	2	1
37	İZMİR UNIVERSITY OF ECONOMY	209	6	2	3
38	YAŞAR UNIVERSITY	192	7	3	2
39	ÇANKAYA UNIVERSITY	183	8	3	4
40	MERSİN UNIVERSITY	778	3	2	1
41	ESKİŞEHİR OSMANGAZİ UNIVERSITY	813	9	2	5
42	HASAN KALYONCU UNIVERSITY	174	0	1	2
43	NİĞDE ÖMER HALİSDEMİR UNIVERSITY	499	0	2	0
44	BAHÇEŞEHİR UNIVERSITY	471	17	1	7
45	ACIBADEM MEHMET ALİ AYDINLAR UNIVERSITY	468	1	1	0
46	BAŞKENT UNIVERSITY	882	4	3	2
47	DÜZCE UNIVERSITY	544	5	2	3
48	ÇANAKKALE ONSEKİZ MART UNIVERSITY	962	2	1	2
49	TEKİRDAĞ NAMIK KEMAL UNIVERSITY	532	0	2	2
50	İSTANBUL ŞEHİR UNIVERSITY	148	15	2	2

Appendix 2

Table 2
The snapshot of the data set including references of criteria

#	University	Number of Academic Member (YÖK- Last Access 20.01.2020)	Number of Academic Publications (ISI Web of Science- Last Access 20.01.2020)	Physical Structures of Universities (Websites of the Universities- Last Access 21.01.2020)	Link of Events Organized by Universities within the Industry 4.0 Concept (Websites of the Universities and Google Search- Last Access 22.01.2020)
1	MIDDLE EAST TECHNICAL UNIVERSITY	829	93	Teknolojik Dönüşüm/Endüstri 4.0 Platformu, ODTÜ Teknokent, ATOM	https://www.facebook.com/METUSPS/posts/1522567977775687/ https://twitter.com/odtugimer/status/826402235844268034 http://www.milscint.com/tr/savtek-savunma-icin-endustri-4-0-paneliyle-kapanisi-yapti/ https://ymg.odtuvt.org.tr/
2	İSTANBUL TECHNICAL UNIVERSITY	1109	88	İTÜNOVA TTO, İTÜ Arı Teknokent, İTÜ ÇEKİRDEK	https://www.endustri40.com/dijital-donusum-ve-endustri-4-0-itu-is-dunyasi-zirvesi/ http://www.hurriyet.com.tr/kampus/itude-saglikta-endustri-devrimi-icin-onemli-bulusma-40431392 https://twitter.com/ieeeitutk/status/842052911844720640 https://etkinlik.webrazzi.com/etkinlik/detay/24-itu-emos-sanal-ronesans/698 http://www.milliyet.com.tr/ekonomi/endustri-4-0-yerine-milli-teknoloji-hamlesi-2428479 https://erphaber.com.tr/itu-endustri-muhendisligi-bolumunde-uygulamali-caniaserp-egitimleri-basliyor/ https://biletino.com/tr/e-4m6/elektrikli-araclar-zirvesi-2018/ https://itusem.itu.edu.tr/egitimler-ve-programlar/isletme-fakultesi-sertifika-programlari/endustri-40-ve-dijital-donusum-uzmanligi-sertifika-programi
3	SABANCI UNIVERSITY	203	33	Sanayi İşbirlikleri ve Teknoloji Lisanslama Ofisi (I·LO), SUCool, Boğaziçi Üniversitesi İnovita	https://gazetesu.sabanciuniv.edu/2017-07/sanayide-dijitallesme-stratejileri-calistayi-sabanci-universitesi-ev-sahipliginde https://www.endustri40.com/maktek-avrasya-endustri-4-0-semineri/ https://biletino.com/tr/e-41v/buyuk-bulusma-18-mega-trendler http://www.aia-istanbul.org/etkinlikler/akilli-enduestri-ve-enduestri-4-0-eurostars-ikili-goeruesme-etkilnigi-28-mayis-2019-liege
4	İHSAN DOĞRAMACI BİLKENT UNIVERSITY	352	52	Bilkent Üniversitesi TTO, Bilkent Cyberpark	http://web2.bilkent.edu.tr/ttoweb/2017/07/24/endustri-4-0-proje-uretme-calistayi-ve-eslestirme-etkinligi/ http://web2.bilkent.edu.tr/ttoweb/2017/05/26/endustri-4-0-adaptasyon-sureci/ https://www.bilkent.edu/www/ctis-i-endustri-4-0-ogan-ozdogan-kidemli-cozum-satis-yoneticisi-sap-dogu-kampus-c-binasi-sinif-no-cd-b01-900-22-subat-tr/ https://www.linkedin.com/pulse/turizm-40-etkinli%C4%9Fi-bilkentmezunlar-merkezi

Acknowledgements

This paper is an extended version of paper published in [1]. We extend our previous work by using Elbow method to determine the optimal cluster number for K-means clustering algorithm. The authors would like to thank both the chair of the session for the useful feedbacks and the reviewers for all comments on their work.

Funding

The authors received no specific funding for this work.

The Declaration of Conflict of Interest/ Common Interest

No conflict of interest or common interest has been declared by the authors.

Authors' Contribution

TD: supervision, conceptualization, methodology, writing-revision and finalizing.

ÖV: literature review, methodology, data analysis, experimental study, writing initial draft.

AD: supervision, conceptualization, methodology, writing-revision and finalizing.

The Declaration of Ethics Committee Approval

The authors declare that this document does not require an ethics committee approval or any special permission.

The Declaration of Research and Publication Ethics

The authors of the paper declare that they comply with the scientific, ethical and quotation rules of SAUJS in all processes of the paper and that they do not make any falsification on the data collected. In addition, they declare that Sakarya University Journal of Science and its editorial board have no responsibility for any ethical violations that may be encountered, and that this study has not been evaluated in any academic publication environment other than Sakarya University Journal of Science.

REFERENCES

[1] T. Dereli, Ö. Var and A. Durmuşoğlu, “Clustering universities in Turkey according to their relevance to Industry 4.0,” in 10th International Symposium on Intelligent Manufacturing and Service Systems, pp.1147-1153, 2019.

[2] A. Yıldız, “Endüstri 4.0 ve akıllı fabrikalar,” Sakarya University Journal of Science, vol. 22, no. 2, pp. 546-556, 2018.

[3] I. Janis and M. Alias, “A systematic literature review: Human roles, competencies and skills in industry 4.0,” in Asia International Multidisciplinary Conference (AIMC), pp. 1052-1072, 2017.

[4] J. Dostal and X. J. Wang, “Digital identity- significant topic to be included in curriculum content in primary schools,” in 10th International Conference of Education, Research and Innovation, pp. 3808-3813, 2017.

[5] M. Baygin, H. Yetis, M. Karakose, and E. Akin, “An effect analysis of industry 4.0 to higher education,” in 15th International Conference on Information Technology Based Higher Education and Training (ITHET), 2016.

[6] N. L. Carutasu and G. Carutasu, “Replicating enterprise environment using Office 365 to enhance graduates' employability,” in 8th International Conference on Manufacturing Science and Education– Trends in New Industrial Revolution, pp. 1-8, 2017.

[7] K. Lensing and J. Friedhoff, “Designing a curriculum for the Internet-of-Things-Laboratory to foster creativity and a maker mindset within varying target groups,” in 8th CIRP Sponsored Conference on

Learning Factories -Advanced Engineering Education & Training for Manufacturing Innovation, pp. 231-236, 2018.

[8] S. Coşkun, Y. Kayıkcı, and E. Gençay, "Adapting engineering education to industry 4.0 vision," Technologies. vol. 7, 2019.

[9] TUBITAK (2019, Aug 15). Entrepreneurial and innovative universities index 2018 [Online]. Available:https://www.tubitak.gov.tr/sites/default/files/289/gyue_ilk50.pdf.

[10] M. R. Cesur, O. Torkul, İ. H. Cedimoğlu, and S. Uçar, "Intelligent campus implementation for smart cities," Sakarya University Journal of Science, vol. 23, no. 6, pp. 1218-1224, 2019.

[11] K. Kaur, D. S. Dhaliwal, and R. K. Vohra, "Statistically refining the initial points for K-Means clustering algorithm," International Journal of Advanced Research in Computer Engineering & Technology, vol. 2, pp. 2972-2977, 2013.

[12] P. N. Tan, M. Steinbach, and V. Kumar, Introduction to Data Mining, 1st ed. Boston: Pearson- Addison Wesley, 2006.

[13] S. B. Kiriş and F. Tüysüz, "Performance comparison of different clustering methods for manufacturing cell formation," Sakarya University Journal of Science, vol. 21, no. 5, pp. 1031-1044, 2017.

[14] S. Solak and U. Altunışık, "Görüntü işleme teknikleri ve kümeleme yöntemleri kullanılarak fındık meyvesinin tespit ve sınıflandırılması," Sakarya University Journal of Science, vol. 22, no. 1, pp. 56-65, 2018.

[15] U. Altınışık and M. Yıldırım, "Veri madenciliği kümeleme algoritmaları kullanarak arıza dayanımlı denetim sistemi tasarımı," Sakarya University Journal of Science, vol. 17, no.1, pp. 9-16, 2013.

[16] J. Zeng, J. Wang, L. Guo, G. Fan, K. Zhang, and G. Gui, "Cell scene division and visualization based on auto encoder and K-means algorithm," IEEE Access, vol. 7, pp. 165217-165225, 2019.

SAKARYA ÜNİVERSİTESİ

FEN BİLİMLERİ ENSTİTÜSÜ
DERGİSİ

Sakarya University Journal of Science
SAUJS

e-ISSN 2147-835X | Period Bimonthly | Founded: 1997 | Publisher Sakarya University |
http://www.saujs.sakarya.edu.tr/en/

Title: Time Fractional Equation with Non-homogenous Dirichlet Boundary Conditions

Authors: Süleyman ÇETİNKAYA, Ali DEMİR

Recieved: 2020-06-09 09:26:24

Accepted: 2020-09-08 11:07:12

Article Type: Research Article

Volume: 24
Issue: 6
Month: December
Year: 2020
Pages: 1185-1190

How to cite
Süleyman ÇETİNKAYA, Ali DEMİR; (2020), Time Fractional Equation with Non-homogenous Dirichlet Boundary Conditions. Sakarya University Journal of Science, 24(6), 1185-1190, DOI: https://doi.org/10.16984/saufenbilder.749168
Access link
http://www.saujs.sakarya.edu.tr/en/pub/issue/57766/749168

Sakarya University Journal of Science 24(6), 1185-1190, 2020

Time Fractional Equation with Non-homogenous Dirichlet Boundary Conditions

Süleyman ÇETİNKAYA*[1], Ali DEMİR[2]

Abstract

In this research, we discuss the construction of analytic solution of non-homogenous initial boundary value problem including PDEs of fractional order. Since non-homogenous initial boundary value problem involves Caputo fractional order derivative, it has classical initial and boundary conditions. By means of separation of variables method and the inner product defined on $L^2[0,l]$, the solution is constructed in the form of a Fourier series with respect to the eigenfunctions of a corresponding Sturm-Liouville eigenvalue problem including fractional derivative in Caputo sense used in this study. Illustrative example presents the applicability and influence of separation of variables method on fractional mathematical problems.

Keywords: Caputo fractional derivative, Time-fractional diffusion equation, Mittag-Leffler function, Initial-boundary-value problems, Spectral method.

1. INTRODUCTION

Partial differential equations (PDEs) of fractional order turns out to be the best choice of modelling for the numerous processes and systems in various scientific research areas such as applied mathematics, industrial mathematics etc., Since PDEs of fractional order becomes an attractive research area, the mathematical knowledge and methods are used effectively to determine and analyze the solution of it. However further mathematical tools are necessary in view of the applications of mathematical models including fractional derivatives. This provides quite strong motivation and inspiration for scientists to make more research on it. This enriches the various branches of mathematics. Since mathematical models including PDEs of fractional order are suitable for the analysis of the behavior of the complex non-linear processes, it attracts increasing number of scientists.

The derivative in the sense of Caputo is one of the most common one since mathematical models with Caputo derivative gives better results compare to the analysis of ones including other fractional derivatives. In literature, increasing number of studies can be found supporting this conclusion [1-9]. Moreover, the Caputo derivative of constant is zero which is not hold by many fractional derivatives. The solutions of fractional PDEs and ordinary differential equations (ODEs) are determined in terms of Mittag-Leffler function.

---

* Corresponding Author: suleyman.cetinkaya@kocaeli.edu.tr

[1] Kocaeli University, ORCID: https://orcid.org/0000-0002-8214-5099

[2] Kocaeli University, E-Mail: ademir@kocaeli.edu.tr ORCID: https://orcid.org/0000-0003-3425-1812

2. PRELIMINARY RESULTS

Some fundamental definitions and accomplished results of fractional derivative in Caputo sense are presented in this section.

Definition 2.1. The Caputo fractional derivative of $u(t)$ of order q where $n-1<q<n$ is given by the equation

$$D^q u(t)=\frac{1}{\Gamma(n-q)}\int_{t_0}^{t}(t-s)^{n-q-1}\,u^{(n)}(s)ds,\quad t\in[t_0,t_0+T] \tag{1}$$

where $u^{(n)}(t)=\frac{d^n u}{dt^n}$. Note that Caputo fractional derivative becomes the integer order derivative when q is an integer.

Definition 2.2. The fractional derivative of order q for $0<q<1$ in the Caputo sense is defined in the following form:

$$D^q u(t)=\frac{1}{\Gamma(1-q)}\int_{t_0}^{t}(t-s)^{-q}\,u'(s)ds,\quad t\in[t_0,t_0+T] \tag{2}$$

Definition 2.3. The two parameter Mittag-Leffler function by which the solution of eigenvalue problem is denoted, defined in the following form:

$$E_{\alpha,\beta}(\lambda(t-t_0)^{\alpha})=\sum_{k=0}^{\infty}\frac{(\lambda(t-t_0)^{\alpha})^k}{\Gamma(\alpha k+\beta)},\alpha,\beta>0 \tag{3}$$

where λ is a constant. Especially, by taking $t_0=0$, $\alpha=\beta=q$ we get

$$E_{q,q}(\lambda t^q)=\sum_{k=0}^{\infty}\frac{(\lambda t^q)^k}{\Gamma(qk+q)},\quad q>0. \tag{4}$$

Moreover substituting $q=1$, in the equation (4) we have $E_{1,1}(\lambda t)=e^{\lambda t}$. For further reading see [10,11].

3. MAIN RESULTS

Let us consider the following initial boundary value problem including time fractional derivative in Caputo sense.

$$D_t^{\alpha}u(x,t)=\gamma^2 u_{xx}(x,t), \tag{8}$$

$$u(x,0)=f(x), \tag{9}$$

$$u(0,t)=u_0,\ u(l,t)=u_1 \tag{10}$$

where $0<\alpha<1, \gamma\in\mathbb{R}, 0\le x\le l, 0\le t\le T$, u_0 and u_1 are constants.

Before investigating the solution of the problem (8)-(10), let us define the function $v(x,t)$ which homogenizes the boundary conditions (10) as follows:

$$v(x,t)=u(x,t)+\frac{x}{l}(u_0-u_1)-u_0. \tag{11}$$

Via (10), the problem (8)-(10) turns into the following problem (12)-(14).

$$D_t^{\alpha}v(x,t)=\gamma^2 v_{xx}(x,t), \tag{12}$$

$$v(x,0)=f(x)+\frac{x}{l}(u_0-u_1)-u_0\ , \tag{13}$$

$$v(0,t)=0, v(l,t)=0 \tag{14}$$

where $0<\alpha<1, \gamma\in\mathbb{R}, 0\le x\le l, 0\le t\le T$, u_0 and u_1 are constants.

By means of separation of variables method, the generalized solution of above problem is constructed in analytical form. Thus a solution of problem (12)-(14) has the following form:

$$v(x,t;\alpha)=X(x)\,T(t;\alpha) \tag{15}$$

where $0\le x\le l$, $0\le t\le T$.

Plugging (15) into (12) and arranging it, we have

$$\frac{D_t^{\alpha}(T(t;\alpha))}{T(t;\alpha)}=\gamma^2\frac{X''(x)}{X(x)}=-\lambda^2. \tag{16}$$

Equation (16) produces a fractional differential equation with respect to time and an ordinary differential equation with respect to space. The first ordinary differential equation is obtained by taking the equation on the right hand side of Eq. (16). Hence with boundary conditions (14), we have the following problem:

$$X''(x)+\lambda^2 X(x)=0, \tag{17}$$

$$X(0) = X(l) = 0. \tag{18}$$

The solution of eigenvalue problem (17)-(18) is accomplished by making use of the exponential function of the following form:

$$X(x) = e^{rx}. \tag{19}$$

Hence the characteristic equation is computed as follows:

$$r^2 + \lambda^2 = 0. \tag{20}$$

Case 1: If $\lambda = 0$, then the characteristic equation have coincident solutions $r_{1,2} = 0$, which leads to the general solution of the eigenvalue problem (17)-(18) have the following form:

$$X(x) = k_1 x + k_2.$$

By making use of the first boundary condition, we have

$$X(0) = k_2 = 0 \Rightarrow k_2 = 0. \tag{21}$$

Hence the solution becomes

$$X(x) = k_1 x. \tag{22}$$

Similarly second boundary condition leads to

$$X(l) = k_1 l \ = 0 \Rightarrow k_1 = 0. \tag{23}$$

which implies that

$$X(x) = 0. \tag{24}$$

As a result, the characteristic equation (20) can not have the solution for $\lambda = 0$.

Case 2: If $\lambda \neq 0$, then the characteristic equation have the solutions

$$r_{1,2} = \mp i\lambda \tag{25}$$

which leads to the general solution of the eigenvalue problem (17)-(18) have the following form:

$$X(x) = c_1 \cos(\lambda x) + c_2 \sin(\lambda x). \tag{26}$$

By making use of the first boundary condition, we have

$$X(0) = c_1 = 0 \Rightarrow c_1 = 0. \tag{27}$$

Hence the solution becomes

$$X(x) = c_2 \sin(\lambda x). \tag{28}$$

Similarly last boundary condition leads to

$$X(l) = c_2 \sin(\lambda l) = 0 \tag{29}$$

which implies that

$$\sin(\lambda l) = 0. \tag{30}$$

Let $w_n = \sqrt{\lambda} l$. The solutions of (30) can be denoted by means of $w_n = n\pi$ which are eigenvalues of the problem (17)-(18). Moreover we have

$$\lambda_n = \frac{w_n^2}{l^2}, 0 < w_1 < w_2 < w_3 < \cdots \tag{31}$$

As a result

$$X_n(x) = c_n \sin\left(w_n \left(\frac{x}{l}\right)\right) = \sin\left(w_n \left(\frac{x}{l}\right)\right),$$

$$n = 1,2,3, \ldots \tag{32}$$

represent the solutions of the eigenvalue problem.

From equation (16) for each eigenvalue λ_n, we have the following differential equation:

$$\frac{D_t^{\alpha}(T(t;\alpha))}{T(t;\alpha)} = -\gamma^2 \lambda^2 \tag{33}$$

which has the following solutions

$$T_n(t;\alpha) = k_1 E_{\alpha,1}(-\gamma^2 \lambda_n^2 t^{\alpha}) = E_{\alpha,1}\left(-\gamma^2 \frac{w_n^2}{l^2} t^{\alpha}\right), n = 1,2,3, \ldots \tag{34}$$

As a result, the specific solutions of problem (12)-(14) can be written as

$$v_n(x,t;\alpha) = X_n(x) T_n(t;\alpha) = E_{\alpha,1}\left(-\gamma^2 \frac{w_n^2}{l^2} t^{\alpha}\right) \sin\left(w_n \left(\frac{x}{l}\right)\right), n = 1,2,3, \ldots \tag{35}$$

which leads to following general solution of problem (12)-(14)

$$v(x,t;\alpha) = \sum_{n=1}^{\infty} d_n \sin\left(w_n\left(\frac{x}{l}\right)\right) E_{\alpha,1}\left(-\gamma^2 \frac{w_n^2}{l^2} t^{\alpha}\right) \quad (36)$$

Note that the general solution (36) satisfies both boundary conditions (14) and the fractional equation (12). By making use of the inner product defined on $L^2[0,l]$, we determine the coefficients d_n in such a way that the general solution (36) satisfies the initial condition (13). Plugging $t = 0$ into the general solution (36) and making equal to the initial condition (13), we have

$$v(x,0) = f(x) + \frac{x}{l}(u_0 - u_1) - u_0 = \sum_{n=1}^{\infty} d_n \sin\left(w_n\left(\frac{x}{l}\right)\right). \quad (37)$$

By means of the inner product on $L^2[0,l]$, the coefficients d_n for $n = 1,2,3, \ldots$ are obtained as follows:

$$d_n = \frac{2}{l}\left[\int_0^l \sin\left(\frac{k\pi x}{l}\right) f(x)dx + (u_0 - u_1)\int_0^l \sin\left(\frac{k\pi x}{l}\right)\frac{x}{l}dx - u_0\int_0^l \sin\left(\frac{k\pi x}{l}\right)dx\right]. \quad (38)$$

Substituting (38) in (36) leads to the solution of the problem (12)-(14). By making use of (11) and this solution, we obtain the general solution of the problem (8)-(10).

4. ILLUSTRATIVE EXAMPLE

In this section, we first consider the following nonhomogenous initial boundary value problem:

$$u_t(x,t) = u_{xx}(x,t)\ , 0 \le x \le 2, 0 \le t \le T$$

$$u(0,t) = 1\ , u(2,t) = 1, 0 \le t \le T$$

$$u(x,0) = -\sin(\pi x) + 1, 0 \le x \le 2 \quad (39)$$

which has the solution in the following form:

$$u(x,t) = -\sin(\pi x)\, e^{-\pi^2 t} + 1. \quad (40)$$

Now let us take the following fractional heat-like problem into consideration:

$$D_t^{\alpha} u(x,t) = u_{xx}(x,t),\ \ 0 < \alpha < 1,\ \ 0 \le x \le 2,\ 0 \le t \le T \quad (41)$$

$$u(x,0) = -\sin(\pi x) + 1, 0 \le x \le 2 \quad (42)$$

$$u(0,t) = 1, u(2,t) = 1, 0 \le t \le T \quad (43)$$

To make the boundary conditions (43) homogenous, we apply the transformation

$$v(x,t) = u(x,t) - 1 \quad (44)$$

to the above problem which leads to the following fractional heat-like problem

$$D_t^{\alpha} v(x,t) = v_{xx}(x,t), \quad (45)$$

$$v(0,t) = 0\ , v(2,t) = 0, \quad (46)$$

$$v(x,0) = -\sin(\pi x) \quad (47)$$

where $0 < \alpha < 1, 0 \le x \le 2, 0 \le t \le T.$

By means of (36), the solution of problem (45)-(47) is represented in the following form:

$$v(x,t;\alpha) = \sum_{n=1}^{\infty} d_n \sin\left(w_n\left(\frac{x}{2}\right)\right) E_{\alpha,1}\left(-\frac{w_n^2}{2^2} t^{\alpha}\right). \quad (48)$$

The coefficients d_n in (48) are obtained by means of the equation (38) as follows:

$$\Rightarrow d_n = \int_0^2 -\sin\left(\frac{k\pi x}{2}\right)\sin(\pi x)\, dx\ .$$

$d_n = 0$ for $n \neq 2$. For $n = 2$, d_2 is obtained as follows:

$$\Rightarrow d_2 = -\int_0^2 \sin^2(\pi x)\, dx = -\frac{1}{2}\left(x + \frac{\sin(2\pi x)}{4\pi}\right)\Big|_{x=0}^{x=2} = -1. \quad (49)$$

Substituting (49) in (48) leads to the solution of the problem (45)-(47).

$$v(x,t;\alpha) = -\sin\left(w_2 \frac{x}{2}\right) E_{\alpha,1}\left(-\frac{w_2^2}{2^2} t^{\alpha}\right). \quad (50)$$

By making use of (44) and the solution (50), we obtain the general solution of the problem (41)-(43) as follows:

$$u(x,t;\alpha) = -\sin(\pi x)\,E_{\alpha,1}(-\pi^2 t^\alpha) + 1. \quad (51)$$

5. CONCLUSION

In this study, we determine the analytic solution of one dimensional time fractional initial boundary value problem with non-homogenous Dirichlet boundary conditions. By making use of seperation of variables, the solution is constructed in the form of a Fourier series in terms of the eigenfunctions of a corresponding Sturm-Liouville eigenvalue problem.

Funding

The authors received no financial support for the research, authorship, and/or publication of this paper.

The Declaration of Conflict of Interest/ Common Interest

No conflict of interest or common interest has been declared by the authors.

Authors' Contribution

All authors have contributed to the theory of the manuscript and the writing of the manuscript equally.

The Declaration of Ethics Committee Approval

The authors declare that this document does not require an ethics committee approval or any special permission.

The Declaration of Research and Publication Ethics

The authors of the paper declare that they comply with the scientific, ethical and quotation rules of SAUJS in all processes of the paper and that they do not make any falsification on the data collected. In addition, they declare that Sakarya University Journal of Science and its editorial board have no responsibility for any ethical violations that may be encountered, and that this study has not been evaluated in any academic publication environment other than Sakarya University Journal of Science.

REFERENCES

[1] A. Demir, M. A. Bayrak and E. Ozbilge, “New approaches for the solution of space-time fractional Schrödinger equation,” Advances in Difference Equation, vol. 2020, no.133, 2020.

[2] A. Demir and M. A. Bayrak, “A New Approach for the Solution of Space-TimeFractional Order Heat-Like Partial Differential Equations by Residual Power Series Method” Communications in Mathematics and Applications, vol. 10, no. 3, pp. 585–597, 2019.

[3] A. Demir, M. A. Bayrak and E. Ozbilge, “A New Approach for the Approximate Analytical Solution of Space-Time Fractional Differential Equations by the Homotopy Analysis Method”, Advances in Mathematical Physics, vol. 2019, Article ID 5602565, 2019.

[4] A. Demir, M. A. Bayrak and E. Ozbilge, “An Approximate Solution of the Time-Fractional FisherEquation with Small Delay by Residual Power Series Method”, Mathematical Problems in Engineering, vol. 2018, Article ID 9471910, 2018.

[5] S. Cetinkaya, A. Demir and H. Kodal Sevindir, “The analytic solution of initial boundary value problem including time-fractional diffusion equation,” Facta Universitatis Ser. Math. Inform, vol. 35, no. 1, pp. 243-252, 2020.

[6] S. Cetinkaya, A. Demir, and H. Kodal Sevindir, “The analytic solution of sequential space-time fractional diffusion equation including periodic boundary conditions,” Journal of Mathematical Analysis, vol. 11, no.1, pp. 17-26, 2020.

[7] S. Cetinkaya and A. Demir, “The Analytic Solution of Time-Space Fractional Diffusion Equation via New Inner Product

with Weighted Function," Communications in Mathematics and Applications, vol. 10, no. 4, pp. 865-873, 2019.

[8] S. Cetinkaya, A. Demir, and H. Kodal Sevindir, "The Analytic Solution of Initial Periodic Boundary Value Problem Including Sequential Time Fractional Diffusion Equation," Communications in Mathematics and Applications, vol. 11, no. 1, pp. 173-179, 2020.

[9] S. Cetinkaya and A. Demir, "Time Fractional Diffusion Equation with Periodic Boundary Conditions," Konuralp Journal of Mathematics, vol. 8, no. 2, pp. 337-342, 2020.

[10] A. A. Kilbas, H. M. Srivastava and J. J. Trujıllo, "Theory and Applications of Fractional Differential Equations," Elsevier, Amsterdam, 2006.

[11] I. Podlubny, "Fractional Differential Equations," Academic Press, San Diego, 1999.

SAKARYA ÜNİVERSİTESİ

FEN BİLİMLERİ ENSTİTÜSÜ
DERGİSİ

Sakarya University Journal of Science
SAUJS

e-ISSN 2147-835X | Period Bimonthly | Founded: 1997 | Publisher Sakarya University |
http://www.saujs.sakarya.edu.tr/en/

Title: Process Model Development of Lithium-ion Batteries — An Electrochemical Impedance Spectroscopy Simulation

Authors: Salim EROL

Recieved: 2020-07-07 12:16:16

Accepted: 2020-09-08 15:38:37

Article Type: Research Article

Volume: 24
Issue: 6
Month: December
Year: 2020
Pages: 1191-1197

How to cite
Salim EROL; (2020), Process Model Development of Lithium-ion Batteries — An Electrochemical Impedance Spectroscopy Simulation. Sakarya University Journal of Science, 24(6), 1191-1197, DOI: https://doi.org/10.16984/saufenbilder.765554
Access link
http://www.saujs.sakarya.edu.tr/en/pub/issue/57766/765554

Sakarya University Journal of Science 24(6), 1191-1197, 2020

Process Model Development of Lithium-ion Batteries — An Electrochemical Impedance Spectroscopy Simulation

Salim EROL*[1]

Abstract

In this study, a simulation of an electrochemical impedance spectroscopy for lithium-ion batteries was proposed. The electrochemical process was developed from battery electrode kinetics and mass transfer of mobile Li^+ ions through negative and positive electrodes and electrolyte. The phenomena used in this process were represented by an equivalent electrical circuit. A mathematical model was designed using the equivalent circuit and its elements which are in fact battery parameters. The parameter values were presented as compared with real experimental impedance result. The results showed that the simulation and process development were in good agreement with the experimental data.

Keywords: Li-ion battery, impedance spectroscopy, equivalent electrical circuit, porous electrode, solid electrolyte interphase

1. INTRODUCTION

Electrochemical impedance spectroscopy (EIS) is a broadly used noninvasive technique for variety of systems including batteries [1-5], fuel cells [6-9], corrosion detecting [10-14], biosensors [15-19], and so on [20].

Typical representation of EIS of an electrochemical system is complex Nyquist diagram. The Nyquist plot a Li-ion battery shown in Figure 1 can be divided into two regions of high frequency and low frequency. The high frequency region is between points corresponding to 100 kHz and 0.5 Hz. The low frequency region is between points corresponding to 0.5 Hz and 20 mHz. Initial examination of the Nyquist plot the following points can be attested as:

1. The high frequency zone corresponds to the interfacial charge transfer kinetics on electrodes.

2. The low frequency zone corresponds that of a diffusion process in a solid phase.

---

* Corresponding Author: esalim@ogu.edu.tr

[1] Eskişehir Osmangazi University, ORCID: https://orcid.org/0000-0002-7219-6642

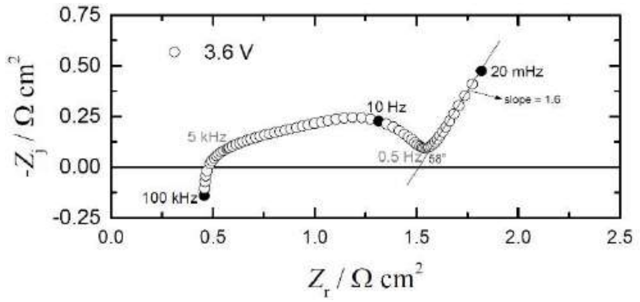

Figure 1 Typical impedance response of a Li-ion battery at 3.6 V cell potential [21]

The objective of the study is to represent a new simulation approach along with a realistic process development for an EIS of the Li-ion batteries.

2. PROCESS DEVELOPMENT

Two prominent theories explain the process of a Li-ion battery. The theory by Doyle et al. [22,23], describes the battery process as given in Figure 1. The battery is considered to include a porous negative electrode, a separator, and a porous positive electrode. Li^+ ions from the positive electrode are released, travel through the electrolyte in the separator region, and are then intercalated into the negative electrode. The following processes may be considered to take place:

1. The de-intercalation reaction of the Li^+ ions in the porous positive electrode.
2. The diffusion of Li^+ ions in the solid phase of positive electrode.
3. Transport of solution in the porous electrode in the positive electrode.
4. Transport of Li^+ ions through the electrolyte in separator region.
5. Transport of solution in porous electrode in the negative electrode.
6. Diffusion of Li^+ ions in the solid phase in the negative electrode.
7. Intercalation reaction of the Li^+ ions in the porous negative electrode.

Along with the above processes, charging of the double layer takes place at both the electrodes. In the analysis charging and Faradaic currents are assumed to be separable, side reactions at the electrode-electrolyte interface are neglected, and Butler-Volmer kinetics are assumed to apply for the reactions at both electrodes. For a single reversible electrochemical reaction, the Butler-Volmer equation is expressed as

$$i = i_0 \left\{ \exp\left[\frac{(1-\alpha)nF}{RT}\eta_s\right] - \exp\left(-\frac{\alpha nF}{RT}\eta_s\right)\right\} \quad (1)$$

where i is the current density, i_0 is called the exchange current density which is the current at zero surface overpotential, η_s is the surface overpotential representing the departure from an equilibrium potential, α is called symmetry factor which is the fraction of the surface overpotential that is with respect to the cathodic reaction, n is the number of electrons transferred through the electrodes, F is the Faraday's constant, R is the universal gas constant, and T is absolute temperature [24].

Doyle et al. [22,23] used a set of equations for the above process and, solving those equations with specific set of conditions, established various parameter relations which enabled them to simulate the impedance spectra and compare it with those of experimental spectra. The complete analysis of the impedance spectra by Doyle et al. enabled them to distinguish the various factors of the battery by separating the terms of the equations which symbolized different processes of the battery. The analysis revealed that the high frequency region of the impedance spectra was mainly due to the interfacial kinetic resistance contributed primarily by the intercalation reaction. It also depended on the depth of discharge of the Li^+ ions. The charge transfer resistance of the de-intercalation reaction is a primary contributor when the depth of discharge was >80% or <20%. The low-frequency region was attributed to the diffusion impedance in the solution phase and the solid phase and to the capacitive double layers at the interface. The summation of all the above regions gave impedance spectra similar to that of the low frequency region.

The other theory, as represented by Aurbach [25], considers a different lithiated graphite electrode structure. This theory places more importance to the reactions at the electrode–electrolyte interface. These reactions lead to the development of an additional film at the interface called the solid electrolyte interphase (SEI). This film also explains the rise in impedance response on cycling of the cell due to continuous formation of additional film during the operation of the battery. The model envisions transport of Li^+ ions through different phases of the film and the final assimilation of Li^+ ions in the negative electrode. Unlike the process described by Doyle et al., interfacial kinetics in the porous electrode is not considered. Instead, diffusion of the Li^+ ions is assumed to occur in the electrode until they reach their final destination. This leads to development of capacitance inside the electrode. Also films on the surface provide different phases; hence, they too contribute to capacitance.

3. MATHEMATICAL MODEL

According to the model that was developed considering the two theories described above, the stages of the battery process are assumed to include:

1. The formation of an SEI due to Li^+ ions reductive strength on the electrode surface,
2. The de-intercalation of Li^+ ions from the positive electrode,
3. Diffusion of Li^+ ions in the solid phase,
4. Transport of solution through the porous electrode and then across the SEI, and
5. Diffusion of Li^+ ions through the electrolyte in the separator.

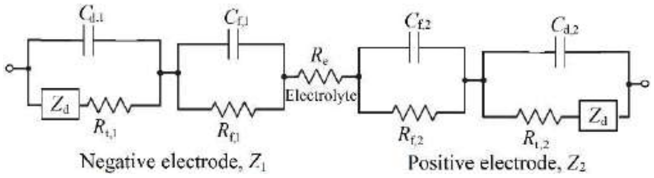

Figure 2 Proposed equivalent electrical circuit for EIS of Li-ion battery

Similar processes are added from stage 1 to 5 in reverse order across the negative electrode with de-intercalation replaced by intercalation reaction in the negative electrode. The capacitance is assumed to exist at both the SEI and the double layer at the electrode surface. The corresponding equivalent circuit is presented as Figure 2.

The impedance of the above circuit can be expressed as

$$Z = Z_1 + R_\mathrm{e} + Z_2 \tag{2}$$

where R_e is the ohmic resistance or the electrolyte resistance; Z_1 and Z_2 are the impedances of corresponding to the negative and positive electrodes, respectively. They are expressed as:

$$Z_1 = \frac{R_{\mathrm{t},1}+Z_\mathrm{d}}{1+\mathrm{j}\omega(R_{\mathrm{t},1}+Z_\mathrm{d})C_{\mathrm{d},1}} + \frac{R_{\mathrm{f},1}}{1+\mathrm{j}\omega R_{\mathrm{f},1}C_{\mathrm{f},1}} \tag{3}$$

and

$$Z_2 = \frac{R_{\mathrm{f},2}}{1+\mathrm{j}\omega R_{\mathrm{f},2}C_{\mathrm{f},2}} + \frac{R_{\mathrm{t},2}+Z_\mathrm{d}}{1+\mathrm{j}\omega(R_{\mathrm{t},2}+Z_\mathrm{d})C_{\mathrm{d},2}} \tag{4}$$

where R_f refers to the SEI film resistances, R_t refers to the charge transfer resistances for the electrode reactions which are intercalation and de-intercalation processes, C_f refers to capacitance representing SEI layer, C_d is the double layer capacitance on the electrode surfaces, and Z_d is the diffusion impedance occurring in both negative and positive electrodes and expressed as:

$$Z_\mathrm{d}(\omega) = Z_\mathrm{d}(0)\frac{\coth(\sqrt{\mathrm{j}K})}{\sqrt{\mathrm{j}K}} \tag{5}$$

where $Z_\mathrm{d}(0)$ refers to the diffusion impedance corresponding to the zero frequency ($f = 0$), and K is the dimensionless frequency given as:

$$K = \frac{\omega\delta^2}{D_{\mathrm{Li}^+}} \tag{6}$$

where δ is the Li^+ ion diffusion layer thickness, and D_{Li^+} is the diffusivity of Li^+ ions. In above Equations (2-6), ω is the angular frequency which is equal to $2\pi f$, and j refers to the imaginary number which is expressed as $\mathrm{j}^2 = -1$.

4. RESULTS AND DISCUSSION

A typical impedance simulation is presented in Figure 3 using the frequency range between 10 kHz to 10 mHz. The model parameters used to obtain this result are presented in Table 1.

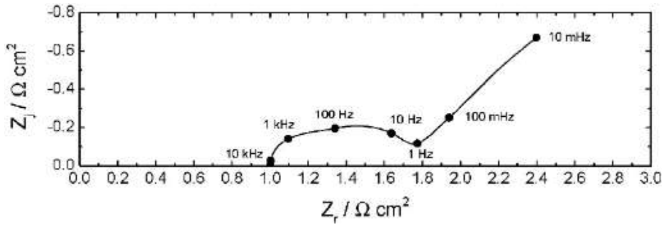

Figure 3 Simulation result for the impedance model in Equations (2-6) shown with the line. The corresponding frequencies are indicated with dots

A certain amount of positive imaginary impedance (Z_j) values can be observed in Figure 1 at a typical impedance response of the Li-ion battery. That type of response is generally interpreted to an inductive behavior of the electrochemical system interested in. However, it is not a case for an energy storage device such as batteries. This inductive behavior at very high frequencies is attributed to noise or impedance related to connection cables in the experimental setup of the Li-ion battery cell. Therefore, only negative values of imaginary impedance forming capacitive loop at high frequencies are observed in the simulation shown in Figure. While doing regression on impedance data, like applied in recently published publications [26-30], one should keep in mind that the positive values of Z_j could be truncated. Thus, no inductive loop could be observed in the simulation result in Figure 3. Also, there are three capacitive loops combined in the simulation constituting a compressed circle like shape similar to the experimental data shown in Figure 1. The large capacitance values in Table 1 forming the capacitive loops here are consistent with assumption of a porous electrode. The capacitive loops are corresponding to the negative electrode, the SEI layer, and the positive electrode. The interception the line of this loop with real impedance (Z_r) axis represents the electrolyte resistance (R_e). If the line is extrapolated to Z_r axis at lower frequencies at the high frequency region, e.g. 10 Hz in Figure 3, the value here is equal to sum of all resistances in the equivalent circuit that are R_e, $R_{f,1}$, $R_{t,1}$, $R_{f,2}$, and $R_{t,2}$. The straight line at low frequencies is attributed to diffusion impedance (Z_d). The simulation values of all above mentioned parameters are indicated in Table 1. The values were selected from the nonrealistic point of view. The aim is to find similar impedance results for Li-ion batteries as obtained in EIS experiments.

Table 1
Model parameters used for the simulation result presented in Figure 3

Parameter	Value
R_e	1.0 Ωcm^2
$R_{f,1}$	0.15 Ωcm^2
$R_{f,2}$	0.15 Ωcm^2
$R_{t,1}$	0.20 Ωcm^2
$R_{t,2}$	0.20 Ωcm^2
$C_{f,1}$	3.16×10^{-3} F/cm^2
$C_{f,2}$	1.00×10^{-2} F/cm^2
$C_{d,1}$	3.16×10^{-2} F/cm^2
$C_{d,2}$	1.00×10^{-1} F/cm^2
D_{Li^+}	1.5×10^{-10} m^2/s
δ	1.5×10^{-4} m
$Z_d(0)$	1.5 Ωcm^2

5. CONCLUSIONS

A detailed preliminary Li-ion battery process model and its mathematical representation in terms of impedance spectroscopy were proposed in this study. Obtained parameters from the equivalent circuit initiate and boost electrochemical modeling for rechargeable batteries. An example of impedance simulation for a Li-ion battery was presented as a result here to express an equivalent circuit of passive electrical elements each representing a physical process. The results show that simulation model could be utilized for modeling Li-ion batteries. This study will give guidance for simulating and modeling not only batteries but also other types of energy storage devices.

Funding

The author received no financial support for the research, authorship, and/or publication of this paper.

The Declaration of Conflict of Interest/ Common Interest

No conflict of interest or common interest has been declared by the author.

The Declaration of Ethics Committee Approval

The author declares that this document does not require an ethics committee approval or any special permission.

The Declaration of Research and Publication Ethics

The author of the paper declares that he complies with the scientific, ethical and quotation rules of SAUJS in all processes of the paper and that he does not make any falsification on the data collected. In addition, he declares that Sakarya University Journal of Science and its editorial board have no responsibility for any ethical violations that may be encountered, and that this study has not been evaluated in any academic publication environment other than Sakarya University Journal of Science.

REFERENCES

[1] S. Buller, M. Thele, E. Karden, and R. W. De Doncker, "Impedance-based non-linear dynamic battery modeling for automotive applications," Journal of Power Sources, vol. 113, no. 2, pp. 422-430, 2003.

[2] H. Blanke et al., "Impedance measurements on lead–acid batteries for state-of-charge, state-of-health and cranking capability prognosis in electric and hybrid electric vehicles," Journal of power Sources, vol. 144, no. 2, pp. 418-425, 2005.

[3] W. Waag, S. Käbitz, and D. U. Sauer, "Experimental investigation of the lithium-ion battery impedance characteristic at various conditions and aging states and its influence on the application," Applied energy, vol. 102, pp. 885-897, 2013.

[4] W. Huang and J. A. A. Qahouq, "An online battery impedance measurement method using DC–DC power converter control," IEEE Transactions on Industrial Electronics, vol. 61, no. 11, pp. 5987-5995, 2014.

[5] J. Landesfeind, D. Pritzl, and H. A. Gasteiger, "An analysis protocol for three-electrode li-ion battery impedance spectra: Part i. analysis of a high-voltage positive electrode," Journal of The Electrochemical Society, vol. 164, no. 7, p. A1773, 2017.

[6] Z. He and F. Mansfeld, "Exploring the use of electrochemical impedance spectroscopy (EIS) in microbial fuel cell studies," Energy & Environmental Science, vol. 2, no. 2, pp. 215-219, 2009.

[7] J. T. Müller, P. M. Urban, and W. F. Hölderich, "Impedance studies on direct methanol fuel cell anodes," Journal of Power Sources, vol. 84, no. 2, pp. 157-160, 1999.

[8] N. Fouquet, C. Doulet, C. Nouillant, G. Dauphin-Tanguy, and B. Ould-Bouamama, "Model based PEM fuel cell state-of-health monitoring via ac impedance measurements," Journal of Power Sources, vol. 159, no. 2, pp. 905-913, 2006.

[9] A. Weiß, S. Schindler, S. Galbiati, M. A. Danzer, and R. Zeis, "Distribution of relaxation times analysis of high-temperature PEM fuel cell impedance spectra," Electrochimica Acta, vol. 230, pp. 391-398, 2017.

[10] M. Kendig, F. Mansfeld, and S. Tsai, "Determination of the long term corrosion behavior of coated steel with AC impedance measurements," Corrosion Science, vol. 23, no. 4, pp. 317-329, 1983.

[11] J. Zhang, P. J. Monteiro, and H. F. Morrison, "Noninvasive surface measurement of corrosion impedance of reinforcing bar in concrete—part 1: experimental results," Materials Journal, vol. 98, no. 2, pp. 116-125, 2001.

[12] K. Jüttner and W. Lorenz, "Electrochemical impedance spectroscopy (EIS) of corrosion processes on inhomogeneous surfaces," in Materials Science Forum, 1989, vol. 44, pp. 191-204: Trans Tech Publ.

[13] M. Behzadnasab, S. Mirabedini, M. Esfandeh, and R. Farnood, "Evaluation of

corrosion performance of a self-healing epoxy-based coating containing linseed oil-filled microcapsules via electrochemical impedance spectroscopy," Progress in Organic Coatings, vol. 105, pp. 212-224, 2017.

[14] J. C. Gomez-Vidal, A. Fernandez, R. Tirawat, C. Turchi, and W. Huddleston, "Corrosion resistance of alumina forming alloys against molten chlorides for energy production. II: Electrochemical impedance spectroscopy under thermal cycling conditions," Solar Energy Materials and Solar Cells, vol. 166, pp. 234-245, 2017.

[15] E. Katz and I. Willner, "Probing biomolecular interactions at conductive and semiconductive surfaces by impedance spectroscopy: routes to impedimetric immunosensors, DNA-sensors, and enzyme biosensors," Electroanalysis: An International Journal Devoted to Fundamental and Practical Aspects of Electroanalysis, vol. 15, no. 11, pp. 913-947, 2003.

[16] M. Varshney and Y. Li, "Interdigitated array microelectrodes based impedance biosensors for detection of bacterial cells," Biosensors and Bioelectronics, vol. 24, no. 10, pp. 2951-2960, 2009.

[17] A. Manickam, A. Chevalier, M. McDermott, A. D. Ellington, and A. Hassibi, "A CMOS electrochemical impedance spectroscopy (EIS) biosensor array," IEEE Transactions on Biomedical Circuits and Systems, vol. 4, no. 6, pp. 379-390, 2010.

[18] W. Cai, S. Xie, J. Zhang, D. Tang, and Y. Tang, "An electrochemical impedance biosensor for Hg2+ detection based on DNA hydrogel by coupling with DNAzyme-assisted target recycling and hybridization chain reaction," Biosensors and Bioelectronics, vol. 98, pp. 466-472, 2017.

[19] J. Dailey, M. Fichera, E. Silbergeld, and H. E. Katz, "Impedance spectroscopic detection of binding and reactions in acid-labile dielectric polymers for biosensor applications," Journal of Materials Chemistry B, vol. 6, no. 19, pp. 2972-2981, 2018.

[20] N. Bonanos et al., "Applications of impedance spectroscopy," Impedance spectroscopy: Theory, experiment, and applications, pp. 175-478, 2018.

[21] S. Erol, "Electrochemical impedance spectroscopy analysis and modeling of lithium cobalt oxide/carbon batteries," Ph.D. Dissertation, University of Florida, 2015.

[22] M. Doyle, J. P. Meyers, and J. Newman, "Computer simulations of the impedance response of lithium rechargeable batteries," Journal of the Electrochemical Society, vol. 147, no. 1, p. 99, 2000.

[23] M. Doyle and J. Newman, "Modeling the performance of rechargeable lithium-based cells: design correlations for limiting cases," Journal of Power Sources, vol. 54, no. 1, pp. 46-51, 1995.

[24] T. F. Fuller and J. N. Harb, Electrochemical engineering. John Wiley & Sons, 2018.

[25] D. Aurbach, "Review of selected electrode–solution interactions which determine the performance of Li and Li ion batteries," Journal of Power Sources, vol. 89, no. 2, pp. 206-218, 2000.

[26] U. Morali and S. Erol, "Analysis of electrochemical impedance spectroscopy response for commercial lithium-ion batteries: modeling of equivalent circuit elements," Turkish Journal of Chemistry, vol. 44, no. 3, pp. 602-613, 2020.

[27] U. Morali and S. Erol, "The comparison of electrochemical impedance behaviors of lithium-ion and nickel-metal hydride batteries at different state-of-charge conditions," Journal of the Engineering and Architecture Faculty of Eskişehir Osmangazi University, vol. 28, no. 1, pp. 1-8, 2020.

[28] U. Morali, "Influence of charge conditions on battery dynamics of a commercial lithium-ion cell," Hacettepe Journal of Biology and Chemistry, vol. 48, no. 3, pp. 203-210, 2020.

[29] U. Morali and S. Erol, "Electrochemical impedance analysis of 18650 lithium-ion and 6HR61 nickel-metal hydride rechargeable batteries," Journal of the Faculty of Engineering and Architecture of Gazi University, vol. 35, no. 1, pp. 297-310, 2020.

[30] S. Erol, Impedance Analysis and Modeling of Lithium-ion Batteries. Lap Lambert, 2016.

SAKARYA ÜNİVERSİTESİ
FEN BİLİMLERİ ENSTİTÜSÜ
DERGİSİ

Sakarya University Journal of Science
SAUJS

e-ISSN 2147-835X | Period Bimonthly | Founded: 1997 | Publisher Sakarya University |
http://www.saujs.sakarya.edu.tr/en/

Title: A Practical Distributed Lightweight Multi-Hop Time Synchronization Algorithm for Linear Wireless Sensor Networks Implemented on a PIC Based System with Realistic Experimental Analysis

Authors: Ahmet ERPAY, Md Abdullah AL IMRAN, Ali KARA

Recieved: 2020-03-29 20:30:10

Accepted: 2020-09-09 11:05:50

Article Type: Research Article

Volume: 24
Issue: 6
Month: December
Year: 2020
Pages: 1198-1209

How to cite
Ahmet ERPAY, Md Abdullah AL IMRAN, Ali KARA; (2020), A Practical Distributed Lightweight Multi-Hop Time Synchronization Algorithm for Linear Wireless Sensor Networks Implemented on a PIC Based System with Realistic Experimental Analysis. Sakarya University Journal of Science, 24(6), 1198-1209, DOI: https://doi.org/10.16984/saufenbilder.710984
Access link
http://www.saujs.sakarya.edu.tr/en/pub/issue/57766/710984

Sakarya University Journal of Science 24(6), 1198-1209, 2020

A Practical Distributed Lightweight Multi-Hop Time Synchronization Algorithm for Linear Wireless Sensor Networks Implemented on a PIC Based System with Realistic Experimental Analysis

Ahmet ERPAY[1], Md Abdullah AL IMRAN[*2], Ali KARA[3]

Abstract

Time synchronization is fundamental in the distributed networked systems, especially in Wireless Sensor Networks where a global time is essential to make sense of the events like collection of data and scheduled sleep/wake-up of nodes. There exists numerous time synchronization algorithms and techniques in the literature. Nonetheless, these proposed methods lack realistic experimentation of the synchronization process which is vital from the realization point of view. This study aims to bridge that gap by presenting a distributed lightweight time synchronization protocol implemented on an inexpensive PIC platform. Furthermore, PIC-based systems hadn't been investigated before and gives an idea of the simplicity of the algorithm. Experimental analysis was done to see the performance of the protocol. The core motivation of the experiments was to the study the impact of the environment (e.g. indoor, outdoors, temperature variations and interference) on the synchronization. Our findings show that temperature indeed impedes the synchronization accuracy.

Keywords: Clock drift and offset, Linear Wireless sensor network, Spanning tree network, Time synchronization.

---

[1] TUSAS, E-Mail: ahmetr@gmail.com ORCID: https://orcid.org/0000-0001-8779-0997
[*] Corresponding Author: alimran.mdabdullah@gmail.com
[2] Atılım University, ORCID: https://orcid.org/0000-0002-2286-7890
[3] Atılım University, E-Mail: ali.kara@atilim.edu.tr ORCID: https://orcid.org/0000-0002-9739-7619

1. INTRODUCTION

Wireless Sensor Networks (WSNs) consist of small, low-power and inexpensive devices that can sense their surroundings such as temperature, humidity, sound and light [1]. WSN devices are called sensor nodes which can form spanning networks without any infrastructure. As these nodes are low-priced and have small form factors, they can be placed in diverse areas to monitor different type of environments on periodic time span or event based. The sensed data often in the form of current, voltage or their electrical derivatives is then sent to a certain node to be processed or routed to a base station. The collected data themselves are not useful if the time stamps are not attached.

Having said so, synchronization of time is essential in the WSN systems as well as all other networked systems. It creates global or reference time within the network. Data fusion, coordination of complex tasks or time division multiple access (TDMA) requires clock synchronization of the nodes [2]. Furthermore, the time synchronization is essential for power efficiency schemes; nodes wake up at precise time intervals with respect to other nodes and turn on/off their transceivers to reduce the power consumption. To synchronize time, there exists well-established methods like Network Time Protocol (NTP) [3] and Global Positioning System (GPS) [4]. NTP is the most widely used technique which necessitates internet availability and is complicated to implement due to computational requirements. GPS is costly and needs open-air to get the timing data from satellites.

These shortcomings lead to search for alternative solutions. The time synchronization process can be basically established by taking time measurements at each node as showcased in [5]. These measurements are susceptible to non-deterministic processes on the processor, communication modules and the environment. This is mainly because each node's local time is derived directly from the on-board oscillator, the inherent clock source. Therefore, the imperfection of the oscillator leads to time drift of the clock which accumulates to an overall offset, even when the clock was initially tuned. Needless to say, the oscillator based problems are related to manufacturing parameters and environmental conditions like temperature. As a result, these non-deterministic factors constraint the time synchronization process [6]. Additionally, these challenges contradict the requirements of synchronization schemes e.g. energy efficiency, scalability, precision and robustness where there may even be some trade-offs.

Since there exists hierarchical relationship between the nodes in a WSN system, it is possible to carry out synchronization using one of the two methods: single-hop or multi-hop. A node directly synchronizing with another node in the network is called a single-hop network. Alternatively, in a multi-hop network two nodes can only communicate via one or more intermediary nodes. The abundant synchronization methods can be categorized into these abovementioned network structures. Reference Broadcast Synchronization (RBS) is a single-hop method where master node broadcasts beacons and others benefit from that periodic beacon [7]. While RBS is freed of some sender-based uncertainty, it is not highly scalable. Flooding Time Synchronization Protocol (FTSP), a single-hop type, is presented in [8]. FTSP method can choose a root node dynamically which then broadcasts periodic messages in the network. Every node that receives this message rebroadcasts it while recording a time stamp at every received message. FTSP can accommodate network topology variations and is robust against failure of nodes. It is also energy efficient. Delay Measurement Time Synchronization (DMTS) is another single-hop type where the leader node broadcasts its time. Nodes hearing this message measures the delay and adds it to the leader's time to set their own clocks [9]. This technique is efficient and simple but precision is low. All single-hop type methods can be extended to multi-hop types with some minor changes. The multi-hop types are: Timing-Sync Protocol for Sensor Networks (TPSN) [10] which consists of two stages: discovery of levels and the system synchronization. In the level discovery phase, one node is selected as a root (level 0) and others are assigned different levels according to the closeness of the nodes. Nodes synchronize with pair-wise synchronization method from level 0 to the last level in synchronization phase. TPSN has good accuracy but does not allow dynamic topology. Lightweight Tree-based Synchronization (LTS) presented in [11] is constructed based on pair-wise synchronization. LTS has two different approaches: first one starts with creating a spanning tree with a sink node that has some reference point. Then it uses $(\mathrm{n}-1)$ pair-wise synchronizations for n nodes in the network. It is a flexible method but complexity can be high or low due to sink node. In [12], Average Time Synchronization (ATS) is presented where the average times are found for every node in the network using pair-wise message exchanges. In ATS, the sequence of averaging nodes is important and uses more energy compared to the classical pair-wise method. In Time-Diffusion Synchronization Protocol (TDP) there is an equilibrium-time that is agreed throughout the network by all the nodes and all local clocks are bounded around this time with a small deviation [13]. TDP is flexible and fault tolerant but needs high time for convergence.

The synchronization methods for both single and multi-hop networks with experimental analysis are presented in [14-17]. These tests were generally carried out in indoor environment and run in ideal conditions. It is seen that in many cases temperature, RF interference and realistic conditions were neglected for implementations on different motes. Additionally, various multi-hop topologies have been established experimentally with the exception of linear topology. It is worthwhile to note the possible application areas of the linear topology e.g. curvilinear entities like roads, tunnels and pipelines [5]. And experiments should be performed in harsh environments e.g. rural or sylvan areas where sensor nodes are usually used for practicality.

In this paper, we propose a linear topology featuring multi-hop time synchronization algorithm experimented on the rural area where different conditions were investigated. Our goal is to demonstrate time synchronization for practical usage. The remainder of the paper is structured as follows: Section II describes the methodology. Section III explains the experiment setup and results. Finally, the conclusions are drawn in Section IV.

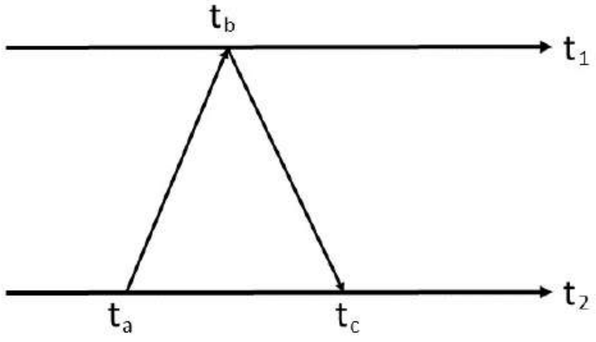

Figure 1 Two-way handshaking

2. METHOD AND IMPLEMENTATION

In this section, we present the time synchronization procedure along with the related implementation details including the system setup.

2.1. Time Synchronization Method

A sensor node's clock is generally represented by Equation 1.

$$t_a = \alpha_a + \beta_a t_u, \tag{1}$$

where t_a is local time, α_a and β_a are the respective offset and drift terms of the node a and t_u is the universal time [17-20]. In an ideal clock, α_a should be zero and β_a should be one; the local time is equal to the universal time (UTC). However, a real clock behaves differently. There is always an offset difference α_a and a clock rate difference which is β_a. Drift and offset values may vary disproportionately for each of the nodes while appearing to be constant for a short period of time. Assuming β_a does not change for a long period or has a very slow rate, Equation 1 can be extending to formulate the local time in a pair-wise synchronization as Equation 2.

$$t_1 = \alpha_{12} + \beta_{12} t_2 \tag{2}$$

On the above equation, parameters t_1 and t_2 are the clocks of nodes 1 and 2 respectively, α_{12} is the relative offset, β_{12} is the relative drift between two clocks. Assuming clocks of two nodes are well-synchronized, relative offset and relative drift should be zero and one respectively. However, since two nodes generally have different clock rates, these ideal values cannot be achieved. In essence, the time synchronization can be carried out if the relative offset and drift are known. A two-way handshake between nodes 1 and 2 can be performed to compute the relative offset and relative drift terms.

Referring to Figure 1, t_a is the local time of node 2 transmitted to node 1. Upon reception of this message at node 1, it responds with its own clock t_b. Node 2 then notes the time of reception, t_c, as it receives the reply from node 1. Finally a data-point or a tuple consisting of the three time-stamps (t_a, t_b, t_c) is formed. This data-point is then utilized by node 2 to make an estimate of node 1's clock. To improve the estimation, several data-points are taken. After enough data-points are recorded, equations 3 and 4 can be employed to put constraints on the relative drift term.

$$\beta_a(i) = \frac{t_a(i) - t_a(i-1)}{t_b(i) - t_b(i-1)} \tag{3}$$

$$\beta_b(i) = \frac{t_c(i) - t_c(i-1)}{t_b(i) - t_b(i-1)} \tag{4}$$

If the clocks' rates are equal, the time duration between consecutive points should be same; the numerator and the denominator ratio in the Equation 3 and 4 should be equal. Usually the drift limits, β_a and β_b, are in the vicinity of one. By using these drift values, upper and lower bounds of relative offset is found as of Equations 5 and 6.

$$\alpha_a(i) = t_a(i) - \beta_a(i) t_b(i) \tag{5}$$

$$\alpha_b(i) = t_c(i) - \beta_b(i) t_b(i) \tag{6}$$

The variation of relative drifts causes variation on α_a and α_b. Large variations of the relative drift can cause accumulations on the relative offsets. Using upper and lower values, estimation parameters α and β can be obtained as Equation 7 and 8.

$$\alpha(i) = \frac{\alpha_a(i) + \alpha_b(i)}{2} \tag{7}$$

$$\beta(i) = \frac{\beta_a(i) + \beta_b(i)}{2} \tag{8}$$

For n consecutive data-points (n − 1) different relative offset and relative drift values are estimated. Taking average of these estimated values eliminates the effect of random delays [17].

$$\alpha_{avg} = \frac{1}{n-1} \sum_{j=1}^{n-1} \alpha(j) \tag{9}$$

$$\beta_{avg} = \frac{1}{n-1} \sum_{j=1}^{n-1} \beta(j) \tag{10}$$

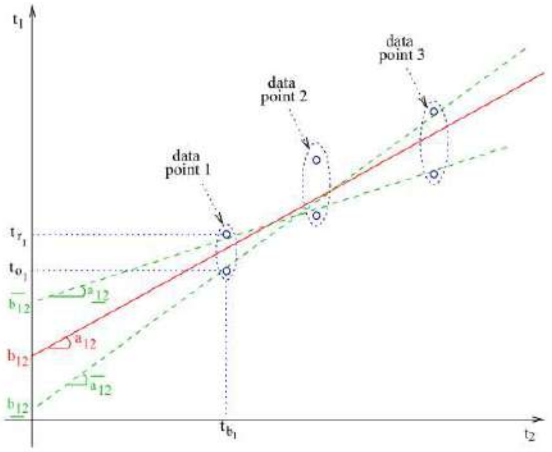

Figure 2 Limitation of the consecutive data-points

In Figure 2, from [10], the limitations of the consecutive data-points are illustrated. When all points are combined, the deciding line should pass between every t_b and t_r pair, where t_b and t_r are equal to t_b and t_c respectively in Figure 1. As the deciding line can not pass between all data points practically, this limitation method is not exactly applicable, however it gives general idea about how to handle data-points like averaging.

After estimation values are calculated, node 2 can update its clock to the reference clock i.e. the clock of node 1 by using Equation 11.

$$t_{2-estimate} = \frac{t_2 - \alpha_{avg}}{\beta_{avg}} \tag{11}$$

2.2. Implementation

Adaptation of synchronization protocol is performed on a PIC platform to investigate the extent of this protocol on a different platform. The *MikroE Clicker 2* board was chosen as the PIC platform where Microchip's *PIC18F87J50* is used as the microcontroller. In conjunction with this base board, the *CC1200* radio manufactured by Texas Instruments as the RF module, powered with Li-ion battery, a node is formed. It is worthwhile to note that, the constructed nodes in this context are used to verify the realization of the time synchronization algorithm rather than a fully functional system.

These nodes are distributed in a wide geographical area where one-hop distance ranges between 1-2 km. A representative distribution of n nodes is seen in Figure 3. Although distances between nodes vary, it is made sure that every node can establish one-hop communication with neighbor nodes.

Nodes' distribution resembles to a bus topology; however, a tree topology is more feasible in this case. Although the structure does not fit in any basic topologies, it is close to a spanning tree where it is a tree topology or mimics a partially connected mesh topology in some sense. There is a root (master) node and other nodes are connected to it preserving the hierarchical relationship in a single branch as shown on the Figure 4.

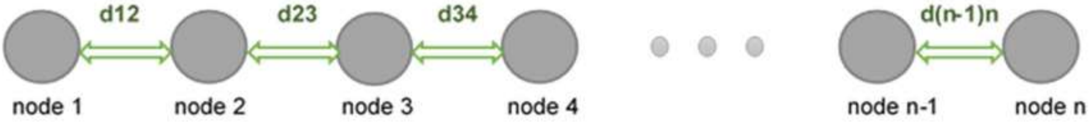

Figure 3 Distribution of nodes

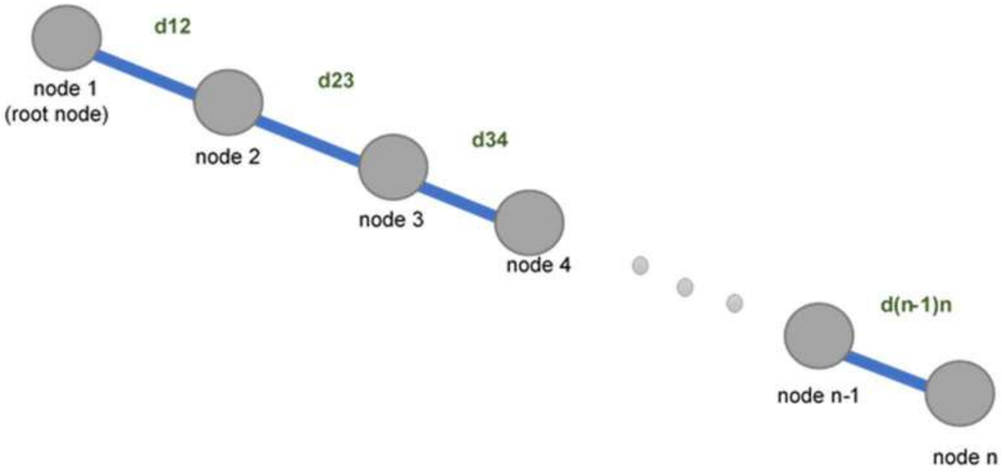

Figure 4 Spanning tree network of nodes

The time synchronization method is implemented such that a parent-child dual is constructed throughout the network from root node to the last node. Parent and child nodes perform pairwise synchronization, where child node updates its time with respect to its parent node. Every node in the WSN network is assigned a distinctive ID which help establish the parent-child relationship. All nodes except root and last node can be parent and child while root node is always parent and last node is always child.

Network's time synchronization process starts with the root node. Root node connects to the second node as a parent. The child node updates its current time with pairwise synchronization with respect to parent node, and then it disconnects from parent node. Then, the previously denoted child node becomes a parent itself whereas the next node down in the hierarchy becomes the child node. This iterative process continues until the last node updates its current time and disconnects from its parent. At the end of the process, the network is considered to be synchronized. Parent-child structure is the place where time synchronization algorithm is applied as explained in section 2.1.

3. EXPERIMENTS AND RESULTS

In this section, the experimental setup and the finding of the experiment are presented.

3.1. Experiments

Experimental setup is composed of two computers and six sensor nodes to demonstrate the discussed method in section 2.1. The general setup is shown in Figure 5 with the test procedure in Figure 6. Initially, the computers' clock is synchronized with each other. Then, first and sixth node are connected to the two computers to see and record their clocks using a custom developed computer application well-suited for this purpose. The program can detect IDs and initiate a time synchronization if ID equals to one which means that is the first node. Test procedure proceeds with the following steps:

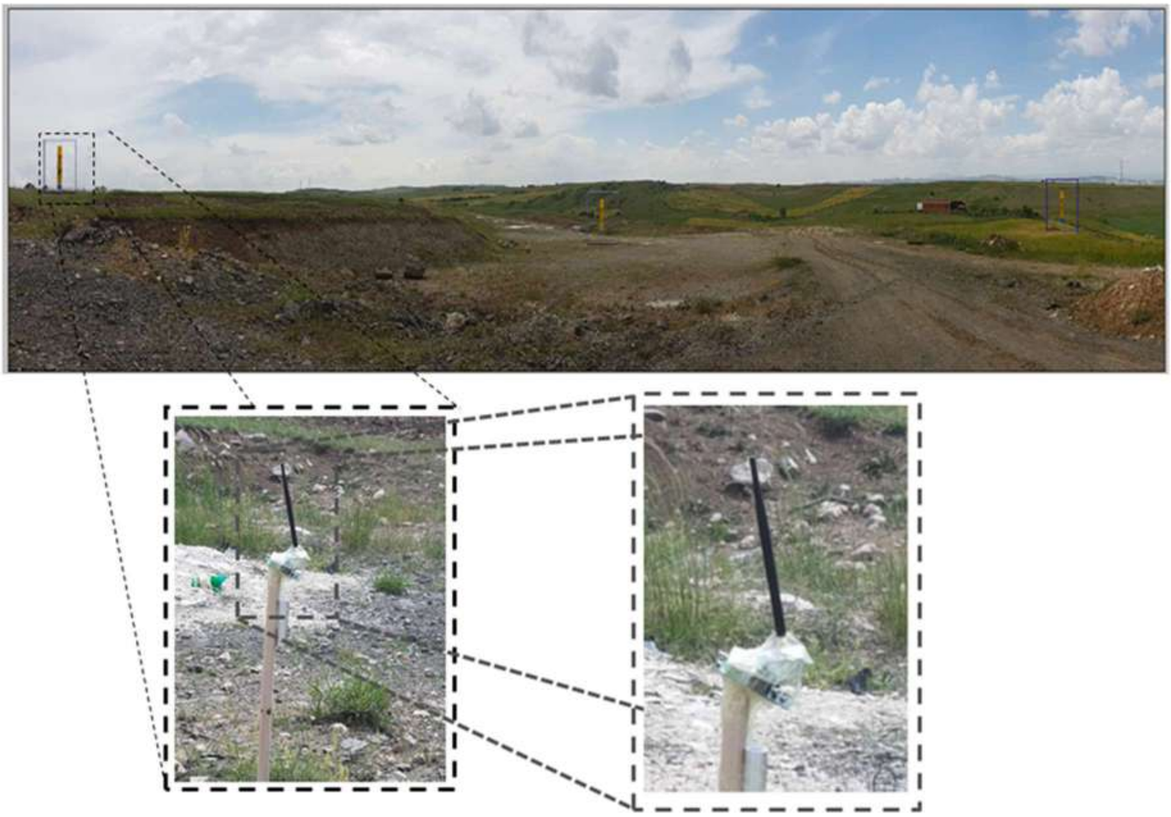

Figure 5 Distribution of nodes in a realistic environment

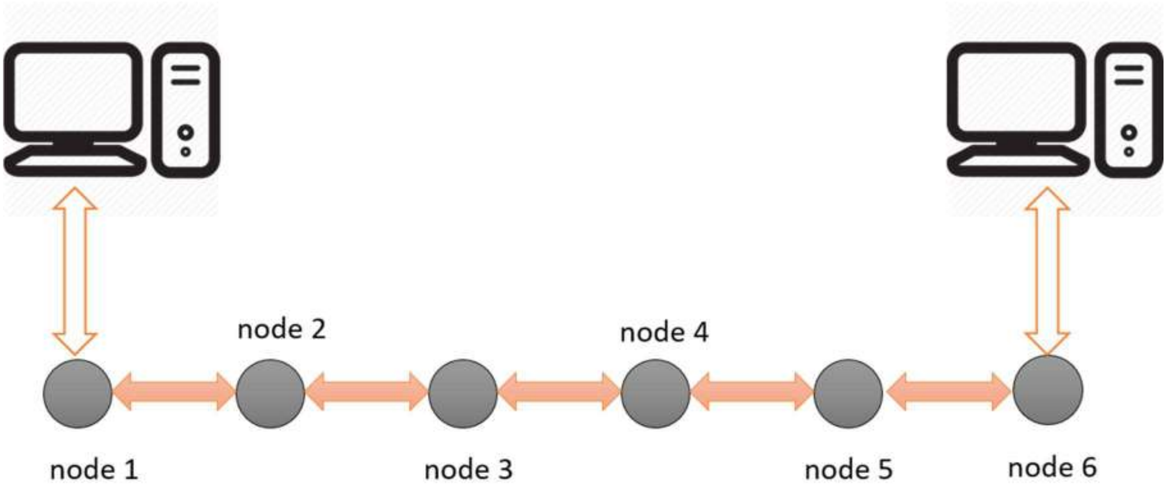

Figure 6 Distribution of nodes in an experiment

- A link is established with different but fixed distances between the nodes.
- 10 data-points of time synchronization process is recorded along with the environment temperature.
- Two random nodes where they are not starting or ending nodes are heated using a heater and the second step is repeated.

Experiments are divided into two types as indoor and outdoor. First two experiment sets are performed at a rural area where different outdoor effects take place like RF interference, fluctuant temperature, humidity, obstructed line of sight links and various RF reflector materials are present. Time synchronization algorithm’s performance is tested at different hours of the day where these conditions also vary with time.

Last two experiment sets take place in a closed area where some sensor nodes have only walls as an obstruction and some has line of sight links. In this area, stable temperature and humidity are kept with an air conditioner and the time synchronization algorithm performance is observed. Then some of nodes’ temperature is increased using a heater and performance is observed once again. Various uncontrollable factors like infrequent failures to establish a connection and low voltage levels of the battery during these tests resulted in a slightly varying outcomes of the experiment.

3.2. Results

In the Experiment 1, six nodes were placed in an outdoor environment with nodes being approximately 150 meters apart. The initial temperature was 23°C and rose to a temperature of 27°C at the end of the experiment for all nodes. The temperature rise was natural; it is not obtained from a heater or artificial sources. Environment of the experiment was selected as an empty remote rural area. Experiment was started early in the morning so RF interference is relatively low. The nodes were attached to a wooden stick at a height of 1m from the ground. The synchronization results varied from 20ms to 54ms contributed by the long intermediate distances between the nodes and the fluctuations on the ambient temperature. The findings depicted in Figure 7 shows a linear increase in the time difference as temperature rises. This behavior is expected as crystal response against temperature is seen in [21].

Second experiment is also carried out at the same location of Experiment 1, so the environmental features remained the same. However, the experiment took place at the noon so RF interference is different. In addition, the temperature rose from 27 °C to 33 °C during the experiment. Results of Experiment 2 (refer to Figure 8) shows that the clock difference starts from 38ms and ends at 102ms. In this experiment a smooth start is observed but then a sudden increase is seen.

Experiment 1 and 2 show similar trends in the results. The first synchronization time values of Experiment 1 and 2 are 20ms and 38ms respectively. But second experiment time values are larger because the initial and end temperatures were higher as it is concluded from [21]. The total temperature difference definitely has a decisive effect on these results.

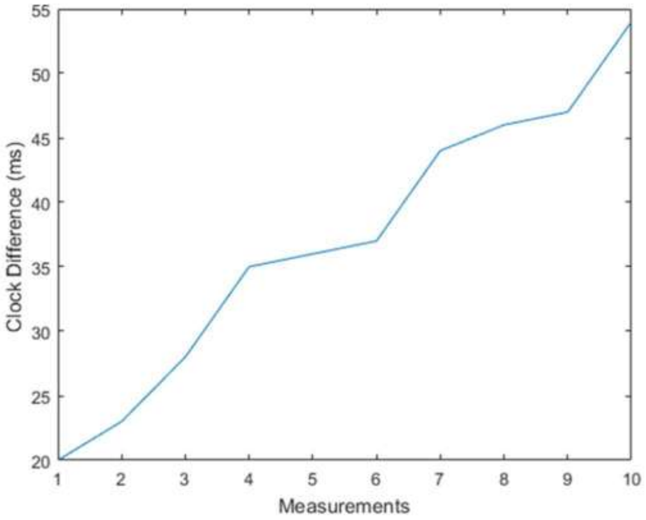

Figure 7 Clock difference in Experiment 1

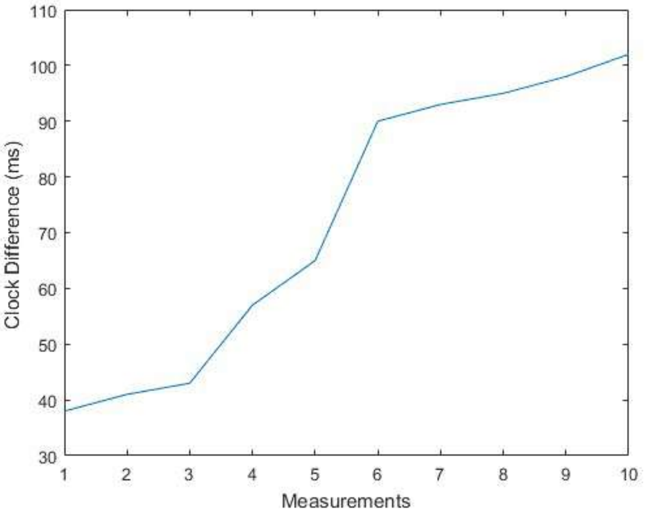

Figure 8 Clock difference in Experiment 2

In Experiment 3, nodes were placed in an indoor environment where walls acted as the obstructions between nodes. Temperature was stable at around 24°C. Experiment was carried out midday. Nodes were placed randomly in rooms where the distances between the nodes ranged from 20 to 40 meters. The environment was busy i.e. numerous people moving at random time and directions. The result is a fluctuating decreasing trend in clock difference as of Figure 9.

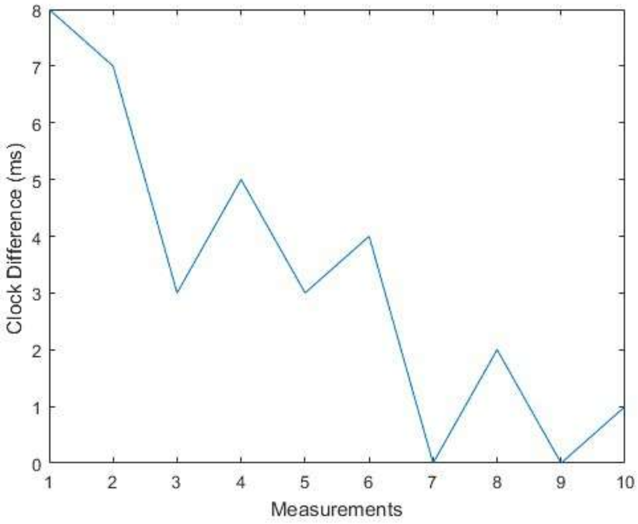

Figure 9 Clock difference in Experiment 3

Experiment 4 took place at the same environment as Experiment 3 but at a later time in the day i.e. afternoon. Two of the nodes were heated from 24°C to 35°C and others were kept at around 24°C. The motivation is to simulate the real-life scenario where nodes are kilometers apart and are exposed to varying temperatures due to geographical locations e.g. mountain valleys and humid forests. This requires the experiment location's temperature to be controlled and what easier way than indoors. The distance between the nodes were same as of Experiment 3. First synchronization time increased to 11ms and the results varied between 8-15ms. The rate of decrease seen in Experiment 3 had slowed down in Experiment 4. This is illustrated in Figure 10. Unlike Figures 7-8 where drastic changes were witnessed, some small scale fluctuations are observed due to the difference in the stability of the environment.

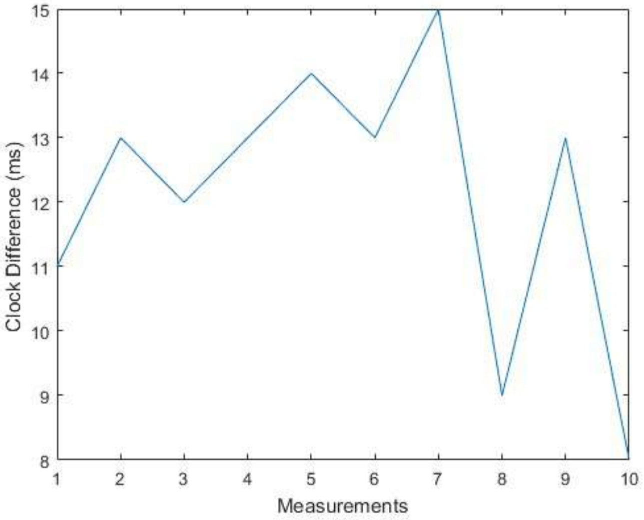

Figure 10 Clock difference in Experiment 4

Table 1
Mean & standard deviation of the experiments

Experiment Number	Mean (ms)	Standard Deviation (ms)
1	37.00	11.00
2	72.30	26.15
3	3.30	2.75
4	12.10	2.18

The mean and standard deviation values of clock differences are tabulated in Table 1. A complete analysis can be done by combining these values with the experiment figures. Experiment 1 and 2 have relatively higher initial synchronization time while the latter being the highest due to high temperatures. Thus, the second experiment has approximately twofold synchronization time values i.e. the mean and standard deviation is doubled. This suggests that higher temperature change in experiment 2 has an effect on the standard deviation. Experiment 3 and 4 have relatively small first synchronization time and a non-spreading behavior of values, indicated by the standard deviation results. Furthermore, the two heated sensor nodes directly have an impact on synchronization time and the mean value takes a big leap; by a factor of about 3.5. Nonetheless, the deviation is slightly less dispersed. The change of standard deviation in Experiment 4 is also the evidence of the influence of ambient temperature on the synchronization, yet it is not high as one would expect.

4. CONCLUSION

Time synchronization is an essential entity in all WSN systems. We intended to investigate the impact of environmental factors on the time synchronization through an effective adaptation of distributed light weight time synchronization implemented on a PIC. Although the board’s crystal is not quite appropriate for this purpose, a custom design with handpicked components can be chosen to fit the needs. We employ bare metal programming thus every detail of synchronization is considered and complexity is avoided to the fullest possible extent in order to discard timing uncertainties. Additionally, design of a network system to support variable number of nodes arbitrarily demands a generic algorithm. Conversely, rising number of nodes can affect performance of synchronization in linear spanning tree networks.

Time synchronization in both indoor and outdoor areas were studied. The impact of temperature and rural effects on the linear spanning tree WSN is significant. Nonetheless, the results are within the limits of expected time intervals. Every clicker board has identical oscillator but since they don’t necessarily have the same skew behavior, the time shifts are inevitable. Outdoor and indoor results also point out some flaws in algorithm whereas the effectual parameters like rounding and averaging increases, the performance decreases. Last two experiments (Experiment 3 and 4) have the numeric high mean difference but small standard deviations; only two nodes’ temperature change does not affect general synchronization values as opposed to outdoors.

Regardless of the interference and temperature instability, most nodes show acceptable results for these experiments. Nevertheless, the disturbance needs to be overcome and still calls for attention. While mean value is high, the standard deviation is small where the time synchronization values are consistent in consecutive samples. In some cases, the result can be better like this where similar experiment is done in [11] and good result is seen.

Of course, use of limited hardware might require further optimizations as presented in [22]. Nevertheless, the objective of this study was to use this algorithm in the outdoors and the results were acceptable, although can be improved by finding the optimum resynchronization interval and forming a temperature based clock formula for generic crystal oscillators.

Acknowledgements

The authors would like to thank the reviewers for all the useful and instructive comments on our manuscript. They would also like to extend acknowledgement to the researchers and staffs of the Electrical and Electronics Engineering department who aided during the experiments.

Funding

The authors received no financial support for the research, authorship or publication of this work.

The Declaration of Conflict of Interest/ Common Interest

The authors do not have any conflict of interest or common interest with any institution or person that they know that could affect their work.

Authors' Contribution

All authors have contributed in experimental study and writing of the manuscript equally.

The Declaration of Ethics Committee Approval

The authors declare that this work does not require an ethics committee approval or any special permission.

The Declaration of Research and Publication Ethics

The authors of the paper declare that they comply with the scientific, ethical and quotation rules of SAUJS in all processes of the paper and that they do not make any falsification on the data collected. In addition, they declare that Sakarya University Journal of Science and its editorial board have no responsibility for any ethical violations that may be encountered, and that this study has not been evaluated in any academic publication environment other than Sakarya University Journal of Science.

REFERENCES

[1] F. Akyildiz, W. Su, Y. Sankarasubramaniam and E. Cayirci. Wireless Sensor Networks: A Survey. Computer Networks, vol. 38, no. 4, pp. 393-422, 2002.

[2] F. Sivrikaya and B. Yener, “Time Synchronization in Sensor Networks: A Survey,” Network, IEEE vol. 18, no. 4, pp. 45–50, 2004.

[3] J. Elson, L. Girod, and D. Estrin, “Fine-grained network time synchronization using reference broadcasts,” in 5th USENIX Symp. Operating System Design and Implementation (OSDI’02), Dec. 2002.

[4] D. Cox, E. Jovanov, A. Milenkovic, "Time Synchronization for ZigBee Networks," in Proc. of the 37th IEEE Southeastern Symposium on System Theory (SSST'05), Tuskegee, AL, pp. 135-138, March 2005.

[5] A. Kara, M. A. Al Imran, K. Karadag, "Linear Wireless Sensor Networks for Cathodic Protection Monitoring of Pipelines," in 2019 International Conference on Mechatronics, Robotics and System Engineering (MoRSE 2019), Bali, Indonesia, 2019.

[6] S. Ping, Delay measurement time synchronization for wireless sensor networks, Intel Research, IRB-TR-03-013, 2003.

[7] L. M. He, "Time Synchronization for Wireless Sensor Networks," 2009 10th ACIS International Conference on Software Engineering, Artificial Intelligences, Networking and

Parallel/Distributed Computing, Daegu, pp. 438-443, 2009.

[8] Jana van Greunen, Jan Rabaey, Lightweight time synchronization for sensor networks, Proceedings of the 2nd ACM international conference on Wireless sensor networks and applications, September 11-19, 2003, San Diego, CA, USA.

[9] J. Wu, L. Zhang, Y. Bai, Y. Sun, Cluster-based consensus time synchronization for wireless sensor networks, IEEE Sens. J., vol. 15, pp. 1404-1413, 2015.

[10] W. Su and I. F. Akyildiz, "Time-diffusion synchronization protocol for wireless sensor networks," in IEEE/ACM Transactions on Networking, vol. 13, no. 2, pp. 384-397, 2005.

[11] Yoon, S., Veerarittiphan, C., and Sichitiu, M. L. 2007. Tiny-Sync: Tight time synchronization for wireless sensor networks. ACM Trans. Sens. Netw. 3, 2, Article 8 (June 2007), 34 pages.

[12] E. Garone, A. Gasparri and F. Lamonaca, “Clock synchronization protocol for wireless sensor networks with bounded communication delays”, Automatica, vol. 59, pp. 60-72, 2015.

[13] M. L. Sichitiu and C. Veerarittiphan, "Simple, accurate time synchronization for wireless sensor networks," 2003 IEEE Wireless Communications and Networking, 2003. WCNC 2003, New Orleans, LA, USA, vol. 2, pp. 1266-1273, 2003.

[14] J. Chen, Q. Yu, Y. Zhang, H. H. Chen and Y. Sun, "Feedback-Based Clock Synchronization in Wireless Sensor Networks: A Control Theoretic Approach," in IEEE Transactions on Vehicular Technology, vol. 59, no. 6, pp. 2963-2973, 2010.

[15] I. F. Akyıldız and M. Vuran, Wireless Sensor Networks. Wiley, 2009.

[16] F. Bonavolontà, A. Tedesco, R. S. L. Moriello and A. Tufano, "Enabling wireless technologies for industry 4.0: State of the art," 2017 IEEE International Workshop on Measurement and Networking (M&N), Naples, pp. 1-5, 2017.

[17] G. Bam, E. Dilcan, B. Dogan, B. Dinc and B. Tavli, "DLWTS: Distributed Light Weight Time Synchronization for Wireless Sensor Networks," 2015 International Symposium on Intelligent Signal Processing and Communication Systems (ISPACS), Nusa Dua, pp. 447-450, 2015.

[18] J. He, P. Cheng, L. Shi, J. Chen and Y. Sun, "Time Synchronization in WSNs: A Maximum-Value-Based Consensus Approach," in IEEE Transactions on Automatic Control, vol. 59, no. 3, pp. 660-675, 2014.

[19] Amulya Ratna Swain, R.C. Hansdah, A model for the classification and survey of clock synchronization protocols in WSNs, Ad Hoc Networks, vol. 27, pp. 219-241, 2015.

[20] Djamel Djenouri, Nassima Merabtine, Fatma Zohra Mekahlia, Messaoud Doudou,Fast distributed multi-hop relative time synchronization protocol and estimators for wireless sensor networks, Ad Hoc Networks, vol. 11, no. 8, pp. 2329-2344, 2013.

[21] F. L. Walls and J. J. Gagnepain, "Environmental sensitivities of quartz oscillators," in IEEE Transactions on Ultrasonics, Ferroelectrics, and Frequency Control, vol. 39, no. 2, pp. 241-249, March 1992.

[22] M. A. Al Imran, Y. Dalveren, B. Tavli, and A. Kara. “Optimal operation mode selection for energy-efficient light-weight

multi-hop time synchronization in linear wireless sensor networks," in 2020 EURASIP Journal on Wireless Communications and Networking, 1, pp. 1-9, 2020.

SAKARYA ÜNİVERSİTESİ

FEN BİLİMLERİ ENSTİTÜSÜ
DERGİSİ

Sakarya University Journal of Science
SAUJS

e-ISSN 2147-835X | Period Bimonthly | Founded: 1997 | Publisher Sakarya University |
http://www.saujs.sakarya.edu.tr/en/

Title: Synthesis of Gd doped TiO2 Thin Film for Photocatalytic Degradation of Malachite Green

Authors: Hasan ESKALEN, Süleyman KERLİ

Recieved: 2020-07-21 16:47:17

Accepted: 2020-09-09 15:23:15

Article Type: Research Article

Volume: 24
Issue: 6
Month: December
Year: 2020
Pages: 1210-1215

How to cite
Hasan ESKALEN, Süleyman KERLİ; (2020), Synthesis of Gd doped TiO2 Thin Film for Photocatalytic Degradation of Malachite Green. Sakarya University Journal of Science, 24(6), 1210-1215, DOI: https://doi.org/10.16984/saufenbilder.772590
Access link
http://www.saujs.sakarya.edu.tr/en/pub/issue/57766/772590

Sakarya University Journal of Science 24(6), 1210-1215, 2020

Synthesis of Gd doped TiO_2 Thin Film for Photocatalytic Degradation of Malachite Green

Hasan ESKALEN*[1], Süleyman KERLİ[2]

Abstract

In this research work, a simple spray pyrolysis method was employed to synthesized gadolinium (Gd) doped titanium oxide (TiO_2) thin film. The crystal structure and morphology of the sample was characterized by X-ray diffraction (XRD) and scanning electron microscope (SEM). According to XRD measurements, no apparent crystal peak was observed. The thickness of the prepared film was found to be 228 nm from SEM observation. The optical transmittance and bandgap energy of the synthesized thin film was investigated by using UV-Vis spectroscopy. The high transmission of the thin film was found in the visible region. The optical bandgap energy of the prepared film was found to be 2.85 eV. The photocatalytic degradation of malachite green solution was studied. As a result of the photocatalytic experiment, the thin film could be used as an effective photocatalyst for malachite green dye.

Keywords: Spray pyrolysis, XRD, SEM, TiO_2, malachite green

1. INTRODUCTION

The increasing interests of researchers from science and industry have been focused on thin films because of the full range of application areas from energy to radiation shielding [1–3]. One of the significant application areas of the thin film is obviously photocatalyst since, among different reasons, especially massive industrialization pollute water that causes unsafe drinking water [4]. The photocatalysis is a valuable and kindly green (since renewable solar energy is utilized) methods to remove toxic organic complexes from wastewater [5]. Semiconductor-based photocatalytic materials have been used for water treatment because of their high potentials [6].

The titanium oxide (TiO_2) has an environmentally friendly nature, low cost, and excellent photocatalytic activity [6]. Moreover, TiO_2 has chemical stability, high redox reactivity, high thermal resistance, and low toxicity [7,8]. Despite all the superior features about TiO_2, the use of visible light is limited. This material only uses about 45 % solar energy of visible light and ~4 % of ultraviolet light [7]. Concerning this drawback, doping TiO_2 with metal and non-metal elements can enhance visible light absorption that can

---

* Corresponding Author: heskalen@gmail.com

[1] Kahramanmaraş Sütçü İmam University, Turkey, ORCID: https://orcid.org/0000-0002-4523-6573

[2] Kahramanmaraş İstiklal University, Turkey, E-Mail: suleymankerli@yahoo.com
ORCID: https://orcid.org/0000-0003-3853-7252

increase photocatalytic activity [9,10]. Boron can place two different positions as an interstitial and substitutional position in TiO_2 lattice and the interstitial boron-doping remarkably increase the photocatalytic activity of TiO_2 film was founded [11]. The enhanced optical absorption was found at boron and nitrogen co-doped TiO_2 synthesized by the sol-gel method [12]. The ZnO/TiO_2 solution of the thin film prepared and photocatalytic activities were investigated recently [13]. The decrease in optical bandgap energy of Cu doped TiO_2 was reported [14]. Gadolinium (Gd) 0-6 % doped TiO_2 was synthesized by sol-gel spin coating methods, and their photocatalytic degradation activity of Rhodamine-B (RhB) dye was studied [15]. TiO_2 was doped Gd, and La same time decrease optical bandgaps and so increase photocatalytic activity was reported [16].

Herein, we explored 10 % Gd doped TiO_2 thin film synthesized by a spray pyrolyzed method. This method is preferred because it has many advantages such as low cost and not requiring vacuum environment. Moreover adjusting the molarity of the solutions, controlling the substrate temperature, and compatible for industry since large area can be coatable with this method [17,18]. The structural, morphological and optical properties of the prepared gadolinium doped TiO_2 thin film were characterized by the X-ray diffraction, SEM, UV-Vis spectroscopy method. The photocatalytic degradation performance of the film was investigated.

2. MATERIALS AND METHOD

The 10 at% Gd doped TiO_2 thin film was obtained by the spray pyrolysis method. Titanium chloride ($TiCl_4$) and gadolinium nitrate ($GdN_3O_9 \cdot 6H_2O$) chemicals were used for thin-film synthesizes. These chemicals were prepared atomic rate of 10/90 (Gd/Ti) in 40 ml pure water and 5 ml ethanol. The temperature of substrates adjusted set as 450 °C and the solution was sprayed the glasses substrates. The diffraction pattern of the obtained thin film was measured using the XRD device (Philips X'Pert PRO brand XRD device (CuKα, λ=0.154056 nm)). The measurement range of the equipment is adjusted from 10˚ to 90˚, the step interval will increase by 0.055 and the waiting time will be 0.5 seconds in each step. The morphological features of the produced film were examined by using the ZEISS EVO LS10 scanning electron microscope (Scanning Electron Microscope). UV-Vis (Ultraviolet) spectrophotometer measurements were conducted using the Shimadzu UV-1800, UV-Vis spectrophotometer device.

3. RESULTS AND DISCUSSION

The crystal structure of gadolinium-doped titanium oxide thin film was not apparent at the obtained XRD results which is shown Figure 1. As seen in the figure, no clear crystalline peak was found in the X-ray pattern. It is believed that the amorphous structure is dominant in this film. In literature, a similar study conducted by Chobba et al., Gd element from 0 to 5 percent was doped to titanium oxide nanoparticle and the XRD results demonstrated that the intensity of peaks decreased with the increasing amount of Gd concentration [19]. There are also some other studies in which the intensity of TiO_2 peaks was reduced by introducing the Gd element to the system [20,21]. In our study, differs from the mentioned works, the concentration of Gd elements was highest with 10 % and this is the main reason for the TiO_2 crystal structure was not apparent at the obtained XRD results.

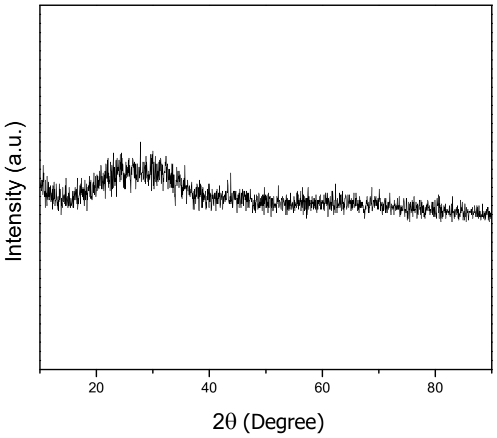

Figure 1 XRD diffraction pattern of 10 % Gd doped TiO_2 thin film

Electron microscopy (SEM) images of 10 % Gd doped TiO_2 thin film obtained by the spray pyrolysis method are shown in Figure 2. The thickness of the film obtained from SEM photographs was measured as approximately 228 nm. Besides, SEM photographs show that thin films have agglomerations at some points and are generally more uniform and more homogeneous.

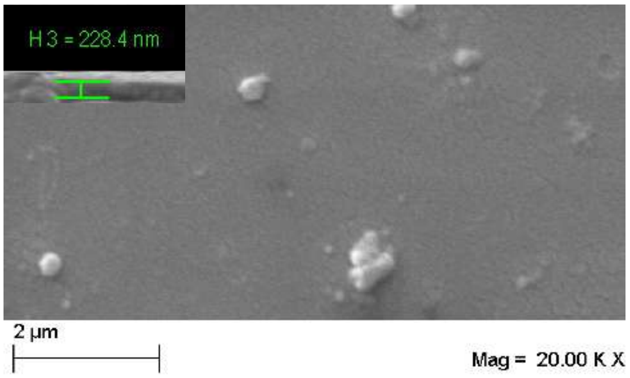

Figure 2 SEM image of 10 % Gd doped TiO_2 thin film. Inset cross-section image of the film

Figure 3 (a) shows the transmission spectra of gadolinium-doped titanium oxide thin film. As can be clearly seen from this figure, the film has a high transmission value of about 94% at 900 nm. Also, it was observed that the optical transmittance of the film decreases inclined with the wavelength. The bandgap energy of the 10 % Gd doped TiO_2 thin film was obtained from the line of the linear section intersects the hv axis $(\alpha h\nu)^2 = 0$. The $(\alpha h\nu)^2 \sim h\nu$ graph relation of Gd doped TiO_2 film was demonstrated in Figure 3b. The optical bandgap energy (Eg) of the thin film was found 2.85 eV and the result is suitable with the previously studied related to doping rare-earth metal in the TiO_2 matrix [22,23]. The oxygen atoms are loosed and free electrons are generated with doping Gd element to TiO_2 matrix and the redshift in the absorbance band is due to the transition of an electron from the valance band to 4f energy level of Gd [22].

Photocatalytic degradation of the 10 % Gd doped TiO_2 thin film was performed with 2 ppm malachite green dye solution under solar light simulator cabin (300W Luzchem Photoreactor). The photocatalytic performance of the used thin film was measured by using UV-Vis spectroscopy as a function of reaction time. The maximum absorption of malachite green solution was recorded at 618 nm and a minor absorption peak at 424 nm. The 2 ppm (10 mL) malachite green solution put into the petri dish and the thin film was kept in the dark for 40 min to achieved absorption desorption equilibrium. After then the petri dish was placed into a solar simulator and regular circulation of the solution was made with the help of magnetic stirrer. The samples were taken from the solution at proper time intervals from 0 min to 110 min, and the samples were analyzed at UV-Vis spectrometry in ranging from 400-700 nm.

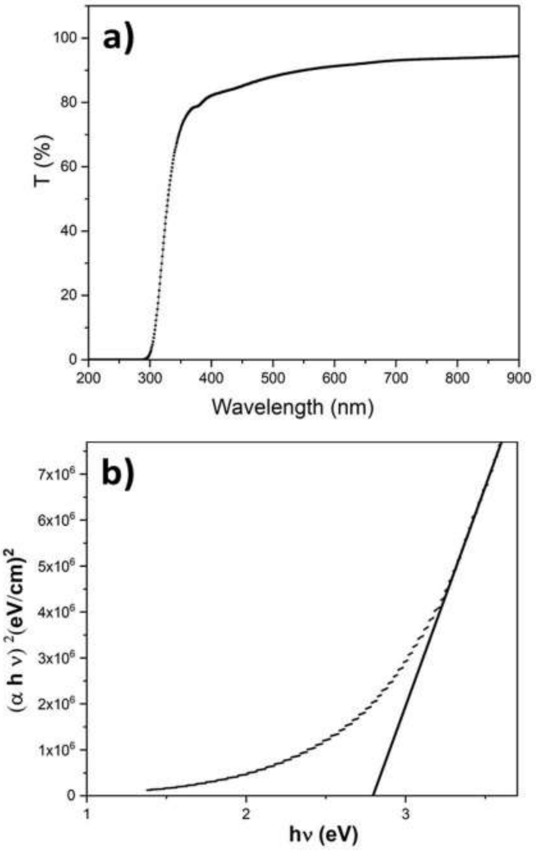

Figure 3 (a) The transmission spectrum of 10 % Gd doped TiO_2 thin film, (b) estimated optical bandgap of the prepared film

The degradation efficiency of the example was found by using the equation:

$$DE = \left(1 - \frac{C_t}{C_0}\right) x\ 100 \qquad (1)$$

where DE implies degradation efficiency, C_0 is the initial concentration, C_t is the represent concentration at the sampling time. The change in

UV-Vis spectra of 10 % Gd doped TiO_2 thin film as a function of time is illustrated in Figure 4. As seen from this figure, the maximum absorption peak linearly decreases as the reaction time increase. The initial green color of solution change to almost white after 110 min of reaction.

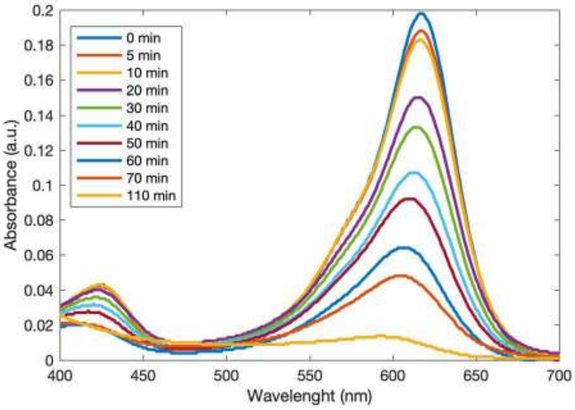

Figure 4 Uv-vis spectra of photocatalytic degradation of 10 % Gd doped TiO_2 as a function of time

The photocatalytic degradation efficiency of the prepared film is given in Figure 5. The self-degradation and 10 % Gd doped TiO_2 film degradation are clearly seen from the figure. The efficiency of the film was reached 87 % in 110 min. The Gd element as a doping agent of TiO_2 has an exciting specification, and the photocatalytic performance of TiO_2 may enhance or reduce with introducing Gd elements. The enhancement of the concert with Gd doping might be attributed to the 4f level of the lanthanide [19]. However, the irradiation environment, annealing of film and doping concentration changes to the photocatalytic performance of the mentioned system [19,23,24]. So further studies are needed.

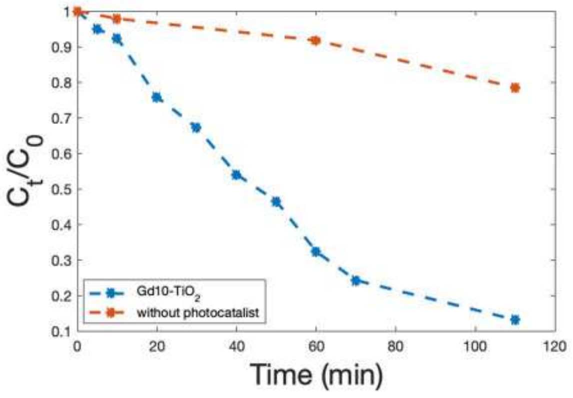

Figure 5 The photocatalytic degradation efficiency of malachite green by 10 % Gd doped TiO_2

4. CONCLUSION

In this study, 10 % Gd doped TiO_2 thin film was successfully synthesized by a simple spray pyrolysis method. The crystal structure of the sample was examined, and no apparent crystalline peak was observed. The thickness of the prepared film was found as 228 nm from SEM observation. The transmission feature of the 10 % Gd doped TiO_2 film was examined by a UV-Vis spectrometer and a highly transparent thin film was found. The optical bandgap energy of the synthesized film was seen as 2.85 eV. The photocatalytic degradation of malachite green solution was examined, and the synthesized thin film can be used as an active photocatalyst for malachite green dye, but further studies are needed to Gd doped TiO_2 thin films. These findings may contribute to the development of new insight on Gd doped TiO_2 thin films.

Acknowledgements

We would like to thank Kahramanmaraş Sütçü İmam University (Project Number: 2020/1-25A and 2020/3-7 YLS) for their financial supports.

The Declaration of Conflict of Interest/ Common Interest

No conflict of interest or common interest has been declared by the authors.

Authors' Contribution

All authors have contributed in experimental study and writing of the manuscript equally.

The Declaration of Ethics Committee Approval

The authors declare that this document does not require an ethics committee approval or any special permission.

The Declaration of Research and Publication Ethics

The authors of the paper declare that they comply with the scientific, ethical and quotation rules of

SAUJS in all processes of the paper and that they do not make any falsification on the data collected. In addition, they declare that Sakarya University Journal of Science and its editorial board have no responsibility for any ethical violations that may be encountered, and that this study has not been evaluated in any academic publication environment other than Sakarya University Journal of Science.

REFERENCES

[1] B. Astinchap, K.G. Laelabadi, Effects of substrate temperature and precursor amount on optical properties and microstructure of CVD deposited amorphous TiO 2 thin films, J. Phys. Chem. Solids. vol. 129, pp. 217–226, 2019.

[2] H. Eskalen, Y. Kavun, S. Kerli, S. Eken, An investigation of radiation shielding properties of boron doped ZnO thin films, Opt. Mater. (Amst). vol. 105, 109871, 2020.

[3] S. Kerli, Ü. Alver, H. Eskalen, A.K. Soğuksu, Electrochemical properties and photocatalytic activity of In2O3-Co3O4 thin films, Comptes Rendus L'Academie Bulg. Des Sci. vol. 72, pp. 327–332, 2019.

[4] Y.M. Hunge, M.A. Mahadik, R.N. Bulakhe, S.P. Yadav, J.J. Shim, A. V. Moholkar, C.H. Bhosale, Oxidative degradation of benzoic acid using spray deposited WO3/TiO2 thin films, J. Mater. Sci. Mater. Electron. vol. 28 pp. 17976–17984, 2017.

[5] S. Dhanapandian, A. Arunachalam, C. Manoharan, Effect of deposition parameters on the properties of TiO2 thin films prepared by spray pyrolysis, J. Sol-Gel Sci. Technol. vol. 77, pp. 119–135, 2016.

[6] Y. Sheng, J. Yang, F. Wang, L. Liu, H. Liu, C. Yan, Z. Guo, Sol-gel synthesized hexagonal boron nitride/titania nanocomposites with enhanced photocatalytic activity, Appl. Surf. Sci. vol. 465 pp. 154–163, 2019.

[7] P. Niu, G. Wu, P. Chen, H. Zheng, Q. Cao, H. Jiang, Optimization of Boron Doped TiO2 as an Efficient Visible Light-Driven Photocatalyst for Organic Dye Degradation With High Reusability, Front. Chem. vol. 8, pp. 1–8, 2020.

[8] A. You, M.A.Y. Be, I. In, Self-cleaning properties of nanostructured TiO2 thin films synthesized via facile , cost- effective spin coating technique Self-Cleaning Properties of Nanostructured TiO 2 Thin Films Synthesized via Facile , Cost-effective Spin Coating Technique, 030319 2019.

[9] C. Xue, W. Wang, T. Han, Y. Wang, Y. Dong, S. Hu, J. Yang, W. Wang, Boron-doped TiO 2 Nanotube Array : In-situ Electrochemical Preparation and Study on its Photocatalytic Activity Bor ron-doped TiO T 2 Nanotu ube Array : In-situ Elec ctrochemica al Preparatio on and Stud dy on its Pho otocatalytic Activity, Chem. Lett. vol. 45, pp. 1460-1462, 2016.

[10] K.R. Reyes-Gil, D.B. Robinson, WO3-enhanced TiO2 Nanotube Photoanodes for Solar Water Splitting with Simultaneous Wastewater Treatment, ACS Appl. Mater. Interfaces. vol. 5, pp. 12400–12410, 2013.

[11] N. Boscher, C.J. Carmalt, Interstitial Boron-Doped TiO2 Thin Films: The Significant Effect of Boron on TiO2 Coatings Grown by Atmospheric Pressure Chemical Vapor Deposition, ACS Appl. Mater. Inter. vol. 8, pp. 25024-25029, 2016.

[12] J. Xu, Y. Ao, M. Chen, D. Fu, Low-temperature preparation of Boron-doped titania by hydrothermal method and its photocatalytic activity, J. Alloys Compd. vol. 484, pp. 73–79, 2009.

[13] D. Tekin, H. Kiziltas, H. Ungan, Kinetic evaluation of ZnO/TiO2 thin film photocatalyst in photocatalytic degradation

of Orange G, J. Mol. Liq. vol. 306, 112905, 2020.

[14] F. Bensouici, M. Bououdina, A.A. Dakhel, R. Tala-Ighil, M. Tounane, A. Iratni, T. Souier, S. Liu, W. Cai, Optical, structural and photocatalysis properties of Cu-doped TiO 2 thin films, Appl. Surf. Sci. vol. 395, pp. 110–116, 2017.

[15] H. Phattepur, B.S. Gowrishankar, G. Nagaraju, Synthesis of gadolinium-doped TiO 2 thin films by sol–gel spin coating technique and its application in degradation of rhodamine-B, Indian Chem. Eng. vol. 61, pp. 167–181, 2019.

[16] H. Lee, I.S. Park, H.J. Bang, Y.K. Park, H. Kim, H.H. Ha, B.J. Kim, S.C. Jung, Fabrication of Gd-La codoped TiO 2 composite via a liquid phase plasma method and its application as visible-light photocatalysts, Appl. Surf. Sci. vol. 471 pp. 893–899, 2019.

[17] H. Mohamed, E. Chikoidze, A. Ratep, A.M.A. Elsoud, M. Boshta, M.B.S. Osman, Synthesis of conducting single-phase CuFeO2 thin films by spray pyrolysis technique, Mater. Sci. Semicond. Process. vol. 107, 104831, 2020.

[18] S. Kerli, Fabrication and Physical Properties of Bor-Fluorine Doped ZnO Particles and Thin Films, PhD Thesis, Kahramanmaraş Sütçü İmam University, 2012.

[19] M. Ben Chobba, M. Messaoud, M.L. Weththimuni, J. Bouaziz, M. Licchelli, F. De Leo, C. Urzì, Preparation and characterization of photocatalytic Gd-doped TiO2 nanoparticles for water treatment, Environ. Sci. Pollut. Res. vol. 26 pp. 32734–32745, 2019.

[20] N. Nithyaa, N.V. Jaya, Structural , Optical , and Magnetic Properties of Gd-Doped TiO 2 Nanoparticles, pp. 4117–4126, 2018.

[21] M. Saif, S.A. El-Molla, S.M.K. Aboul-Fotouh, M.M. Ibrahim, L.F.M. Ismail, D.C. Dahn, Nanostructured Gd3+-TiO2 surfaces for self-cleaning application, J. Mol. Struct. vol. 1067, pp. 120–126, 2014.

[22] A. Ahmad, G. Yerlikaya, Zia-ur-Rehman, H. Paksoy, G. Kardaş, Enhanced photoelectrochemical water splitting using gadolinium doped titanium dioxide nanorod array photoanodes, Int. J. Hydrogen Energy. vol. 45, pp. 2709–2719, 2020.

[23] S. Paul, P. Chetri, B. Choudhury, G. Ameen Ahmed, A. Choudhury, Enhanced visible light photocatalytic activity of Gadolinium doped nanocrystalline titania: An experimental and theoretical study, J. Colloid Interface Sci. vol. 439, pp. 54–61, 2015.

[24] X.Q. Cheng, C.Y. Ma, X.Y. Yi, F. Yuan, Y. Xie, J.M. Hu, B.C. Hu, Q.Y. Zhang, Structural, morphological, optical and photocatalytic properties of Gd-doped TiO2 films, Thin Solid Films. vol. 615, pp. 13–18, 2016.

SAKARYA ÜNİVERSİTESİ

FEN BİLİMLERİ ENSTİTÜSÜ
DERGİSİ

Sakarya University Journal of Science
SAUJS

e-ISSN 2147-835X | Period Bimonthly | Founded: 1997 | Publisher Sakarya University |
http://www.saujs.sakarya.edu.tr/en/

Title: Optimization of the S-Rotor Savonius Wind Turbine

Authors: Cemil YİĞİT

Recieved: 2020-08-15 02:09:06

Accepted: 2020-09-11 15:20:28

Article Type: Research Article

Volume: 24
Issue: 6
Month: December
Year: 2020
Pages: 1216-1222

How to cite
Cemil YİĞİT; (2020), Optimization of the S-Rotor Savonius Wind Turbine. Sakarya University Journal of Science, 24(6), 1216-1222, DOI: https://doi.org/10.16984/saufenbilder.780890
Access link
http://www.saujs.sakarya.edu.tr/en/pub/issue/57766/780890

Sakarya University Journal of Science 24(6), 1216-1222, 2020

Optimization of the S-Rotor Savonius Wind Turbine

Cemil YİĞİT*[1]

Abstract

In this study, 2D Computational Fluid Dynamics (CFD) model was used to investigate the optimum working conditions of the S-Rotor Savonius (S-RS) wind turbine and to determine the most suitable geometry. The CFD model has been validated by studies on the S-RS wind turbine in the literature. The sliding mesh method which uses a mesh motion was utilized to perform the numerical study. CFD analysis was carried out under various tip-speed ratio at 4 m/s airspeed for the S-RS wind turbine which has a frontal swept area of approximately 0.3 m^2. Within the scope of the optimization study, aspect-ratio (AR) and overlap ratio (OR) of the S-RS wind turbine's rotor in the fixed frontal swept area were taken as parameters. The geometry of the S-rotor has been optimized using the Ansys/Response Surface Optimization (RSO) tool. Under the constraints in which the optimization study was carried out, aerodynamic efficiency was obtained as %22.19 at 0.848 AR and 0.068 OR. This yield is significant when the efficiency of S-RS's wind turbine is taken into consideration.

Keywords: aspect ratio, overlap ratio, response surface optimization, power coefficient, vertical axis wind turbine

1. INTRODUCTION

Generally, wind turbines fall into two as vertical axis wind turbines (VAWTs) and horizontal axis wind turbines (HAWTs) according to the position of the rotor. Power plants using renewable and clean energy sources such as HAWTs have come to the fore in the last four decades for the purpose of generating electricity. Unlike fossil fuels, the lack of payment for the resource was helped to grow in popularity of the wind turbine. Although a lot of progress has been made in sound insulation, HAWTs work relatively noisy. In addition, HAWTs cause visual pollution due to its huge structure. For all these reasons, HAWTs cannot find application areas in areas close to residential areas. On the other hand, VAWTs have the capacity to fill this gap, considering their relatively quiet operation, their ability to operate

---

* Corresponding Author: cyigit@sakarya.edu.tr

[1] Sakarya University, Department of Mechanical Engineering, 54187, Sakarya, Turkey
ORCID: https://orcid.org/0000-0003-0908-2148

even in unstable wind conditions [1], and their modular and aesthetic structure. But an important handicap is that they operate at lower efficiency than HAWTs.

Although many academic studies have been conducted on improving the VAWT's aerodynamic performance [2-9], the effects of AR and OR on performance have been widely studied in the fixed frontal swept area [10-12]. The AR is the main design parameter of the VAWT because it is extremely effective in the performance of the rotor [13, 14]. In their study, Li et al. [15] investigated the effect of the AR and the solidity on the VAWT performance, at constant solidity ($\sigma = 0.064$) the peak of the power coefficient (C_p) enhanced with the increase of the AR. Rabei and Gutu [16], in the study where they investigate VAWT rotor performance, reported that an increase in the C_p was obtained in parallel with the increase in AR for the rotor with a fixed frontal swept area.

The OR is a very important parameter to improve the VAWT performance [17] and many researchers [18-23] have investigated the effect of the OR on the performance of the VAWT. Menet and Bourabaa [24] reported that the S-rotor produced maximum torque for a value of 0.24 of OR. Akwa et al. [25] found that the pressure force effect increased in the advancing blade with increasing OR up to a critical value (0.15), and accordingly, the drag force in the S-rotor decrease and reported that the VAWT performance would improve as a result.

In this study, the optimum rotor geometry of the S-RS wind turbine was designed by considering AR and OR parameters. In this context, key design parameters AR and OR were optimized to achieve the maximum performance of S-RS wind turbines by using the RSO method. Numerical optimization studies were performed using Ansys/Fluent software.

2. METHOD

2.1. Optimization

An S-RS wind turbine was design by utilizing the RSO method in order to investigate the effect of key parameters such as AR and OR on the turbine aerodynamic performance and increase the C_p of the S-rotor. The S-rotor comprises two semicircular buckets and, a geometric top view of it resembles an S as shown in Figure 1. The RSO method is a goal-oriented optimization method. This method provides the best possible design to correspond with the constraints set for parameters.

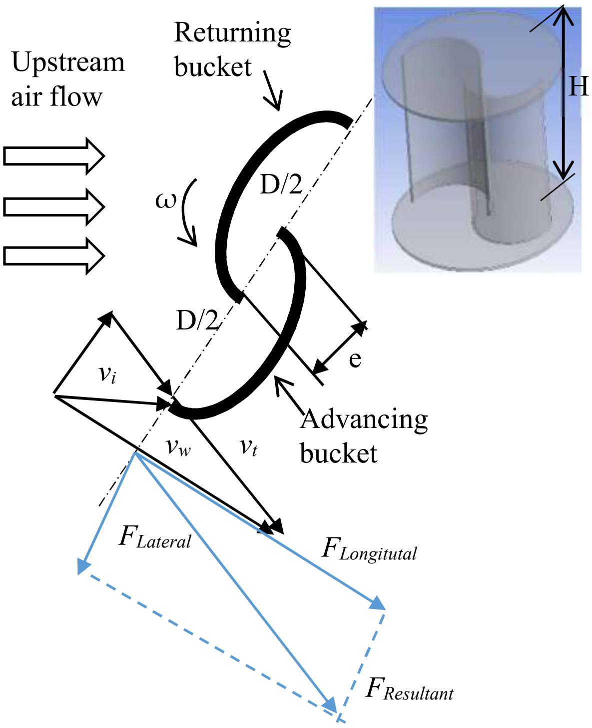

Figure 1 Demonstration both of force and velocity on a cross-section of a S-RS wind turbine

The AR and OR are the key design parameters of the S-RS wind turbine. AR (α) is the ratio of the height (H) to diameter (D) of the rotor as shown in Equation 1. OR (β) is the ratio of the overlap distance (e) to D as shown in Equation 2.

$$\alpha = {}^{H}/_{D} \tag{1}$$

$$\beta = {}^{e}/_{D} \tag{2}$$

The minimum and maximum values that the key parameters can take were determined by CFD analysis by changing the value of only one parameter at a time. These values of the shape parameters, which generate the key parameters, are given in Table 1. Depending on the shape parameters, AR varies between 0.623 and 0.848, and OR varies between 0.015 and 0.068. L4 orthogonal array was created for optimization. Hence, the Design of Experiment (DOE) which has 4 design points was obtained. The response surface was calculated from the DOE results for the output parameter based on the minimum and maximum values that input parameters can take. Excel was used to create DOE and drive the RSO method.

Table 1
The maximum and minimum value of the shape parameters

	D [m]	e [m]	H [m]
DOE-01	0.59	0.01	0.50
DOE-02	0.59	0.04	0.50
DOE-03	0.69	0.01	0.43
DOE-04	0.69	0.04	0.43

2.2. Numerical Study

A CFD model was developed to examine the operation conditions of the S-RS wind turbine with 0.43-0.50 m height and 0.59-0.69 m diameter was developed at 4 m/s airspeed by using Ansys/Fluent software. Turbulence, momentum and continuity equations were solved by adapting a pressure-based solution. Transient Shear Stress Transport (T-SST) turbulence model which is a high-resolution turbulence model, was used to solve the airflow in the S-rotor. Besides, the flow in the rotating and stationary zones was solved in the unsteady model by the so-called Sliding mesh method. In the literature, there are many studies in which VAWTs were modeled with the sliding mesh method and satisfactory results were obtained. Lanzafame et al. [27] used SST k-ω and modified T-SST as the turbulence model in their study in which they modeled the vertical axis H-type Darrieus wind turbine with sliding mesh method. In particular, they reported that the modified T-SST turbulence model achieved very consistent results with experimental data. The Pressure-Implicit with Splitting of Operators (PISO) pressure-velocity coupling scheme was used as a solution method.

The 2D computational domain was created utilizing Ansys/Design Modeler software. It is highly important that the computational domain is created a proper size. Dimensions of the computational domain also affect the C_p and moment coefficient (C_m) to be obtained for the S-RS wind turbine. It is recommended that the distance from the inlet to the S-rotor center (d_i) is between 10D and 15D, the distance from the center to the outlet (d_o) is between 20D and 25D, and the width of the computational domain (W) should be at least 20D [26]. Therefore, the dimensions of the computational domain were determined depending on D. Calculation domain has two zones, one of them is the inner domain, and the other one is the outer domain. S-rotor was located in the inner domain. An interface was defined between these domains. Outlet (pressure outlet) and inlet (velocity inlet) boundary conditions were defined as exit and entrance, respectively. The wall boundary was applied at the semicircular buckets of the S-rotor and the horizontal edges of the domain. The boundary conditions in the calculation domain are shown in Figure 2.

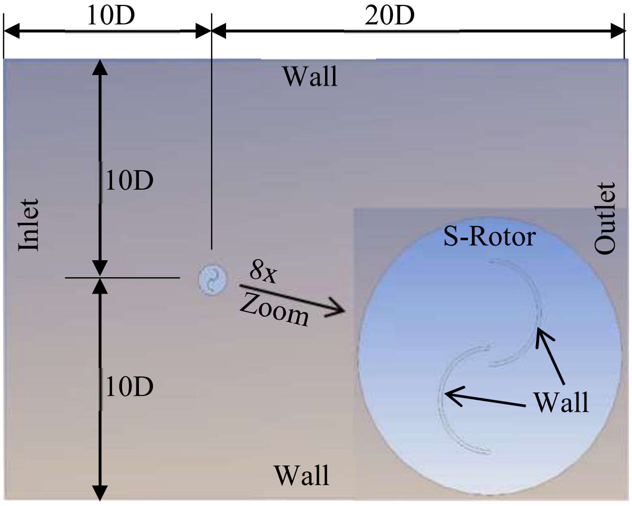

Figure 2 Computational domain and boundary conditions

The mesh should be suitable for the accuracy of the results. Thus, it is important to keep the skewness values of the mesh to be formed within the limits accepted in the literature. The average, minimum and maximum skewness values of the mesh are 8.91×10^{-2}, 2.58×10^{-7}, and 0.74, respectively. Since the serious speed changes and reverse pressure gradients were in the inner domain, smaller mesh elements were used here compared to the outer domain. Therefore, the elements in the inner domain have been minimized by using a weight factor. Besides, to capture the surface-airflow interaction an 8-layer boundary layer was created on the buckets. The total layer ($9.54 \times 10^{-4}\ m$) and the first layer thickness ($5.93 \times 10^{-5}\ m$) were calculated as a function of the Reynolds number, thickness of the bucket and y^+ value. Mesh independence study was carried out, after approximately $100.48k$ elements, it was determined that there was no significant change (<3.2%) in the results. Mesh of the CFD model is shown in Figure 3.

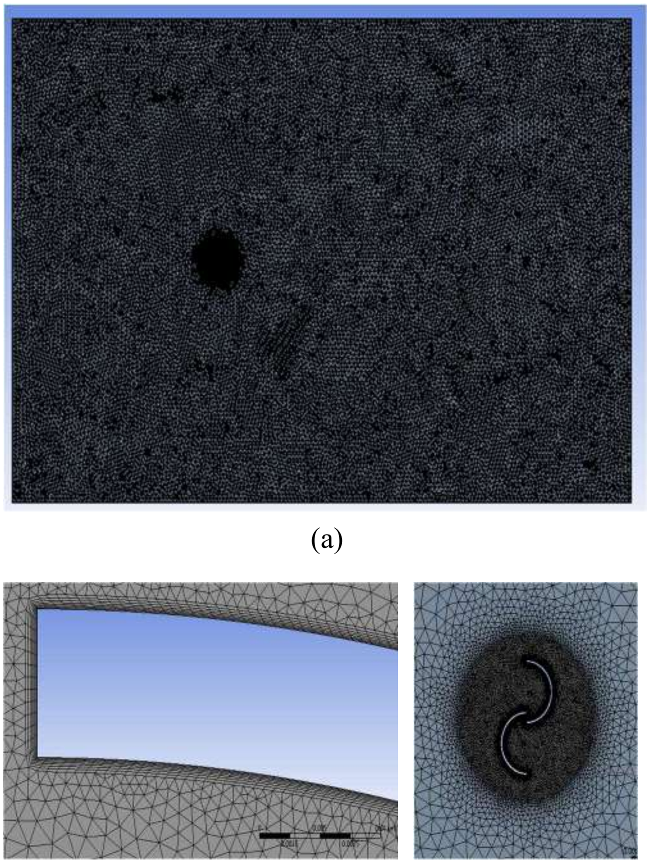

(a)

(b) (c)

Figure 3 (a) Mesh of the CFD model, (b) Bucket, (c) S-rotor

Owing to the complexity of the flow field and the variety of the rotational speed, identify an optimum time step (Δt) for the solution is very hard and sensitivity analysis is necessary. For that aim, a lot of simulations were conducted for different rotational speeds and the Δt for the beginning simulation was computed from Equation 3.

$$\Delta t = (\pi/180)h\lambda^{-1}v^{-1} \tag{3}$$

where h is turbine height, λ is tip-speed ratio (TSR), and v is air velocity. CFD analysis was conducted for about 52 hours utilizing a 12-core workstation with 32 GB DDR4 RAM.

3. RESULTS and DISCUSSION

C_p values obtained from CFD analyzes performed for various TSR at 4 m/s wind speed are shown in Figure 4. Among all design parameters, the maximum C_p was obtained as 0.22 for the value of AR=0.848 and OR=0.068. A maximum C_p was obtained for about 1.1 values of TSR for all DOEs. In other words, after exceedingly approximately 1.2 TSR value for all designs, the stall effect began to be seen in the S-rotor. The shape parameter levels that give the best C_p value and their AR and OR values are given in Table 2.

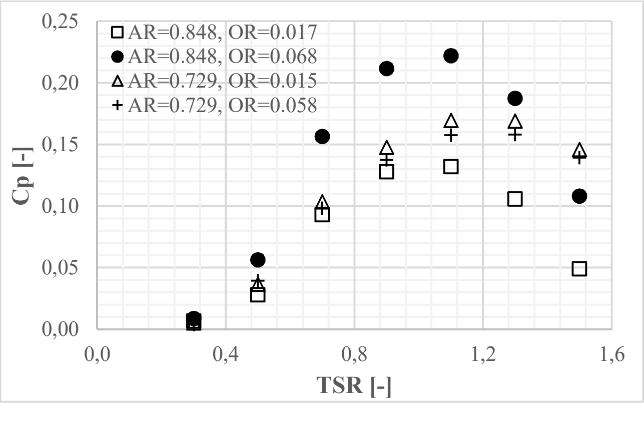

Figure 4 Variation of C_p according to TSR for various DOEs

Table 2
The optimum shape parameter values for the three highest C_p values

D [m]	H [m]	e [m]	AR	OR	C_p
0.59	0.50	0.04	0.848	0.068	0.2219
0.59	0.43	0.01	0.729	0.017	0.1702
0.69	0.43	0.01	0.620	0.015	0.169

The pressure distribution in the S-rotor region depending on the position of the buckets is shown in Figure 5. At the 6 o'clock position of the bucket, the high-pressure zone on the back of the returning bucket trying to stop the S-rotor shifted to the tip of the bucket when the bucket reached the 9 o'clock position. At the same time, a low-pressure zone has been formed in the center of the S-rotor. In this case, the airflow occurs from the high-pressure region to the low-pressure region and passes through the overlap distance.

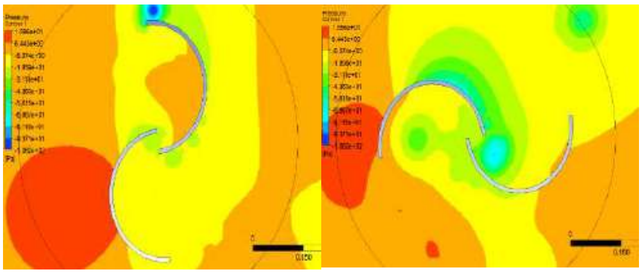

Figure 5 Variation of the pressure on the S-rotor

The velocity vectors in the S-rotor for the various positions of the buckets are shown in Figure 6. It is seen that the airflow continues through the returning bucket, passing through the overlap distance after entering the advancing bucket. When the airflow passes through the overlap distance and hits the inside of the returning bucket, it has an auxiliary effect on the rotation of the rotor.

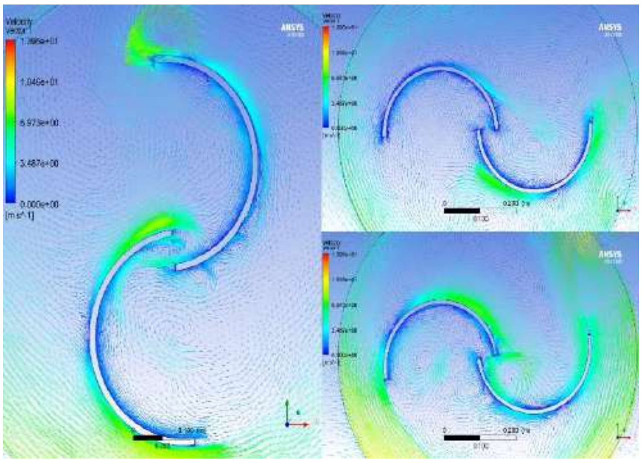

Figure 6 The velocity vectors on the S-rotor

The local sensitivity curves created within the scope of the optimization study carried out by considering the D, e, and H shape parameters are given in Figure 7. In the fixed frontal swept area, it has been determined that the C_p changes inversely with the D and in direct proportion to e and H.

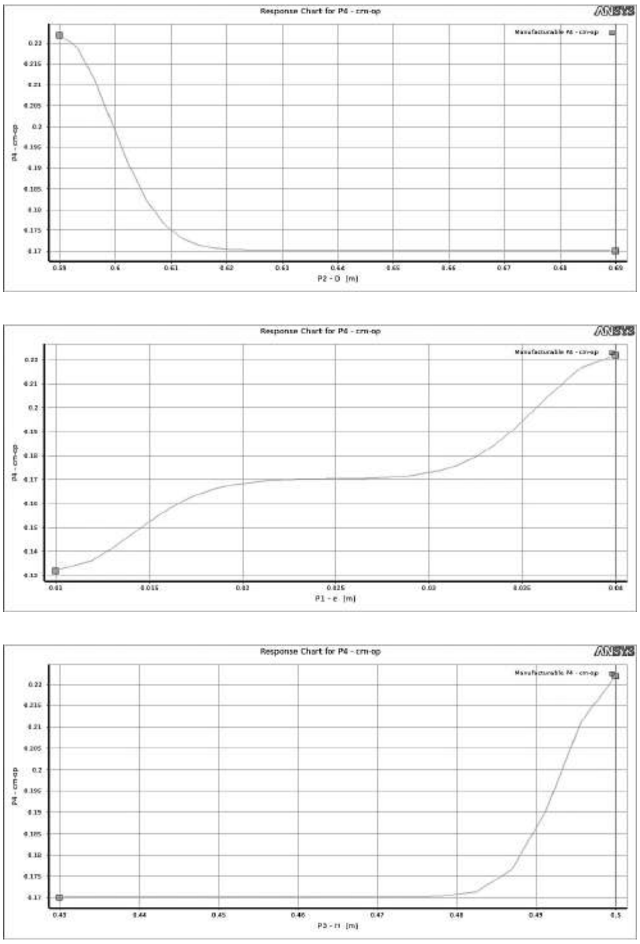

Figure 7 The local sensitivity curves

4. CONCLUSIONS

In the optimization study, the most suitable design with maximum efficiency was determined. Thus, in optimizing the S-RS wind turbine design, maximizing C_p was considered a high priority design criterion. The main findings obtained from the study are as follows:

In the conducted optimization study, different AR and OR values have emerged for the S-rotor. The highest yield from the S-rotor was obtained for values of 0.848 for AR and 0.068 for OR.

Opening the overlap distance to the center of the S-rotor made a positive effect on the rotor performance. The airflow passing through the overlap distance helps the rotor to rotate by hitting the inner surface of the rotating bucket. Besides, increasing AR at low-AR (AR<1) and the fixed frontal swept area also was made a positive effect on rotor performance.

Funding

The author received no financial support for the research, authorship, and/or publication of this paper.

The Declaration of Conflict of Interest/Common Interest

No conflict of interest or common interests has been declared by the author.

The Declaration of Ethics Committee Approval

The author declares that this document does not require an ethics committee approval or any special permission.

The Declaration of Research and Publication Ethics

The author of the paper declare that he complies with the scientific, ethical and quotation rules of SAUJS in all processes of the paper and that he does not make any falsification on the data collected. Additionally, he declares that Sakarya University Journal of Science and its editorial board have no responsibility for any ethical violations that may be encountered, and that this study has not been evaluated in any academic publication environment other than Sakarya University Journal of Science.

REFERENCES

[1] S. Armstrong, A. Fiedler and S. Tullis, “Flow separation on a high Reynolds number, high solidity vertical axis wind turbine with straight and canted blades and canted blades with fences,” Renewable Energy, vol. 41, pp. 13-22, 2012.

[2] J. Chen, L. Chen, H. Xu, H. Yang, C. Ye and D. Liu, “Performance improvement of a vertical axis wind turbine by comprehensive assessment of an airfoil family,” Energy, vol. 114, pp. 318-331, 2016.

[3] W.H. Chen, C.Y. Chen, C.Y. Huang and C.J. Hwang, “Power output analysis and optimization of two straight-bladed vertical axis wind turbines,” Applied Energy, vol. 185, pp. 223-232, 2017.

[4] K.S. Jeon, J.I. Jeong, J.K. Pan and K.W. Ryu, “Effects of end plates with various shapes and sizes on helical Savonius wind turbines,” Renewable Energy, vol. 79, pp. 167-176, 2015.

[5] H. Jeong, S. Lee and S.D. Kwon, “Wind tunnel interference effects on power performance of small Darrieus wind turbines,” Advances in Civil, Environmental, and Materials Research (ACEM14), pp. 1-5, 2014.

[6] C. Kang, H. Liu and X. Yang, “Review of fluid dynamics aspects of Savonius-rotor-based vertical-axis wind rotors,” Renewable and Sustainable Energy Reviews, vol. 33, pp. 499-508, 2014.

[7] S.M.H. Karimian and A. Abdolahifar, “Performance investigation of a new Darrieus vertical axis wind turbine,” Energy, vol. 191, pp. 1-18, 2020.

[8] A.S. Saad, I.I. El-Sharkawy, S. Ookawara and M. Ahmed, “Performance enhancement of twisted-bladed Savonius vertical axis wind turbines,” Energy Conversion and Management, vol. 209, pp. 1-19, 2020.

[9] S. Sharma and R.K. Sharma, “Performance improvement of Savonius rotor using multiple quarter blades – a CFD investigation,” Energy Conversion and Management, vol. 127, pp. 43-54, 2016.

[10] S. Brusca, R. Lanzafame and M. Messina, “Design of a vertical-axis wind turbine: how the aspect ratio effects the turbine’s performance,” Int. J. Energy Environ. Eng., vol. 5, pp. 333-340, 2014.

[11] P. Jaohindy, S. McTavish, F. Garde and A. Bastide, “An analysis of the transient forces acting on Savonius rotors with different aspect ratios,” Renewable Energy, vol. 55, pp. 286-295, 2013.

[12] H.Y. Peng, H.F. Lam and H.J. Liu, “Power performance assessment of H-rotor vertical axis wind turbines with different aspect ratios in turbulent flows via experiments,” Energy, vol. 173, pp. 121-132, 2019.

[13] H.H. Al-Kayiem, B.A. Bhayo and M. Assadi, “Comparative critique on the design parameters and their effect on the performance of S-rotors,” Renewable Energy, vol. 99, pp. 1306-1317, 2016.

[14] S. Zanforlin and S. Deluca, “Effects of the Reynolds number and the tip losses on the optimal aspect ratio of straight-bladed vertical axis wind turbines,” Energy, vol. 148, pp. 179-195, 2018.

[15] Q. Li, T. Maeda, Y. Kamada, K. Shimizu, T. Ogasawara, A. Nakai and T. Kasuya, “Effect of rotor aspect ratio and solidity on a straight-bladed vertical axis wind turbine in three-dimensional analysis by the panel method,” Energy, vol. 121, pp. 1-9, 2017.

[16] I. Rabei and M. Gutu, “Analysis of the influence of the aspect ratio on the vertical axis wind rotor performance,” IOP Conf. Series: Materials Science and Engineering, vol. 564, pp. 1-6, 2019.

[17] M. Zemamou, M. Aggour and A. Toumi, “Review of savonius wind turbine design and performance,” Energy Procedia, vol. 141, pp. 383-388, 2017.

[18] N. Alom and U.K. Saha, “Arriving at the optimum overlap ratio for an elliptical-bladed Savonius,” in:Proceedings of ASME Turbo Expo 2017 Turbine Technical Conference and Exposition, pp. 1-10, 2017.

[19] W.A. El-Askary, A.S. Saad and A.M. AbdelSalam, “Experimental and theoretical studies for improving the performance of a modified shape Savonius wind turbine,” J. Energy Resour. Technol., vol. 142, no. 12, pp. 1-12, 2020.

[20] M.H. Nasef, W.A. El-Askary, A.A. AbdEl-Hamid and H.E. Gad, “Evaluation of Savonius rotor performance: Static and dynamic studies,” J. Wind Eng. Ind. Aerodyn., vol. 123, pp. 1-11, 2013.

[21] M.A. Kamoji, S.B. Kedare and S.V. Prabhu, “Experimental investigation on single stage modified Savonius rotor,” Applied Energy, vol. 86, pp. 1064-1073, 2009.

[22] R. Tania, R.L. Florin, I.D. Adriana, M. Roxana, A. Ancuta and D. Florin, “Experimental investigation on the influence of overlap ratio on Savonius turbines performance,” International Journal of Renewable Energy Research, vol. 8, no. 3, pp. 1791-1799, 2018.

[23] J. Yao, F. Li, J. Chen, Z. Yuan and W. Mai, “Parameter analysis of Savonius hydraulic turbine considering the effect of reducing flow velocity,” Energies, vol. 13, pp. 1-16, 2020.

[24] J.L. Menet and N. Bourabaa, “Increase in the Savonius rotors efficiency via a parametric investigation,” European Wind Energy Conference, pp. 1-11, 2004.

[25] A. Rezaeiha, I. Kalkman and B. Blocken, “CFD simulation of a vertical axis wind turbine operating at a moderate tip speed ratio: Guidelines for minimum domain size and azimuthal increment,” Renewable Energy, vol. 107, pp. 373-385, 2017.

[26] R. Lanzafame, S. Mauro and M. Messina, “2D CFD modeling of h-Darrieus wind turbines using a transition turbulence model,” Energy Procedia, vol. 45, pp. 131-140, 2014.

SAKARYA ÜNİVERSİTESİ
FEN BİLİMLERİ ENSTİTÜSÜ
DERGİSİ

Sakarya University Journal of Science
SAUJS
e-ISSN 2147-835X | Period Bimonthly | Founded: 1997 | Publisher Sakarya University |
http://www.saujs.sakarya.edu.tr/en/

Title: Supervised Learning Approaches to Flight Delay Prediction

Authors: Mehmet Cemal ATLIOĞLU, Mustafa BOLAT, Murat ŞAHİN, Volkan TUNALI, Deniz KILINÇ

Recieved: 2020-03-27 16:00:07

Accepted: 2020-09-11 20:02:56

Article Type: Research Article

Volume: 24
Issue: 6
Month: December
Year: 2020
Pages: 1223-1231

How to cite
Mehmet Cemal ATLIOĞLU, Mustafa BOLAT, Murat ŞAHİN, Volkan TUNALI, Deniz KILINÇ; (2020), Supervised Learning Approaches to Flight Delay Prediction. Sakarya University Journal of Science, 24(6), 1223-1231, DOI: https://doi.org/10.16984/saufenbilder.710107
Access link
http://www.saujs.sakarya.edu.tr/en/pub/issue/57766/710107

Sakarya University Journal of Science 24(6), 1223-1231, 2020

Supervised Learning Approaches to Flight Delay Prediction

Mehmet Cemal ATLIOĞLU[1], Mustafa BOLAT[1], Murat ŞAHİN[2], Volkan TUNALI[*3],
Deniz KILINÇ[4]

Abstract

Delays in flights and other airline operations have significant consequences in quality of service, operational costs, and customer satisfaction. Therefore, it is important to predict the occurrence of delays and take necessary actions accordingly. In this study, we addressed the flight delay prediction problem from a supervised machine learning perspective. Using a real-world airline operations dataset provided by a leading airline company, we identified optimum dataset features for optimum prediction accuracy. In addition, we trained and tested 11 machine learning models on the datasets that we created from the original dataset via feature selection and transformation. CART and KNN showed consistently good performance in almost all cases achieving 0.816 and 0.807 F-Scores respectively. Similarly, GBM, XGB, and LGBM showed very good performance in most of the cases, achieving F-Scores around 0.810.

Keywords: air transportation, flight delay prediction, machine learning, data science

---

[1] Tav Technology, İstanbul, E-Mail: MehmetCemal.Atlioglu@tav.aero
E-Mail: Mustafa.Bolat@tav.aero ORCID: https://orcid.org/0000-0003-1289-2715
ORCID: https://orcid.org/0000-0001-8169-0629

[2] Manisa Celal Bayar University, Faculty of Technology, E-Mail: muratpq@gmail.com
ORCID: https://orcid.org/0000-0002-2866-8796

[*] Corresponding Author: volkan.tunali@gmail.com

[3] Maltepe University, Faculty of Engineering and Natural Sciences
ORCID: https://orcid.org/0000-0002-2735-7996

[4] İzmir Bakırçay University, Faculty of Engineering and Architecture,
E-Mail: drdenizkilinc@gmail.com
ORCID: https://orcid.org/0000-0002-2336-8831

1. INTRODUCTION

Airline operations are too complex to manage with complete accuracy. There are a lot of resources and constraints to be synchronized to have an adequate accuracy of timing. Trying to increase the synchronization accuracy of airline operations is a major field of study and practice in the business of Airline Management. One of the alternative approaches to gaining accuracy is to predict some anomalies and seemingly unexpected delays in operations in advance and to react and adapt accordingly [1]. Therefore, predicting the delays in well-defined flight milestone points can provide improvements in the overall predictability of the airline operations and may result in considerable level of cost savings and increase in passenger satisfaction [2].

In this study, we addressed the flight delay prediction problem from a supervised machine learning perspective. Using a real-world airline operations dataset provided by a leading airline company, we identified optimum dataset features that improve prediction accuracy. Moreover, we trained and tested a lot of machine learning models such as K-Nearest Neighbor (KNN), Support Vector Machine (SVM), Decision Tree (CART), and Gaussian Naïve Bayes (GNB) on the datasets that we created from the original dataset via feature selection and transformation.

This paper is organized as follows: Section 2 presents some timely work on flight delay prediction in the literature. Section 3 explains the details of the datasets and machine learning models that we experimented with. In Section 4, we present our empirical findings and discuss them. Finally, Section 5 concludes the study and provides some future directions for further research.

2. RELATED WORK

Due to increasing demand to airline transportation, flight delay prediction is an important problem that researchers have been actively investigating. In this section, we present some notable and recent work on the topic. Most of these studies rely on data mining and machine learning techniques because large quantities of operational data regarding aviation operations are now possible to collect, store, and process. Besides, applications based on machine learning techniques have already achieved promising performances in very diverse domains like computer vision, natural language processing, medical diagnosis, fraud detection, and so on. Therefore, it is perfectly normal to see many studies that try to utilize machine learning for flight delay prediction.

In a study by Ding, flight delay prediction was considered as a regression problem, and a solution based on multiple linear regression was proposed and compared with Naïve Bayes and C4.5 [3].

A Gradient Boosting classification model was created using hyper-parameter optimization by Chakrabarty in [4]. In addition, to overcome the imbalance problem of the training data, over-sampling via Randomized SMOTE technique was also employed in the study.

In [5] by Yu et al., key factors causing the delays were analyzed, and a prediction model that used a deep belief network along with a support vector regression was proposed for optimal prediction accuracy.

Khaksar and Sheikholeslami investigated the factors affecting the flight delay prediction using several datasets and machine learning techniques like Bayesian modeling, decision tree, random forest, and so on [6].

In a very recent study by Gui et al., flight delay prediction was also studied from big data and machine learning perspective [7]. In the study, several machine learning models were examined and it was experimentally shown that random forest-based model achieved very high prediction accuracy without overfitting.

When we examine the previous studies mentioned above, we observe that the datasets used and the methodologies applied were highly similar to those in our study. All of them used the flight datasets of from the commercial airline companies of their respective countries, and these datasets had very similar features. In some studies, however, the datasets were enriched with new features like weather conditions, fleet age, and so on. In our study, we did not apply such kind of feature enrichment, instead, we only used the data as obtained from the airline operations. All studies consistently reported that their datasets were imbalanced in terms of class distribution, and some of them applied several dataset balancing techniques. In our study, we did not make use of any kind of balancing. While some of the studies approached the problem as a binary classification problem (i.e., delay or no-delay), some used several delay classes like delays of 0-15 (minutes), 15-30, 30-60, and so on, making them a multi-class classification problem. In our study, however, we addressed the flight delay problem as a binary classification problem. The previous studies usually trained and tested a relatively small number of classification algorithms and they reported classification accuracy around 70-90%. Different from them, we trained and tested a large number of classification models on several datasets with hand-picked features, we obtained accuracy around 82%.

3. MATERIALS AND METHOD

In this section, we give the details of the dataset used and the method applied in this study.

3.1. Dataset

The dataset used in this study was provided by a leading airline company in Turkey. It contains 8,086 lines of data records that belonged to operations of the Dammam King Fahd International Airport, Saudi Arabia, during the three-year period from January 1st, 2017 to December 9th, 2019. Detailed information about the dataset structure is given in Table 1.

Table 1
Structure of the original dataset

Column name	Description	Number of distinct values
line_no	Unique row ID	NA
origin	IATA code of the airport from which the incoming aircraft departed	12
airline_icao	Airline carrier ICAO code of the incoming aircraft	1
etad_stad	Difference between Estimated Time and Scheduled Time in minutes	NA
flight_category	International vs. Domestic	2
ac_subtype	Aircraft subtype	5
terminal_resource	International vs. Domestic	2
pax_count	Number of passengers	NA
gate_resource_id	Gate ID used by incoming passengers	19
stand_resource_id	Area ID where the aircraft parked	32
etad	Estimated time of arrival/departure	NA
stad	Scheduled time of arrival/departure	NA
tobt	Target Off Block Time	NA
aobt	Actual On Block Time	NA
atad	Actual time of arrival/departure	NA

3.2. Data Preprocessing

In this study, we considered the flight delay prediction problem as a binary classification problem such that if *etad_stad* (difference between Estimated Time and Scheduled Time in minutes) was greater than 15 minutes, we considered it a delay, and no-delay otherwise. Therefore, we generated a class variable with two values as delay and no-delay. This 15-minute period was decided after consultations with domain experts from the airline company. After the class variable generation, the dataset had an imbalanced class distribution of 1,174 delay and 6,912 no-delay records.

As seen in Table 1, the data columns *origin*, *flight_category*, *ac_subtype*, *terminal_resource*, *gate_resource_id*, and *stand_resource_id* are categorical variables with a number of distinct values. Because there was no ordinal relationship between the values of these variables, we treated them as nominal variables during experiment datasets creation. Applying one-hot-encoding technique to each categorical variable, we created a large number of binary features.

The variables other than the categorical ones are simply ignored in the experiment datasets creation phase since they did not present any useful information for delay prediction. We manually combined the categorical variables in different ways to create six different experiment datasets. Besides, we augmented the experiment datasets with the *year* of *etad* value as a numerical variable by simply adding this new variable to each dataset. Details of the experiment datasets are given in Table 2.

Table 2
Details of the experiment datasets

	Experiment Dataset ID					
Variable used	**1**	**2**	**3**	**4**	**5**	**6**
Origin	✓	✓	✓	✓	✓	✓
ac_subtype	✓	✓		✓	✓	✓
gate_resource_id	✓	✓	✓		✓	
stand_resource_id	✓	✓	✓	✓		
Year	✓		✓	✓	✓	✓
flight_category	✓	✓	✓	✓	✓	✓
Number of features	71	70	66	52	39	20

3.3. Supervised Learning Models

Machine Learning is a subfield of Artificial Intelligence dealing with algorithms that learn through experience that is supplied in the form of past data [8]. Machine Learning algorithms are divided into two well-established categories depending on their approach and the type of the problem they are expected to solve: supervised learning and unsupervised learning [9]. In supervised learning, the data contains a class (or target) variable, and the task is to predict the class value upon learning the correlations between the class labels and the other variables from the data via a process called training. Regression and classification are the main types of supervised learning algorithms. In unsupervised learning, on the other hand, the algorithm learns the patterns and structures like clusters in the data without being supplied with any class labels.

In this study, our main objective was to predict flight delays using past labeled data. Therefore, we employed a supervised learning approach to the problem. Rather than predicting the flight delay time in minutes and thus considering the flight delay prediction problem as a regression problem, we approached it as a classification problem where we tried to predict whether a delay would occur or not with respect to some flight information given. Classification is the task of predicting the class of a data instance whose class is previously unknown using a model trained with data instances with previously known class labels [9].

There are a lot of classification algorithms in the literature. In this study, we trained 11 different classification models for each experiment dataset using 11 different classification algorithms, namely, K-Nearest Neighbor (KNN), Support Vector Machine (SVM), Decision Tree (CART), Gaussian Naïve Bayes (GNB), Logistic Regression (LR), Multilayer Perceptron (MLP), Random Forest (RF), Gradient Boosting (GBM), XGBoost (XGB), CatBoost (CB), and LightGBM (LGBM) [9-14]. First five of these algorithms are called base classifiers because only one classifier instance is trained for each one. Multilayer Perceptron, also a base classifier, is also called Artificial Neural Network, where there is a series of interconnected neuronal layers. The rest of the algorithms are called ensemble classifiers because more than one instance of base classifiers are trained and their collective decision is reported as the final prediction [9].

3.4. Experimental Setup

Throughout this study, we used Python 3.7 for all data preprocessing, model training, and model evaluation tasks because Python is a very powerful programming language with extensive data manipulation capabilities with pandas package (version 1.0.3) [15] and machine learning capabilities with scikit-learn package (version 0.22.2) [16]. In our experiments, we ran all classifiers with their default parameters in their scikit-learn implementations. The most important of these default parameters are presented in Table 3. In addition, we applied 10-fold cross validation to get more reliable model performance prediction since our datasets were imbalanced and number of training and testing data instances were quite small.

Table 3
Default parameter values of classifiers

Algorithm	Default parameter values
KNN	n_neighbors:5, metric:'minkowski'
SVM	regularization:1.0, kernel:'rbf', degree:3, gamma:'scale'
CART	criterion:'gini', splitter:'best', max_depth:None,
GNB	priors:None, var_smoothing:1e-09
LR	regularization:1.0, class_weight:None, fit_intercept:True, intercept_scaling:1, l1_ratio:None, max_iter:100, solver:'liblinear'
MLP	hidden_layer_sizes:(100,) activation:'relu', solver:'adam', alpha:0.0001
RF	n_estimators:100, criterion:'gini', max_depth:None, min_samples_split:2, min_samples_leaf:1
GBM	loss:'deviance', learning_rate:0.1, n_estimators:100, subsample:1.0, criterion:'friedman_mse', min_samples_split:2, min_samples_leaf:1
XGB	max_depth:3, learning_rate:0.1, n_estimators:100
CB	iterations:None, learning_rate:None, depth:None, min_child_samples:None, max_leaves:None, num_leaves:None, max_depth:None, n_estimators:None
LGBM	boosting_type:'gbdt', num_leaves:31, max_depth:-1, learning_rate:0.1, n_estimators:100

3.5. Model Evaluation Metrics

In order to measure the classification performance of the selected algorithms, we used Precision, Recall, F-Score, and ROC Area metrics. Since our dataset was imbalanced in terms of class distribution, these were very reliable metrics to predict the model performance in a real-world scenario. For each of these metrics, the higher the metric value, the higher the performance of a classifier is.

When we test a binary classifier, we obtain four different counts as True Positive (TP), False Positive (FP), True Negative (TN), and False Negative (FN). Using these counts, it is possible to compute the above metrics as given in Equations 1, 2, 3, and 4, respectively.

$$Precision = \frac{TP}{TP+F} \tag{1}$$

$$Recall = \frac{TP}{TP+} \tag{2}$$

$$F\text{-}Score = \frac{2\times Precision\times Recall}{Precision+Rec} \tag{3}$$

$$ROC\ Area = \frac{1}{2}\left(\frac{TP}{TP+FN} + \frac{TN}{TN+FP}\right) \tag{4}$$

We used the related metric functions of the scikit-learn package with the *average* parameter set to ‘weighted’ in order to take into consideration the imbalanced nature of the class labels. With this option, respective metrics are calculated for each class independently, and then their average weighted by the number of true instances for each class is calculated.

For example, for a binary classification with TP = 1744, FP = 278, FN = 0, and TN = 0, precision (P) is calculated as follows. First, precision for each class label is calculated independently as P_{pos} = 1744 / 2022 = 0.862, and P_{neg} = 278 / 2022 = 0.137. Then, the weighted average of these values is calculated using the number of true instances for each class label as P = (0.862 × 1744 + 0.137 × 0) / 2022, and it is found 0.743.

As a result of this parameter decision for imbalanced datasets, for instance, calculated F-Score values may not fall into between related Precision and Recall values. For the very same reason, calculated ROC Area values may seem rather low when Precision and Recall values are considered. For the previous example, ROC Area is calculated as 0.5 × (1744 / 1744 + 0 / 278) = 0.5, which is much lower than the calculated Precision and Recall values.

4. FINDINGS AND DISCUSSION

We trained 11 machine learning models and tested them on six experiment datasets using 10-fold cross validation. We present model scores for each dataset in Tables 4 to 9, respectively. In the tables, highest values for each score are emphasized with boldface font.

Table 4
Experiment results for Experiment Dataset 1

Algorithm	Precision	Recall	F-Score	ROC Area
KNN	0.807	0.861	0.807	0.514
SVM	0.744	0.860	0.797	0.498
CART	0.814	0.861	**0.816**	**0.532**
GNB	**0.882**	0.143	0.044	0.503
LR	0.744	**0.863**	0.799	0.500
MLP	0.744	**0.863**	0.799	0.500
RF	0.744	**0.863**	0.799	0.500
GBM	0.814	0.862	0.812	0.524
XGB	0.817	**0.863**	0.812	0.523
CB	0.744	**0.863**	0.799	0.500
LGBM	0.817	**0.863**	0.811	0.521

Table 5
Experiment results for Experiment Dataset 2

Algorithm	Precision	Recall	F-Score	ROC Area
KNN	0.815	**0.863**	0.805	0.511
SVM	0.744	0.860	0.797	0.498
CART	0.810	0.862	0.805	0.510
GNB	**0.882**	0.143	0.044	0.503
LR	0.836	**0.863**	0.801	0.503
MLP	0.744	**0.863**	0.799	0.500
RF	0.744	**0.863**	0.799	0.500
GBM	0.744	0.862	0.799	0.500
XGB	0.810	0.862	0.805	0.510
CB	0.744	**0.863**	0.799	0.500
LGBM	0.820	**0.863**	**0.807**	**0.514**

Table 6
Experiment results for Experiment Dataset 3

Algorithm	Precision	Recall	F-Score	ROC Area
KNN	0.807	0.861	0.807	0.514
SVM	0.744	0.860	0.797	0.498
CART	0.814	0.861	**0.816**	**0.532**
GNB	**0.831**	0.145	0.049	0.503
LR	0.744	0.863	0.799	0.500
MLP	0.019	0.137	0.033	0.500
RF	0.744	0.863	0.799	0.500
GBM	0.810	0.861	0.811	0.523
XGB	0.820	0.863	0.812	0.523
CB	0.744	0.863	0.799	0.500
LGBM	0.830	**0.864**	0.809	0.516

Table 7
Experiment results for Experiment Dataset 4

Algorithm	Precision	Recall	F-Score	ROC Area
KNN	0.799	0.860	**0.805**	**0.511**
SVM	0.744	**0.863**	0.799	0.500
CART	0.744	**0.863**	0.799	0.500
GNB	**0.882**	0.143	0.044	0.503
LR	0.744	**0.863**	0.799	0.500
MLP	0.744	**0.863**	0.799	0.500
RF	0.744	**0.863**	0.799	0.500
GBM	0.744	0.861	0.798	0.499
XGB	0.836	**0.863**	0.801	0.503
CB	0.744	**0.863**	0.799	0.500
LGBM	0.836	**0.863**	0.801	0.503

Table 8
Experiment results for Experiment Dataset 5

Algorithm	Precision	Recall	F-Score	ROC Area
KNN	0.799	0.862	0.800	0.503
SVM	0.744	0.861	0.798	0.499
CART	0.779	0.860	0.800	0.503
GNB	**0.882**	0.142	0.043	0.503
LR	0.744	**0.863**	0.799	0.500
MLP	0.744	**0.863**	0.799	0.500
RF	0.744	**0.863**	0.799	0.500
GBM	0.767	0.861	0.799	0.500
XGB	0.804	0.862	**0.801**	**0.504**
CB	0.744	**0.863**	0.799	0.500
LGBM	0.804	0.862	**0.801**	**0.504**

Table 9
Experiment results for Experiment Dataset 6

Algorithm	Precision	Recall	F-Score	ROC Area
KNN	0.744	**0.863**	**0.799**	0.500
SVM	0.744	**0.863**	**0.799**	0.500
CART	0.744	**0.863**	**0.799**	0.500
GNB	**0.882**	0.142	0.043	**0.503**
LR	0.744	**0.863**	**0.799**	0.500
MLP	0.744	**0.863**	**0.799**	0.500
RF	0.744	**0.863**	**0.799**	0.500
GBM	0.744	**0.863**	**0.799**	0.500
XGB	0.744	**0.863**	**0.799**	0.500
CB	0.744	**0.863**	**0.799**	0.500
LGBM	0.744	**0.863**	**0.799**	0.500

4.1. Evaluation of Datasets

High F-Score and ROC Area together are good indicators of a good prediction model. When we examine the results in the tables, we see consistently higher F-Score and ROC Area scores in Tables 4 and 6 for Experiments Datasets 1 and 3, respectively. Experiment Dataset 1 is the dataset where all variables are used as the features (71 features in total). Experiment Dataset 3, on the other hand, is the one with features without *ac_subtype* variable (66 features in total). Almost all prediction algorithms performed similarly on these two datasets. Based on this finding, we can infer that *ac_subtype* (aircraft subtype) does not contribute much to the predictive ability of the machine learning algorithms. As a result, it can be excluded from real-world model creation.

We see that model scores for Experiment Datasets 4, 5, and 6 are consistently very low when compared to the scores of the other datasets. The common factor for these three datasets is the absence of either *gate_resource_id* or *stand_resource_id* variable, or both. Therefore, we can infer that these two variables play highly important role for flight delay prediction, although their absence resulted in less number of features, which was good for model training and testing.

The model score results in Table 9 show such an interesting pattern that all algorithms other than GNB performed exactly the same in terms of all metrics. This also suggests that the absence of both *gate_resource_id* and *stand_resource_id* variables created machine learning models with no predictive power at all. ROC Area score with 0.5 value also supports this finding. The same pattern is also observed in Tables 7 and 8 to some degree, where either *gate_resource_id* or *stand_resource_id* variable was absent in the respective experiment datasets.

4.2. Evaluation of Algorithms

We have an important observation that GNB algorithm performed very poorly for all experiment datasets. Although it presented higher precision than all other competing algorithms, its recall values were very low, which also resulted in very low F-Score values.

According to the results in Tables 4, 5, and 6, the decision tree (CART) algorithm performed well, reaching almost the highest F-Score and ROC Area scores.

From our previous experience, we would expect that RF algorithm, which is an ensemble learning algorithm, would perform well. However, its performance was almost always very low. On the other hand, we see that other ensemble learning algorithms GBM, XGB, and LGBM showed very good performance in most of the cases. CB, which is also an ensemble classifier, however, performed very poorly in all cases.

Besides CART algorithm, KNN also showed consistently good performance in almost all cases. Although it is the simplest learning algorithm and no learning model is actually created at all due to its lazy nature, it performed surprisingly well in flight delay prediction.

Finally, the other algorithms, which are very well-known for their good performances in classification tasks, failed drastically in flight delay prediction in all cases. That is, SVM, LR, and MLP algorithms did not exhibit any good performance as opposed to their good reputations.

5. CONCLUSION AND FUTURE DIRECTIONS

Delays in flights and other airline operations have significant consequences in quality of service, operational costs, and customer satisfaction. Therefore, it is important to predict the occurrence of delays and take necessary actions accordingly. In this study, we considered the flight delay prediction problem as a machine learning problem. More specifically, we offered a solution to the problem by transforming it to classification problem.

Using the operational data from a three-year period made available by an airline company, we generated six different experiment datasets by applying several preprocessing techniques like feature selection and data transformation. Once we obtained these datasets, we trained and tested 11 different machine learning models on each one. Whereas some machine learning models showed promising performance in flight delay prediction, some failed very badly. For example, CART (decision tree) and KNN algorithms showed consistently good performance in almost all cases achieving 0.816 and 0.807 F-Scores respectively. Similarly, GBM, XGB, and LGBM algorithms showed very good performance in most of the cases, achieving F-Scores around 0.810. GNB, RF, CB, SVM, LR, and MLP algorithms, on the other hand, did not show acceptable performance.

Performances of the machine learning models were not independent of the datasets on which they were trained. The datasets that the machine learning algorithms showed good performance were the ones that contained the features *gate_resource_id* and *stand_resource_id.* These two variables were the ones with the most predictive power in flight delay prediction. Therefore, these variables should definitely be included in the production model creation. Nevertheless, *ac_subtype* variable did not contribute much to the predictive ability of the machine learning algorithms, and it can be excluded in production.

When we examine the previous studies, we see that they all used the flight datasets of from the commercial airline companies of their respective countries. Similarly, in this study, we introduced a new, genuine, and recent flight dataset from a Turkish airline company. Moreover, the previous studies usually trained and tested a relatively small number of classification algorithms on their datasets. We, on the other hand, trained and tested a quite large number of classification models on several datasets with hand-picked and engineered features.

The dataset used in this study was imbalanced in terms of delay and no-delay class distributions. This could be the main reason why some machine learning algorithms did very poorly while some did well. As a future work, we plan to repeat the experiments on a dataset that we made balanced using several techniques like over-sampling, SMOTE, and so on. Furthermore, we also consider that the machine learning algorithms that are based on decision trees may perform better when the categorical data are not transformed into binary features.

Funding

This work was partially supported by the Research and Development Center of TAV Airports Holding accredited on Turkey-Ministry of Science.

The Declaration of Conflict of Interest/ Common Interest

No conflict of interest or common interest has been declared by the authors.

Authors' Contribution

M.C.A: Investigation, experimental design.

M.B: Experimental design, investigation, data analysis.

M.Ş: Experimental design, investigation, data analysis.

V.T: Review, writing, editing, investigation, supervision.

D.K: Review, writing, investigation.

The Declaration of Ethics Committee Approval

The authors declare that this document does not require an ethics committee approval or any special permission.

The Declaration of Research and Publication Ethics

The authors of the paper declare that they comply with the scientific, ethical and quotation rules of SAUJS in all processes of the paper and that they do not make any falsification on the data collected. In addition, they declare that Sakarya University Journal of Science and its editorial board have no responsibility for any ethical violations that may be encountered, and that this study has not been evaluated in any academic publication environment other than Sakarya University Journal of Science.

REFERENCES

[1] N. Pyrgiotis, K. M. Malone, and A. Odoni, "Modelling delay propagation within an airport network," Transportation Research Part C: Emerging Technologies, vol. 27, pp. 60-75, 2013.

[2] J. J. Rebollo and H. Balakrishnan, "Characterization and prediction of air traffic delays," Transportation Research Part C: Emerging Technologies, vol. 44, pp. 231-241, 2014.

[3] Y. Ding, "Predicting flight delay based on multiple linear regression," in 2nd International Conference on Materials Science, Energy Technology and Environmental Engineering (MSETEE 2017), Zhuhai, China, pp. 1-8, 2017.

[4] N. Chakrabarty, "A Data Mining Approach to Flight Arrival Delay Prediction for American Airlines," CoRR, vol. abs/1903.06740, 2019.

[5] B. Yu, Z. Guo, S. Asian, H. Wang, and G. Chen, "Flight delay prediction for commercial air transport: A deep learning approach," Transportation Research Part E: Logistics and Transportation Review, vol. 125, pp. 203-221, 2019.

[6] H. Khaksar and A. Sheikholeslami, "Airline delay prediction by machine learning algorithms," Scientia Iranica, vol. 26, pp. 2689-2702, 2017.

[7] G. Gui, F. Liu, J. Sun, J. Yang, Z. Zhou, and D. Zhao, "Flight Delay Prediction Based on Aviation Big Data and Machine Learning," IEEE Transactions on Vehicular Technology, vol. 69, pp. 140-150, 2020.

[8] E. Alpaydın, Introduction to Machine Learning, 3rd ed. London, England: The MIT Press, 2014.

[9] J. Han and M. Kamber, Data Mining: Concepts and Techniques. USA: Morgan Kaufmann Publishers, 2006.

[10] J. C. Platt, "Fast training of support vector machines using sequential minimal optimization," in Advances in kernel methods, S. Bernhard, J. C. B. Christopher, and J. S. Alexander, Eds., ed: MIT Press, pp. 185-208, 1999.

[11] L. Breiman, "Random Forests," Machine Learning, vol. 45, pp. 5-32, 2001.

[12] T. Chen and C. Guestrin, "XGBoost: A Scalable Tree Boosting System," presented at the Proceedings of the 22nd ACM SIGKDD International Conference on Knowledge Discovery and Data Mining, San Francisco, California, USA, 2016.

[13] G. Ke, Q. Meng, T. Finley, T. Wang, W. Chen, W. Ma, Q. Ye, and T.-Y. Liu, "LightGBM: a highly efficient gradient boosting decision tree," presented at the Proceedings of the 31st International Conference on Neural Information Processing Systems, Long Beach, California, USA, 2017.

[14] A. V. Dorogush, V. Ershov, and A. Gulin, "CatBoost: gradient boosting with categorical features support," CoRR, vol. abs/1810.11363, 2018.

[15] W. McKinney, "pandas: a foundational Python library for data analysis and statistics," Python for High Performance and Scientific Computing, vol. 14, 2011.

[16] F. Pedregosa, G. Varoquaux, A. Gramfort, V. Michel, B. Thirion, O. Grisel, M. Blondel, P. Prettenhofer, R. Weiss, V. Dubourg, J. Vanderplas, A. Passos, D. Cournapeau, M. Brucher, M. Perrot, and É. Duchesnay, "Scikit-learn: Machine Learning in Python," Journal of Machine Learning Research, vol. 12, pp. 2825-2830, 2011.

SAKARYA ÜNİVERSİTESİ
FEN BİLİMLERİ ENSTİTÜSÜ
DERGİSİ

Sakarya University Journal of Science
SAUJS
e-ISSN 2147-835X | Period Bimonthly | Founded: 1997 | Publisher Sakarya University |
http://www.saujs.sakarya.edu.tr/en/

Title: Study of the Effect of Various Chemical Polishing Treatments on MBE-Grown CdTe/GaAs (211)B Heterostructures

Authors: Elif BİLGİLİSOY, Elif ÖZÇERİ, Enver TARHAN

Recieved: 2020-06-05 18:00:08

Accepted: 2020-09-11 23:24:26

Article Type: Research Article

Volume: 24
Issue: 6
Month: December
Year: 2020
Pages: 1232-1247

How to cite
Elif BİLGİLİSOY, Elif ÖZÇERİ, Enver TARHAN; (2020), Study of the Effect of Various Chemical Polishing Treatments on MBE-Grown CdTe/GaAs (211)B Heterostructures. Sakarya University Journal of Science, 24(6), 1232-1247, DOI: https://doi.org/10.16984/saufenbilder.748315
Access link
http://www.saujs.sakarya.edu.tr/en/pub/issue/57766/748315

Sakarya University Journal of Science 24(6), 1232-1247, 2020

Study of the Effect of Various Chemical Polishing Treatments on MBE-Grown CdTe/GaAs (211)B Heterostructures

Elif BİLGİLİSOY[1], Elif ÖZÇERİ[2], Enver TARHAN[*3]

Abstract

A three-inch-diameter high quality CdTe thin film was grown on a GaAs (211)B substrate by molecular beam epitaxy (MBE) in ultra-high vacuum conditions. The CdTe/GaAs (211)B heterostructure was then cut into several sample pieces. A few as-grown sample pieces were subjected to chemical etching solutions which created etch pits on the surface. The scanning electron microscopy images of such samples were used to calculate the etch pit densities on the surface. In addition, several as-grown samples were subjected to chemical polishing treatments under different conditions to quantify the removal of O and Te-O structures from the surface. Atomic force microscopy was used to determine as-grown and polished surface morphology and the polish rate of chemical solutions. A study of the surface stoichiometry and the chemical composition of the as-grown and polished CdTe (211)B surfaces were carried out by using X-ray photoelectron spectroscopy. Bulk structural qualities of the as-grown and polished samples were studied in terms of the vibrational and phonon modes via confocal Raman spectroscopy. From a comparative analyses of the results, the best chemical polishing conditions for the MBE-grown CdTe (211)B heterostructure were determined.

Keywords: Molecular beam epitaxy, CdTe thin film, GaAs substrate, thin film polishing, XPS, Raman spectroscopy, AFM

1. INTRODUCTION

The cadmium telluride (CdTe) – gallium arsenide (GaAs) heterostructure is one of the most important material structures for various applications, such as; imaging and sensing systems [1,2], solar cells [3,4], and digital information storage devices [5]. CdTe is a II-VI ionic semiconductor with a zinc-blende crystal structure. Due to its

---

[1] Friedrich-Alexander-Universität Erlangen, E-Mail: bilgilisoy.elif@gmail.com
ORCID: https://orcid.org/0000-0002-5295-213X
[2] İzmir Institute of Technology, E-Mail: ozcerielif@gmail.com
ORCID: https://orcid.org/0000-0001-6116-076X
[*] Corresponding Author: envertarhan@iyte.edu.tr
[3] İzmir Institute of Technology, ORCID: https://orcid.org/0000-0003-3167-3956

room temperature (RT) band gap energy being 1.47 eV with a direct gap, CdTe can absorb most of the solar radiation [6]. In addition to infrared and visible light detection, CdTe based detectors are widely used for the detection of X-rays and γ radiation, which are especially needed in the fields of medicine, astrophysics, solar energy conversion, and electro-optical modulation applications [7]. Furthermore, CdTe is commonly used as a buffer layer for HgCdTe (MCT) which is one of the most widely used materials for infrared detectors [8,9]. For the growth of MCT, the most widely used substrate is CdZnTe (CZT). By adjusting the Cd/Zn ratio during the growth, the best lattice parameter match can be achieved [7]. However, due to the difficulties to obtain large area and high quality CZT substrates, GaAs wafers are among the best substrate choices. There are many studies on GaAs(211)B substrates which especially show suppression of twin defect formations in MCT [10]. CdTe is commonly used as a buffer layer for MCT on GaAs to minimize the lattice mismatch between MCT and GaAs which is a detrimental effect that causes defect formation such as misfit dislocations, [11–13].

Epitaxial growth of these films by molecular beam epitaxy (MBE) allows the manufacture of high quality materials which are not easily available or very expensive in the bulk form. These thin films are of fundamental importance for microelectronic and optoelectronic technologies. In hetero-epitaxial films, the interfaces greatly affect the subsequent junction performance. For this reason, before the hetero-epitaxial growth of the films on CdTe, it is crucial to study the effect of the preparation treatments on the film surface. To achieve high performance devices, the native oxide layer or oxygen defects on the surface of a material (such as CdTe), which are among the most prevalent defects, must be removed for hetero-epitaxial growth of thin films on them. A coherent native oxide layer grows on CdTe under the influence of UV light in ambient conditions. Oxygen atoms originating from air diffuse through the CdTe lattice mostly replacing Cd atoms [14]. Before growing heteroepitaxial layers on substrates, their surfaces must be prepared. Among the most common ways of surface preparation are chemical etching and chemical polishing methods with certain solutions which are the main focus of this work [15,16]. While removing the native oxide layer at the top, these treatments also give the opportunity for a detailed analysis of the chemical composition and structure of the layers of the film under the oxide layer.

For the removal of oxide layers and surface defects, several methods involving various etching and polishing solutions are reported in the literature. Chemical polishing is used for a slow and controlled removal of top layers via chemical solutions. The most widely used and standard polishing solution for elimination of Te-oxides from the surface is a Br_2 – MeOH (methanol) solution [15,16]. In these studies, it was reported that a shiny and residue-free surface was obtained prior to further treatments. However, in another study, it was stated that Br_2 – MeOH solution leaves a very thin amorphous-Te layer on the polished surface [17]. In another study, it was reported that iodine is less corrosive than bromine and reacts with the crystal surface at a lower rate which results a gentle polishing of the surface [18,19]. The most widely used low rate interacting iodine-based solutions are I_2 - MeOH [19] and KIO_3 - KI - Lactic acid [20] which are also suitable for CdTe-based surfaces [21].

In contrast to polishing, etching is a fast removal of many layers of a sample surface which requires stronger solutions (acids or bases) than those used for polishing. For CdTe surfaces, etching solutions containing HCl and Br_2 - Ethylene glycol have already been reported [17,22]. Even though there are many studies in literature about the effects of polishing and etching treatments, to our knowledge, there is no comprehensive investigation comparing the effects of the most widely used polishing and etching solutions on CdTe film surfaces grown on GaAs substrates for further epitaxial treatments. The major goal of this study is, thus, to establish a comparative understanding of several widely used etching and polishing solutions on the chemical composition (hence stoichiometry) of the layers below the surface of an MBE grown CdTe film on a GaAs substrate, in terms of the concentrations of Cd, Te, and oxygen atoms on or near the film surface after removal of the top layers.

2. EXPERIMENTAL METHODS

A highly crystalline thin layer of CdTe was-grown on a 3-inch epi-ready GaAs (211)B substrate in a Veeco GEN20MZ MBE system. The growth procedure was as follows: After placing the GaAs substrate in the growth chamber, first, the oxide layer on the substrate was removed under In flux while the temperature of the substrate was measured by a band-edge thermometer (BandiT). For that purpose, when temperature of the substrate reached 534 °C, In flux was started at 4.43×10^{-8} torr beam equivalent pressure (BEP), which was continued for 300 seconds until the substrate temperature reached 554 °C. The substrate was then kept at this temperature for 330 seconds for the desorption of In compounds (InAs, InO2). Structural properties of the surface during thermal deoxidation was observed by an in-situ reflection high-energy electron diffraction (RHEED) system. Then, the deoxidized substrate was cooled down to 200 °C under As4 flux to assure that the surface of the CdTe film to be grown on the substrate had an As terminated polar face. Next, a nucleation layer of CdTe was-grown for 10 minutes followed by an annealing at 385 °C for 4 minutes. Finally, the substrate temperature was reduced to 300 °C and the growth of the CdTe layer was started. The growth continued until the thickness of the CdTe layer reached 6 μm. During the growth, the substrate was rotated with 2 revolutions per minute (rpm) to ensure a uniform growth profile.

When the growth was completed, the as-grown 3-inch CdTe film on the GaAs substrate was cut into several pieces. A few of them were used as reference; one of which was transferred to the XPS chamber while another one was transferred to the XRD chamber quickly for reference measurements. Both measurements were carried out almost simultaneously only a few minutes after the growth was completed. The other pieces were subjected to various chemical etching and polishing procedures. Each sample, treated or untreated, was then analyzed and characterized. All chemically treated samples were placed in XRD and XPS chambers in a very short duration (a few minutes) after the treatment was ended to minimize contamination from air. Finally, the results were compared and discussed. The methods and characterizations used in this study are given more or less in the following order:

The crystal structure of an as-grown (reference) sample was analyzed using a Philips X'Pert Pro MRD X-Ray Diffraction (XRD) system equipped with a Cu-K-alpha X-ray source. X-ray double crystal rocking curve (DCRC) analyses of the peaks from CdTe (422) planes measured at [0-11] and [-111] azimuths were carried out. Full width at half maximum (FWHM) values of the peaks were studied to assess the crystal quality of the as-grown film [23].

The growth of CdTe on GaAs substrate results in dislocations because of lattice and thermal expansion coefficient mismatches of the films. Next analysis was the study of the density of dislocation defects, which is the average number of dislocations per unit area, on or near the film surface to assess the crystal quality of the as-grown CdTe wafer. Dislocation related defects can be revealed on a film surface by a suitable wet chemical etching method. The methods used to calculate the dislocation densities of as-grown CdTe films were explained in detail in our previous studies [23,24]. For that purpose, the process, named as defect decoration, was carried out in three main steps; oxidation, dissolution, and dilution [25]. The etching rate of a film was controlled by varying the parameters of these steps. In the first step, oxidizing agents were used such as bromine, chromic acid, nitric acid, and hydrogen peroxide. Oxidization occurs by taking an electron from a surface Te atom by an oxidizing agent molecule since Te is more reactive than Cd. SEM micrograph images of the etched film surfaces were then investigated visually for etch pits which take place at the surface end of dislocation defects in the film. Then, depending on the etching solution, surface polarity, and the crystal orientation, surface pits with certain geometric shapes were observed by eye from these images.

Two different etching solutions were used to calculate the etch pit densities (EPDs). One of them was an Everson solution (1HF:4HNO3:25C2H4OHCOOH) [26] which was applied for 25 seconds at room temperature (RT). The other one was a Nakagawa solution (1HF:2H2O2:2H2O) [27] applied for 7 seconds at RT. Then, the etched films were rinsed in DI-water and dried under dry N2 gas flow. The EPDs were calculated by manually counting the number of pits for any given area from the SEM images (obtained by a FEI Quanta 250 FEG system) of the etched samples. The EPD value for a particular sample surface was then calculated as the average of such numbers per unit sample surface area.

The oxide layer was studied with various chemical polishing methods [15,16] in order to understand the nature of oxygen contamination on the surface of CdTe films as well as to obtain the concentrations of Cd and Te atoms near the surface. Chemical polishing of the native oxide and the top surface layers of the CdTe films were carried out with several distinct solutions of chemicals such as hydrofluoric acid and hydrochloric acid [3]. In the last step, the solutions were diluted by DI water, lactic acid, acetic acid etc. [10]. Table 1 lists five different polishing solutions for five samples (named E1, E2, etc.). All sample pieces were cut from the middle section of the wafer to ensure uniformity. A study about the uniformity of similar CdTe/GaAs wafers grown by MBE by the same group of authors is given in the literature [28]. Each polishing was followed by a rinsing solution involving a methanol (MeOH) solution and DI water and ended with a dry nitrogen flux. The etching rates of the polishing solutions were calculated by a Solver Pro 7 atomic force microscopy (AFM) instrument (NT-MDT) system. The root mean square (RMS) surface roughness values of as-grown and chemically polished CdTe films were obtained from the topography images recorded in the tapping mode of the AFM system in a class-100 cleanroom environment.

Table 1
Wet Chemical Polishing Treatment Conditions for five different sample pieces

Sample	Solution*	Time (sec.)	Rinse-1	Rinse-2
E1	%0.5Br$_2$ - MeOH [4,5]	25	MeOH	DI
E2	1HCl - 9DI [13]	3	-	DI
E3	6.5gr I$_2$ - 150 ml MeOH [6]	30	MeOH	DI
E4	$^{(*)}$%5KIO$_3$ - %55KI - %80Lactic (10:10:80) [7]	20	-	DI
E5	%0.5Br$_2$ - Ethylene glycol [28]	25	Ethylene glycol	DI

(*) The percentages indicated in the mixture were prepared as a solution in pure water (DI) and a mixture of the aqueous solutions in the ratio of 10:10:80 was prepared. After the aqueous solutions were prepared, they were allowed to equilibrate for 2 hours. The 2-hour residence time was also applied after the preparation of the 10:10:80 mixture.

Atomic concentrations of oxide agents on the surface of the chemically treated and untreated samples were studied by X-ray photoelectron spectroscopy (XPS) (SPECS EA200 XPS system). The XPS system is composed of an Al X-ray source and a Phoibos 150 hemispherical analyzer with a 3D-DLD detector. To reduce the noise in the XPS spectra, a large area focus and a 40 eV E-pass energy was used. After the growth, when the CdTe film was cut into several pieces, one sample piece was immediately transferred to the XPS system under the atmospheric conditions. The transfer did not last more than 5 minutes. The same transfer duration was taken for all other sample pieces right after chemical polishing and etching treatments in order to minimize the contamination during the transfer. All XPS spectra were calibrated with respect to C-1s peak position at 284 eV. After a linear background subtraction, each spectrum was deconvoluted, using a mixed Gaussian–Lorentzian profile for each individual component, with the help of a CasaXPS software.

After an initial compositional analysis by XPS, each film was then further analyzed structurally by confocal Raman spectroscopy. The structural quality of a film near the surface was assessed by studying the intensity ratio of the 2LO Raman peak to that of the LO peak [23]. This procedure was used both for the as-grown and chemically polished samples. Raman measurements were carried out at various temperatures ranging from RT to 80 K to monitor the changes in the 2LO/LO intensity ratios for comparison. Especially, the Raman data taken at 80 K was used for analyses since it gave the best phonon mode intensities and also provided a better comparison with those in the literature. The temperature of the samples was changed in a controlled manner in a Linkam (THMS600E) cooling chamber with proper optical windows placed under the objective of the microscope of our confocal Raman system. The employed Raman system (an S&I Mono Vista System) consists of an Ar-Ion laser operating at 488 nm and 514 nm wavelengths each with a 120 mW exit power. We employed the 488 nm excitation line since it is in resonance with the energy separation between the top of the Γ_7 split-off valence band and the bottom of the Γ_6 conduction band in the energy-momentum space of CdTe [30], which intensifies most of the observable (especially the LO and 2LO) Raman peaks of CdTe. The scattered light was then collected by the objective of an Olympus BX51 microscope. After a proper filtering of the Rayleigh line with a narrow band (~100 cm-1) notch filter, the scattered light was directed onto an entrance slit of an ACTON SP2750 Princeton Instruments monochromator with a 750 mm focal length and a set of three holographic gratings (150, 600, and 1800 grooves/mm). The dispersed light from the monochromator was then focused on to the exit slit of the monochromator where it was collected by a high resolution charge-coupled device (CCD) detector. The recorded signal by the CCD was then converted into digital data and sent to the controlling computer to be analyzed as spectrum.

3. RESULTS AND DISCUSSIONS

An example of a high resolution double crystal rocking curve (DCRC) measurement of X-rays scattered from (422) planes of an as-grown CdTe on GaAs (211)B sample is given in Figure 1. The peak centered at 35.61 degree was measured at [0-11] azimuth direction. It has a full width at half maximum (FWHM) value of 75.24 arcseconds. Another DCRC measurement taken at [-111] direction gives a FWHM value of 58.2 arcseconds. Considering that the thickness of the CdTe film is about 6 μm, these values are very close to those of good quality MBE grown CdTe on GaAs samples given in the literature for similar thicknesses [16,17]. Hence, we can say that our CdTe film has a good crystal structure for the (211) surface orientation [17,18].

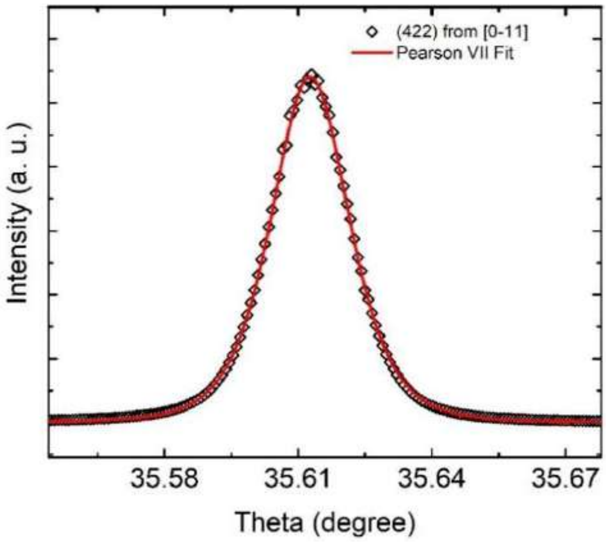

Figure 1 An X-ray DCRC measurement of the CdTe (422) peak taken at [0-11] azimuth direction. Data points are given as diamonds along with a continuous theoretical fit curve

Next, we focused on the study of etch pit densities (EPD). Figure 2 (a) and (c) are the SEM images of sample A etched with an Everson solution for 15 seconds recorded at 20 kV resolution with 50- and 10-micron scales, respectively. Figure 2 (b) and (d) show 10 kV SEM images of sample B etched with a Nakagawa solution with 50- and 10-

micron scale bars, respectively. For sample A, the dislocation-induced etch pit density (EPD) was calculated as 1.2x10^7 cm^{-2} from these images by the manual counting method as given earlier [26,33]. It is seen that Everson etched sample surfaces exhibit triangular shaped etch pits that are concentrated at certain type of surface defects only. The etch pits formed after the Nakagawa etching are larger than those formed after the Everson etching with some degree of overlaps between some of the adjacent pits. These overlaps and the shape differences indicate that the Nakagawa solution acts on different type of surface defects than those observed with the Everson method. We also observed that the Nakagawa etching technique eroded surface defects caused under Te rich growth conditions. Hence, we can conclude that the Nakagawa etch pits form in the regions of Te precipitates [34] while the Everson etch pits form at dislocation sites. We did not calculate any EPD value for sample B due to overlapping pits.

For the study of the surface stoichiometry and chemical structure of the as-grown and chemically polished samples (see Table 1), we utilized X-ray photoelectron spectroscopy (XPS). A collection of XPS spectra of an as-grown sample and chemically polished samples are displayed in Figure 3. Figure 3 (a), (b), and (c) show the XPS spectra of the as-grown sample piece displaying cadmium (Cd-3d3/2), oxygen (O-1s), and tellurium (Te-3d3/2) peaks, in that order, along with their theoretical fits. A linear background subtraction was used for all experimental data before the fittings. The Cd-3d3/2 peak seen in Figure 3 (a) results from the Te-Cd bonds. We could not see any peak originating from the Cd-O structure. The band observed in Figure 3 (b) is made of two subbands as seen from the theoretical fittings, the one at 533 eV is due to oxygen 1s electrons while the other centered at 531.5 eV indicates a Te-O complex [35]. Figure 3 (c) shows a Te-3d3/2 spectrum that has two components centered at 586 and 582 eV. The 582-eV peak is a Te-Cd peak which originates from the CdTe film and the other one is a Te-O peak which is due to the oxidation of tellurium [36]. Figure 3 (d) shows the Te-3d3/2 spectra of five chemically polished samples (E1,…,E5) as given in Table 1. Each spectrum in (d) shows a strong Te-3d3/2 peak and a weak Te-O peak with a smaller FWHM value.

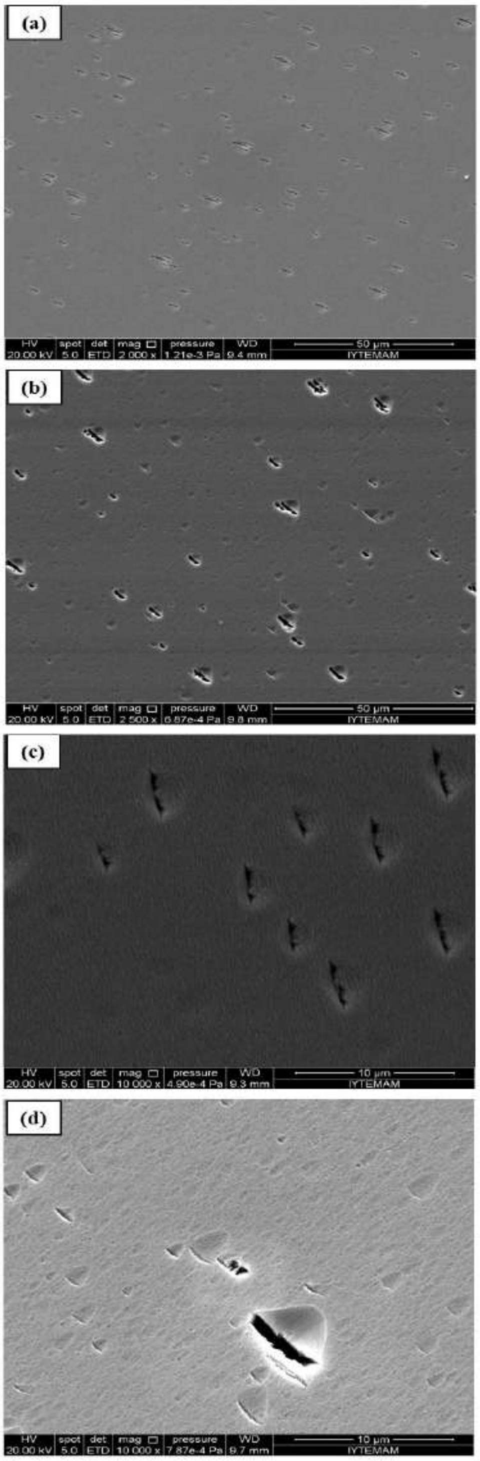

Figure 2 SEM images of samples A and B etched with Everson and Nakagawa solutions, respectively. Insets (a) and (c) are for sample A with 50- and 10-micron scale bars while (b) and (d) are for sample B with 50- and 10-micron scale bars

In all XPS results, the Te-O peak indicates a 3.54 ± 0.01 eV higher binding energy than that of the Te-Cd structure. Also it is seen that cadmium bonds only with Te.

One must consider that XPS signal comes mostly from a few top surface layers, hence, it reveals mostly the surface or near surface structure of the samples.

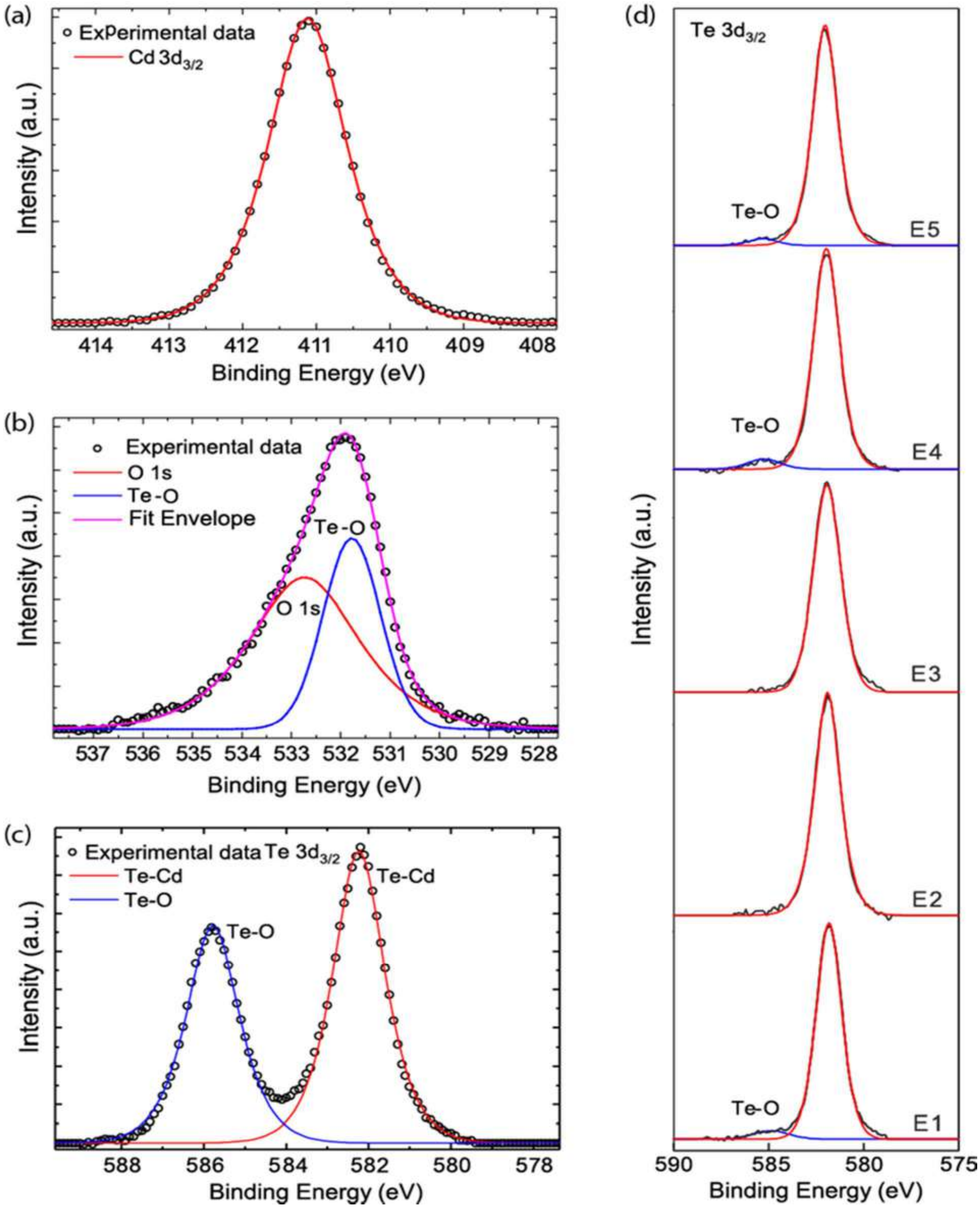

Figure 3 XPS results of (a) Cd-3d3/2, (b) O-1s, and (c) Te-3d3/2 scan of the as-grown CdTe sample. Black dots are experimental data while the continuous red and blue lines are the fit curves. (d) Te-3d3/2 scan of the wet chemically polished CdTe surfaces

The lack of other Cd compounds such as Cd-O structures on the surface indicate that the as-grown film surface ends with Te. Furthermore, the O-1s peak was fitted with two oxygen peaks instead of a single one, which are O-1s and Te-O peaks as seen in Figure 3 (b). We were able to calculate the elemental compositions of Te, Cd, and O at the surface of a film from the Te-Cd, Te-O, Cd-3d3/2, and O-1s XPS peaks. Such calculations were carried out based on the spectra obtained from different regions of the films where the contribution of the relative sensitivity factor (RSF) of each fitting to a spectrum was also taken into account [36].

The results of our elemental concentration (atomic percentages: at. %) analyses obtained from the XPS spectra of the as-grown sample piece and five chemically polished samples are collected in Table 2. Clearly, for the as-grown sample a Cd and Te-O rich surface was seen right after the growth. Its Cd concentration ratio was about 58% which was reduced down to about 40% for all polished samples. While the ratio of Te bound to Cd was about 27% in the as-grown sample it increased to 53-60% range for the polished samples. Additionally, the concentration of the oxidized Te for the as-grown sample was 18% which dropped down to 3 percent or less for the polished samples. These results indicate that the as-grown film surface was indeed Te terminated and a native oxide layer was formed on top of it right after its exposure to ambient air. We also see that the samples E2 and E3 show no oxygen concentration at all. Thus, the chemical polishing methods employed for these samples effectively removed all of the oxygen atoms located on or near the surface. Another point is that we see a smaller Cd concentration for the sample E1. This suggests that the solution used to polish that sample (see Table 1) aggressively eroded Cd-Te and Te-O structures.

We also notice that, the concentration of Te-Cd bonds increased from about 27 percent for the as-grown sample to nearly 60 percent for the polished samples. This leads us to conclude that the Te-rich layers are limited only to the upper layers of the as-grown film, hence, the stoichiometry of the deeper layers is more regular.

Table 2
Elemental concentration analyses obtained from the XPS spectra of the as-grown and chemically polished CdTe samples

Samples	Cd (at. %)	Te-Cd at. %)	Te-O (at. %)
As-grown	58.34	26.66	18
E1	38.49	58.38	3.13
E2	46.14	53.86	0
E3	40.32	59.68	0
E4	40.85	56.07	3.08
E5	40.23	57.79	1.97

The fact that the ratio of oxidized Te is very close to that of Cd bound Te for the as-grown sample indicates that Te atoms form Te-Te dimers or multiple structures instead of Cd-Te bonds at the defect centers in the CdTe crystal. These Te-Te structures are then easily oxidized when exposed to atmospheric conditions yielding Te-O peaks in the XPS spectra. Similarly, high oxygen content observed in the films reveal that the film surfaces are very rich in Te. To clarify this point and to further analyze the quality of the as-grown film, we also carried out Raman spectroscopy measurements on all polished samples mentioned so far.

Raman spectra of the samples were recorded at 80 K after completing their XPS analyses to obtain information about the crystal quality of the chemically polished films and to determine how the chemical polishing methods affected the hetero-epitaxially grown CdTe film quality. Figure 4 shows several Raman peaks that are related to the fundamental TO (Transverse Optic), LO (Longitudinal Optic) and 2LO phonon modes of CdTe crystal structure [37]. The peaks labelled as E and A1 are due to vibrations of Te-Te structures. Generally, in the Roman spectra of all samples the intensities of A1 vibrational modes of Te-Te structures were greater than those of Cd-samples, the intensities of A1 Te phonon modes (TO, LO and 2LO). Figure 4 (a) and (b) show theoretical fittings to the observed spectra.

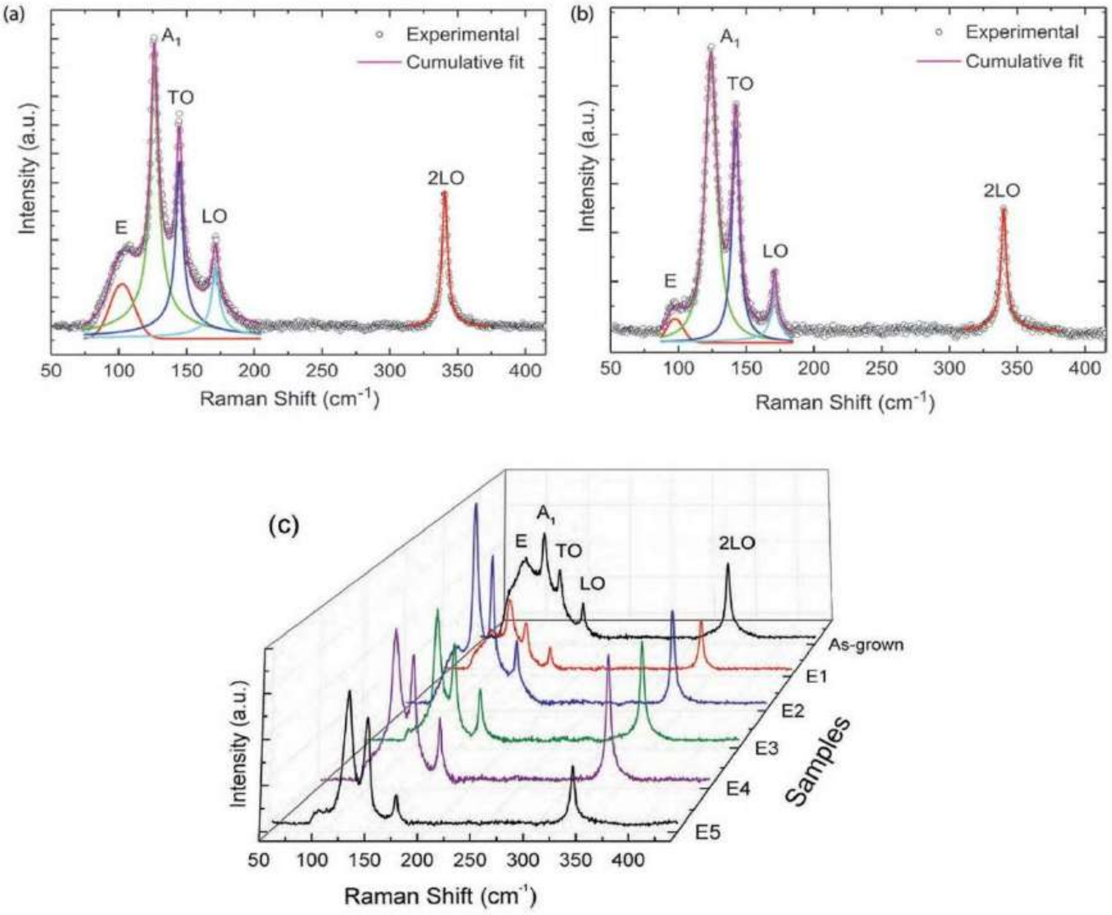

Figure 4 Raman spectra of (a) sample E2 and (b) sample E5. (c); Raman spectra of all samples. All measurements were collected at 80 K

The fittings were carried out using a Person VII type fitting function which is basically a generalized Lorentzian function to an arbitrary integer power [38]. It is seen that the TO and LO phonon modes of all polished CdTe films are at about 141 cm-1 and 168 cm-1, respectively, which are almost the same as those of a bulk CdTe crystal [39]. It is well known that when there is stress in the crystal, the frequencies of these modes blueshift to higher values. All our samples (which are obtained from the same as-grown film) used in this study, show blueshifts of a few (about 2) wavenumbers only, indicating a relatively small stress in the crystal structure. Thus, it is safe to conclude that all our samples, before and after polishing, show high crystal quality.

LO phonon modes are electric dipole forbidden in the Raman backscattering geometry. This is because an LO phonon carry a large momentum and photon scattering cannot account for such a momentum exchange since visible photon momenta are much smaller than those of LO phonons. Various mechanisms have been proposed to explain the nature of the experimentally observed LO mode peaks in the Raman spectra of III-V and II-VI semiconductors. These are mainly; deformation potential scattering [40], impurity mediated scattering [39,41], and exciton (electron-hole pair) mediated scattering which is due to long range Fröhlich interactions [40,42]. Contrarily, multiphonon modes may be dipole allowed. Especially, when two LO phonons of opposite momentum (from the opposite regions of the first Brillouin zone of phonon energy-momentum space) are created simultaneously, their sum may carry almost zero momentum, hence, requiring no net momentum transfer [32]. This point will be discussed further below.

The room temperature Raman spectra of most CdTe samples are dominated by Te precipitates on the surface [43]. However, in the case of resonant Raman scattering (RRS), at low temperatures, Raman intensities of the intrinsic phonon modes become much more pronounced [29,40,42]. We clearly see that the observed RRS at low temperatures (80 K) were dominated by phonon modes of CdTe as seen in Figure 4. Thus, to minimize the surface effects on the observation of phonon modes in Raman spectra, we carried out measurements at 80 K. Indeed, our RT Raman measurements do not yield strong phonon modes and we do not show them here.

Table 3 summarizes the results of our Raman measurements. The peak intensities of A and E modes of Te precipitates on the polished samples are normalized with respect to that of the as-grown sample. We also show the 2LO/LO intensity ratios for all polished samples and the as-grown sample. Although the A_1 mode intensity increases for all samples except for the sample E1, there is a clear reduction in the intensity of the E mode of Te in all polished samples. This suggests that polishing removed some of the Te precipitates from the surface albeit not totally. Only in the sample E1 the removal is quite substantial. We will discuss this sample again below.

Table 3
Raman intensities of A_1 and E modes of Te-Te vibrations of polished samples normalized with respect to that of the as-grown sample along with the 2LO/LO intensity ratios of all polished samples and the as-grown sample. All measurements were carried out at 80 K

Samples	Normalized A_1 int.	Normalized E int.	2LO/ LO
As-grown	-	-	2.61
E1	0.8	0.4	2.38
E2	2.1	0.5	1.86
E3	1.3	0.1	2.26
E4	1.6	0.4	2.16
E5	1.3	0.1	1.88

In the case of resonant Raman scattering, since the simultaneous emission of two LO phonons easily satisfy the momentum conservation rule for electric dipole scattering (near zero phonon momentum), in principle, for a good quality sample, the observed 2LO phonon intensity should always be stronger than that of the LO phonon intensity since the latter is either due to impurities or the long range Fröhlich interactions, provided the impurity concentrations are sufficiently low [29,40,42]. We can assume that the observed intensity variations in the Raman spectra of the polished and as-grown samples, which are given by the intensity ratio of 2LO to that of LO phonons (seen as 2LO/LO in Table 3) should be due to the effect of chemical treatment on the polished samples. As we see from the table that the 2LO/LO ratio is highest for the as-grown sample but reduced somewhat in the polished samples. Since, chemical polishing will not change the excitonic effects on LO and 2LO modes because Fröhlich interactions also play a role in the 2LO phonon mechanism [14], there are only two candidates for the increased LO intensities for the polished samples: First one is increases in the impurity concentrations and second one is changes in the deformation potential due to polishing. In principle, we can say that both processes may play a role. Since polishing will remove many surface layers, it might change the crystal potential in the bulk which will increase the role of the deformation potential. However, the observed blueshifts in the LO and 2LO phonon modes are almost the same for both as grown and the polished samples. Which means polishing does not change the crystal potential considerably, and hence, we can rule out its effect on the observed 2LO/LO intensity variations. On the other hand, polishing might increase the impurity concentration in the bulk of the film (although the surface may improve) by removing the protective oxide layer on the surface which may act like a barrier for the penetration of impurities either from the polishing solution or from air. For that reason, we think that the increased impurity concentrations in the polished samples are the major cause of the increased LO phonon intensities. Hence, even though the polishing increases the surface quality of the CdTe samples by removing Te precipitates and the oxide layer, it may decrease the bulk quality somewhat by increasing the impurity concentrations. However, in all our polished samples, the possible increase in the impurity concentration cannot be larger than two folds since all 2LO/LO ratios remain in that range. Hence, the reduction in the crystalline quality due to polishing can be ignored safely for small impurity concentrations to improve the surface quality for a suitable set of polishing parameters. Thus, one must find the best chemical polishing conditions to optimize the method. Based on these discussions about our Raman results, the polished samples with the better structural quality should be the samples E1, E3, and E4, in that order.

In order to reach a sound conclusion, we must also discuss the atomic force microscopy (AFM) results. The AFM images were used to obtain information about the surface morphology of the samples and polish rates of the polishing solutions (E1…, E5). Figure 5 (a) shows an AFM image of the as-grown sample while (b) shows that of the polished sample E5. We have calculated the average depths of the pits (local minima) on the surface for as-grown and polished samples from the AFM image data to obtain the polishing rates.

Table 4 gives the polishing rates and durations of all polished samples. Also listed in the table are the RMS roughness values and average topographic local minima (pit) depths of all samples (polished and as-grown) as found from the AFM measurements. We see that the sample E5 has the smallest average pit depth and RMS roughness value. One might say that the polishing parameters (see Table 1) for this sample were optimum for the best quality surface. However, the best samples in terms of internal structure (smaller impurity concentration or smaller structural deformation) are the samples E3 and E4 as seen from Table 3 with the highest 2LO/LO intensity ratios. When the cleanest and the smoothest surface is needed, the best polishing treatment is probably the one used for the sample E5 since it has the best surface quality with a tolerable reduction in the bulk quality for which the 2LO/LO ratio is still high (1.88 versus 2.26 for E3). On the other hand, if one wants to grow a HgCdTe layer for infrared detector applications, probably a Te rich surface is needed. For that purpose, the sample E2 maybe the best choice since it has a good stoichiometry as seen from the XPS results with no native oxide layer, as seen in Table 2, and it also has a very small RMS surface roughness value (Table 4) along with a highest concentration of Raman A1 peak of Te-Te structures, as seen in Figure 4 (c) and also from Table 3, which indicates existence of Te precipitates on the surface needed to start HgCdTe growth at the top [22]. In conclusion, when polishing is necessary to remove the native oxide layer and other unwanted structures on the surface such as Te precipitates, the best polishing procedure to carry out may be the polishing procedure used for the sample E5, that is, polishing with %0.5 Br2 - ethylene glycol for 25 seconds followed by rinsing in ethylene glycol and DI water. But, when a CdTe/GaAs heterostructure such as the one studied in this work is to be used as a substrate for the growth of

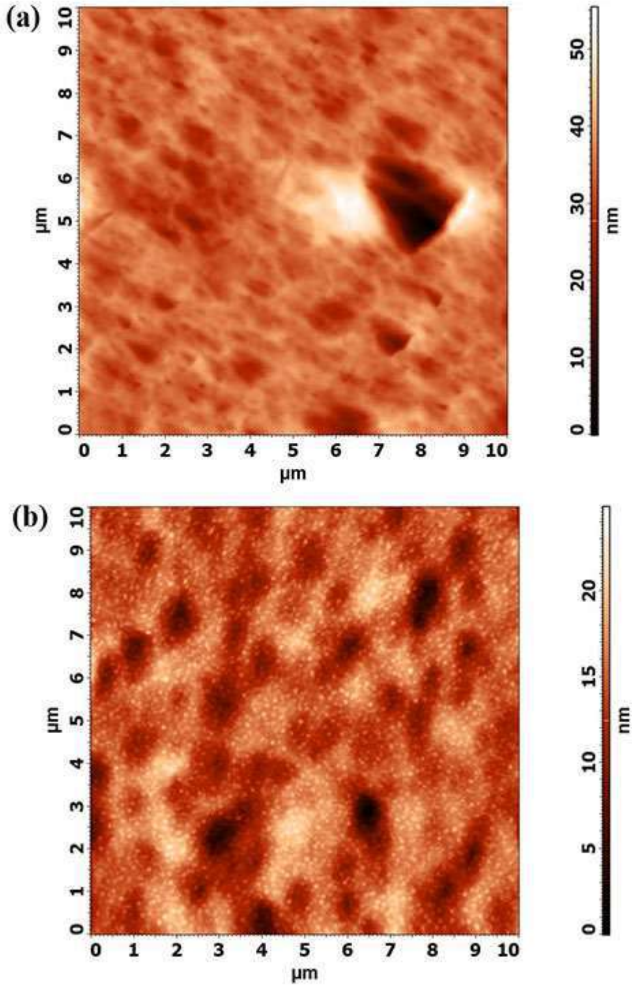

Figure 5 Atomic force microscopy images of (a) as-grown and (b) polished (E5) samples

a HgCdTe detector layer at the top, the polishing procedure for the sample E2, that is, 1HCl - 9DI solution for 3 seconds followed by rinsing in DI water, is probably the best choice since it still has very good surface and bulk qualities with some amount of Te precipitates needed for the growth of a HgCdTe layer at the top.

Table 4
Polishing parameters and AFM characterization results

Samples	Polishing Time (sec)	Polishing Rate (nm/sec)	RMS Roughness (nm)	Average Local Minima Depth (nm)
As-grown	-	-	5.6	50
E1	25	-	-	-
E2	3	10	3.8	18
E3	30	4	9.4	-
E4	20	2	3.5	19
E5	25	2	2.9	16

4. CONCLUSIONS

In this study, we grew a 6 μm thick highly crystalline CdTe film on a GaAs (211)B substrate. XRD and AFM measurements carried on the as-grown film indicated a good crystal quality. Then, Surface contamination with oxygen was removed by five different chemical polishing solutions. Before wet chemical polishing treatments, the CdTe film included Te-O structures at the surface indicating a Te rich surface. After the wet chemical polishing treatments, almost all solutions removed the native oxide layer perfectly. When we compared the results of all XPS, Raman, and AFM analyses, the most effective polishing solution for the best surface quality was the one used for the sample E5 that is %0.5 Br2 - Ethylene glycol. If the as-grown CdTe film is to be used as a buffer layer for a HgCdTe thin film detector at the top, probably the solution used for the sample E2, that is, 1HCl - 9DI, applied for 3 seconds, is the best choice since it shows a small amount of Te precipitates needed to start HgCdTe growth at the top. Both samples E2 and E5 show good surface and bulk qualities as seen their AFM, XPS, and Raman results.

In conclusion, a detailed comparative study of the effects of several etching and polishing solutions on a high quality MBE grown CdTe/GaAs(211)B film is carried out. The effect of these solutions on the polished CdTe surfaces are discussed. Since each polishing solution removed many layers from the top surface, chemical compositions, hence the stoichiometry of the as-grown film, and natural structural defects beneath the top surface of the as-grown CdTe film were exposed and studied in detail. Our results indicate that best polishing methods are those used for the samples E2 and E5 as given in Table 1.

Acknowledgements

We would like to thank Orhan Öztürk for his help in XRD measurements. We are also thankful to Gülnur Aygün and Lütfi Özyüzer for the help they provided especially with the XPS measurements. Additionally, we thank IYTE Material Research Center staff, especially Emine Bakali, for obtaining SEM images. We are deeply grateful to Yusuf Selamet who played a pivotal role in all the studies mentioned in this work. Finally, we are grateful to SSM (Undersecretariat for Defence Industries of Turkey) and ASELSAN for their financial support.

Funding

The authors received no specific funding for this work.

The Declaration of Conflict of Interest/ Common Interest

No conflict of interest or common interest has been declared by the authors.

Authors' Contribution

E.B: Experimental section, especially chemical polishing and removal procedures, data analysis, discussion of results, and conclusions

E.Ö: General literature review and writing the introduction, XRD, SEM and XPS measurements, general data analysis, discussion of results, and conclusions

E.T: Writing the entire article, general data analysis, discussion of all experimental results, and conclusions

The Declaration of Ethics Committee Approval

The authors declare that this document does not require an ethics committee approval or any special permission.

The Declaration of Research and Publication Ethics

The authors of the paper declare that they comply with the scientific, ethical and quotation rules of SAUJS in all processes of the paper and that they do not make any falsification on the data collected. In addition, they declare that Sakarya University Journal of Science and its editorial board have no responsibility for any ethical violations that may be encountered, and that this study has not been evaluated in any academic publication environment other than Sakarya University Journal of Science.

REFERENCES

[1] M. Niraula, K. Yasuda, H. Ohnishi, H. Takahashi, K. Eguchi, K. Noda, and Y. Agata, “Direct growth of high-quality thick CdTe epilayers on Si (211) substrates by metalorganic vapor phase epitaxy for nuclear radiation detection and imaging,” J. Electron. Mater. vol.35, no. 6, pp. 1257–1261, 2006.

[2] M. Niraula, K. Yasuda, Y. Nakanishi, K. Uchida, T. Mabuchi, Y. Agata, and K. Suzuki, J. Electron. Mater. vol. 33, pp. 645–650, 2004.

[3] H. C. Chou, A. Rohatgi, N. M. Jokerst, E. W. Thomas, and S. Kamra, “Copper migration in cdte heterojunction solar cells”, J. Electron. Mater. vol. 25, no. 7, pp. 1093–1098, 1996.

[4] M. Y. Simmons, H. M. Al Allak, A. W. Brinkman, & K. Durose, “Electrical and optical characterisation of epitaxial ZnTe/CdTe/CdS and ZnTe/CdTe/GaAs p-i-n solar cell structures grown by metalorginic vapour phase epitaxy”, J. Cryst. Growth, vol. 117, no. 4, pp. 959–963, 1992.

[5] S.-I. Mho, S. Wen, M. Jung, and I.-H. Yeo, “CdTe/GaAs Nanodot Arrays and Carbon Nanotubes Prepared Utilizing Nanoporous Alumina Templates”, J. Korean Phys. Soc. vol. 52, no. 5, pp. 1355–1358, 2008.

[6] L. A. Kosyachenko, V. M. Sklyarchuk, O. V. Sklyarchuk, and O. L. Maslyanchuk, “Band gap of CdTe and $Cd_{0.9}Zn_{0.1}Te$ crystals,” Semiconductors, vol. 45, no. 10, pp. 1273–1280, 2011.

[7] J. P. Faurie, R. Sporken, Y. P. Chen, M. D. Lange, and S. Sivananthan, “Heteroepitaxy of CdTe on GaAs and silicon substrates”, Mater. Sci. Eng. B, vol. 16, no. 1, pp. 51–56, 1993.

[8] T. J. de Lyon, R. D. Rajavel, J. A. Vigil, J. E. Jensen, O. K. Wu, C. A. Cockrum, S. M.

Johnson, G. M. Venzor, S. L. Bailey, I. Kasai, W. L. Ahlgren, and M. S. Smith, "Molecular-beam epitaxial growth of HgCdTe infrared focal-plane arrays on silicon substrates for midwave infrared applications," J. Electron. Mater., vol. 27, no. 6, pp. 550–555, 1998.

[9] N. Otsuka, L. A. Kolodziejski, R. L. Gunshor, S. Datta, R. N. Bicknell, and J. F. Schetzina, "High resolution electron microscope study of epitaxial CdTe-GaAs interfaces", Appl. Phys. Lett., vol. 46, no. 9, pp. 860–862, 1985.

[10] M. D. Lange, R. Sporken, K. K. Mahavadi, J. P. Faurie, Y. Nakamura, and N. Otsuka, "Molecular beam epitaxy and characterization of CdTe(211) and CdTe(133) films on GaAs(211)B substrates", Appl. Phys. Lett., vol. 58, no. 18, pp. 1988–1990, 1991.

[11] A. Zur and T. C. McGill, "Lattice match: An application to heteroepitaxy", J. Appl. Phys., vol. 55, no. 2, pp. 378–386, 1984.

[12] R. N. Bicknell, R. W. Yanka, N. C. Giles, J. F. Schetzina, T. J. Magee, C. Leung, and H. Kawayoshi, "Growth of (100)CdTe films of high structural perfection on (100)GaAs substrates by molecular beam epitaxy", Appl. Phys. Lett., vol. 44, no. 3, pp. 313–315, 1984.

[13] M. Carmody, A. Yulius, D. Edwall, D. Lee, E. Piquette, R. Jacobs, D. Benson, A. Stoltz, J. Markunas, A. Almeida, and J. Arias, "Recent Progress in MBE Growth of CdTe and HgCdTe on (211)B GaAs Substrates," J. Electron. Mater., vol. 41, no. 10, pp. 2719–2724, 2012.

[14] F. A. Ponce, R. Sinclair, and R. H. Bube, "Native tellurium dioxide layer on cadmium telluride: A high-resolution electron microscopy study," Appl. Phys. Lett., vol. 39, no. 12, pp. 951–953, 1998.

[15] R. Zia, F. Saleemi, S. Naseem, and Z. Kayani, "Study the efficiency of single crystal CdTe/ZnCdS solar cell at various temperatures and illumination levels," Energy Reports, vol. 1, no. 1, pp. 58–61, 2015.

[16] J. G. Werthen, J. P. Haring, A. L. Fahrenbruch, and R. H. Bube, "Surface effects on metal/CdTe junctions and CdTe heterojunctions," J. Phys. D. Appl. Phys., vol. 16, no. 12, pp. 2391–2404, 1983.

[17] K. D. Dobson, P. D. Paulson, B. E. McCandless, and R. W. Birkmire, "The Dynamics of Cadmium Telluride Etching", Mater. Res. Soc. Symp. Proc., vol. 763, no. B3.1, p. 107-118, 2003.

[18] P. Moravec, V. G. Ivanits'ka, J. Franc, Z. F. Tomashik, V. M. Tomashik, K. Mašek, P. I. Feychuk, L. P. Shcherbak, P. Höschl, R. Grill, and J. Walter, "Chemical Interaction of CdTe and CdZnTe with Aqueous Solutions of H2O2-HI-Tartaric Acid", J. Electron. Mater. vo. 38, no. 8, pp. 1645–1651, 2009.

[19] V. G. Ivanits'ka, P. Moravec, J. Franc, V. M. Tomashik, Z. F. Tomashik, K. Mašek, P. S. Chukhnenko, P. Höschl, and J. Ulrych, "Chemical Polishing of CdTe and CdZnTe in Iodine–Methanol Etching Solutions," J. Electron. Mater., vol. 40, no. 8, pp. 1802–1808, 2011.

[20] V. G. Ivanits'ka, P. Moravec, V. M. Tomashik, K. Mašek, Z. F. Tomashik, J. Franc, R. Grill, and P. Höschl, "A Slightly Oxidizing Etchant for Polishing of CdTe and CdZnTe Surfaces," J. Electron. Mater., vol. 42, no. 11, pp. 3059–3065, 2013.

[21] P. Moravec, Z. F. Tomashik, V. G. Ivanits'ka, V. M. Tomashik, J. Franc, K. Mašek, and P. Höschl, "Slow-Polishing Iodine-Based Etchant for CdTe and CdZnTe Single Crystals" J. Electron. Mater. vol. 41, no. 10, pp. 2838–2845, 2012.

[22] Y. S. Wu, C. R. Becker, A. Waag, R. Schmiedl, S. Einfeldt, and G. Landwehr,

"Oxygen on the (100) CdTe surface," J. Appl. Phys., vol. 73, no. 11, pp. 7385–7388, 1993.

[23] E. Bakali, Y. Selamet, and E. Tarhan, "Effect of Annealing on the Density of Defects in Epitaxial CdTe (211)/GaAs," J. Electron. Mater., vol. 47, no. 8, pp. 4780–4792, 2018.

[24] E. Bilgilisoy, S. Özden, E. Bakali, M. Karakaya, and Y. Selamet, "Characterization of CdTe Growth on GaAs Using Different Etching Techniques," J. Electron. Mater., vol. 44, no. 9, pp. 3124–3133, 2015.

[25] J. Frühauf, E. Gärtner, and S. Krönert, Shape and Functional Elements of the Bulk Silicon Microtechnique, Springer, Berlin/Heidelberg, 2005.

[26] W. J. Everson, C. K. Ard, J. L. Sepich, B. E. Dean, G. T. Neugebauer, and H. F. Schaake, "Etch pit characterization of CdTe and CdZnTe substrates for use in mercury cadmium telluride epitaxy," J. Electron. Mater., vol. 24, no. 5, pp. 505–510, 1995.

[27] E. P. Warekois, M. C. Lavine, A. N. Mariano, and H. C. Gatos, "Crystallographic Polarity in the II-VI Compounds," J. Appl. Phys., vol. 33, no. 2, pp. 690–696, 1962.

[28] Polat, M., Bilgilisoy, E., Arı, O., Öztürk, O., and Selamet, Y., "Identifying threading dislocations in CdTe films by reciprocal space mapping and defect decoration etching", Journal of Applied Physics. vol. 124, no. 8, pp. 085710 1-7, 2018.

[29] J. A. Garcia, A. Remón, V. Muñoz, and R. Triboulet, "Photoluminescence study of radiative transitions in ZnTe bulk crystals," J. Cryst. Growth, vol. 191, no. 4, pp. 685–691, 1998.

[30] Z. C. Feng, S. Perkowitz, J. M. Wrobel, and J. J. Dubowski, "Outgoing multiphonon resonant Raman scattering and luminescence near the $E_0 + \Delta_0$ gap in epitaxial CdTe films," Phys. Rev. B, vol. 39, no. 17, pp. 12997–13000, 1989.

[31] L. He, X. Fu, Q. Wei, W. Wang, L. Chen, Y. Wu, X. Hu, J. Yang, Q. Zhang, R. Ding, X. Chen, and W. Lu, "MBE HgCdTe on Alternative Substrates for FPA Applications," J. Electron. Mater., vol. 37, no. 9, pp. 1189–1199, 2008.

[32] X. J. Wang, Y. B. Hou, Y. Chang, C. R. Becker, R. F. Klie, and S. Sivananthan, "Microstructure of Heteroepitaxial ZnTe Grown on GaAs(211)B by Molecular Beam Epitaxy," J. Electron. Mater., vol. 38, no. 8, pp. 1776–1780, 2009.

[33] K. Nakagawa, K. Maeda, and S. Takeuchi, "Observation of dislocations in cadmium telluride by cathodoluminescence microscopy," Appl. Phys. Lett., vol. 34, no. 9, pp. 574–575, 1979.

[34] R. Bommena, T. Seldrum, L. Samain, R. Sporken, S. Sivananthan, and S. R. J. Brueck, "Strain Reduction in Selectively Grown CdTe by MBE on Nanopatterned Silicon on Insulator (SOI) Substrates," J. Electron. Mater., vol. 37, no. 9, pp. 1255–1260, 2008.

[35] S. S. Choi, and G. Lucovsky, "Native oxide formation on CdTe,", J. Vac. Sci. Technol. B Microelectron. Nanom. Struct., vol. 6, no. 4, pp. 1198-1203, 1988.

[36] R. A. Muñoz Hernández, A. Calderón, A. Cruz-Orea, S. A. Tomas, F. Sánchez Sinencio, and G. Peña Rodriguez, "Caracterización Óptica de Centros Absorbentes en Películas Biopoliméricas Obtenidas de Pericarpio de Maíz," Superficies y Vacio, vol. 8, no. 1, pp. 59–63, 1999.

[37] A. Mooradian, "Light Scattering from Single-Particle Electron Excitations in Semiconductors,", Phys. Rev. Lett., vol. 20, no. 20, pp. 1102–1104, 1968.

[38] H. G. Schulze, C. G. Atkins, D. V. Devine, M. W. Blades, and R. F. B. Turner, “Fully Automated Decomposition of Raman Spectra into Individual Pearson's Type VII Distributions Applied to Biological and Biomedical Samples,” Appl. Spectrosc., vol. 69, no. 1, pp. 26–36, 2015.

[39] A. Lusson, J. Wagner, and M. Ramsteiner, “Resonant Raman scattering of In+-implanted CdTe and Cd0.23Hg0.77Te,” Appl. Phys. Lett., vol. 54, no. 18, pp. 1787–1789, 1989.

[40] A. Cantarero, C. Trallero-Giner, and M. Cardona, “Excitons in one-phonon resonant Raman scattering: Fröhlich and interference effects,” Phys. Rev. B, vol. 40, no. 18, pp. 12290–12295, 1989.

[41] J. Menéndez, M. Cardona, and L. K. Vodopyanov, “Resonance Raman scattering by LO phonons in CdxHg1-xTe at the $E_0 + \Delta_0$ gap,” Phys. Rev. B, vol 31, no. 6, pp. 3705–3711, 1985.

[42] S. S. Islam, S. Rath, K. P. Jain, S. C. Abbi, C. Julien, and M. Balkanski, “Forbidden one-LO-phonon resonant Raman scattering and multiphonon scattering in pure CdTe crystals,” Phys. Rev. B, vol. 46, no. 8, pp. 4982–4985, 1992.

[43] S. H. Shin, J. Bajaj, L. A. Moudy, and D. T. Cheung, “Characterization of Te precipitates in CdTe crystals,” Appl. Phys. Lett., vol. 43, no. 1, pp. 68–70, 1983.

SAKARYA ÜNİVERSİTESİ

FEN BİLİMLERİ ENSTİTÜSÜ DERGİSİ

Sakarya University Journal of Science
SAUJS

e-ISSN 2147-835X | Period Bimonthly | Founded: 1997 | Publisher Sakarya University |
http://www.saujs.sakarya.edu.tr/en/

Title: Comparison of the IUCN and the National Biodiversity (Noah's Ark) Database

Authors: Levent BİLER, Seda BİKRİÇ

Recieved: 2020-03-23 13:25:32

Accepted: 2020-09-15 15:01:09

Article Type: Research Article

Volume: 24
Issue: 6
Month: December
Year: 2020
Pages: 1248-1251

How to cite
Levent BİLER, Seda BİKRİÇ; (2020), Comparison of the IUCN and the National Biodiversity (Noah's Ark) Database. Sakarya University Journal of Science, 24(6), 1248-1251, DOI: https://doi.org/10.16984/saufenbilder.707791
Access link
http://www.saujs.sakarya.edu.tr/en/pub/issue/57766/707791

Sakarya University Journal of Science 24(6), 1248-1251, 2020

Comparison of the IUCN and the National Biodiversity (Noah's Ark) Database

Levent BİLER*[1], Seda BİKRİÇ[2]

Abstract

This study aimed to compare the IUCN and The National Biodiversity (Noah's Ark) Data of plant and terrestrial animals (mammals, birds, reptiles, amphibians, and fish). When the number of plant taxa is compared, it is seen that the difference between the two databases is very high. The main reason for this difference is that the plant species are not thoroughly evaluated in the IUCN. Also, there are differences in animal species. One possible reason is that marine species have not been evaluated in Noah's Ark Database. Another possible reason is that as a result of researchers' taxonomic studies, some species are combined or separated. Elimination of the difference between these databases will provide a more accurate evaluation and interpretation.

Keywords: IUCN Red List, The National Biodiversity (Noah's Ark) Database, Red List Categories.

1. INTRODUCTION

Biodiversity loss is one of the world’s critical issues nowadays. Many species are threatened and threatened with extinction. There is also an increasing awareness of how biodiversity supports human livelihoods. Governments and civil society set targets, as the Convention on Biological Diversity's 2010 reduces the current rate of biodiversity loss. In this context, The IUCN Red List of Threatened Species™ provides information on the state of and trends in wild species [1].

The IUCN Red List Categories and Criteria are considered the most objective and authoritative system available to assess the risk of species extinction globally [2, 3, 4, 5]. The IUCN Red List itself is the world's most comprehensive source of information updated annually about the global conservation status of plant and animal species. Population trends are based on an objective system that allows any species to be assigned to one of the eight Red List Categories, depending on whether they meet criteria based on size, structure, and geographic range [4].

One of the main goals of The IUCN Red List is to highlight species with a high risk of global

---

* Corresponding Author: leventbiler@gmail.com

[1] Çınar Mühendislik Müşavirlik A.Ş., ORCID: : https://orcid.org/0000-0002-2578-8530

[2] Çınar Mühendislik Müşavirlik A.Ş., E-Mail: sedabikric@gmail.com
ORCID: : https://orcid.org/0000-0002-8415-153X

extinction. However, it is not just a record of names and related threat categories. The real strength and utility of the IUCN Red List are what lies beneath: they are working on a rich expert-guided summary of information about the ecological requirements of the species, their geographical distribution, and what threats to nature are and how they will crusade them [1].

The IUCN Red List is not just limited to providing threat categorization. For an increasing number of species, whether threatened or not, it offers comprehensive information covering taxonomy (classification of species), conservation status, geographical distribution, habitat requirements, biology, threats, population, use, and conservation actions. All this information allows scientists to make detailed analyzes of biodiversity globally [1].

Only 2.5% of the estimated 1.8 million species in the world have been evaluated in the IUCN Red List. Therefore, the number of threatened species reported is much less than the actual amount at risk of severe extinction. The IUCN Red List, however, is the almost complete global list of these available species [1].

The Ministry of Agriculture and Forestry, General Directorate of Nature Conservation and National Parks prepared the National Biological Diversity Inventory and Monitoring Project, to reveal and protect Turkey’s biodiversity, and inventory researches started in 81 provinces in 2013. By the beginning of 2020, the inventory studies of 81 provinces are complete, and Turkey's Biological Diversity Map revealed. In this context, plant, mammalian, bird, freshwater fish, reptile, and amphibian species were studied [6, 7].

Biodiversity inventory data from all Turkey's provinces is stored in National Biodiversity (Noah's Ark) Database. Thus, Turkey's biodiversity data can be queried on a table, graphic, and map basis through a database. Changes that will occur to protect and sustain the biodiversity can be observed [6, 7]. Mammalian, bird, freshwater fish, reptiles, and amphibian species threatened categories taken from the IUCN, but plant species categories were also assigned by expert judgment.

This research aims to compare the IUCN Red List and the National Biodiversity (Noah's Ark) Database for the plant, mammalian, bird, freshwater fish, reptile, and amphibian species in Turkey.

2. MATERIALS AND METHODS

The IUCN data is taken from the Summary Statistic Table 6a [Red List Category summary country totals (Animals)] and Table 6b [Red List Category summary country totals (Plants)] [8]. The National Biodiversity (Noah's Ark) Data were taken from the [7] source.

Both two databases were listed and prepared to compare with each other. While the IUCN only gives the animals a whole, The National Biodiversity (Noah's Ark) Data were combined. Comparisons and tables of the data were created.

3. RESULTS

The IUCN data included a total of 868 plant species for Turkey. The National Biodiversity (Noah's Ark) Data includes 11840 plant species. The comparison of the two data is given in Table 1 and demonstrated in Figure 1.

Table 1
The comparison of the IUCN and the National Biodiversity (Noah’s Ark) Data of Plants in Turkey

	IUCN	**The National Biodiversity (Noah's Ark) Data**
EX *	0	4
EW *	0	0
CR *	67	482
EN *	41	707
VU *	23	1.316
NT *	31	291
LR/cd *	0	112
DD *	70	227
LC *	636	5.149
NE*	0	3.552
Total	**868**	**11.840**

*IUCN Red List Categories: EX - Extinct, EW - Extinct in the Wild, CR - Critically Endangered, EN - Endangered, VU - Vulnerable, LR/cd - Lower Risk/conservation dependent, NT - Near Threatened (includes LR/nt - Lower Risk/near threatened), DD - Data Deficient, LC – Least Concern (includes LR/lc - Lower Risk, least concern), NE – Not Evaluated.

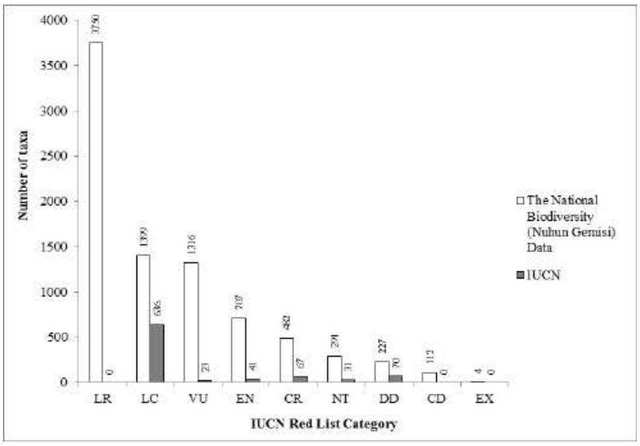

Figure 1 Comparison of The IUCN and The National Biodiversity (Noah’s Ark) Data

The comparison of the IUCN and the National Biodiversity (Noah's Ark) Data for animals is given in Table 2 and demonstrated in Figure 2. The IUCN contains 1879 animal species, whereas the National Biodiversity (Noah's Ark) Database 1285.

Table 2
The comparison of The IUCN and The National Biodiversity (Noah's Ark) Data of Animals in Turkey

	IUCN	**The National Biodiversity (Noah's Ark) Data**
EX *	4	1
EW *	0	0
CR *	68	49
EN *	104	62
VU *	124	89
NT *	104	103
DD *	191	24
LC *	1.284	887
CD *	0	1
NE *	0	69
Total	**1879**	**1285**

*IUCN Red List Categories: EX - Extinct, EW - Extinct in the Wild, CR - Critically Endangered, EN - Endangered, VU - Vulnerable, LR/cd - Lower Risk/conservation dependent, NT - Near Threatened (includes LR/nt - Lower Risk/near threatened), DD - Data Deficient, LC – Least Concern (includes LR/lc - Lower Risk, least concern), NE – Not Evaluated.

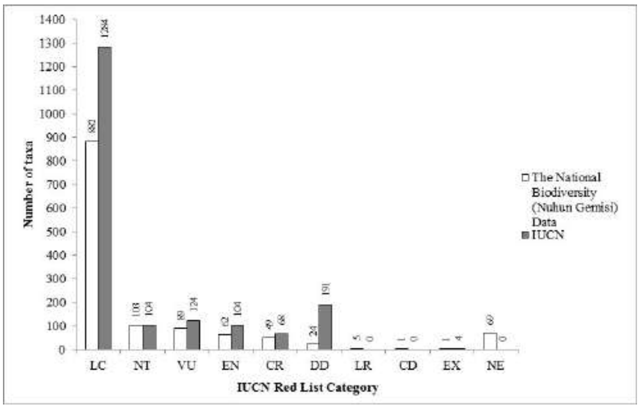

Figure 2 Comparison of The IUCN and The National Biodiversity (Noah's Ark) Data of animal species in Turkey

4. DISCUSSION

The results showed that differences between the IUCN and The National Biodiversity (Noah's Ark) Data exist. There are two main explanations for these differences. One possible explanation is that the plant species in Turkey are not entirely evaluated. Also, not all species are listed in the IUCN. Therefore, a project to determine and assess the plant species and the red list categories continue, which is with the IUCN in cooperation. After the project, plant species in Turkey will be thoroughly searched and evaluated in the IUCN Red List. Another possible explanation is that the fauna data of the IUCN involves marine species, which may cause the differences between the databases. Another possible explanation is that according to taxonomic studies, some species were combined or separated. Taken together, this offers a novel perspective on the evaluation and status of biodiversity in Turkey.

It is important to eliminate these differences for all living species by conducting extensive studies. The results to be made compatible with each of the two databases are extremely important due to ensure the conservation and sustainability of biological diversity. Therefore projects carried out and will be carried out in collaboration with the IUCN will assure the accurate evaluation of the species in Turkey.

Acknowledgments

The authors wish to thank Umut Adıgüzel and Emrah Erdoğan (Ministry of Agriculture and Forestry General Directorate of Nature Conservation and National Parks).

Funding

The authors received no specific funding for this work.

The Declaration of Conflict of Interest/ Common Interest

No conflict of interest or common interest has been declared by the authors.

Authors' Contribution

All authors have contributed in analyzing and writing of the manuscript equally.

The Declaration of Ethics Committee Approval

The authors declare that this document does not require an ethics committee approval or any special permission.

The Declaration of Research and Publication Ethics

The authors of the paper declare that they comply with the scientific, ethical and quotation rules of SAUJS in all processes of the paper and that they do not make any falsification on the data collected. In addition, they declare that Sakarya University Journal of Science and its editorial board have no responsibility for any ethical violations that may be encountered, and that this study has not been evaluated in any academic publication environment other than Sakarya University Journal of Science.

REFERENCES

[1] J.-C. Vié, C. Hilton-Taylor, C. Pollock, J. Ragle, J. Smart, S. N. Stuart, and R. Tong, “The IUCN Red List: a key conservation tool” The 2008 Review of The IUCN Red List of Threatened Species. IUCN Gland, Switzerland, 2008.

[2] P. C. De Grammont and A. D. Cuarón, “An evaluation of threatened species categorization systems used on the American continent” Conservation Biology vol. 20, no. 1, pp. 14-27, 2006.

[3] J. Lamoreux, H. R. Akçakaya, L. Bennun, N. J. Collar, L. Boitani, D. Brackett, A. Brautigam, T. M. Brooks, G. A. B. Fonseca, and R. A. Mittermeier, “Value of the IUCN Red List” Trends in Ecology & Evolution vol. 18, pp. 214-215, 2003.

[4] G. M. Mace, N. J. Collar, K. J. Gaston, C. Hilton Taylor, H. R. Akçakaya, N. Leader-Williams, E. J. Milner-Gulland, and S. N. Stuart, “Quantification of extinction risk: IUCN’s system for classifying threatened species” Conservation Biology vol. 22, no. 6, pp. 1424-1442, 2008.

[5] A. S. L. Rodrigues, J. D. Pilgrim, J. F. Lamoreux, M. Hoffmann, and T. M. Brooks, “The value of the IUCN Red List for conservation” Trends in Ecology and Evolution, vol. 21, no. 2, pp. 71-76, 2006.

[6] Anonymous, “Biyolojik Çeşitlilik 2018 Yılı Envanter Raporu” T.C. Tarım ve Orman Bakanlığı Doğa Koruma ve Milli Parklar Genel Müdürlüğü, Ankara, 2008.

[7] Anonymous, http://www.nuhungemisi.gov.tr/Projects/Ubenis. © 2018 T.C. Tarım ve Orman Bakanlığı Bilgi İşlem Dairesi Başkanlığı, Ankara, 2019.

[8] IUCN 2019. The IUCN Red List of Threatened Species. Version 2019-3. http://www.iucnredlist.org. Downloaded on 10 December 2019.

SAKARYA ÜNİVERSİTESİ

FEN BİLİMLERİ ENSTİTÜSÜ
DERGİSİ

Sakarya University Journal of Science
SAUJS

e-ISSN 2147-835X | Period Bimonthly | Founded: 1997 | Publisher Sakarya University |
http://www.saujs.sakarya.edu.tr/en/

Title: Solution of Test Problems with Grey Wolf Optimization Algorithm and Comparison with Particle Swarm Optimization

Authors: Alper KÖYBAŞI, İrfan YAZICI

Recieved: 2020-09-02 08:45:09

Accepted: 2020-09-15 18:34:31

Article Type: Research Article

Volume: 24
Issue: 6
Month: December
Year: 2020
Pages: 1252-1264

How to cite
Alper KÖYBAŞI, İrfan YAZICI; (2020), Solution of Test Problems with Grey Wolf Optimization Algorithm and Comparison with Particle Swarm Optimization. Sakarya University Journal of Science, 24(6), 1252-1264, DOI: https://doi.org/10.16984/saufenbilder.788681
Access link
http://www.saujs.sakarya.edu.tr/en/pub/issue/57766/788681

Sakarya University Journal of Science 24(6), 1252-1264, 2020

Solution of Test Problems with Grey Wolf Optimization Algorithm and Comparison with Particle Swarm Optimization

Alper KÖYBAŞI*[1], İrfan YAZICI[2]

Abstract

In this study, Grey Wolf Optimization (GWO), which is a new method with swarm intelligence is compared with another metaheuristic optimization method, Particle Swarm Optimization (PSO), using optimization benchmark functions. Simulation studies on test functions are presented as a table by obtaining mean, standard deviation, best and worst values. In addition, the effects of population and iteration number change on the GWO algorithm are presented in separate tables. The GWO algorithm has establish a good balance between exploration and exploitation. Simulation studies have shown that GWO has better convergence performance and optimization accuracy.

Keywords: Grey Wolf Optimization, Metaheuristic Optimization, Particle Swarm Optimization

1. INTRODUCTION

The process of finding the smallest or largest values under a given constraint that gives a purpose function that changes depending on various variables mathematically is defined as an optimization problem [1]. Optimization is used in a wide range of fields such as electronics, computers, economics, transportation, production. In the design of heuristic and metaheuristic algorithms, inspired by biological systems or the behaviour of physical events in nature [2]. For instance, Ant Colony Optimization (ACO), is based on the talent of ants to find the shortest way from the anthill to the food source [3], Whale Optimization Algorithm (WOA), imitating the hunting behaviour of whales [4]. Grey Wolf Optimization (GWO), which has been developed by imitating the hunting and social behaviour of grey wolves, has been one of the most studied metaheuristic methods in recent years. The reasons why population-based metaheuristic optimization methods such as GWO, Particle Swarm Optimization (PSO), Bat Algorithm (BA), ACO, WOA have become so popular can be shown; simplicity, flexibility, non-derivative system, and avoidance of local optimal values [5]. The purpose of these methods is to find

---

* Corresponding Author: alper.koybasi@gmail.com

[1] Sakarya University, Institute of Science, Electrical and Electronics Engineering
ORCID: https://orcid.org/0000-0003-4210-7757

[2] Sakarya University, Department of Electrical and Electronics Engineering
E-Mail: iyazici@sakarya.edu.tr ORCID: https://orcid.org/0000-0003-3603-7051

the best solution quality and better convergence performance [6].

In this study, GWO was compared with the PSO algorithm by using 23 test functions in the literature. Experimental solutions are presented as a table by obtaining mean, standard deviation, best and worst values. Experimental results have shown that GWO has better convergence performance and optimization accuracy.

2. GREY WOLF OPTIMIZATION (GWO)

GWO is a population-based metaheuristic optimization method created by Mirjalili et al., [5] by considering the hunting and social behaviour of grey wolves. Grey wolves live in flocks and which are at the top of the food chain. There are 4 types of grey wolves in the GWO method in terms of social hierarchy: alpha (α), beta (β), delta (δ) and omega (ω). It has a strict social hierarchy that decrease from top to bottom as shown in Figure 1.

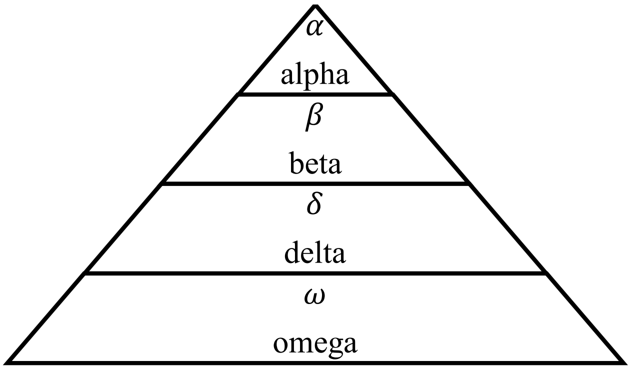

Figure 1 Grey wolf hierarchy (dominance decreases from top to bottom.)

Alpha is the group leader in GWO and responsible for taking decisions on topics such as hunting. Alpha's decisions are obeyed by the other wolves. Beta wolves help alpha in decision making. Delta wolves obeys alpha and beta wolves, and which is dominate omega. Omega wolves take the last place in the grey wolf hierarchy. Hunting in GWO takes place in 3 main steps. Tracking, encircling and attack towards the prey.

2.1. Social Hierarchy

In the GWO the social hierarchy and hunting behaviour of grey wolves are mathematically modelled. Alpha is considered the best candidate solution. Optimization is directed by alpha, beta and delta, respectively. These wolves are followed by omega.

2.2. Encircling Prey

Grey wolves surround their prey during hunting. The following equations are used for the mathematical model of the siege [5]:

$$\vec{D} = \left|\vec{C} \cdot \vec{X}_p(k) - \vec{X}(k)\right| \quad (1)$$

$$\vec{X}(k+1) = \vec{X}_p(k) - \vec{A} \cdot \vec{D} \quad (2)$$

where k indicates current iteration, $\vec{A}$, $\vec{C}$ and $\vec{D}$ are coefficient vectors, $\vec{X}_p$ is the position vector of prey, $\vec{X}$ points the position vector of grey wolves. The coefficients $\vec{A}$, $\vec{C}$ and $\vec{a}$ are calculated as follows:

$$\vec{A} = 2\vec{a} \cdot \vec{r}_1 - \vec{a} \quad (3)$$

$$\vec{C} = 2 \cdot \vec{r}_2 \quad (4)$$

$$\vec{a} = 2 - k * (\frac{2}{k_{max}}) \quad (5)$$

$\vec{A}$ and $\vec{C}$ are the coefficients, to equilibrium the exploration and the exploitation [7]. Value of $\vec{a}$ are updated from 2 to 0 as given (**5**), $\vec{r}_1$ and $\vec{r}_2$, can be randomly selected in the range [0-1]. Grey wolves can update their position around the prey according to (**1**) and (**2**). The $\vec{C}$ vector, can be also considered as the effect of impediments in nature in the hunting process.

2.3. Hunting

Hunting is done by being directed by alpha. Beta and delta can also join hunting. The best three solutions obtained are recorded and it is ensured that the positions of other wolfs (including omega) are updated regarding the position of the best search agents. The following formulas are recommended in this respect [5].

$$\vec{D}_\alpha = |\vec{C}_1\vec{X}_\alpha - \vec{X}|, \qquad \vec{D}_\beta = |\vec{C}_2\vec{X}_\beta - \vec{X}|,$$

$$\vec{D}_\delta = |\vec{C}_3\vec{X}_\delta - \vec{X}| \tag{6}$$

$$\vec{X}_1 = \vec{X}_a - \vec{A}_1(\vec{D}_a), \qquad \vec{X}_2 = \vec{X}_\beta - \vec{A}_2(\vec{D}_\beta),$$

$$\vec{X}_3 = \vec{X}_\delta - \vec{A}_3(\vec{D}_\delta) \tag{7}$$

$$\vec{X}(k+1) = \frac{\vec{X}_1+\vec{X}_2+\vec{X}_3}{3} \tag{8}$$

The GWO search process starts by creating a random population of grey wolf. During the iterations, alpha, beta and delta update the distance from the hunt by predicting the possible location of the prey. Value of $\vec{a}$ is updated as given (**5**), to emphasise exploration and exploitation. As shown in Figure 2, grey wolves move away from prey when $\vec{A}$>1, and approach prey when $\vec{A}$<1. GWO's equilibrium between exploration and exploitation it is carried out with parameters $\vec{A}, \vec{C}$ ve $\vec{a}$.

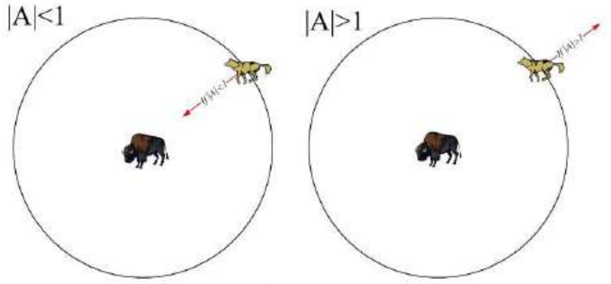

Figure 2 Attacking prey and searching for prey

GWO algorithm flow chart is as shown in Figure 3.

```
Initialize all the parameters
Calculation of the fitness of search agent
$\vec{X}_a$ = the finest solution
$\vec{X}_\beta$ = the second finest solution
$\vec{X}_\delta$ = the third finest solution
 while (k < $k_{max}$)
     for each grey wolf
         Update the position of the current wolf by
          equation (8)
     end for
     Update parameters $\alpha$, $A$, and $C$
     Calculate the fitness of all grey wolves
     Update $\vec{X}_a$, $\vec{X}_\beta$ , and $\vec{X}_\delta$
      k = k+1
 end while
return $\vec{X}_a$
```

Figure 3 GWO Pseudo Code

3. TEST STUDIES

3.1. Test Benchmark Functions

In this study, GWO algorithm has been compared with another metaheuristic optimization method, standard PSO algorithm. The PSO algorithm was proposed by Eberhart and Kennedy in 1995. PSO algorithm has been developed inspired by the behaviour of flocks of birds and fish [8]. Various studies on PSO such as Clubs-Based PSO [9], The Modified Power Mutation PSO [10] are continuing.

Optimization benchmark functions used in similar studies were used [11]. The $f_1 - f_7$ single-mode test functions shown in Table 1 have only one global optimum and no local optimum.

Table 1
Unimodal benchmark functions

Function	f_{min}	Range	Dimensions
$f_1(x)=\sum_{i=1}^{n} x_i^2$	0	[-100,100]	30
$f_2(x)=\sum_{i=1}^{n}\lvert x_i\rvert+\prod_{i=1}^{n}\lvert x_i\rvert$	0	[-10,10]	30
$f_3(x)=\sum_{i=1}^{n}\left(\sum_{j-1}^{i} x_j\right)^2$	0	[-100,100]	30
$f_4(x)=max_i\{\lvert x_i\rvert, 1\le i\le n\}$	0	[-100,100]	30
$f_5(x)=\sum_{i=1}^{n-1}[100(x_{i+1}-x_i^2)^2+(x_i-1)^2]$	0	[-30,30]	30
$f_6(x)=\sum_{i=1}^{n}([x_i+0.5])^2$	0	[-100,100]	30
$f_7(x)=\sum_{i=1}^{n} ix_i^4+random[0,1]$	0	[-1.28,1.28]	30

The f_8-f_{13} multimodal test functions shown in Table 2 have multiple optima, making them more demanding than unimodal functions. Only one of the optimum points is global optimum and the others are local optimum [12].

Table 2
Multimodal benchmark functions

Function	f_{min}	Range	Dimensions
$f_8(x)=\sum_{i=1}^{n}-x_i\sin\left(\sqrt{\lvert x_i\rvert}\right)$	-418.9829× 5	[-500,500]	30
$f_9(x)=\sum_{i=1}^{n}\left[x_i^2-10\cos(2\pi x_i)+10\right]$	0	[-5.12,5.12]	30
$f_{10}(x)=-20\,exp\left(-0.2\sqrt{\frac{1}{n}\sum_{i=1}^{n}x_i^2}\right)-exp\left(\frac{1}{n}\sum_{i=1}^{n}\cos(2\pi x_i)\right)+20+e$	0	[-32,32]	30
$f_{11}(x)=\frac{1}{4000}\sum_{i=1}^{n}x_i^2-\prod_{i=1}^{n}\cos\left(\frac{x_i}{\sqrt{i}}\right)+1$	0	[-600,600]	30
$f_{12}(x)=\frac{\pi}{n}\left\{10\sin(\pi y_1)+\sum_{i=1}^{n-1}(y_i-1)^2[1+10\sin^2(\pi y_{i+1})]+(y_n-1)^2\right\}+\sum_{i=1}^{n}u(x_i,10,100,4)$ $y_i=1+\frac{x_i+1}{4}$ $u(x_i,a,k,m)=\left\{\begin{matrix} k(x_i-a)^m & x_i>a \\ 0 & -a< x_i<a \\ k(-x_i-a)^m & x_i<-a\end{matrix}\right\}$	0	[-50,50]	30
$f_{13}(x)=0.1\left\{sin^2(3\pi x_1)+\sum_{i=1}^{n}(x_i-1)^2\,[1+sin^2(3\pi x_i+1)]+(x_n-1)^2[1+sin^2(2\pi x_n)]\right\}+\sum_{i=1}^{n}u(x_i,5,100,4)$	0	[-50,50]	30

The only difference of the $f_{14}-f_{23}$ fixed-size multimodal test functions shown in Table 3 from the multimodal functions is that they contain a small number of local minimums due to their low size [13]. If the exploration of an algorithm is poorly designed, it will not be able to effectively scan at a wide angle, causing the algorithm to get stuck at the local optimum. Therefore, multimodal functions with containing many local optima are shown as the most difficult problem classes for many algorithms [14].

Table 3
Fixed-dimensions multimodal benchmark functions

Function	f_{min}	**Range**	**Dimensions**
$f_{14}(x) = (\frac{1}{500} + \sum_{j=1}^{25} \frac{1}{j + \sum_{i=1}^{2}(x_i - a_{ij})^6})^{-1}$	1	[-65,65]	2
$f_{15}(x) = \sum_{i=1}^{11} [\ a_i - \frac{x_1({b_i}^2 + b_i x_2)}{{b_i}^2 + b_i x_3 + x_4}]^2$	0.00030	[-5,5]	4
$f_{16}(x) = 4x_1^2 - 2.1x_1^4 + \frac{1}{3}x_1^6 + x_1x_2 - 4x_2^2 + 4x_2^4$	-1.0316	[-5,5]	2
$f_{17}(x) = (x_2 - \frac{5.1}{4\pi^2}x_1^2 + \frac{5}{\pi}x_1 - 6)^2 + 10(1 - \frac{1}{8\pi})\cos x_1 + 10$	0.398	[-5,5]	2
$f_{18}(x) = [1 + (x_1 + x_2 + 1)^2(19 - 14x_1 + 3x_1^2 - 14x_2 + 6x_1x_2 + 3x_2^2)] \times [30 + (2x_1 - 3x_2)^2 \times (18 - 32x_1 + 12x_1^2 + 48x_2 - 36x_1x_2 + 27x_2^2)]$	3	[-2,2]	2
$f_{19}(x) = -\sum_{i=1}^{4} c_i exp(-\sum_{j=1}^{3} a_{ij}(x_j - p_{ij})^2)$	-3.86	[1,3]	3
$f_{20}(x) = -\sum_{i=1}^{4} c_i exp(-\sum_{j=1}^{6} a_{ij}(x_j - p_{ij})^2)$	−3.32	[0,1]	6
$f_{21}(x) = -\sum_{i=1}^{5} [(X - a_i)(X - a_i)^T + c_i]^{-1}$	−10.1532	[0,10]	4
$f_{22}(x) = -\sum_{i=1}^{7} [(X - a_i)(X - a_i)^T + c_i]^{-1}$	-10.4028	[0,10]	4
$f_{23}(x) = -\sum_{i=1}^{10} [(X - a_i)(X - a_i)^T + c_i]^{-1}$	-10.5363	[0,10]	4

3.2. Comparison of Test Results of GWO and PSO

The GWO and PSO pseudocodes are coded in MATLAB R2017A and implemented on Nvidia GeForce GTX1650, 16 GB Memory, i7 9750H Processor and 256 GB SSD. In all tests, the same parameter settings were used in both algorithms, with a population number of 30 and a maximum number of iterations of 500. All benchmark functions were run 30 times and presented as a table by obtaining mean, standard deviation, best values, worst values, and computation time. The algorithm with better average solution in each function is solved in bold font.

The $f_1 - f_7$ Functions are unimodal test functions used only to examine the convergence rates of optimization algorithms that have global optimum solution. As shown in Table 4, GWO outperformed 6 of these 7 $(f_1, f_2, f_3, f_4, f_5, f_7)$ functions. Performance curves of unimodal functions are shown in Figure 4 through Figure 10.

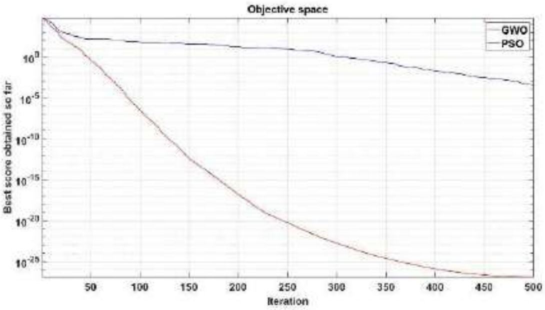

Figure 4 F1 Function convergence curve

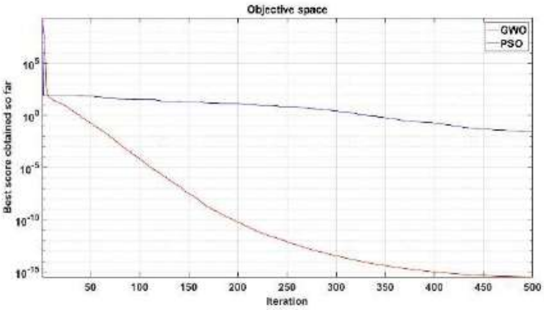

Figure 5 F2 Function convergence curve

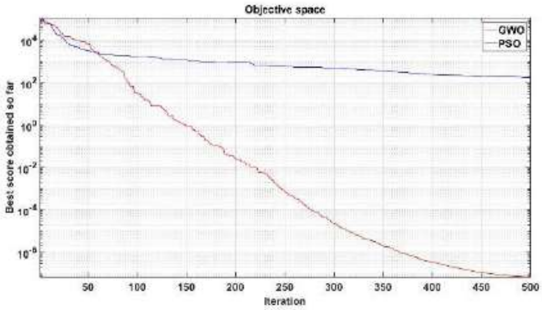

Figure 6 F3 Function convergence curve

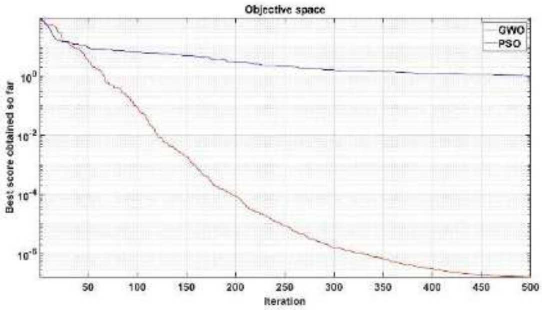

Figure 7 F4 Function convergence curve

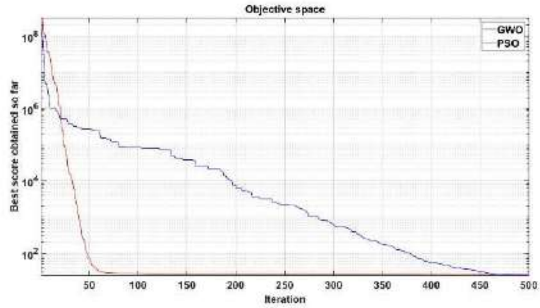

Figure 8 F5 Function convergence curve

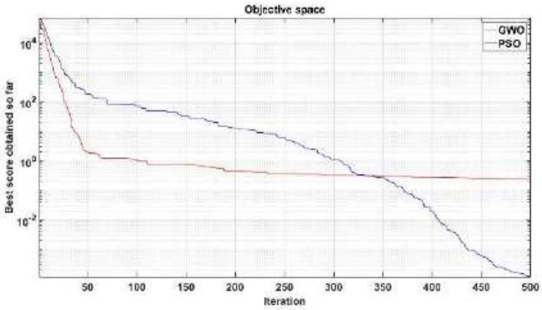

Figure 9 F6 Function convergence curve

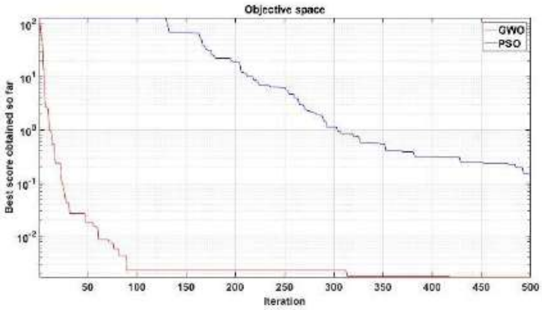

Figure 10 F7 Function convergence curve

As shown in Table 5, GWO outperformed 3 of these 6 multimodal functions (f_9, f_{10}, f_{11}) containing many local minimums. The performance curves of the multimodal functions are shown in Figure 11 to Figure 16.

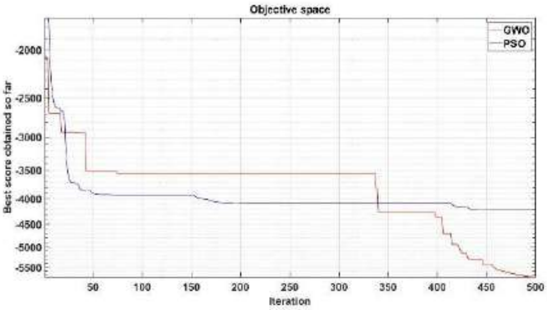

Figure 11 F8 Function convergence curve

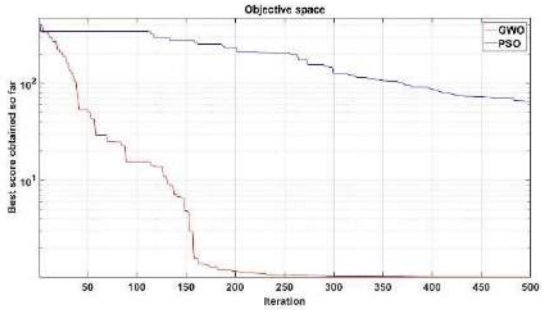

Figure 12 F9 Function convergence curve

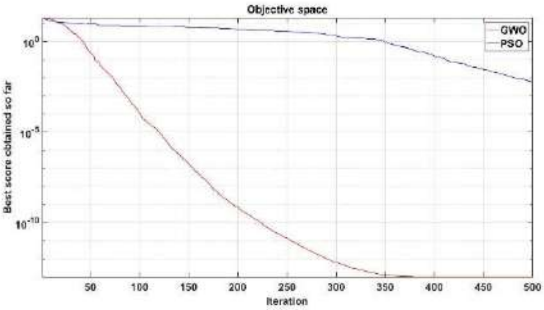

Figure 13 F10 Function convergence curve

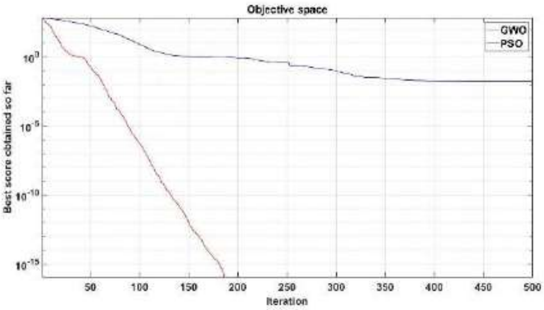

Figure 14 F11 Function convergence curve

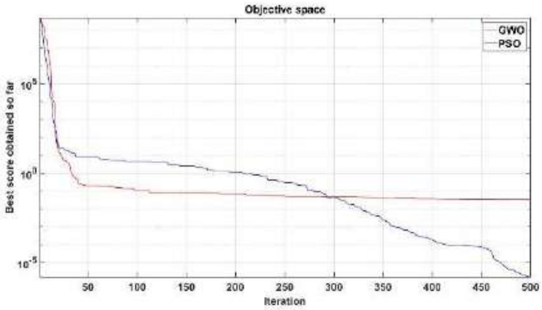

Figure 15 F12 Function convergence curve

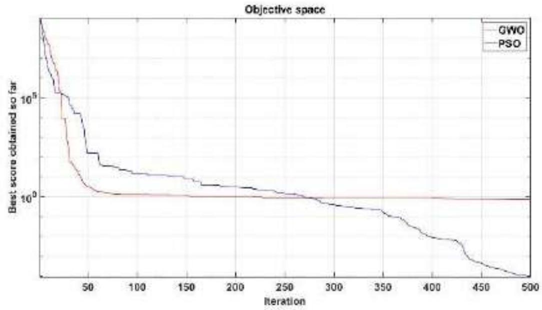

Figure 16 F13 Function convergence curve

GWO showed better results in 6 of 10 functions ($f_{17}, f_{19}, f_{20}, f_{21}, f_{22}, f_{23}$) that contain fewer local minimum and low dimensions compared to multimodal functions. Both algorithms showed good results in f_{16} functions. The results are shown in Table 6. Performance curves of fixed-size multimodal functions are shown between Figure 17 with Figure 26.

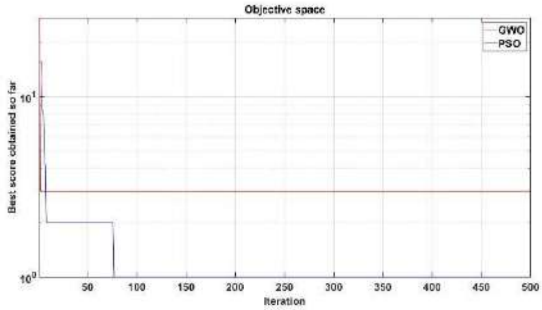

Figure 17 F14 Function convergence curve

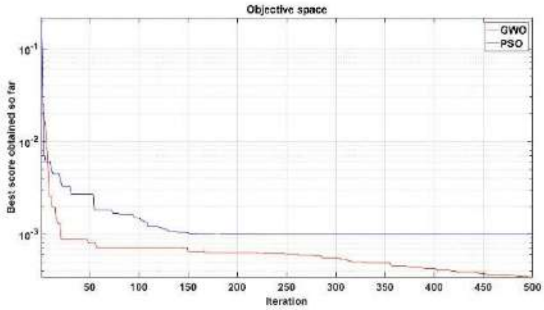

Figure 18 F15 Function convergence curve

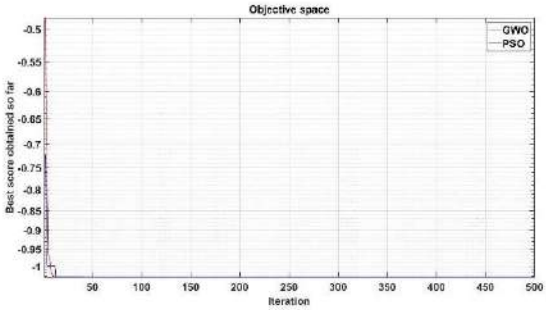

Figure 19 F16 Function convergence curve

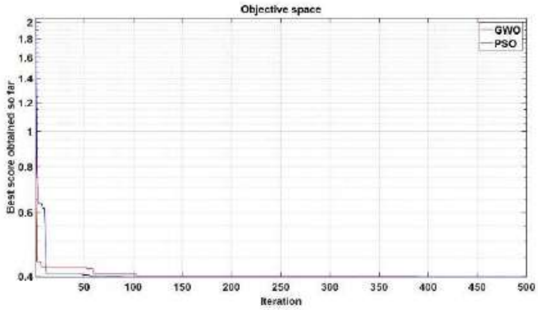

Figure 20 F17 Function convergence curve

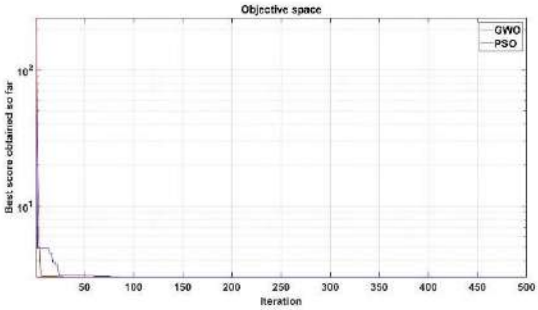

Figure 21 F18 Function convergence curve

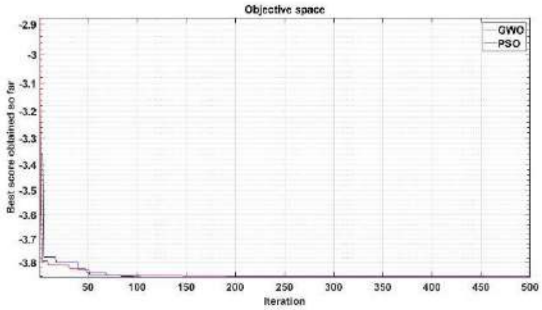

Figure 22 F19 Function convergence curve

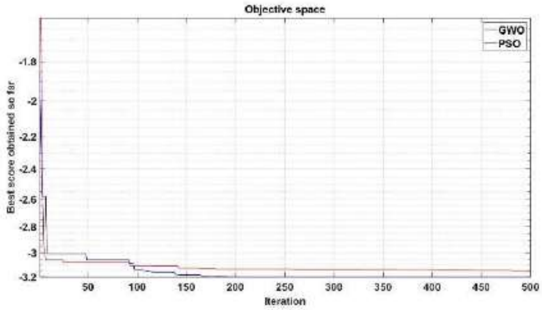

Figure 23 F20 Function convergence curve

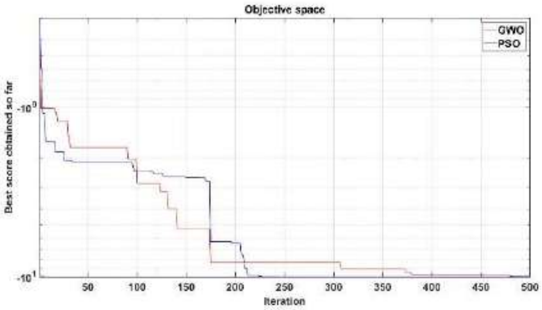

Figure 24 F21 Function convergence curve

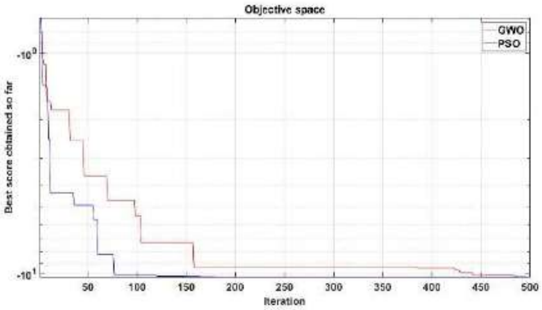

Figure 25 F22 Function convergence curve

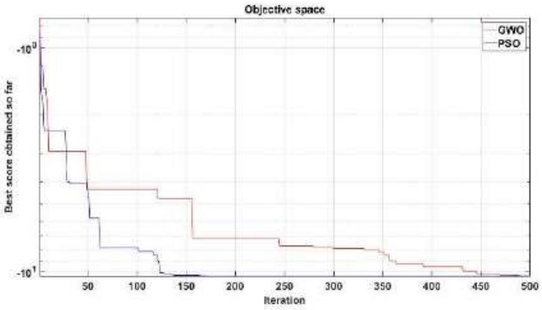

Figure 26 F23 Function convergence curve

3.3. The Effect of Change of Population Number and Iteration Number on GWO Algorithm.

In this part, the effects of the number of populations and iteration number on the GWO algorithm are examined. In the tests, the population number was applied as 15 and 30. The maximum number of iterations has been applied separately as 100 and 500. All benchmark functions were run 30 times and presented as a table by obtaining mean, standard deviation, best and worst values.

Increasing the number of populations and iteration had a positive effect on all single-mode test functions. The importance of the number of iterations was observed sharply in (f_3, f_4, f_5) functions. The results are shown in Table 7.

As shown in Table 8, in 5 of 6 multimodal functions, $(f_8, f_9, f_{10}, f_{12}, f_{13})$ high population number positively affected. The importance of the number of iterations was observed sharply in (f_9, f_{10}, f_{13}) functions.

As shown in Table 9, in 6 of 10 $(f_{14}, f_{15}, f_{18}, f_{20}, f_{21}, f_{23})$ fixed sized multimodal functions, high population and iteration number positively affected. The F_{16} function showed good results in both population and iteration numbers.

4. CONCLUSION

GWO is a metaheuristic optimization method developed inspired by the hunting and social behaviour of grey wolves. In this study, GWO was compared with PSO algorithm using 23 optimization test functions. Comparison results and performance curves are presented. GWO's exploration and exploitation performance has been observed to be better. In addition, increasing the number of populations and iterations in GWO has better convergence performance and optimization accuracy.

Funding

The authors received no financial support for research and publication of this article.

Acknowledgements

The authors thank the reviewers for their positive contribution to the article.

The Declaration of Conflict of Interest/ Common Interest

No conflict of interest or common interest has been declared by the authors.

Authors' Contribution

A.K: Literature research, simulation study, literary and technical editing.

İ.Y: Coordinating the studies related to article, directing A.K.

The Declaration of Ethics Committee Approval

The authors declare that this document does not require an ethics committee approval or any special permission.

The Declaration of Research and Publication Ethics

The authors of the paper declare that they comply with the scientific, ethical and quotation rules of SAUJS in all processes of the paper and that they do not make any falsification on the data collected. In addition, they declare that Sakarya University Journal of Science and its editorial board have no responsibility for any ethical violations that may be encountered, and that this study has not been evaluated in any academic publication environment other than Sakarya University Journal of Science.

REFERENCES

[1] P. Erdoğmuş and E. Yalçın, “Parçacık Sürü Optimizasyonu ile Kısıtsız Optimizasyon Test Problemlerinin Çözümü,” Journal of Advanced Technology Sciences, vol. 4, no. 1, pp. 14–22, 2015.

[2] X.S. Yang, A New Metaheuristic Bat-Inspired Algorithm, in: Nature Inspired Cooperative Strategies for Optimization (NISCO 2010) (Eds. J. R. Gonzalez et al.), Studies in Computational Intelligence, Springer Berlin, 284, pp. 65-74, 2010.

[3] C. Blum, “Ant colony optimization: Introduction and recent trends,” Physics of Life Reviews, vol. 2, pp. 353-373, 2005.

[4] S. Mirjalili and A. Lewis, “The Whale Optimization Algorithm,” Advances in Engineering Software, vol. 95, pp. 51–67, 2016.

[5] S. Mirjalili, S. M. Mirjalili, and A. Lewis, “Grey Wolf Optimizer,” Advances in Engineering Software, vol. 69, pp. 46–61, 2014.

[6] N. Singh and S. B. Singh, “Hybrid Algorithm of Particle Swarm Optimization and Grey Wolf Optimizer for Improving Convergence Performance,” Journal of Applied Mathematics, vol. 2017, pp. 1-15, 2017.

[7] S. Cherukuri and S. Rayapudi, “Enhanced Grey Wolf Optimizer Based MPPT Algorithm of PV System Under Partial Shaded Condition,” International Journal of Renewable Energy Development, vol. 6, no. 3, pp. 203-212, 2017.

[8] J. Kennedy and R. Eberhart, “Particle Swarm Optimization,” Proceedings of ICNN'95 -International Conference on Neural Networks, Perth, WA, Australia, vol. 4, pp. 1942-1948, 1995.

[9] W. Elshamy, H. M. Emara and A. Bahgat, “Clubs-based Particle Swarm Optimization,” IEEE Swarm Intelligence Symposium, Honolulu, HI, pp. 289-296, 2007.

[10] P. Chauhan, K. Deep, and M. Pant, “Power Mutation Embedded Modified PSO for Global Optimization Problems,” Lecture Notes in Computer Science, vol. 6466, pp. 139-146, 2010.

[11] M. Molga and C. Smutnicki, “Test functions for optimization needs,” Available:https://www.robertmarks.org/Classes/ENGR5358/Papers/functions.pdf.

[12] B. Alızada, “Sürü Tabanlı Karınca Aslanı ve Balina Optimizasyonu Algoritmalarının Fiziki Tabanlı Algoritmalarla Hibritleştirilmesi,” Erciyes Üniversitesi / Fen Bilimleri Enstitüsü, Kayseri, 2019.

[13] G. Demir and E. Tanyıldızı, “Optimizasyon Problemlerinin Çözümünde Sinüs Kosinüs Algoritması (SKA)’nın Kullanılması,” Fırat University Journal of Science and Engineering*.,* vol.29, no. 1, pp. 225-236, 2017.

[14] M. Jamil and X.S Yang, “A Literature Survey of Benchmark Functions for Global Optimization Problems,” Int. Journal of Mathematical Modelling and Numerical Optimisation, vol. 4, no. 2, pp. 150-194, 2013.

APPENDİX

Table 4
GWO-PSO performance comparison with unimodal benchmark functions

Function	Method	Best	Mean	Worst	Std	Computation Time
f_1	GWO PSO	2.8155e-29 1.8645e-05	**1.2770e-27** 1.8152e-04	1.0236e-26 0.0015	2.1109e-27 3.4239e-04	0.1171 0.0722
f_2	GWO PSO	1.8533e-17 0.0048	**9.5313e-17** 0.0320	3.6638e-16 0.1727	7.9800e-17 0.0392	0.1291 0.0778
f_3	GWO PSO	6.3728e-08 19.8364	**1.1175e-05** 73.6746	5.4032e-05 157.0681	1.6984e-05 30.9306	0.3805 0.5378
f_4	GWO PSO	3.4488e-08 0.6978	**1.0720e-06** 1.1559	5.3905e-06 1.7896	1.2244e-06 0.2664	0.1287 0.0699
f_5	GWO PSO	25.4990 17.0043	**26.9089** 98.0932	28.5607 498.7949	0.7535 104.7435	0.1473 0.1379
f_6	GWO PSO	6.5542e-05 9.0093e-06	0.7089 **1.3498e-04**	1.4975 5.1873e-04	0.3452 1.2357e-04	0.1388 0.0803
f_7	GWO PSO	5.1824e-04 0.0734	**0.0023** 0.1768	0.0067 0.3456	0.0014 0.0600	0.1860 0.2059

Table 5
GWO-PSO performance comparison with multimodal benchmark functions

Function	Method	Best	Mean	Worst	Std	Computation Time
f_8	GWO PSO	-3.1897e+03 -3.0109e+03	-6.0773e+03 **-4.9471e+03**	-7.3092e+03 -7.0724e+03	971.4041 1.2770e+03	0.2227 0.0994
f_9	GWO PSO	0 29.9706	**2.6344** 58.3851	15.4156 96.7560	3.9016 16.4032	0.2092 0.1409
f_{10}	GWO PSO	6.8390e-14 0.0022	**9.9179e-14** 0.0560	1.3234e-13 1.1558	1.5979e-14 0.2082	0.1334 0.0953
f_{11}	GWO PSO	0 2.1291e-06	**0.0035** 0.0078	0.0280 0.0320	0.0078 0.0089	0.1502 0.1046
f_{12}	GWO PSO	0.0193 3.9338e-08	0.0444 **0.0138**	0.0820 0.2074	0.0150 0.0450	0.2923 0.2555
f_{13}	GWO PSO	0.3080 5.0410e-06	0.5907 **0.0056**	1.3103 0.0210	0.1985 0.0067	0.2915 0.2577

Table 6
GWO-PSO performance comparison with fixed size multimodal functions

Function	Method	Best	Mean	Worst	Std	Computation Time
f_{14}	GWO PSO	0.9980 0.9980	5.1762 **2.8430**	12.6705 7.8740	4.2581 1.9284	0.5141 0.5071
f_{15}	GWO PSO	3.0750e-04 6.6311e-04	0.0031 **8.8895e-04**	0.0204 0.0012	0.0069 1.3007e-04	0.0846 0.0792
f_{16}	GWO PSO	-1.0316 -1.0316	**-1.0316** **-1.0316**	-1.0316 -1.0316	6.7752e-16 6.7752e-16	0.0683 0.0698
f_{17}	GWO PSO	0.39790 0.39789	**0.397891** 0.397890	0.397891 0.39789	3.4575e-06 1.6938e-16	0.1126 0.0623
f_{18}	GWO PSO	3 3	3.00003 **3**	3.0002 3	5.4667e-05 0	0.0783 0.0989

f_{19}	GWO	-3.8604	**-3.8611**	-3.8628	0.0026	0.1162
	PSO	-3.8628	-3.8628	-3.8628	3.6114e-15	0.1081
f_{20}	GWO	-3.3220	**-3.2879**	-3.1375	0.0586	0.2001
	PSO	-3.3220	-3.2784	-3.2031	0.0583	0.1107
f_{21}	GWO	-10.1530	**-8.9193**	-2.6303	2.5581	0.1679
	PSO	-10.1532	-6.0438	-2.6305	2.9052	0.1542
f_{22}	GWO	-10.4026	**-10.0480**	-5.0876	1.3434	0.1943
	PSO	-10.4029	-9.1608	-3.7243	2.5445	0.1887
f_{23}	GWO	-10.5362	**-10.3545**	-5.1284	0.9871	0.2526
	PSO	-10.5364	-9.2591	-2,8066	2.6405	0.2422

Table 7
The effects of changing the number of populations and iterations, on unimodal benchmark functions

Function	**Method**	**Population Number**	**Iteration Number**	**Best**	**Mean**	**Worst**	**Std**	**Computation Time**
f_1	GWO	30	500	2.8155e-29	**1.2770e-27**	1.0236e-26	2.1109e-27	0.1171
	GWO	15	500	3.3304e-21	6.2407e-20	2.4847e-19	6.5138e-20	0.0766
	GWO	30	100	1.8645e-05	0.0147	0.0326	0.0083	0.0750
	GWO	15	100	0.17745	0.6804	2.3128	0.4345	0.0570
f_2	GWO	30	500	1.8533e-17	**9.5313e-17**	3.6638e-16	7.9800e-17	0.1291
	GWO	15	500	6.4614e-13	2.3781e-12	6.1267e-12	1.6860e-12	0.0796
	GWO	30	100	0.0122	0.0230	0.0359	0.0069	0.0619
	GWO	15	100	0.1001	0.1950	0.3660	0.0646	0.0510
f_3	GWO	30	500	6.3728e-08	**1.1175e-05**	5.4032e-05	1.6984e-05	0.3805
	GWO	15	500	5.2722e-05	0.0102	0.0549	0.0152	0.2202
	GWO	30	100	52.7035	382.4511	2.4758e+03	459.5907	0.1864
	GWO	15	100	197.3679	1.2317e+03	4.6694e+03	946.8118	0.1578
f_4	GWO	30	500	3.4488e-08	**1.0720e-06**	5.3905e-06	1.2244e-06	0.1287
	GWO	15	500	5.9714e-06	8.9815e-05	4.7227e-04	9.5299e-05	0.0803
	GWO	30	100	0.5224	1.4898	2.9883	0.6714	0.0636
	GWO	15	100	0.9107	4.2749	8.0857	1.6376	0.0525
f_5	GWO	30	500	25.4990	**26.9089**	28.5607	0.7535	0.1473
	GWO	15	500	26.2671	27.7108	28.7986	0.7353	0.0828
	GWO	30	100	28.7672	30.9848	42.8574	3.0148	0.0699
	GWO	15	100	35.5374	88.1632	287.0783	51.4240	0.0542
f_6	GWO	30	500	6.5542e-05	**0.7089**	1.4975	0.3452	0.1388
	GWO	15	500	0.3679	1.4966	2.5180	0.6316	0.1208
	GWO	30	100	1.7964	2.9401	4.1530	0.6346	0.1107
	GWO	15	100	2.8815	4.8694	7.6166	1.0635	0.0973
f_7	GWO	30	500	5.1824e-04	**0.0023**	0.0067	0.0014	0.1860
	GWO	15	500	14.126e-04	0.0045	0.0100	0.0022	0.1098
	GWO	30	100	0.0081	0.0196	0.0399	0.0085	0.0819
	GWO	15	100	0.0065	0.0399	0.0734	0.0182	0.0786

Table 8
The effects of changing the number of populations and iterations, on multimodal benchmark functions.

Function	**Method**	**Population Number**	**Iteration Number**	**Best**	**Mean**	**Worst**	**Std**	**Computation Time**
f_8	GWO	30	500	-3.1897e+03	**-6.0773e+03**	-7.3092e+03	971.4041	0.2227
	GWO	15	500	-3.7541e+03	-5.7933e+03	-7.3390e+03	769.0020	0.1492
	GWO	30	100	-2.7952e+03	-5.5985e+03	-6.8392e+03	946.5625	0.0797
	GWO	15	100	-2.2474e+03	-4.6750e+03	-7.1282e+03	1.3882e+03	0.0781
f_9	GWO	30	500	0	**2.6344**	15.4156	3.9016	0.2092
	GWO	15	500	5.6843e-14	3.9220	15.5209	4.0141	0.0885
	GWO	30	100	10.0693	41.9163	229.1786	39.5007	0.0791
	GWO	15	100	23.3764	45.9260	81.3144	14.6026	0.0762
f_{10}	GWO	30	500	6.8390e-14	**9.9179e-14**	1.3234e-13	1.5979e-14	0.1334
	GWO	15	500	8.6127e-12	4.3345e-11	1.1429e-10	2.8252e-11	0.0955
	GWO	30	100	0.0127	0.0282	0.0792	0.0140	0.0852
	GWO	15	100	0.1232	0.3316	0.8121	0.1600	0.0659
f_{11}	GWO	30	500	0	0.0035	0.0280	0.0078	0.1502
	GWO	15	500	0	**0.0032**	0.0244	0.0074	0.0959
	GWO	30	100	0.0033	0.0919	0.1950	0.0615	0.0886
	GWO	15	100	0.3125	0.6201	0.9780	0.1637	0.0846
f_{12}	GWO	30	500	0.0193	**0.0444**	0.0820	0.0150	0.2923
	GWO	15	500	0.0370	0.0946	0.1763	0.0404	0.2821
	GWO	30	100	0.1037	0.4369	1.1312	0.2598	0.1264
	GWO	15	100	0.2496	0.9956	3.8609	0.6986	0.1099

f_{13}	GWO	30	500	0.3080	**0.5907**	1.3103	0.1985	0.2915
	GWO	15	500	0.3873	1.1492	1.5388	0.2549	0.2781
	GWO	30	100	1.4057	2.2815	3.2969	0.4376	0.2002
	GWO	15	100	2.3542	3.6059	6.6733	1.0975	0.1592

Table 9
The effects of changing the number of populations on fixed sized multimodal benchmark functions

Function	Method	Population Number	Iteration Number	Best	Mean	Worst	Std	Computation Time
f_{14}	GWO	30	500	0.9980	**5.1762**	12.6705	4.2581	0.5141
	GWO	15	500	1.9920	7.6726	12.6705	4.5098	0.4820
	GWO	30	100	0.9980	5.3432	12.6705	4.0264	0.2799
	GWO	15	100	1.1046	8.3693	17.3744	4.6689	0.1831
f_{15}	GWO	30	500	3.0750e-04	**0.0031**	0.0204	0.0069	0.0846
	GWO	15	500	3.0750e-04	0.0032	0.0204	0.0068	0.0712
	GWO	30	100	3.1176e-04	0.0049	0.0204	0.0080	0.0814
	GWO	15	100	3.8972e-04	0.0065	0.0204	0.0087	0.0811
f_{16}	GWO	30	500	-1.0316	**-1.0316**	-1.0316	6.7752e-16	0.0683
	GWO	15	500	-1.0316	**-1.0316**	-1.0316	6.7752e-16	0.0684
	GWO	30	100	-1.0316	**-1.0316**	-1.0316	6.7752e-16	0.0984
	GWO	15	100	-1.0316	**-1.0316**	-1.0316	6.7752e-16	0.0930
f_{17}	GWO	30	500	0.39790	0.3978913	0.39789	3.4575e-06	0.1126
	GWO	15	500	0.39791	**0.3979230**	0.39881	1.6762e-04	0.1094
	GWO	30	100	0.398	0.3981783	0.40253	9.0173e-04	0.0992
	GWO	15	100	0.398	0.3984403	0.40744	17.75e-04	0.0622
f_{18}	GWO	30	500	3	**3.00003**	3.0002	5.4667e-05	0.0783
	GWO	15	500	3	5.7001	84.0001	14.7885	0.0751
	GWO	30	100	3	3.0009	3.0028	8.6061e-04	0.1064
	GWO	15	100	3.0001	11.103	84.0036	24.7150	0.0545
f_{19}	GWO	30	500	-3.8604	-3.8611	-3.8628	0.0026	0.1162
	GWO	15	500	-3.8628	-3.8613	-3.8549	0.0027	0.0759
	GWO	30	100	-3.8601	-3.8610	-3.8553	0.0019	0.0664
	GWO	15	100	-3.8597	**-3.8604**	-3.8515	0.0030	0.0608
f_{20}	GWO	30	500	-3.3220	**-3.2879**	-3.1375	0.0586	0.2001
	GWO	15	500	-3.3220	-3.2525	-2.8404	0.1062	0.1180
	GWO	30	100	-3.3202	-3.2436	-2.8558	0.1037	0.0708
	GWO	15	100	-3.3197	-3.2319	-2.8403	0.1309	0.0651
f_{21}	GWO	30	500	-10.1530	**-8.9193**	-2.6303	2.5581	0.1679
	GWO	15	500	-10.1530	-8.2287	-2.6302	3.0591	0.1488
	GWO	30	100	-10.1499	-8.3714	-2.6244	3.2080	0.0856
	GWO	15	100	-10.1412	-9.1689	-2.6595	2.1374	0.0660
f_{22}	GWO	30	500	-10.4026	-10.0480	-5.0876	1.3434	0.1943
	GWO	15	500	-10.4028	**-10.3998**	-10.3964	0.0016	0.1787
	GWO	30	100	-10.3949	-9.70229	-2.76460	2.0055	0.0956
	GWO	15	100	-10.3852	-9.0812	-1.8358	2.8628	0.0684
f_{23}	GWO	30	500	-10.5362	**-10.3545**	-5.1284	0.9871	0.2526
	GWO	15	500	-10.5361	-10.3101	-3.8352	1.2229	0.2205
	GWO	30	100	-10.5311	-9.73273	-2.4172	2.3299	0.1123
	GWO	15	100	-10.5131	-8.84514	-2.4209	3.0127	0.1073

Sakarya University Journal of Science
SAUJS

e-ISSN 2147-835X | Period Bimonthly | Founded: 1997 | Publisher Sakarya University |
http://www.saujs.sakarya.edu.tr/en/

Title: Reviewing Phlomis rigida Labill From Turkey as a Antimicrobial Efficacy

Authors: Pınar ERECEVİT SÖNMEZ, Sevda KIRBAĞ, Uğur ÇAKILCIOĞLU

Recieved: 2020-07-24 01:55:56

Accepted: 2020-09-18 13:26:56

Article Type: Research Article

Volume: 24
Issue: 6
Month: December
Year: 2020
Pages: 1265-1271

How to cite
Pınar ERECEVİT SÖNMEZ, Sevda KIRBAĞ, Uğur ÇAKILCIOĞLU; (2020), Reviewing Phlomis rigida Labill From Turkey as a Antimicrobial Efficacy. Sakarya University Journal of Science, 24(6), 1265-1271, DOI: https://doi.org/10.16984/saufenbilder.769854
Access link
http://www.saujs.sakarya.edu.tr/en/pub/issue/57766/769854

Sakarya University Journal of Science 24(6), 1265-1271, 2020

Reviewing Phlomis rigida Labill From Turkey as a Antimicrobial Efficacy

Pınar ERECEVİT SÖNMEZ*[1], Sevda KIRBAĞ[2], Uğur ÇAKILCIOĞLU[3]

Abstract

This work researched the inhibitory properties of the extract of *Phlomis rigida* Labill plant including chloroform on gram-negative and positive bacteria, yeasts and dermatophyta; the related plant is used for therapeutic purpose in public. For the disk diffusion method, this extract is effective on *Pseudomonas aeruginosa* that is one of the negative bacterias by 11.33 ± 0.57 mm inhibition areas. Regarding other bacterias, the effect of the related extract is so low in avoiding the improvement of *Escherichia coli*, *Staphylococcus aureus* and *Bacillus megaterium* by 8.33 ± 0.57 mm inhibition area. It has highly effective on *Trichopyton sp.* and *Candida albicans* that are from dermatophytes fungis and yeast by 16.33 ± 0.57 mm inhibition area. About yeast and dermatophytes fungi it has a remarkable impact on *Candida glabrata* (14.33 ± 0.57 mm inhibition area), *Epidermophyton sp.* (12.33 ± 0.57 mm inhibition area). Antimicrobial activity of this natural extract against all the microorganisms that were tested by MIC method by concentrations vary by 100 uL and 6.25 uL. Acording to this; the results showed good inhibitory effect with 6.25 µL for *C. albicans*, *Trichophyton* sp. with 12.25 µL for *C. glabrata*. In the other hand it is effective with 25 µL for *P. aeruginosa*, *Epidermophyton sp*. with 50 µL for *E. coli*, *S. aureus*, *B. megaterium*. Being used plants for medical purposes as from since the early ages show that these plants can be used as alternatives of available antibiotics; including important medical components is the other reason for being an alternative at the same time. Concerning results, *P. rigida* can be utilized as a therapeutic drug for the healing of infections caused by microorganisms. In this study, we believe that the P. rigida is important in the search for new antibiotics and will contribute to the literature and the world of drug as it affects different types of microorganisms at the lowest level for the first time.

Keywords: *Phlomis rigida* Labill, therapeutic medicine, dermatophyta, bacteria, yeast

1. INTRODUCTION

Inspite of developments in the medical world related to people are progressing; Pandemics caused by bacteria, fungi, viruses cause serious health problems and even loss of life in our world [1].

Plants have been a natural source of drug compositions and pure products from past to present [2].

---

* Corresponding Author: perecevit@munzur.edu.tr

[1] Munzur University, Tunceli, Turkey, ORCID: https://orcid.org/0000-0003-2389-0694

[2] Fırat University, Elazığ, Turkey, E-Mail: skirbag@firat.edu.tr ORCID: https://orcid.org/0000-0002-4337-8236

[3] Munzur University, Tunceli, Turkey, E-Mail: ucakilcioglu@yahoo.com
ORCID: https://orcid.org/0000-0002-3627-3604

Every year, two or three antibiotics from microorganisms become ineffective. With the realization that the duration of antibiotics has been limited in the last decade, new sources of antibiotics have been directed especially to herbal antibiotics [3].

The genus Phlomis has an important effect on the emergence of natural therapeutic products [4]. Ulukanlı and Akkaya (2011) informed that Phlomis species in Turkey are recognized with the names specific to that region as ''Ballıkotu, Calba, Çalba or Şalba" [5].

Phlomis genus belonging to Lamiaceae family has more than 100 species in the world. In folk medicine, many Phlomis species are mostly consumed as herbal teas (Dağçayı) in the treatment of many diseases as tonic, carminative, appetizing and stimulating and pain reliever [6].

In addition, it is present several studies showing that this species has various biological and pharmacological activities for some plants such as malaria, antimicrobial, anti-allergic, antifibriel effects, immunosuppressive and free radical scavenging properties. Different secondary medicinal products have been previously identified on the Phlomis genera [7-9].

It is seen that there are studies about antimicrobial and biological characteristics of diverse Phlomis species in the literatüre [10-13].

According to our literature search, this is the first report on the antibacterial, antidermatophyte and antifungal features of *P. rigida*. It may have natural therapeutic drug on diseases caused by microorganisms in humans. This study researched the medical use areas of *P. rigida* plant by reviewing its antimicrobial characteristics by aiming new active ingredients for disease treatments.

2. MATERIAL-METHOD

2.1. Screening of antimicrobial Characteristics

2.1.1.The collection and preparation of the sample

Phlomis rigida Labill's collection (Lamiaceae) was made during appropriate vegetation (in June 2018) in Bingöl kuruca bight on northern slopes in the Turkey. This plant sample has been maintained in the Herbarium of Munzur University (UC - 145) in Tunceli, Turkey (UC - 145). The Flora of Turkey was utilized for the taxonomic diagnosis [14]. The diagnosed plant was made suitable for grinding. The grinded plant (2 g) was treated in 10 mL chloroform (98.1 %) solvent by keeping on a rotary shaker (100 rpm) for 24 h. The remaining extract was dissolved again in its own solvent. Thus, the plant extract was obtained. These plant materials were filtered under suitable aseptic conditions and left at 4 ° C for further study. Then, 100 μL (20 mg L^{-1}) of plant extracts were injected into 6 mm diameter (Schleicher & Shüll No: 2668, Germany) blank antibiotic paper discs to try the test isolates separately.

2.1.2. Microbial strain

The bacteria (*Escherichia coli* ATCC 25922, *Pseudomonas aeruginosa* DSM 50071, *Staphylococcus aureus* COWAN 1, *Bacillus megaterium* DSM 32), yeasts (*Candida albicans* FMC 17, *Candida glabrata* ATCC 66032) and dermatophyte (*Trichophyton sp.*, *Epidermophyton sp.*) were tested as species for the current study. The tested pathogens were taken by the Department of Biology, Firat University, Microbiology Laboratory, Elazig-Turkey.

2.1.3. Inhibitory characteristic test

The agar disc diffusion method was performed in order to detect inhibitory effect. Mueller Hinton Agar, Yeast Malt Extract Agar and Sabouraud Dextrose Agar were prepared separately in erlenmeyer bottles under laboratory conditions and brought to 45-50 ° C pouring temperature, with the culture of microorganisms to be prepared as explained, will be added at the incidence of % 1 (10^6 cells mL^{-1} of bacteria, 10^4 cells mL-1 yeast and cells mL^{-1} dermatophyta fungi as per Mc Farland standard). 15 ml medium by shaking well is poured in to sterile petri plates and homogenously distributed. The discs (6 mm diameter) with treated 100 microliters of plant extract were added to the appropriate agar media inoculated with microorganism. Then, petri dishes was stored at 4 ^{0} C for 2 h. The cultivated petri dishes were left in the incubator at 37 ± 0.1 ^{0} C at 24 h for bacterial isolates and also at 25 ± 0.1 ^{0} C at 72 h for yeasts and dermatophyte. The antibacterial, antifungal, antidermatophyta characteristic of plant extract was evaluated by observing the inhibition area on the disks [15]. Micostatin and ampicillin sulbactam were used as positive control. Chloroform injected discs were tested as negative control.

2.1.4. Minimal inhibition concentration

Minimal inhibitory concentrations (MIC) were detected using the Broth dilution assay. The cultures were obtained in Mueller Hinton Broth (Difco, Difco Laboratories, Detroit, MI, USA). The passages of microorganisms were prepared with 12- hour broth cultures and the passages were set at a blur of 0.5 Mc Farland Standard. The plant sample was first rarefied to the maximum value 100 µL to be evaluated, and then serial 2-fold subtilizations were acquired in a value serial from 6.25 to 100 µL (1562 - 25000 µg) in 10 mL aseptic test tubes including nutrient broth for bacteria and sabouraud dextrose broth for yeast and dermatophyta fungi. MIC values of this plant against analyzed microorganisms were revealed with a micro-well dilution method [16]. The propagation of microorganisms was determined by an EL x 800 universal microtiter plate reader at 600 nm with optical density quantity. After incubation for 18 - 24 h at 37±1^0 C for bacteria, 25 ± 0.10 C at 72 h for yeast and dermatophyte pathogens. It was defined as the smallest value of that sample for the nominal value of the plant material used to prevent proliferation of microorganisms. This is the last tube symbolization (mg mL^{-1}) whose demectric is not microbial growth.

2.1.5. Statistical analysis

Statistical comparisons were made between the extract and control groups (chloroform, ampicillin sulbactam, micostatin) in relation to measurable preventive activity against bacteria, yeast and dermatophytes. SPSS 15.0 soft ware was used for statistical evaluation (SPSS Inc., Chicago IL). The values were achieved by analysis of variance (ANOVA) and the lowest significant difference (LSD) tests were specified as mean ± SE. $P<0.0001$, $P<0.001$, $P<0.01$, $P>0.05$ were evaluated for the variations between extract and control groups. *P* values given as footnotes below Table 1 and 2 were considered extremely effect, highly effect and moderately effect. This study was conducted in three repetition.

3. RESULTS

The datas of the antimicrobial measurement showed that this extract has highly effective, effective, very low effective against the tested microorganisms (Table 1-2). *P. rigida* extract has highly effective with 16.33 ± 0.57 mm inhibition area on *C. albicans*, *Trichophyton sp.*, from yeast and dermatophyta fungi ($P<0.001$). In the microorganisms: It is effective in destroying the proliferation of *P. aeruginosa* (11.33 ± 0.57 mm inhibition area), *C. glabrata* (14.33 ± 0.57 mm inhibition area), *Epidermophyton sp.* (12.33 ±0.57 mm inhibition area) ($P<0.001$).

In the gram negative and positive bacteria; In the gram negative and positive bacteria; It is very low effective with 8.33±0.57 mm inhibition area against *E. coli*, *S. aureus* and *B. megaterium* ($P> 0.05$). This means that it contributes as a natural drug raw material for treatment works on microorganisms, notably dermatophytes that derange the human health.

In conclusion, antimicrobial characteristic of *P. rigida* is pretty high yeast and dermatophyte fungi compared to standard antibiotic and chloroform.

The reason why we use chloroform as a solvent in the antimicrobial efficacy test is that it is among the effective solvents used in researches on this subject and the chloroform extract generally shows a high antimicrobial effect. This is because chloroform produces inhibitory compounds in the composition of plants [17, 18].

Table 1
The antimicrobial characteristic of *Phlomis rigida* Labill by the agar disc diffusion method

Microorganisms	**Inhibition area (mm)**		
	P. rigida	**Control**	
		Chloroform	**Standart antibiotics**
E. coli	8.33±0.57^{a}	9.00±1.57^{c}	14.33±0.57*
S. aureus	8.33±0.57^{a}	9.33±0.57 ^{c}	14.33±0.57*
B. megaterium	8.33±0.5^{a}	10.33±0.57^{c}	13.00±1.00*
P. aeruginosa	11.33±0.5^{d}	10.33±0.57^{c}	12.33±0.57*
C. albicans	16.33±0.5^{d}	8.33±0.57c	12.33±0.57*
C. glabrata	14.33±0.5^{d}	8.33±0.57^{c}	9.66±0.57**
Epidermophyton sp.	12.33±0.5^{d}	9.33±0.57^{c}	9.66±0.57**
Trichophyton sp.	16.33±0.5^{d}	8.33±0.57^{a}	9.66±0.57**

Extract positive control; ampicillin sulbactam (*) and mikostatin (**) (120 µL and 20µg/disc), the negative control; chloroform. Inhibition zone > 20 mm (extremely effect; *P< 0.0001*; cd), 15 – 19 mm (highly effect*; P< 0.001*;d), 9-14 mm (effective; *P<0.001*;d), very low effect (a: *P>0.05*)

The antimicrobial features of this plant extract in concentrations ranging from 100 µL to 6.25 µL of was evaluated against all of the tested microorganisms with MIC. Table 2. shows the MIC value of all pathogen microrganisms for this extract. The MIC values ranged from an average of 6.25 µL to 50 µL. Acording to this; the results showed good inhibitory effect with 6.25 µL for *C.* albicans, *Trichophyton sp.* with 12.25 µL for *C.* glabrata. In the other hand it is effective with 25 µL for *P. aeruginosa*, *Epidermophyton sp.* with 50 µL for *E. coli*, *S. aureus*, *B. megaterium*.

So that means; this natural extract showed its antimicrobial affect at the lowest inhibition value tested against the development of yeast and dermatophyte fungi (6.25-12.25 µL). This once again proved that this plant extract, which we use with the MIC method, is very effective against the development of microorganisms causing diseases in humans.

Table 2
The antimicrobial characteristic of *Phlomis rigida* Labill by the minimum inhibition concentration (MIC in 100 µL)

Microorganisms	**Inhibition area (µL)**
	MIC values
	P. rigida
E. coli	50
S. aureus	50
B. megaterium	50
P. aeruginosa	25
C. albicans	6.25
C. glabrata	12.25
Epidermophyton sp.	25
Trichophyton sp.	6.25

The antimicrobial feature of *P. rigida* has been found to create a rather high inhibition zone against bacteria, yeast and dermatophyte fungi compared to standard antibiotics and chloroform used for control purposes. Therefore, it can be a natural antimicrobial agent.

Microorganisms developing resistance against antibiotics, it requires the continuity of the search for new natural therapeutic compounds. Just to clarify, our study is highly significant effect on both dermatophyte fungi and microorganisms by the smallest concentration even.
Plants for the isolation of natural antimicrobial compounds have been the focus of many researchers' previous scientific studies on this topic. It is the first report in the literature about antimicrobial analysis of *P. rigida* in studies performed to date.

In many studies conducted in- vitro, it has been determined that extracts of various Phlomis species have antimicrobial effects on the development of microorganisms. It has been stated in the studies conducted on diverse Phlomis species from different regions, that the vast majority of pathogenic microorganism species including bacteria and various fungi have an preventing characteristic on development [2].

Nikan et al. (2017) stated that essential oil from *P. rigida* is the most active oil that prevents the development of *S. aureus* and *C. albicans* [19]. In a study by Kulani et al. (2013), *P. rigida* oils were determined an preventing and biological characteristic, chemical content [20].

The different species of Phlomis essential oils showed an preventing effect on the disease-causing microorganisms in the development of pathogenic bacteria. In addition, methanol extracts from several Phlomis kinds also have the same effect. Extracts obtained with different solvents of *Phlomis* species have a preventive effect on the development of *Candida* species [4].

Another study found which *P. kurdica* essential oil prevented the development of food-borne B. cereus, while *H. pylori* was the most resistant [9].

Ristic et al. (2000) stated in their study that the ethanol extract and essential oils of *P. fruticosa* demonstrated preventing effect on the tested some bacteria and fungi. The largest inhibition zones were found for *B. subtilis*, *E. coli* and *M. luteus*. Substantial activity against *P. aeruginosa* and *S. faecalis* was not found [21].

In the study by Aligiannis et al. (2004), essential oils obtained from Phlomis species other than our study were found to have moderate activity on bacteria and have a stronger activity on pathogenic fungi [22].

Morteza-Semnani et al. (2006) expressed that the methanol extracts of different species of Phlomis prevented the development of *Streptococcus sanguis* and *S. aureus* at high levels. It also does not have any antifungal effects [23].

In another study, the methanol extracts from *P. rigida* were identified to be more effective than *H. bracteosa* as percent of inhibition [24].

It was determined in the study by Toroğlu et al. (2013), that extracts of *P. oppositiflora* using different solvents showed inhibitory activity on bacteria and fungi. In addition, essential oil and methanol extract have inhibitory activity in *E. coli* [6].

This study verifies the places used in folk medicine practices in a way. This plant has a potential to be a natural antimicrobial agent to be used as a medicine for human health and life quality.

Acknowledgements

The authors would like to thank the reviewers for all useful and instructive comments on our manuscript.

Funding

The authors received no specific funding for this study.

The Declaration Conflict of Interests/Common Interest

The authors declared no potential conflicts of interest with respect to the research, authorship, and/or publication of this paper.

Authors' Contribution

All authors have contributed in experimental study and writing of the manuscript equally.

The Declaration of Ethics Committee Approval

The authors declare that this document does not require an ethics committee approval or any special permission.

The Declaration of Research and Publication Ethics

The authors of the paper declare that they comply with the scientific, ethical and quotation rules of SAUJS in all processes of the paper and that they do not make any falsification on the data collected. In addition, they declare that Sakarya University Journal of Science and its editorial board have no responsibility for any ethical violations that may be encountered, and that this study has not been evaluated in any academic publication environment other than Sakarya University Journal of Science.

REFERENCES

[1] E. M. Altuner and I. Akata, “Antimicrobial activity of some macrofungi extracts,” Sakarya Üniversitesi Fen Bilimleri Dergisi, vol. 14, no.1, pp. 45-49, 2010.

[2] F. Demirci, K. Guven, B. Demirci, M. Y. Dadandi, and K. H. C. Baser, “Antibacterial activity of two Phlomis essential oils against food pathogens,” Food Control, vol. 19, pp. 1159–1164, 2008.

[3] Y. Akgül, “Antibacterial activities of some plant extracts against Pseudomonas aeruginosa and K. pneumoniae isolates

causing ürinary tract infection (M. Sc.), İdrar yolu enfeksiyonlarına neden olan Pseudomonas aeruginosa ve Klebsiella pneumoniae izolatlarına karşı bazı bitki ekstraktlarının antibakteriyal aktiviteleri," Yüsek Lisans Tezi, Nevşehir Hacı Bektaş Veli Üniversitesi Fen Bilimleri Enstitüsü, Nevşehir, pp. 75, 2014.

[4] I. Limem-Ben Amor, J. Boubaker, M. B. Sgaier, I. Skandrani, W. Bhouri, A. Neffati, S. Kilani, I. Bouhlel, K. Ghedira, and L. Chekir-Ghedira, "Phytochemistry and biological activities of Phlomis species," Journal of Ethnopharmacology, vol. 125, pp. 183–202, 2009.

[5] Z. Ulukanlı and A. Akkaya, "Antibacterial activities of Marrubium catariifolium and Phlomis pungens var. Hirta grown wild in eastern Anatolia, Turkey," Internatioanal Journal of Agriculture & Biology, pp. 1560–8530, 2011.

[6] S. Toroğlu and M. Çenet, "Comparsion of antimicrobial activities of essential oil and solvent extracts of endemic Phlomis oppositiflora Boiss. & Hausskn. From Turkey," Pakistan Journal of Zoology, vol. 45, pp. 475-482, 2013.

[7] Y. Takeda, H. Matsumura, T. Masuda, G. Honda, H. Otsuka, Y. Takaishi, and E. Sezik, "Phlorigidosides A–C, iridoid glucosides from Phlomis rigida," Phytochemistry, vol. 53, pp. 931–935, 2000.

[8] I. Kyriakopoulou, P. Magiatis, A. L. Skaltsounis, N. Aligiannis, and C. Harvala, "Samioside, a new phenylethanoid gycoside with free-radical scavenging and antimicrobial activities from Phlomis samia," Journal of Natural Products, vol. 64, pp. 1095-1097, 2001.

[9] A. E. Karadağ, A. E. Demirci, B. Kültür, Ş. F. Demirci, and K. H. C. Başer, "Antimicrobial, anticholinesterase evaluation and chemical characterization of essential oil Phlomis kurdica Rech. fil. Growing in Turkey," Journal of Essential Oil Research, vol. 32, pp. 242-246, 2020.

[10] T. Y. Shin and J. K. Lee, "Effect of Phlomis umbrosa root on mastcell-dependent immediate-type allergic reactions by anal therapy," Immunopharmacology and Immunotoxicology, vol. 25, pp. 73-85, 2003.

[11] E. Souri, G. Amin, A. Dehmobed-Sharifabadi, A. Nazifi, and H. Farsam, "Antioxidative activity of sixty plants from Iran," Iranian Journal of Pharmaceutical Research, vol. 3, pp. 55-59, 2004.

[12] M. M. Balos and H. Akan, "Zeytinbahçe - Akargay (Birecik, Şanliurfa) arasında kalan bölgenin etnobotanik özellikleri," Selçuk Üniversitesi Fen Fakültesi Fen Dergisi, vol. 29, pp. 155- 171, 2007.

[13] M. A. Khalilzadeh, M. Tajbakhsh, A. Rineh, "Study of the essential oils composition of leaves and flowers of two subspecies Phlomis herba-Venti (Pungens And Lenkoranica) from Iran," Journal of Essential Oil Research, vol. 20, pp. 46–48, 2008.

[14] P. H. Davis "Flora of turkey and the aegean islands," England: Edinburgh Univ. Press, vol. 7, 8, 9, 1970-1984-1985.

[15] C. H. Collins and P. M. Lyne "Microbiological methods," London: Butter worths & Co. (Publishers) Ltd, pp. 410, 1989.

[16] P. Erecevit, and S. Kırbağ, "Antimicrobial activity of some plant species used for the medical purpose in Turkey," The Journal of Phytopharmacology, vol. 6, pp. 93-97, 2017.

[17] B. Dülger, "Coriolus versicolor (L. ex Fr.) Quel. makrofungusunun antimikrobiyal aktivitesi,"Uludağ Turkısh Journal of Biology, vol. 23, pp. 385–392, 1999.

[18] K. Hürkan, M. Ballı Yüksel, Y. Kemeç Hürkan, and N. Demir, "Bazı salep orkidelerinin antioksidan ve antimikrobiyal özellikleri," 2019 UMTEB 6. Uluslararası

Mesleki ve Teknik Bilimler Bilimler Kongresi, pp. 29, 2019.

[19] M. Nikan, S. Saeidnia, A. Manayi, and S. Saadatmand, “Essential oils of four Phlomis species growing in Iran: chemical composition, antimicrobial and antifungal activity,” Progress in Nutrition, vol. 19, pp. 75-79, 2017.

[20] E. Kulani, M. Kazemi, and M. Dakhili, “Chemical composition and biological activities of Phlomis rigida Labill essential oil,” 2nd National Congress on Medicinal Plants 15-16 May, Tehran, Iran, p. 291. 2013.

[21] M. D. Ristic, S. Duletic-Lausevic, J. Knezevic-Vukcevic, P. D. Marin, D. Simic, Vukojevic, P. Janackovic, and V. Vajs, “Antimicrobial activity of essential oils and ethanol extract of Phlomis fruticosa L. (Lamiaceae),” Phytotherapy Research,” vol. 14, pp. 267–271, 2000.

[22] N. Aligiannis, E. Kalpoutzakis, I. Kyriakopoulou, S. Mitaku, and I. B. Chinou, “Essential oils of Phlomis species growing in Greece: chemical composition and antimicrobial activity,” Flavour and Fragrance Journal, vol. 19, pp. 320–324, 2004.

[23] K. Morteza-Semnani, M. Saeedi, M. R. Mahdavi, F. Rahimi, “Antimicrobial studies on extracts of three species of Phlomis,” Pharmaceutical Biology,” vol. 44, pp. 426–429, 2006.

[24] M. D. C. Zinsou, F. Assogba, F. Gbaguidi, and M. Moudachirou, “Chemical composition and in vitro investigation of biological activities of Hemizygia bracteosa (Benth.) Briq leaves,” Journal of Pharmacognosy and Phytotherapy, vol. 10, pp. 11-20, 2018.

SAKARYA ÜNİVERSİTESİ

FEN BİLİMLERİ ENSTİTÜSÜ
DERGİSİ

Sakarya University Journal of Science
SAUJS

e-ISSN 2147-835X | Period Bimonthly | Founded: 1997 | Publisher Sakarya University |
http://www.saujs.sakarya.edu.tr/en/

Title: An Experimental Method for Estimating Combined Friction Torque in Vane Type Pneumatic Semi Rotary Actuators

Authors: Mustafa DAĞDELEN, Mehmet İlteriş SARIGEÇİLİ

Recieved: 2019-12-05 10:00:07

Accepted: 2020-09-18 14:43:57

Article Type: Research Article

Volume: 24
Issue: 6
Month: December
Year: 2020
Pages: 1272-1283

How to cite
Mustafa DAĞDELEN, Mehmet İlteriş SARIGEÇİLİ; (2020), An Experimental Method for Estimating Combined Friction Torque in Vane Type Pneumatic Semi Rotary Actuators. Sakarya University Journal of Science, 24(6), 1272-1283, DOI: https://doi.org/10.16984/saufenbilder.652782
Access link
http://www.saujs.sakarya.edu.tr/en/pub/issue/57766/652782

Sakarya University Journal of Science 24(6), 1272-1283, 2020

An Experimental Method for Estimating Combined Friction Torque in Vane Type Pneumatic Semi Rotary Actuators

Mustafa DAĞDELEN*[1], Mehmet İlteriş SARIGEÇİLİ[2]

Abstract

In this paper, an experimental method is proposed for estimation of friction torque in vane type pneumatic semi rotary actuators. The friction is modelled in the form of fully combined Stribeck model since this combined friction model provides good solutions for precise control applications. The study aims estimating static friction torque, Coulomb friction torque, Stribeck speed and viscous friction&damping coefficient which is included in fully combined Stribeck model for both counterclockwise and clockwise directions of the rotary actuator since these unknown parameters show differences when direction of motion is altered. For that purpose, an experimental setup is designed which includes pressure sensors for measuring the chamber pressures of actuator, analogue potentiometer for reading angular position as well as speed of vane and Arduino microcontroller card for data acquisition. A proper MATLAB Simulink block diagram is prepared for the simultaneous estimation of processed data from experimental data. Nonlinear curve fitting operation is applied and the unknown friction parameters are estimated on the fitted curve easily.

Keywords: Friction torque, Stribeck model, pneumatic semi rotary actuator, curve fitting

1. INTRODUCTION

Rotational motion needed in mechanical applications, especially in robotic platforms, is generally supplied by electrical motor actuators and hydraulic actuators due to their availability and convenience in control. However, these two actuators have high weight and high impedance. Especially, electrical motor actuators need high transmission ratios to reach requested speed and torque levels which is limiting their back-drivability and reducing safety in contact. On the other side, pneumatic actuation systems are clean systems which use pressurized air as power source and can provide both linear and rotational motion for mechanical applications. These actuation systems can be used as an alternative to both hydraulic systems and commonly used

---

* Corresponding Author: mdagdelennn@gmail.com

[1] Çukurova University, ORCID: https://orcid.org/0000-0002-1448-104X

[2] Çukurova University, E-Mail: msarigecili@gmail.com
ORCID: https://orcid.org/0000-0002-9969-2005

electrical motor actuators due to their outstanding properties such as high power to weight ratio, high compliancy, easy to maintain, wide range of force and speed arrangements without a transmission element [1]. Also, these remarkable actuators are favorable for harsh and spark-prohibited environments like mining factories, chemical working stations etc.

Pneumatics can provide rotational motions in two forms as full rotational motion and semi-rotational motion. Air motors which have several types as piston type, gear type, turbine type and vane type can deliver full rotational motion. However, semi rotary type actuators fit better where only limited rotational motion is needed at rotational joints. Semi rotary actuators can be in two different types as vane type and rack and pinion type. Vane type semi rotary pneumatic actuators work with the principle of vane rotating inside a chamber. Whereas, rack and pinion type semi-rotary actuators work with a linear cylinder functioning as a rack and pairing with a pinion for converting linear motion to rotational motion. This arrangement increases the size and weight of these actuators inherently and limits their usage areas. Hence, vane type semi rotary actuators in rotational joints become more advantageous. Even though pneumatic semi rotary actuators are well suited for rotational joints in robotics, these actuators have non-linear characteristics due to resisting friction, air compressibility and non-linear relationship between pressure and air flow rate. Any precise control of motion characteristics (i.e. angular position, velocity and acceleration) coupled with torque output requirement would necessitate the information of inertia characteristics (i.e. mass and mass moment of inertia) as well as friction force resisting to input torque. Hence, in this study, the friction models of semi rotary actuators will be estimated and their dynamics will be developed to utilize them efficiently.

Many friction force and torque models can be found in literature. Coulomb [2], combined Coulomb-Viscous [3], fully combined Stribeck [4] and LuGre model [5] are mostly preferred friction models in previous studies. In this study, we will focus on fully combined Stribeck model since it includes satisfactory friction parameters which is sufficient for many pneumatic applications that operate generally in medium to high speeds. The Stribeck model includes the parameters of static friction torque (T_s), Coulomb friction torque (T_c), Stribeck speed (w_s) and viscous friction&damping coefficient (B). There exist other friction models in the literature which take into account pre-sliding regime in detail. However, this type of friction models is complex and more suitable for systems which operate in very low speed ranges. More information about these complex friction models can be found in [4]. In addition, there are many friction estimation studies for linear pneumatic cylinders [6,7,8] available in the literature. However, there exist very limited number of studies on friction in semi-rotary actuators.

The first friction study on rotary pneumatic actuators was performed by Belforte and Raparelli [9]. They tested three different actuators under different working pressures and provided the characteristics of static torque-pressure curves, adhesion torque curves, active and passive efficiency curves. Their designed experimental bench consisted of many electronic parts such as electric motor, torque sensor, pressure sensor making their setup complex and costly. Schlüter and Perondi [10] proposed a full mathematical model of semi-rotary actuators including friction in the form of LuGre model. The friction torque-angular speed map was constructed and the parameters of LuGre friction model were found by curve fitting operations. Then, Schlüter and Perondi [11] tested their model on a SCRARA robot with semi-rotary actuator. On the other studies about rotary pneumatic actuator, the researchers focused mainly on the mathematical model of pneumatic actuators and valves where the detailed information about friction were not available. A general mathematical model for vane type air motors were developed by Luo et al. [12] by describing the mechanical structure of rotary actuators and their working principles very well. However, there is only assumptions about friction torque in their study. In another study, Sorli et al. [13] provided a general mathematical model for both linear and rotary pneumatic actuators. They assumed friction torque as constant in their study.

But, constant friction torque cannot be accepted for precise control applications of pneumatic rotary actuators. Lan and Cheng [14] provided modelling and design of air vane motors to reduce ripples in torque by proposing a non-circular profile of stator to eliminate the variations in angular speed and torque. Their study did not include actuator vane friction. Zhang et al. [15] applied servo position control in rack and pinion type semi-rotary pneumatic actuators and they claimed that position instabilities had been observed because of ignored friction torque models.

The unavailable information on friction torque characteristics of vane type pneumatic semi rotary actuators prohibit wide application of these actuators. Therefore, in this study, an experimental method is proposed for quick estimation of resisting friction torque in this type of pneumatic actuators.

In the paper, the mechanical structure and mathematical models will be discussed in Section 2. In Section 3, experimental setup and measurement techniques will be demonstrated. The proposed method will be presented in detail in Section 4. Section 5 will provide the experimental results. Lastly, the conclusion and discussion will be provided in Section 6.

2. MECHANICAL STRUCTURE AND MATHEMATICAL MODELS OF SEMI ROTARY ACTUATORS

The general cross-sectional view of a semi rotary actuator is shown in Fig.1. This type of actuators is permitted to oscillate between two angles i.e. the higher (θ_H) and lower (θ_L) oscillation angles, respectively, whereas θ_M is the half-stroke angle of the actuator. Then, the range of motion would be calculated from ($\theta_H - \theta_L$). The stationary body is called as stator and placed on a ground whereas the rotor unit rotate inside the stator unit. The rotor unit includes the combination of two separate parts as rotating shaft and vane as shown in detail in Fig.2.

Semi-rotary actuators can rotate either in counter clockwise (CCW) or clockwise (CW) direction according to the pressurized chamber (A or B in Fig.1). To rotate the actuator in CCW direction, the air is filled to the chamber A through port A with a certain mass flow rate $\dot{m}_A$. The pressure is increased in the chamber and this increased pressure P_A acts on the vane surface area generating a torque that tends to rotate the rotor unit in CCW direction. During CCW movement, the air inside the chamber B is exhausted to the atmosphere through directional control valve (DCV). To move the actuator in CW direction, the air is filled to the chamber B through port B with a certain mass flow rate $\dot{m}_B$ and the resulting pressure P_B drives the rotor unit in CW direction while air in the chamber A is exhausted.

The torque produced by pressurized air about point O (Fig.1) is calculated by multiplying the net pressure force acting on the vane and the distance from point O to the acting point of this force. The net pressure force is the multiplication of the pressure difference in the two chambers and the net vane area. From the vane and rotating shaft structure shown in Fig.2., D is the rotating shaft diameter, H is the vane surface height and W is the vane surface width. Hence, the vane surface area denoted by A_v is calculated by $H * W$. Since the net pressure force is assumed as acting on the center of the vane surface area which is vane torque centerline (Fig.2), r is $(H + D)/2$.

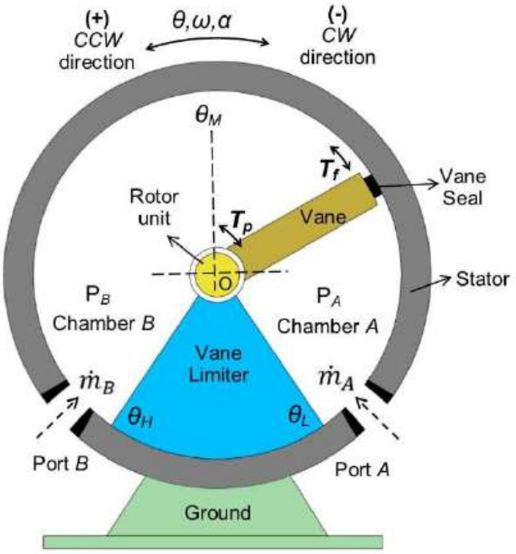

Figure 1 The cross-section of semi rotary pneumatic actuators

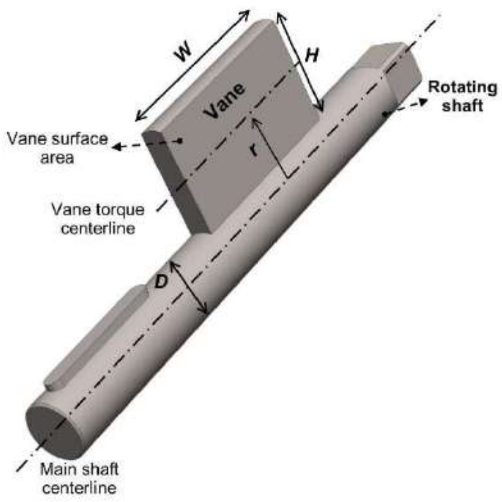

Figure 2 Rotor unit

The net produced torque of the actuator is defined from Euler equation (Eq.1) where T_p, T_f, T_L, I and α represent pneumatic torque produced from the pressure difference in chambers, friction torque that is to be estimated with the proposed method, payload torque, mass moment of inertia of the rotating parts of the actuator and angular acceleration, respectively.

$$T_{net} = T_p - T_f - T_L = I * \alpha \tag{1}$$

In the proposed study, experiments are carried out at constant angular speed where angular acceleration becomes zero ($\alpha = 0$) and also there is no payload in experiments ($T_L = 0$). Therefore, in experiments, the pneumatic torque (T_p) will be equal to the friction torque (T_f) as shown in Eq.2.

$$T_p = (P_A - P_B) * A_v * r = T_f \tag{2}$$

The main cause of friction torque originates at the contact surface between vane seal and the rotor internal surface (Figs.1 and 2). In reality, there exist other friction torques in the actuator such as friction in shaft bearings and coaxially attached position sensors (potentiometer, encoder etc.) to the actuator shaft. However, this type of friction forces is very small compared to the friction force caused by vane seal. Therefore, they are assumed negligible for the purpose of this study.

The full Stribeck friction model formed for both motion directions of actuator is shown in Fig.3. Positive values correspond to the CCW direction parameters, whereas negative values (except B) correspond to the CW friction torque parameters. The change in friction torque with respect to angular speed can be seen in Fig.3. The mathematical model of the Stribeck friction model is given in Eq.3 [10]. In this equation, T_s and T_c correspond to the static friction torque and Coulomb friction torque, respectively. The Stribeck effect is observed in the low speed ranges. w_s is the Stribeck speed where beyond this point, friction torque starts to behave linearly with increasing speed. B is the viscous friction&damping coefficient and j corresponds to a constant which determines the level of Stribeck effect. For linear pneumatic cylinders, this constant can take values between 0.5-2 which is also accepted for rotary pneumatic actuators in [10].

$$T_f = T_c + (T_s - T_c) * e^{-\left(\frac{w}{w_s}\right)^j} + B * w \tag{3}$$

By recalling that the pneumatic torque (T_p) from Eq.2 will be equal to the friction torque (T_f) from Eq.3 then Eq.4 can be written as:

$$(P_A - P_B) * A_v * r = T_c + (T_s - T_c) * e^{-\left(\frac{w}{w_s}\right)^j} + B * w \tag{4}$$

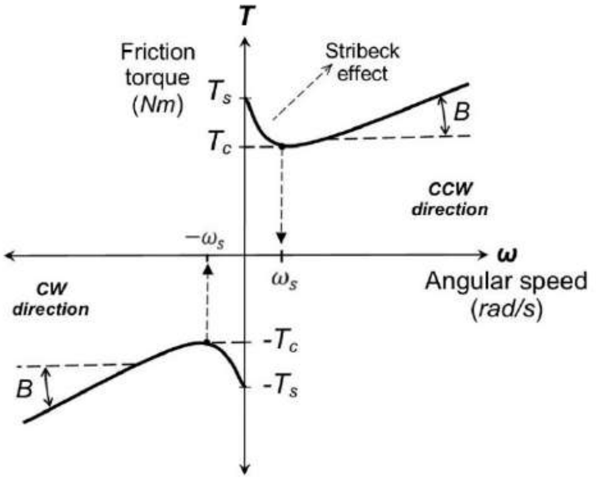

Figure 3 Stribeck friction torque model

3. EXPERIMENTAL SETUP

Full experimental setup in the proposed methodology includes two subsystems: rotary pneumatic system and measurement system. The pneumatic system is shown in Fig.4 and it consists of an air compressor, an air tank, a filterregulation-lubrication (FRL) unit, a manually adjustable pressure control valve (APV), a 5/3 closed center solenoid directional control valve (DCV), two one-way flow control valves (FCV) and a semi rotary actuator which has 270° range of motion (ROM). S_A and S_B represents the solenoids of the DCV. When one of these solenoids is energized, the air is sent to the corresponding chamber (i.e. chamber A or B) and the semi-rotary actuator rotates either in CCW or CW direction based on its working principle.

Measurement system setup responsible from data receiving and recording consists of a data acquisition and control card, two analogue output pressure sensors to read the chamber pressures, an analogue output rotary position sensor for angular position and speed, a two-way relay card and a PC as schematized in Fig.5. The working principle of the system is as follows: when one of the movement buttons is pressed, the control card produces a triggering signal for relay card (u_a,u_b) and the relay card switches the electric power which is coming from the power supply for the solenoids of directional control valve (S_A, S_B). Then, during motion, the pressures in chambers (P_A, P_B) as well as angular position and speed (θ, ω) values are measured via the sensors. The sensor measurements are carried out by Arduino Software Package environment existing in MATLAB Simulink. For this purpose, a proper block diagram is constructed by the help of this package (Fig.6). In this figure, blocks of “Pin 1”, “Pin 2” and “Pin 3” represent the pressure signal from sensors at chambers A and B, and angular position signal from rotary potentiometer outputted by Arduino micro control card, respectively. These three sensors produce analog signals between 0-5V. Therefore, in order to get meaningful data from each sensor, separate calibrations were made. Therefore, P_A and P_B coming out of the signal calibrations (Fig.6) corresponds to the pressure in the actuator chambers in “*Pascal*” unit, while θ parameter represents the angle in “*degree*” unit. In order to read angular velocity, the first order derivative of the position is taken. In order to calculate the torque, the difference of the pressures is taken with a help of the difference block and multiplied by the constant that will convert the pressure value to torque, and as a result, the net torque is obtained. On the other hand, in order to express the angular velocity in terms of “*rad/s*”, it is multiplied by the constant that will make the “*degree*” to “*radian*” conversion and the angular velocity is recorded in “*rad/s*”. The equipment used in this experimental setup and their specifications are tabulated in Table 1 and complete experimental setup is also shown in Fig.7.

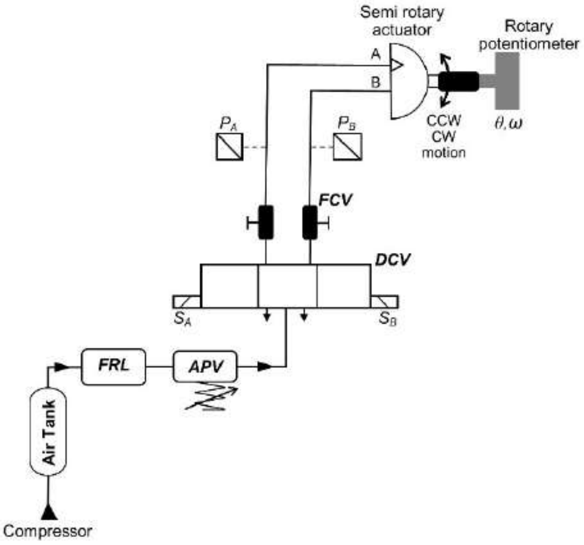

Figure 4 Pneumatic system setup

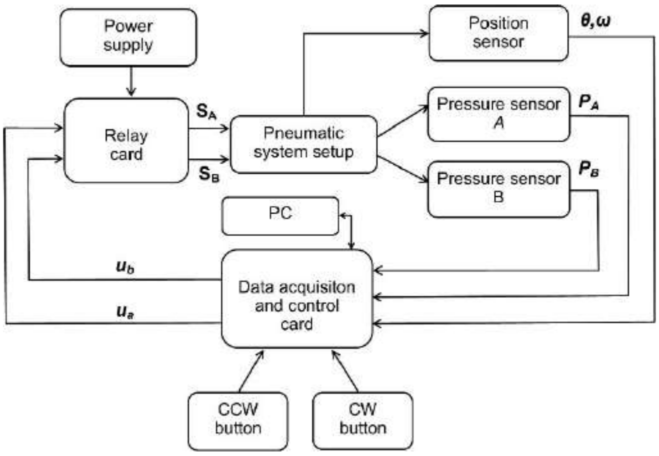

Figure 5 Measurement system setup

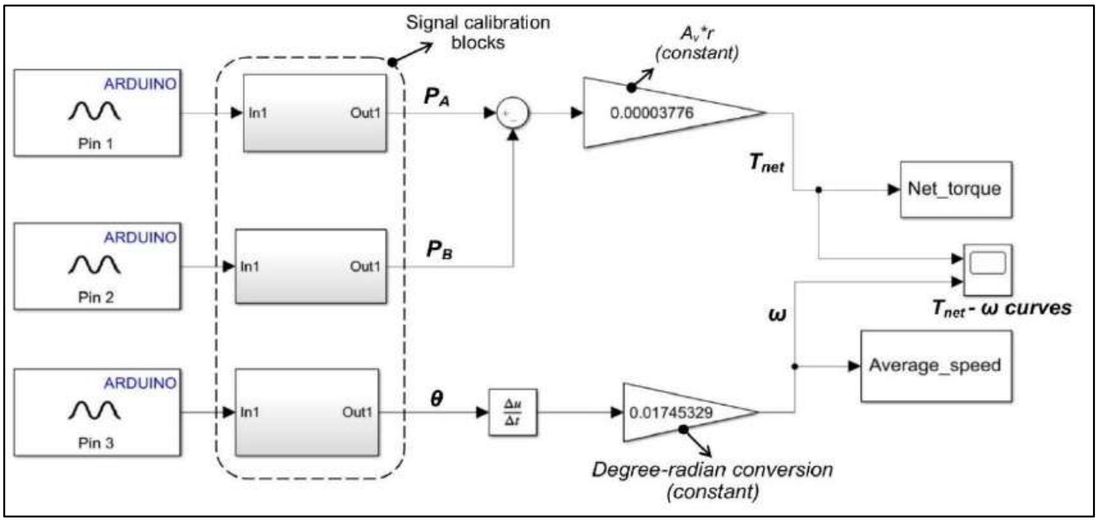

Figure 6 MATLAB Simulink block diagram

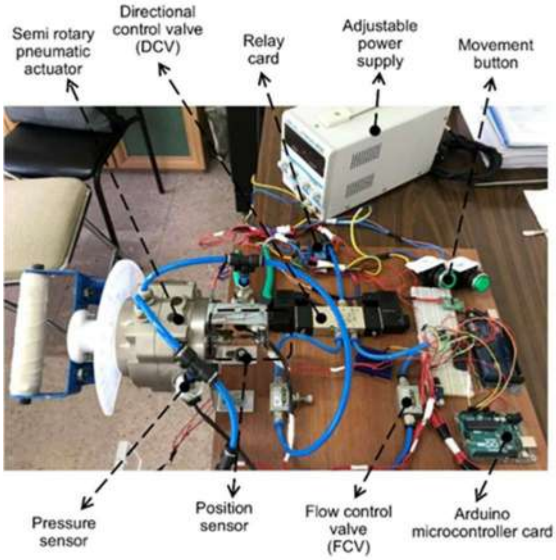

Figure 7 Complete experimental setup

4. PROPOSED METHOD

4.1. Estimation of Static Friction Torque (T_s)-Part 1

In the first part of the experimental method, static friction torque (T_s) corresponding to the maximum friction value for impending motion is estimated (Fig.3). Therefore, static friction torque (T_s) is estimated from Eq.4 by setting w=0 and following the steps described below:

1. Set supply pressure (P_s) to zero gage pressure from adjustable flow control valve.
2. Fully open flow control valves.
3. Press CCW movement button.
4. Turn gradually pressure control valve until the actuator just starts to move.
5. At the instant of motion initialization deactivate the CCW button and stop actuator movement.
6. Get the highest friction torque value from MATLAB graphs and record the data.

7. Repeat these procedures 24 times to complete the experiment.
8. Tabulate the results and take the average of 24 values.

The steps listed above is applied to find the static friction torque of CCW direction. To find CW static friction torque, the same procedures are applied except that the CW button is pressed in step 3 and CW button is deactivated in step 5.

Table 1
Equipment used in experimental setup and their specifications

Experimental setup and their specifications		
Rotary pneumatic actuator	Vane type	Single vane
	Shaft type	Double ended
	Range of motion (ROM)	270 °
	Dimensions	D=0.017 *m*; H=0.02988 *m*; W=0.054 *m*; A_v=0.00161352 m^2; r=0.0234 *m*
Directional control valve	Type	5/3 closed center
	Operating voltage	12 *VDC*
Position sensor	Type	Rotary potentiometer
	Output range	0-5 *VDC* analogue
Pressure sensors	Measurement range	0-1.2 *MPa*
	Output range	0-5 *VDC* analogue
Pressure regulating valve	Working type	Manually adjustable
	Max. input pressure	16 *bar*
	Output pressure range	0.5-10 *bar*
Data acquisition and control card	Arduino Uno	
PC	64bit ; 2400 CPU; 3.10*Ghz* processor	

4.2. Estimation of Coulomb Friction Torque, Stribeck Speed, Viscous Friction&Damping Coefficient and Stribeck Coefficient (T_c, w_s, B and j)- Part 2

In the second part of the experimental method, after the estimation of static friction torque, other friction torque parameters (B, T_c, w_s and j) are found by consecutive experiments at distinct angular speeds (w). The following steps should be carried out to estimate these four friction torque parameters.

1. Set supply pressure to $Ps = 5$ bar from pressure regulating valve.
2. Fully open the flow control valves.
3. Adjust CCW flow control valve to get a certain angular speed.
4. Press CCW movement button and move the actuator at a specified speed.
5. At the end of the motion, deactivate the button and free pneumatic actuator.
6. Record the pressure data and angular speed.
7. Calculate net friction torque on vane.
8. Set back actuator position to the initial experimental position.
9. Repeat the procedure from 1-8 for 15 times on the actuator.
10. Apply nonlinear curve fitting to these 15 friction torque-angular speed data to find T_c, w_s, B and j paramaters.

In order to find T_c, w_s, B and j for CW direction, the same procedure is followed except at step 3 CW flow control valve is adjusted and at step 4 CW movement button is pressed.

5. EXPERIMENTAL RESULTS

In this section, experiments are carried out on the semi-rotary actuator (Table 1) for both movement directions. According to the proposed methodology, the first part is the estimation of the static friction torque. Hence, the experimental procedures are applied to the tested actuator and the results are tabulated in Table 2 for both CCW and CW movement directions.

As presented in Table 2, the results are very convergent in each experiment. As a result of this part, the average static fiction torque values for CCW and CW directions are obtained as 1.637 *Nm* and -1.564 *Nm* respectively. As an example, the process of obtaining static friction torque from the tested actuator is shown in Fig.8. In Fig.8, the push button is pressed at the instant t=0*s* even though the figure only represents the time interval t=15*s* to t=25*s*. Between the points “a.” and “b.”, there is no pressure applied because the pressure is adjusted from pressure regulating valve during this period However, as the pressure is started to be increasing gradually, the first motion is observed at point "b.". Between points "b." and "c.", the pressure is increased very fast. When it reaches the point "c.", the actuator starts motion and the friction value is reduced inherently. In each experiment, the maximum point of friction torque "c." is recorded and tabulated.

Table 2
Static friction torque measurements- Part 1

Experiment #	T_s for CCW direction (Nm)	T_s for CW direction (Nm)
1	1.668	-1.570
2	1.556	-1.514
3	1.723	-1.458
4	1.612	-1.569
5	1.667	-1.513
6	1.556	-1.514
7	1.779	-1.626
8	1.667	-1.402
9	1.667	-1.514
10	1.500	-1.514
11	1.612	-1.569
12	1.444	-1.680
13	1.556	-1.625
14	1.612	-1.570
15	1.612	-1.681
16	1.723	-1.681
17	1.724	-1.736
18	1.668	-1.458
19	1.668	-1.570
20	1.780	-1.514
21	1.724	-1.570
22	1.556	-1.570
23	1.612	-1.514
24	1.612	-1.625
Average	1.637	-1.564

The procedures of the second part are applied to the tested actuator after the estimation of static friction torque (T_s). The obtained net friction torque (T_f) and angular speed (w) values are tabulated in Table 3.

As an example, the process of obtaining net friction torque and angular speed readings are shown in Figs. 9 and 10, respectively. In these figures, the point "b." represents the instant that movement button is pressed. Between points "b." and "c.", there is a small delay naturally existing in pneumatic systems. The actuator moves between points "c." and "d.", and the results are extracted between this time interval. The point "d." represents the end of the actuator's stroke and the button is deactivated at this point. There is a sudden jump at the calculated friction torque value from points "d." to "e." until the equilibrium is satisfied due to the response time. On the other side, angular speed measurements (Fig.10) have noisier signal than pressure measurements due to the numerical derivation of angular position data. Hence, average friction torque and average angular speed value are calculated between points "c." and "d." and listed in Table 3.

Table 3
Angular speed and net friction torque measurements- Part 2

	CCW direction		CW direction	
Exp. #	w (rad/s)	T_f (Nm)	w (rad/s)	T_f (Nm)
1	0.802	1.637	-0.379	-1.120
2	2.840	1.203	-1.012	-1.326
3	3.138	1.317	-2.044	-1.430
4	3.930	1.374	-2.661	-1.562
5	4.252	1.448	-3.353	-1.667
6	4.665	1.467	-4.105	-1.521
7	4.753	1.517	-4.208	-1.794
8	5.367	1.610	-4.962	-1.696
9	5.745	1.703	-5.405	-1.785
10	5.846	1.665	-6.923	-1.895
11	6.787	1.857	-7.046	-2.053
12	6.879	1.847	-7.459	-2.143
13	7.464	1.952	-7.671	-2.039
14	8.843	2.208	-7.999	-2.213
15	9.005	2.391	-9.274	-2.257

After application of procedures in Parts 1 and 2 to the tested rotary actuator, nonlinear curve fitting operations are applied to the experimental data of both CCW and CW directions. In the result of the successful curve fitting operations, Stribeck friction torque models (Eqs. 5 and 6) are determined as in Figs. 11 and 12.

$$\left(T_f\right)_{CCW} = 0.691 + 0.946 * e^{-\left(\frac{w}{0.995}\right)^{2.016}} + 0.174 * w \tag{5}$$

$$(T_f)_{CW} = -1.170 - 0.394 * e^{-\left(\frac{w}{-0.074}\right)^{3.060}} + 0.120 * w \qquad (6)$$

The Stribeck friction model parameters are also estimated automatically and given in Table 4. The goodness of fit value in the form of sum of squared errors (SSE) for curve fitting operation for CCW and CW directions are 0.0315 and 0.0937, respectively.

Table 4
Estimated friction model parameters

Stribeck model parameters	**CCW direction**	**CW direction**
$T_s\ (Nm)$	1.637	-1.564
$T_c\ (Nm)$	0.691	-1.170
$w_s\ (rad/s)$	0.995	-0.074
$B\ (Nsm/rad)$	0.174	0.120
j	2.016	3.060

6. DISCUSSION AND CONCLUSION

In this study, an experimental setup and methodology are developed for friction torque estimation of vane type semi rotary pneumatic actuators. For experimental setup, only two pressure sensors and one rotary potentiometer are used to evaluate the friction torque parameters. The chamber pressures (P_A, P_B) and angular speed (w) data is gathered using Arduino microcontroller card with MATLAB Simulink software. The tested actuator is examined at angular speeds between $w = 0 - 10\ rad/s$ since the curves will continue to behave linear for speeds higher than Stribeck speed (w_s) (Figs. 11-12). The supply pressure is set to $5\ bar$ in the experiments, because pneumatic working pressure is generally between $4 - 6\ bars$ in literature. The data collected are curve fitted and friction torque parameters are estimated easily for both directions of actuator. In most of the studies, the friction torque models assumed as the same for both CCW and CW directions. However, it has been presented in this study that the friction torque characteristics change when the direction of motion is changed. In conclusion, both friction torque curves and Stribeck friction torque models are provided as a function of angular speed in the proposed methodology. It has been also shown that the friction torque resisted by rotary actuator does not behave linearly at lower speeds. Even though, Stribeck coefficient (j) is assumed generally as 2 in previous studies, it has been realized that it differs for both of the movement directions and can take the values higher than 2. Furthermore, the obtained Stribeck friction torque model can be used at the precise control applications of vane type semi rotary pneumatic actuators.

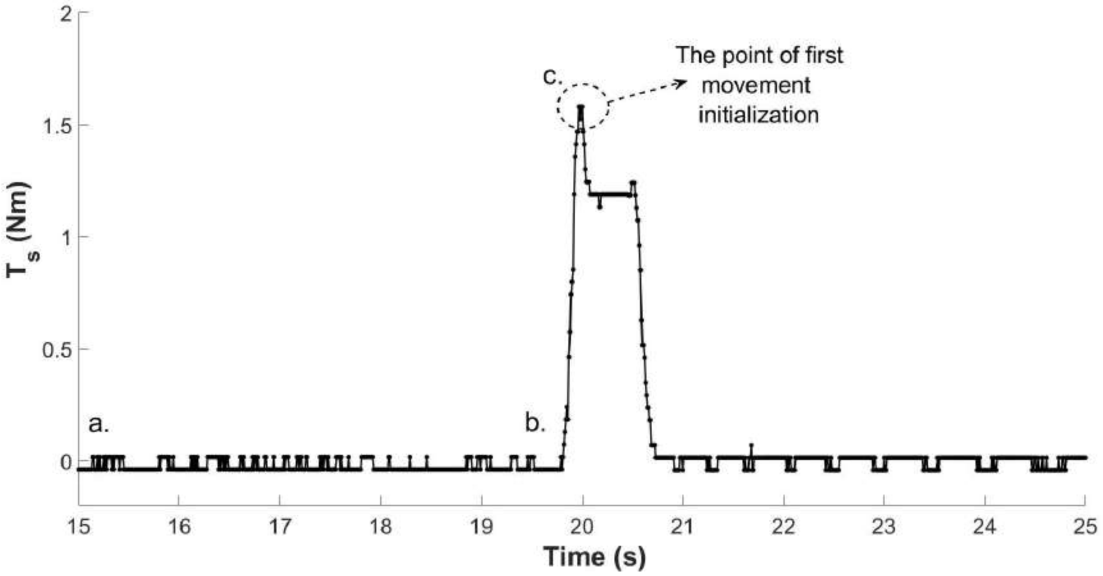

Figure 8 Static friction torque measurement graph- Part 1

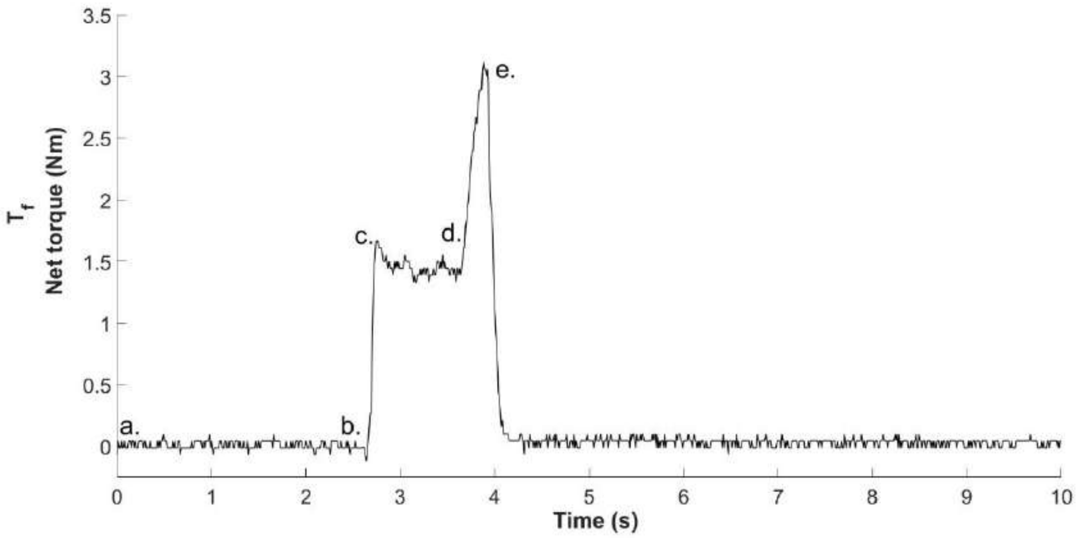

Figure 9 An example net friction torque reading- Part 2

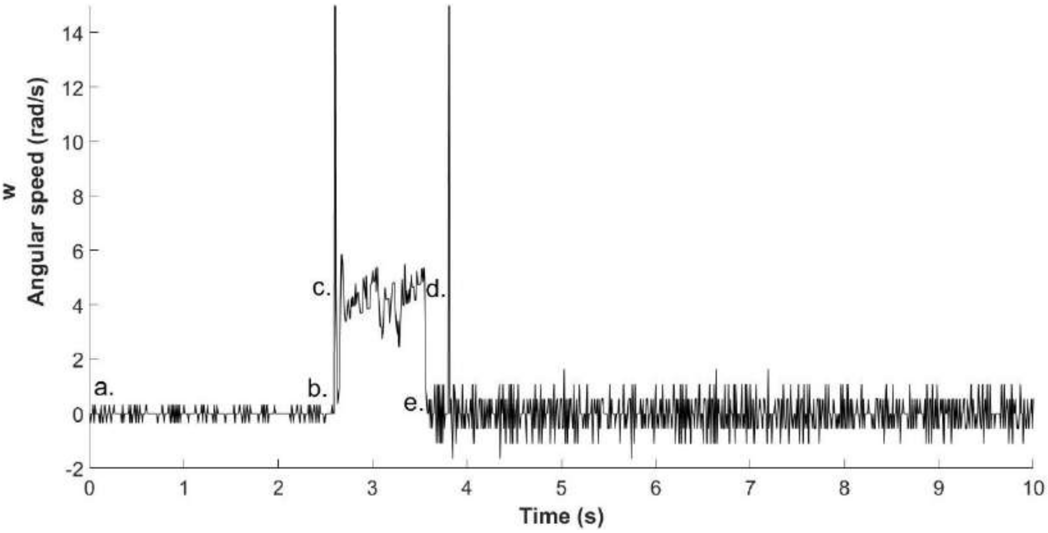

Figure 10 An example angular speed reading- Part 2

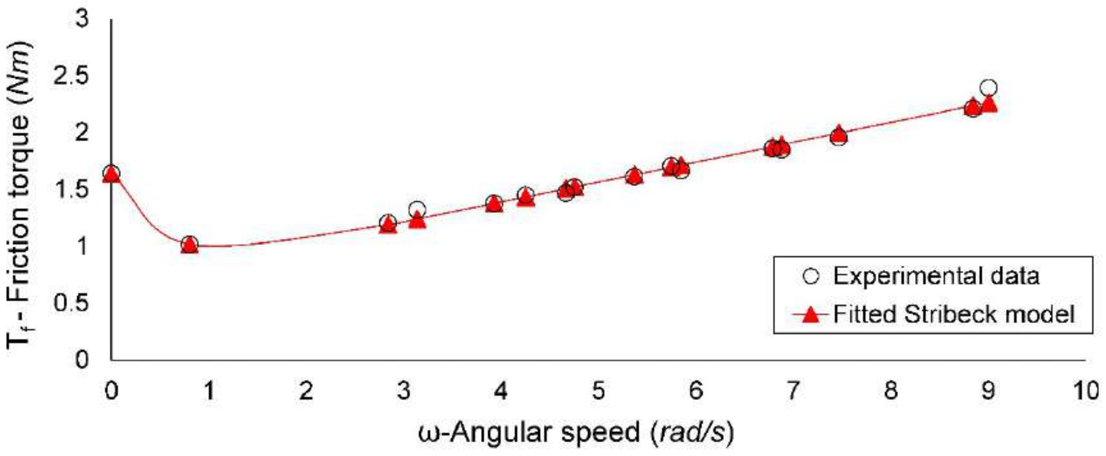

Figure 11 Stribeck friction torque model for CCW direction

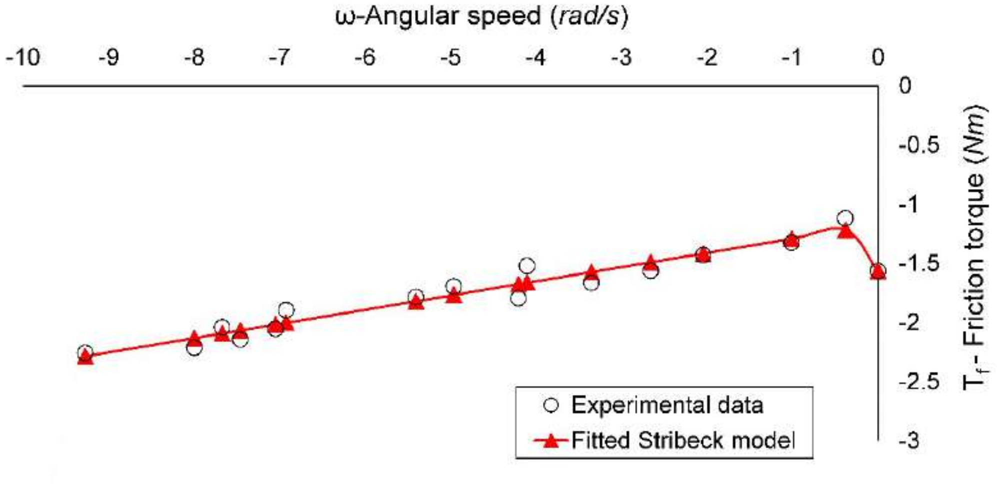

Figure 12 Stribeck friction torque model for CW direction

Acknowledgement

The authors would like to thank the reviewers for all useful and instructive comments on the paper.

Funding

This study was funded by Çukurova University-ÖYP coordination.

The Declaration of Conflict of Interest/ Common Interest

The authors do not have any conflict of interest or common interest with any institution or person that they know that could affect their work.

Authors' Contribution

MD: Literature review, research, methodology, simulation, writing the initial draft.

MİS: Supervision, research, methodology, interpretation, writing-revision, and finalizing.

The Declaration of Ethics Committee Approval

The authors declare that this work does not require an ethics committee approval or any special permission.

The Declaration of Research and Publication Ethics

The authors of the paper declare that they comply with the scientific, ethical and quotation rules of SAUJS in all processes of the paper and that they do not make any falsification on the data collected. In addition, they declare that Sakarya University Journal of Science and its editorial board have no responsibility for any ethical violations that may be encountered, and that this study has not been evaluated in any academic publication environment other than Sakarya University Journal of Science.

REFERENCES

[1] E. Richer and Y. Hurmuzlu, “A High Performance Pneumatic Force Actuator System: Part I—Nonlinear Mathematical Model,” Journal of Dynamic Systems, Measurement, and Control, vol. 122, no. 3, pp. 416–425, 1999.

[2] A.Harnoy and B. Friedland, “Modelling and Measuring Friction Effects,” IEEE Control Systems, pp. 82-91, 2008.

[3] H. Olsson, K. Åström, C. C. D. Wit, M. Gäfvert, and P. Lischinsky, “Friction Models and Friction Compensation,” European Journal of Control, vol. 4, no. 3, pp. 176–195, 1998.

[4] Y. F. Liu, J. Li, Z. M. Zhang, X. H. Hu, and W. J. Zhang, "Experimental Comparison of Five Friction Models on the Same Test-Bed of the Micro Stick-Slip Motion System," Mechanical Sciences, vol. 6, no. 1, pp. 15–28, 2015.

[5] C. C. D. Wit, H. Olsson, K. Astrom, and P. Lischinsky, "A new model for control of systems with friction," IEEE Transactions on Automatic Control, vol. 40, no. 3, pp. 419–425, 1995.

[6] G. Belforte, G. Mattiazzo, S. Mauro, and L. R. Tokashiki, "Measurement of friction force in pneumatic cylinders," Tribotest, vol. 10, no. 1, pp. 33–48, 2003.

[7] P.L.Andrighetto, A.C.Valdiero and L.Carlotto, "Study of the Friction Behavior in Industrial Pneumatic Actuators," ABCM Symposium Series in Mechatronics, vol. 2, pp. 369-376, 2006.

[8] H.Kosari, S.A.A.Moosavian, "Friction Compensation in a Pneumatic Actuator Using Recursive Least Square Algorithm," 5th Australian Control Conference (AUCC), Austalia, pp. 81-86, 2015.

[9] G. Belforte and T. Raparelli, "Friction Analysis of Pneumatic Semi-Rotary Actuators," Tribology Transactions, vol. 40, no. 1, pp. 57–62, 1997.

[10] M. S. Schlüter and E. A. Perondi, "Mathematical Modeling of Pneumatic Semi-Rotary Actuator with Friction," Journal of the Brazilian Society of Mechanical Sciences and Engineering, vol. 40, no. 11, 2018.

[11] M. S. Schlüter and E. A. Perondi, "Mathematical Modelling with Friction of a SCARA Robot Driven by Pneumatic Semi-Rotary Atuators," IEEE Latin America Transactions, vol.18, no. 6, pp. 1066-1076, 2020.

[12] X. Luo, J.Wang, L.Shpanian, N.Jia, G.Liu, A.S.I. Zinober, "Development of a Mathematical Model for Vane Type Air Motors with Arbitrary N Vanes," Proceedings of the World Congress on Engineering (WCE 2008), London, 2008.

[13] M. Sorli, L. Gastaldi, E. Codina, and S. D. L. Heras, "Dynamic Analysis of Pneumatic Actuators," Simulation Practice and Theory, vol. 7, no. 5-6, pp. 589–602, 1999.

[14] C.-C. Lan and C.-W. Cheng, "Modeling and design of air vane motors for minimal torque ripples," 2010 IEEE/ASME International Conference on Advanced Intelligent Mechatronics, 2010.

[15] Y. Zhang, K. Li, S.Wei and G. Wang, "Pneumatic rotary actuator position servo system based on ADE-PD control," Applied Sciences, vol. 8, no. 406, 2018.

SAKARYA ÜNİVERSİTESİ
FEN BİLİMLERİ ENSTİTÜSÜ
DERGİSİ

Sakarya University Journal of Science
SAUJS
e-ISSN 2147-835X | Period Bimonthly | Founded: 1997 | Publisher Sakarya University |
http://www.saujs.sakarya.edu.tr/en/

Title: Surface Improvement of Low Carbon Steels (St37) by Duplex Treatments

Authors: Yıldız YARALI ÖZBEK

Recieved: 2019-11-28 16:18:48

Accepted: 2020-09-21 22:05:43

Article Type: Research Article

Volume: 24
Issue: 6
Month: December
Year: 2020
Pages: 1284-1293

How to cite
Yıldız YARALI ÖZBEK; (2020), Surface Improvement of Low Carbon Steels (St37) by Duplex Treatments. Sakarya University Journal of Science, 24(6), 1284-1293, DOI: https://doi.org/10.16984/saufenbilder.652456

Sakarya University Journal of Science 24(6), 1284-1293, 2020

Surface Improvement of Low Carbon Steels (St37) by Duplex Treatments

Yıldız YARALI ÖZBEK*[1]

Abstract

The aim of this work was seen to effect to duplex treatment on steel surface. Firstly, arc spray and secondly pulse plasma treatment were applied to sample surface. The influence of these duplex process and process parameters want to see on surface. Swm Inox 446-TW wire was used in arc spray process. Then the pulse plasma process was applied to surface. The different distances and number of pulse were used as the pulse plasma treatment. After duplex treatments, the samples were characterized by using OM (optical micrograph), scanning electron microscopy (SEM-EDS). X-ray diffractometer (XRD) analyses and microhardness tests were applied. The surface roughness of samples was measured with 3D-roughness device. The microhardness values of treated surfaces are about four times higher than that of un-treated surfaces. After duplex treatments, the improved performance of surface the St 37 steel was presented.

Key words: surface, steel, duplex treatment, arc, pulse plasma

1. INTRODUCTION

The arc thermal spraying has been effective in long-term anticorrosion and wear properties of the steel structures in the aggressive conditions [1-4]. Especially, the wear failure of the samples begins mostly on the surface or subsurface. The coating to the surfaces of a component can effectively decrease wear. So, the component's service life of sample was improve [2]. The arc spraying yields production of the coatings with good bonding strength and a low degree of porosity. Arc Spray is the most economical and efficient of all thermal spray coating systems [4].

The wire are melted. The melted metal is atomized into molten micro-droplets using compressed air, and the droplets are sprayed onto a surface. Arc Spray has two conductive wires: one positive and the other negative. These energized wires are raised through a feeder into a gun head. It is at the gun head that the wires compensated and arc against each other, thus formed molten material [5,7].

The dry compressed air transferred to the arc zone, atomizing the molten material into small droplets while also pushing them toward the prepared part. The droplets hit to the work piece or part, and flatten out and make splats [2]. The splats connect one on top of another to create an extremely intense mechanical bond. An air stream the back of the gun atomizes and propels the molten particles towards a

---

* Corresponding Author: yyarali@sakarya.edu.tr

[1] Sakarya University, Department of Metallurgy and Materials Engineering
ORCID: https://orcid.org/0000-0001-9198-4612

prepared surface. The regulable parameters including voltage and amperage arc temperatures can reach 5000° C, enough to melt any material, simultaneously the part surface continue cool. All of the entry energy is used to melt the spray materials. So, the arc spray is considered as an energy efficient process [3]. Only the porosities are problem in this system.

the pulse plasma process is another technique used to devolope the surface properties of the steel surface [6]. The pulse treatment distributed to surface, the near surface layer of the target pass on a rapid melt and solidification with heating and cooling rates from 10^7 to 10^{10} K/s. These rates can supported mixing, rapid diffusion, and the formation of amorphous surface on sample. Therefore, the mechanical properties of material surfaces can be increased [8-10].

The surfaces of the samples were subjected to pulse detonation process accompanied under a plasma atmosphere containing alloying elements dissolved from the metal electrode rod in interaction with the constituents of propane and nitrogen gases used for the process. The tungsten was chosen as consumable electrode in this work. This process provided the workpiece surfaces with alloying of plasma components and hardening of surfaces [1,4].

The Duplex process was applied to sample surface to develop the surface properties [8]. The purpose of the present paper is to investigate the effect of the duplex coatings prepared with an arc spray process and pulse plasma technique. The aim of the study is to decrease the amount of the pores after duplex trearment. We want to see the effect of process and parameters. There were some porosite on surface coated by arc spray process. The pulse plasma process may solve porosite problem.

The optic and SEM micrograph were taken from cross-section of samples. XRD, EDS analyses were applied. The microhardness were taken from surface by microhardness apparatus. The surface roughness was measure 3D- roughness device.

2. EXPERIMENTAL PROCEDURE

St37 steel was chosen as the substrate material for the surface modification, because it is cost-effective and commonly used in industrial applications. The chemical composition of the St37 steel was given in Table 1. The diameter of the cylindrical samples was 22 mm, and their thickness was10 mm. They were machined with a CNC lathe. The machined samples were not subjected to any heat treatment prior to duplex treatment.

The sand blasting process was applied to sample surface. The SWM INOX 446-TW wire of about 2 mm in diameter was used in the arc spraying material. The chemical composition of arc wire used in arc spray process was given in Table 2.

The process parameters that were applied to the machined samples were presented in Table 3.

After the arc spray process, all samples were exposed to pulse plasma treatment. The arc spray process parameters were given in Table 3.

Table 1
The chemical spectrum of the ST 37 steel

	(%wt.)			
Steel	C	P	S	N
St37	≤ 0,17	0,035	0,04	0,009

Table 2
The chemical composition of the arc wire

Wire (%wt)	**%C**	**%Cr**	**%Mn**	**%Si**
SWM INOX 446-TW	0.3	13.0	1.0	1.0

Table 3

Parameters of arc spraying

Technological parameters	**Value of parameters**
Arc voltage (V)	34
Arc current (A)	150
Atomizing gas pressure (MPa)	0.6 ± 0.1
Spraying distance (mm)	150 ± 20
Feed voltage (V)	100

2.1 Pulse plasma system

Fig.1.shows the schematic of the pulse plasma process. The pulse plasmatron formed in a detonation chamber where the fuel gas mixture is occurred and its detonation combustion is initiated, a central electrode-anode, a conical electrode-cathode, inter-electrode gap

(4), a consumable electrode (*5)* and a power supply (*6)* [3].

At the beginning of the detonation the ionized combustion products were fed from detonation chamber (*1)* to the inter-electrode gap (*4)* in order to fulfil the electric circuit. This led to formation of conducting layer (*7)* formed by the combustion products under the effect of gas-dynamic and electromagnetic forces. The consumable metal rod (*5)* was fixed in a position along the axis of central electrode. The end of the rod was evaporated during heating and enabled alloying elements to be introduced into the plasma jet. After the samples were ejected from the plasmatron, plasma jet (*8)* had broken the circuit between the anode electrode and the cathode work piece (*9*). The current flowing through the jet the plasma was heated due to Joulean heat [1,3]. The pulse plasma process parameters were given in Table 4. The tungsten electrode was used for pulse plasma treatment

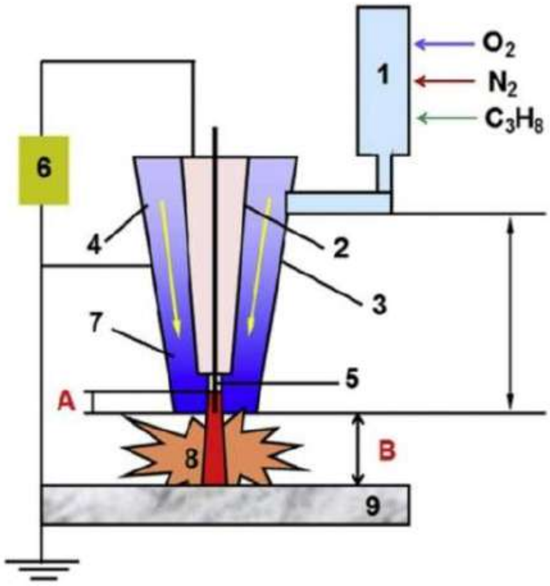

Figure 1 Schematic presentation of the pulsed-plasma modification system

The microstructure of the coatings was examined using an optical and scanning electron microscope (Leica and Jeol) equipped with energy dispersive spectroscopy. The phase composition of the duplex layer was determined by means of X-ray diffraction (XRD; Rigaku 6600) with Cu-Kα radiation (λ = 1.54 Å) operated at 40 kV, 40 mA and with steps of 0.02°. The microhardness test was carried out on the cross-section of the coating (Leica-1000TC) under a load of 10gr. The hardness value was calculated from the average of 5 measurements for each sample to ensure the data repeatability. The roughness of coated surface was measured with 3D profilometer.

Table 4
The process parameters of pulse plasma treatment

Sample No	***Nozzle distance (mm)***	***Number of pulse***	***Electrode***	***Battery capacity (mf)***
1	*50*	*4*	*W*	*800*
2	*50*	*8*	*W*	*800*
3	*50*	*12*	*W*	*800*
4	*60*	*4*	*W*	*800*
5	*60*	*8*	*W*	*800*
6	*60*	*12*	*W*	*800*
7	*70*	*4*	*W*	*800*
8	*70*	*8*	*W*	*800*
9	*70*	*12*	*W*	*800*
10	*80*	*4*	*W*	*800*
11	*80*	*8*	*W*	*800*
12	*80*	*12*	*W*	*800*

Nozzle distance (mm); distance of between sample-nozzle
Pulse number: number of shots (pulse)
Consumable electrode: tungsten

3. Results and Discussion

The optic micrograph of samples 1, 2 and 3 were shown in Fig.2. The cross-sectional microstructure images revealed that the as-sprayed coatings were densely deposited into a lamellar structure with porosity. The structure was homogeneous. The nature of the arc spray has been created some pores The interfacial defect was shown at 2–4%. High temperatures and high velocities of the unmelted particle usually form the important droplet deformation on impact at a sample surface [6]. The formation of pores is closely associated with large unmelted particles. So, a relatively broad range of microhardness was obtained due to the rough surface morphology resulting from pore defects. But we have applied pulse plasma process in addition to arc spray. So the amount of porosity decreased after pulse plasma process [5]. We can see the three phases in optic micrograph. The layer was composed of : the light gray metal matrix, medium gray metal oxides, and black void spaces [3,6].

The solidified droplets establish rapidly, as a continuous stream of completely melted particles' impact to form continuous solidified layers. However, the sprayed particles from the nozzle actually reach the substrate in fully melted and semi-melted conditions because of the use of wires as a feedstock material produces different sized particles by the nonuniform heating. When the particles are not fully melted or do not have enough high rate velocity until the collision with the substrate, the particles cannot fully fill the void in the coating and pores are formed.

The SEM micrograph of the all samples were seen in Fig.3. The duplex coating structure was shown from the cross-section. Pulse plasma layer was seen on top of the coated layer (Fig.3a-b-c). The very small pores were seen in the coated layer. The thickness of layer modificated by pulse plasma is thinner than the layer coated by arc spray plasma.

The amount of the oxides (thin grey lamella) in the coating, which were identified by EDS. This indicates that the grey areas in Fig.3a were oxides of Fe or Cr. This was consistent with the XRD results and the oxygen content (analyzed by Oxygen, Nitrogen Analyzer), suggesting the severe oxidation of the coating during the spraying process.

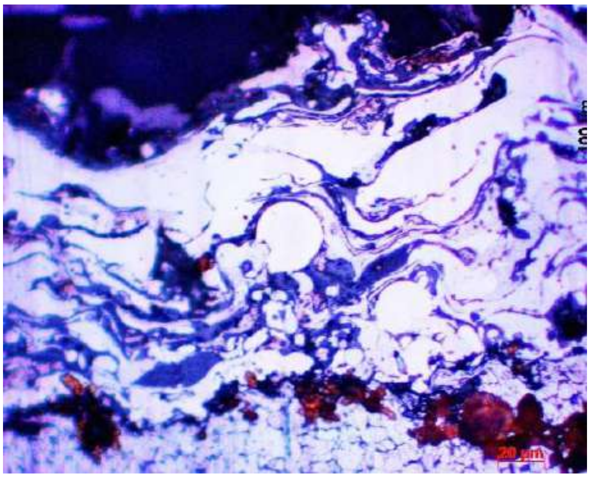

a)

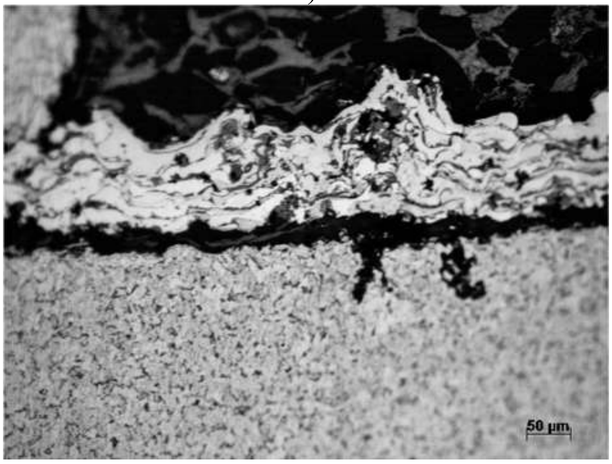

b)

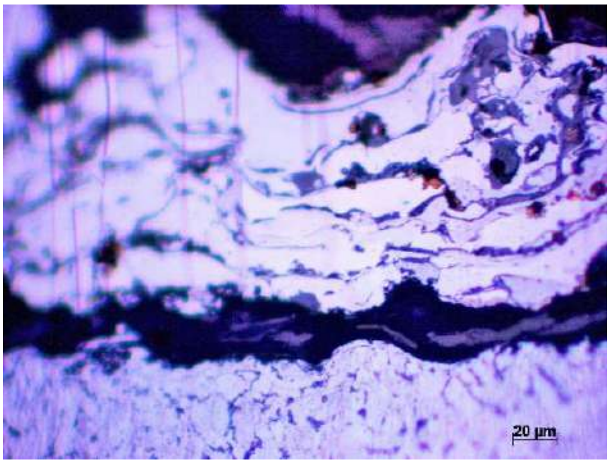

c)

Figure 2 The optic micrograph a) sample 1, b)sample 2, c) sample3

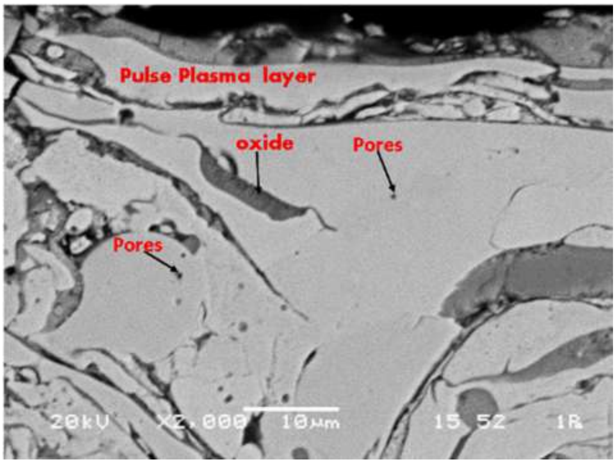

a)

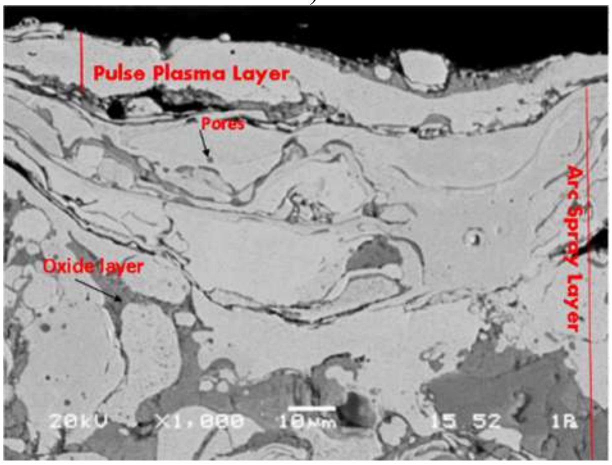

b)

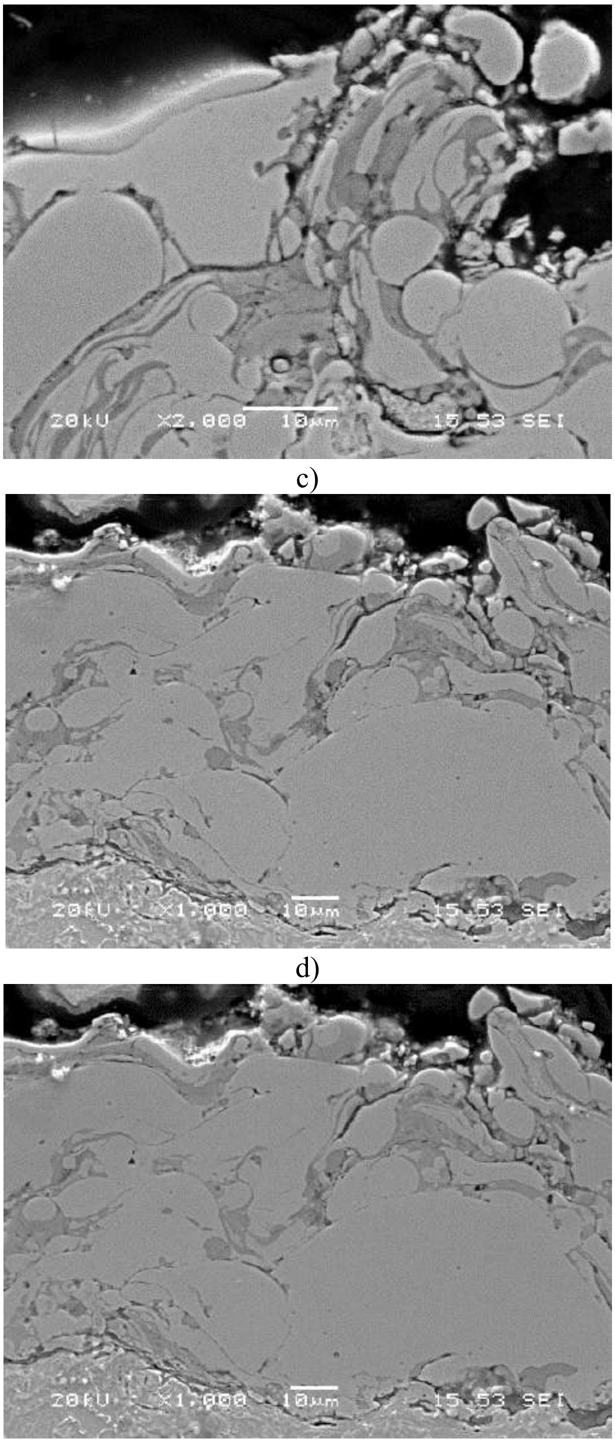

c)

d)

e)

Figure 3 The SEM micrograph of samples a) sample 2, b) sample 3, c)sample 4, d)sample 5, e)sample6

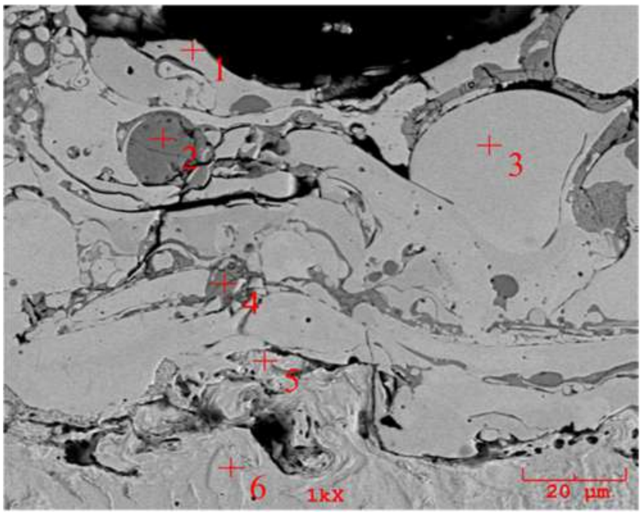

a)

%Wt.	1	2	3	4	5	6
O	5.524	32.769	4.335	27.632	0.612	0
Cr	27.218	12.213	32.983	44.370	1.771	0.240
Fe	67.258	55.018	62.682	27.998	97.617	99.760

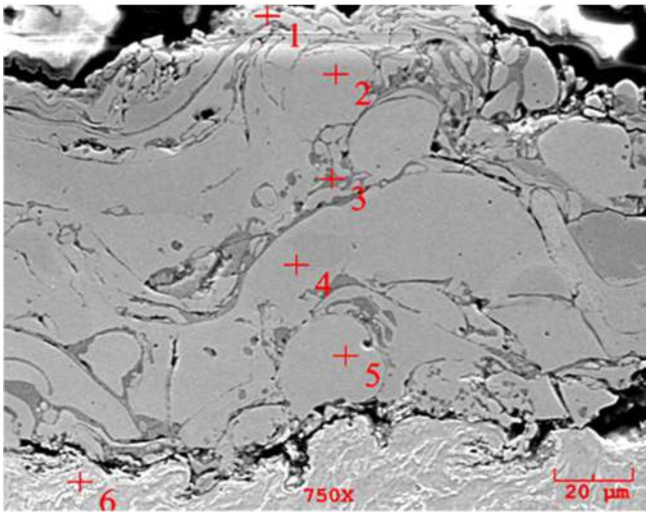

b)

%Wt	1	2	3	4	5	6
N	2.093	0.459	0.680	1.214	0.482	0
O	5.916	0	30.307	6.200	0	0
Cr	40.402	27.085	36.724	48.284	29.086	0.388
Fe	48.969	71.258	30.597	43.013	68.459	99.028
W	2.620	1.198	1.693	0.983	1.972	0

Figure 4 The EDS analyses of sample a) arc spray,b)arc spray+pulse plasma proces (duplex treatment)

The Fig.4a shows the EDS analyses applied sample of arc spray and Fig.4b shows sample of duplex (arc spray+pulse plasma) process. The duplex treatment was changing the structure of the coating layer. The nitride and tungsten were seen on the surface after duplex treatment (Fig.4b). The chromium wire was used duration arc spray. The tungsten consumable electrode and nitride gases were used in pulse plasma process. So, these elements have emerged with the duplex process [5].

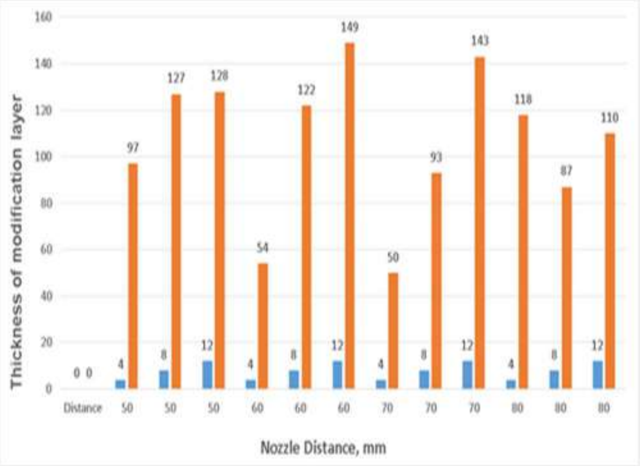

Figure 5 The changing of thickness of coating layer to pulse plasma parameters

After the pulse plasma process, the thickness of then coating layer was measured. The process parameters were effected the thickness of the coating layer (Fig.5). With the increase of the number of pulse, the thickness of coating layer was increased. The nozzle distance was affected to thickness of coating. The focusing problem was occurred in system, ionization gases was randomly dispersed to surface. So the thickness of the modified layer was not compatible with process parameters. However manual optimization in the pulse plasma system could be formed inhomogeneities to surface properties.

The roughness is very changing by arc spray (Fig.6a) and then pulse plasma process applied to surface (Fig.6b). The Ra value was changed from 8.79 to 10.9 (The Ra; arithmetic average deviation). The roughness was increased after duplex treatment. Because of the heat is high. The heat was led to the melting of some areas at the surface. However, changing the heat of the surface was increased the roughness [7].

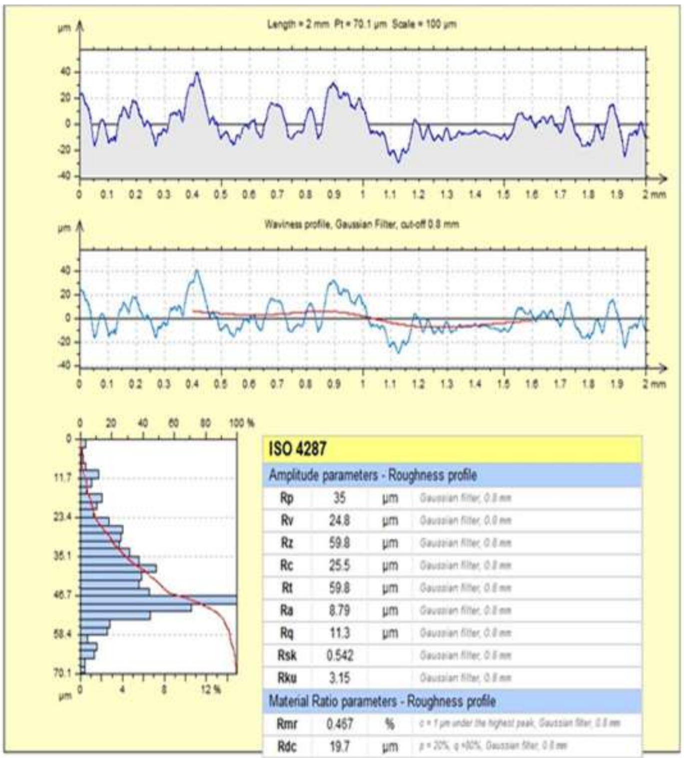

ISO 4287			
Amplitude parameters - Roughness profile			
Rp	35	µm	Gaussian filter, 0.8 mm
Rv	24.8	µm	Gaussian filter, 0.8 mm
Rz	59.8	µm	Gaussian filter, 0.8 mm
Rc	25.5	µm	Gaussian filter, 0.8 mm
Rt	59.8	µm	Gaussian filter, 0.8 mm
Ra	8.79	µm	Gaussian filter, 0.8 mm
Rq	11.3	µm	Gaussian filter, 0.8 mm
Rsk	0.542		Gaussian filter, 0.8 mm
Rku	3.15		Gaussian filter, 0.8 mm
Material Ratio parameters - Roughness profile			
Rmr	0.467	%	c = 1 µm under the highest peak, Gaussian filter, 0.8 mm
Rdc	19.7	µm	p = 20%, q =80%, Gaussian filter, 0.8 mm

a)

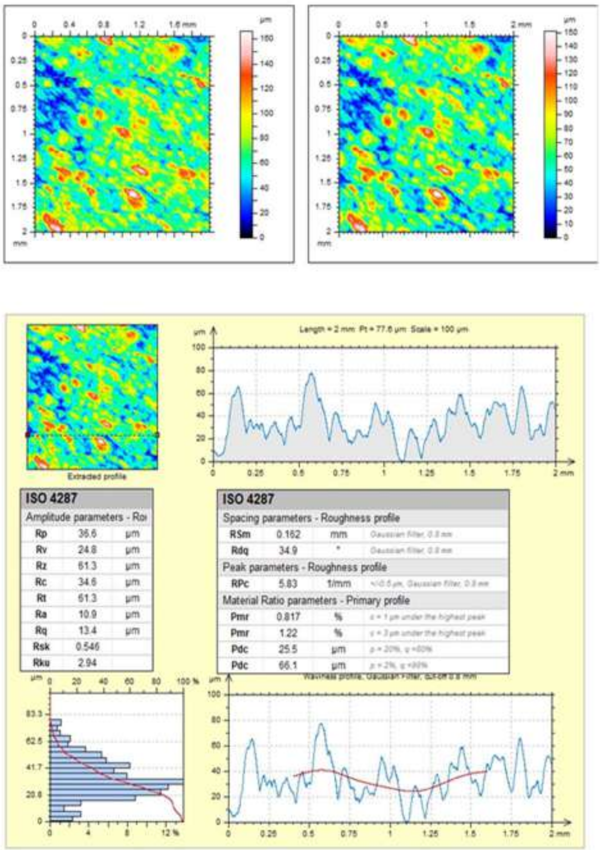

ISO 4287		
Amplitude parameters - Ro		
Rp	36.6	µm
Rv	24.8	µm
Rz	61.3	µm
Rc	34.6	µm
Rt	61.3	µm
Ra	10.9	µm
Rq	13.4	µm
Rsk	0.546	
Rku	2.94	

ISO 4287			
Spacing parameters - Roughness profile			
RSm	0.162	mm	Gaussian filter, 0.8 mm
Rdq	34.9	°	Gaussian filter, 0.8 mm
Peak parameters - Roughness profile			
RPc	5.83	1/mm	+/-0.5 µm, Gaussian filter, 0.8 mm
Material Ratio parameters - Primary profile			
Pmr	0.817	%	c = 1 µm under the highest peak
Pmr	1.22	%	c = 3 µm under the highest peak
Pdc	25.5	µm	p = 20%, q =80%
Pdc	66.1	µm	p = 2%, q =80%

b)

Figure 6 The surface roughness 3D a) arc spray, b) duplex process (arc spray +pulse plasma)

XRD pattern of the samples after duplex treatment is shown in Fig. 7(a-b). substantial phase of the coating is the crystalline phase of α-Fe. The new hard phases were obtained after duplex treatment. Before duplex treatment, there was only α-Fe phase in steel structure, but after duplex treatment new phases such as FeN, W_3O, γ-Fe were formed [8-16].

The coating layer was composed of the amorphous and crystalline structure. The Fig.7b show that the crystalline phase was established in the amorphous matrix. The formation of an amorphous alloy structure requires the high cooling rates. During pulse plasma process, the cooling rate is 10^5 K/s, which is suitable for forming an amorphous phase. W (consumable electrode) can develop the glass forming ability of the coating as a consequence of their additive to the large atom and large negative heat mixing among the constituent elements [7,9,14].

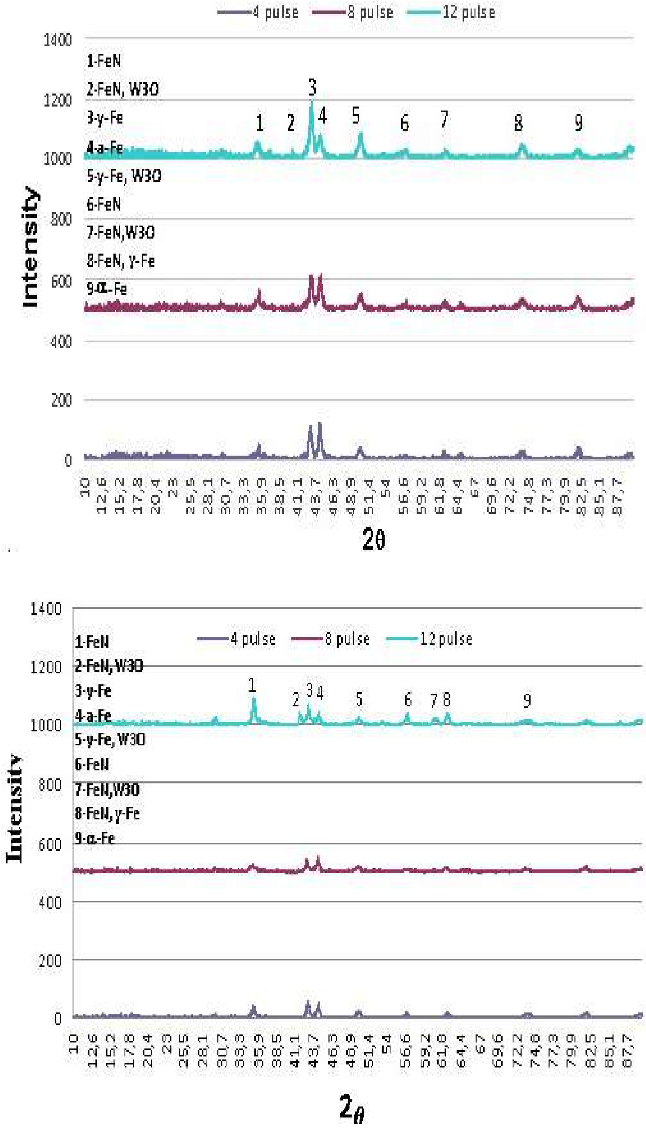

Figure 7 The XRD analyses of sample a) sample 4,5 and 6, b)sample 10,11 and 12

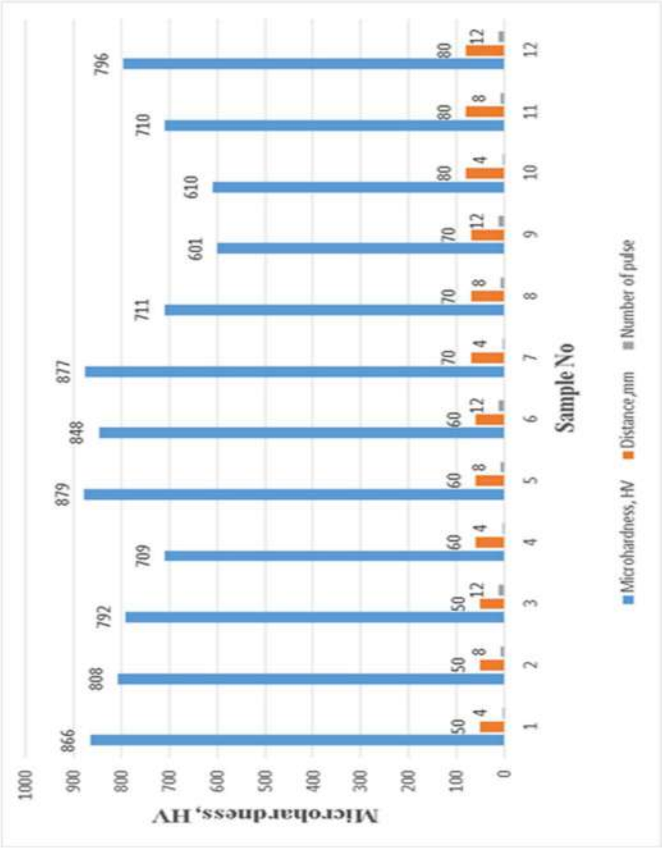

Figure 8 The microhardness values of samples

Fig.8 shows the change of the hardness values after duplex treatment. The hardness of the substrate metal was measured as 180 HV. After the arc spray the hardness values increased up to 400-500HV. The microhardness values were changed with pulse plasma process. The parameters of pulse plasma treatment affected the values of the surface hardness. It can be observed that the hardness values of surface decrease by increasing the spraying distance, presenting maximum values of 879 HV at the spraying distance of 60 mm. When the number of pulse increased, the hardness was increased [13-16]. The amount of ionization gases was increased by increasing the number of pulse. The hardness of modified samples gradually decreases due to the alloy concentration near the core, resulting in a diffused case–core interface. The high cooling rate and solidification of surface melting material could produce very fine microstructure. The microstructure of treated surface will become finer with increasing the number of pulses [16,11].

The surface layer consists of a composed of sub-grains with many defects, such as dislocations and grain boundaries that can be formed using the pulse plasma method. The nanostructured surface layer of the St37 steel significantly promotes the nitrogen diffusion process when many pulses are used, resulting in the formation of new hard phases [14,15,17,18]. The new hard phases were increased the surface hardness [15,16]. The nozzle distance was effected the microhardness values.

In addition, the hard phases and new structure improved the surface hardness [5,12]. Not only the St37 steel but also M2 steel hardness values were increased after the pulse plasma treatment [17].

4.CONCLUSION

In this work, the effect of duplex process on the hardness and microstructure of the samples was studied. Two step process namely the arc spray and then the pulse plasma treatment were applied to surface. The duplex treatment was improved to sample surface. The gradient coating layer was formed on surface layer after duplex treatment.

1) The layer was composed of (i)light gray metal matrix, (ii) medium gray metal oxides, and (iii) black void spaces in arc spray treatment. The white layer occurred on the top layer after pulse plasma treatment.
2) The duplex treatment was increased the surface roughness. The arc spray was caused porosity and low density, but the pulse plasma was covered porosities. The porosity problem was overcome by duplex treatment.
3) The arc spray was caused the partial melting of the surface. The pulse plasma covered the melted area.
4) In the pulse plasma process, rapid heating-cooling and diffusion lead to a change in the surface structure. This new structure improved the mechanical properties of the steel.
5) The consumable electrode (W) causes the ionization of Tungsten (W) and Nitrogen (N) atoms. These atoms are doped into the surface by means of diffusion mechanism.
6) The process parameters, such as the nozzle distance and the number of pulses, were need to be adjusted to improve and change the mechanical properties of the surface. The thickness of the modified layer increased with increasing number of pulses at the optimum nozzle distance.
7) The surface process for the St37 steel produced a surface layer with more favourable properties. New phases formed on the modified surface due to the pulse plasma treatment. tungsten and nitride-rich phases were formed: FeN, W_3O, and γ-Fe. These phases play a key role in developing the increased surface hardness.
8) The duplex treatment was contributed to the mechanical properties. The hardness values of the specimens that were exposed to the treatment were 4 to 6 times greater than the untreated specimens. When only arc spray was applied, the hardness was increased 3 times, whereas the duplex treatment (arc spray+pulse plasma) yields increased hardness up to 4-6 times more than that of the bare steel substrate.

Acknowledgments

The author would like to thank SARGEM for supporting in experimental studies. It also expresses its gratitude and thanks to the valuable referees who spent their valuable time in the review of the article.

Funding

The author received no financial support for the research, authorship or publication of this study.

The Declaration of Conflict of Interest/ Common Interest

No conflict of interest or common interest has been declared by the author.

The Declaration of Ethics Committee Approval

This work does not require ethics committee permission or any special permission.

The Declaration of Research and Publication Ethics

The author of the paper declares that she complies with the scientific, ethical and quotation rules of SAUJS in all processes of the paper and that she does not make any falsification on the data collected. In addition, she declares that Sakarya University Journal of Science and its editorial board have no responsibility for any ethical violations that may be encountered, and that this study has not been evaluated in any academic publication environment other than Sakarya University Journal of Science."

REFERENCES

[1] H. Tian, C. Wang, M. Guo, Z. Tang, "Tribological behaviour of a self-lubricated GO/WC–12Co thermal spray coating", Surface Engineering, vol. 353, pp 237-246, 2018.

[2] W. Tillmann, L. Hagen, D. Kokalj, "Embedment of eutectic tungsten carbides in arc sprayed steel"Surface and Coatings Technology, vol. 331, pp. 153-162, 2017.

[3] S.Salavati, T.W.Coyle, J.Mostaghimi, "Twin wire arc spray process modification for production of porous metallic coatings", vol. 286, pp. 1-396, 2016.

[4] B. Podgornik, F. Majdic, V. Leskovsek, J. Vizintin, "Improving tribological properties of tool steels through combination of deep-cryogenic treatment and plasma nitriding", Wear, vol. 288, pp. 88–93, 2012.

[5] Y.Y.Özbek, M.Durman, H.Akbulut,"Wear Behaviour of Steel Modıfied by Pulse Plasma Technıque", Tribology Transaction, vol. 52, pp. 213–222, 2009.

[6] http://www.thermioninc.com/

[7] http://www.mbicoatings.com

[8] X. Zhang, Z. Wang, J. Lin, Z. Zhou, "A study on high temperature oxidation behavior of high-velocity arc sprayed Fe-based coatings" Surface and Coatings Technology, vol. 283, pp. 255-261, 2015.

[9] Y.Y.Özbek, H.Akbulut, "M.Durman, Surface properties of M2 steel treated by pulse plasma technique", Vacuum, vol.122, pp. 90-95,2015.

[10] J. Piekoszewski, Z.Werner, W.Szymczyk, "Application of high intensity pulsed ion and plasma beams in modification of materials", Vacuum, vol. 63, pp. 475-481, 2001.

[11] V.V. Uglov, V.M. Anishchik, N.N. Cherenda, Y.V.Sveshnikov, V.M. Astashynski, E.A. Kostyukevich, A.M. Kuzmitski, V.V. Askerko, "The formation of a tungsten containing surface layer in a carbon steel by compression plasma flow",Surface & Coatings Technology, vol. 202, pp. 2439–2442, 2008.

[12] M.F. Yana, Y.Q. Wua, R.L. Li, "Grain and grain boundary characters in surface layer of untreated and plasma nitrocarburized 18Ni maraging steel with nanocrystalline structure", Applied Surface Science, 273, pp. 520–526, 2013.

[13] B. Podgornik, S. Hogmark, O. Sandberg, V. Leskovsek, "Wear resistance and anti-sticking properties of duplex treated forming tool steel", Wear vol. 254, pp. 1113–1121, 2003.

[14] N.Y,Tyurin, O.V, Kolısnıchenko, N.G, Tsygankov," The Pulse Plasma Technology", The Paton Welding Journal, vol. 1, pp. 38-43, 2004.

[15] J. Langnera, J. Piekoszewskia, Z. Wernera, U, V.I. Tereshin, V.V. Chebotarev, I. Garkusha, L. Wali´s, B. Sartowska, W. Starosta, W. Szymczyk, M. Kopcewicz, A. Grabias, "Surface modification of constructional steels by irradiation with high intensity pulsed nitrogen plasma beams", Surface and Coatings Technology, vol. 128-129, pp. 105-111, 2000.

[16] M. Ulutan, O. N. Celik, H. Gasan, U. Er, "Effect of different surface treatment methods on the friction and wear behavior of AISI 4140 steel", J. Mater. Sci. Technol, vol. 26, pp. 251-257, 2010.

[17] Y.Y. Ozbek, C. Sarioglu, M.Durman," The effect of plasma detonation parameters on residual stresses developed in the plasma

modified layer", Vacuum, vol. 106, pp. 11-15, 2014.

[18] Q.F. Guana, H. Zoua, G.T. Zoua, A.M. Wub, S.Z. Haob, J.X. Zoub, Y. Qinb, C. Dongb, Q.Y. Zhang, "Surface nanostructure and amorphous state of a low carbon steel induced by high-current pulsed electron beam", Surface & Coatings Technology, vol. 196, pp. 145– 149, 2005.

SAKARYA ÜNİVERSİTESİ
FEN BİLİMLERİ ENSTİTÜSÜ
DERGİSİ

Sakarya University Journal of Science
SAUJS

e-ISSN 2147-835X | Period Bimonthly | Founded: 1997 | Publisher Sakarya University |
http://www.saujs.sakarya.edu.tr/en/

Title: A Sentiment Analysis Model for Terrorist Attacks Reviews on Twitter

Authors: Ibrahim A. FADEL, Cemil ÖZ

Recieved: 2020-03-31 05:27:09

Accepted: 2020-09-22 13:00:33

Article Type: Research Article

Volume: 24
Issue: 6
Month: December
Year: 2020
Pages: 1294-1302

How to cite
Ibrahim A. FADEL, Cemil ÖZ; (2020), A Sentiment Analysis Model for Terrorist Attacks Reviews on Twitter . Sakarya University Journal of Science, 24(6), 1294-1302, DOI: https://doi.org/10.16984/saufenbilder.711612
Access link
http://www.saujs.sakarya.edu.tr/en/pub/issue/57766/711612

Sakarya University Journal of Science 24(6), 1294-1302, 2020

A Sentiment Analysis Model for Terrorist Attacks Reviews on Twitter

Ibrahim A. FADEL*[1], Cemil ÖZ[2]

Abstract

Twitter is considered as one of the famous microblogs that attract politicians and individuals to express their views on political, economic and social issues. The phenomenon of terrorist operations is one of the largest security and economic problem facing the world in recent years. Twitter users' comments on terrorism issues are important to understand users' sentiment about terrorist events. Sentiment analysis is a field of research for understanding and extracting users' views. In this paper, we propose a model for automatically classifying users' reviews on Twitter after occurrence of a terrorist attack, the model is built using lexicon and machine learning approaches. Lexicon approach is used to create labelled training dataset while machine learning approach was used to build the model. Scores of some domain related words were neutralized to avoid their negative effect. Features were selected based on PoS. Majority voting between NB, SVM and LR machine learning classification algorithms was applied. The performance of classification algorithms was measured using accuracy and F1 scores. The results obtained are compared to identify the best classification algorithm for features selection. Result show that our model achieved 94.8% accuracy with 95.9% F1 score.

Keywords: Sentiment Analysis, Machine Learning, lexicon-based approach, Terrorist mining.

1. INTRODUCTION

The phenomenon of terrorism has become a distinctive feature of this century. Terrorist groups have changed from their traditional ways of communicating and have increasingly adapted the use of internet and social media platforms [1] for propaganda, financing, training, planning, executing cyberattacks, and recruiting new members and followers [2].

In order to prevent future terrorist attacks, law enforcement and intelligence agencies have

---

[*] Corresponding Author: ibrahim.fadel@ogr.sakarya.edu.tr

[1] Sakarya University, ORCID: https://orcid.org/0000-0003-4726-7805

[2] Sakarya University, E-Mail: coz@sakarya.edu.tr ORCID: https://orcid.org/0000-0001-9742-6021

adopted the use of computer technologies to develop effective deterrent strategies. Group detection, link prediction and Key-Player Identification are among the mostly used strategies [3]. However, growing use of sentiment analysis and opinion mining affirms the adoption of these techniques in detecting terrorist groups and their activities on social media platforms [4]–[6].

Sentiment Analysis (SA), also known as opinion mining, is a challenging Text Mining and Natural Language Processing (NLP) problem. It deals with deriving sentiments and opinions from people's attitudes and emotions about events, topics and their attributes [7] to detect user's feelings, reactions and beliefs [8]. Most of the research work in this area focus on classifying texts according to their sentiment polarity, which can be positive, negative or neutral.

Sentiment classification techniques can be traditionally done in two ways: Machine learning (ML) approach and lexicon-based approach. However, a hybrid of both approaches has also been used. The ML approaches apply the famous ML algorithms and uses linguistic features. Lexicon-based approach is dependent on the collection of known and precompiled sentiments and terms [9],[10].

In this study we combine ML and lexicon approaches to build a model for automatically detecting terrorist sympathizers on twitter from their comments that are posted immediately after occurrence of a terrorist attack to express their feelings and opinions after their success in carrying out a terrorist attack. About one hundred thousand tweets after nine terrorist attacks in different countries across the globe was collected. Verb, adjective, and a combination of verb and adjective Part-of-Speech (PoS) types was used on selection features. Classification in the model employs majority voting (MV) between 3 different ML algorithms to determine tweet polarity.

The rest of the paper is outlined as follows. Section 2 presents related works that have been done in the area. Section 3 covers details of the proposed work including the pre-processing, labelling and classifying. Section 4 presents experiments and the results obtained. The conclusion and future works are presented in Section 5.

2. RELATED WORK

The increasing use of internet and social media by terrorist groups to disseminate their ideologies and attracting individuals has prompted researchers to analyze text using sentiment analysis approaches to detect terrorists. Text containing terrorism content on social media and internet exist in different forms. To detect this content lots of data is collected to build a dataset using different search terms. For example (Ashcrof et al.) [11] used terrorist groups' tweets to detect new terrorist supporters. They used AdaBoost, Naive Bayes (NB), and Support Vector Machines (SVM) machine learning algorithms to automatically classify tweets that were released by jihadist groups on Twitter as radical or non-radical. Three different datasets were used such as: TW-PRO consist of tweets of known Jihadist sympathizers, TW-CON containing tweets from accounts that were talking or against Islamic State of Iraq and Syria (ISIS) and TW-RAND contain random tweets discussed in various topics not related to ISIS. TW-RAND and TW-CON labelled as negative while TW-PRO is positive. Then, stylometry-based, time-based and sentiment-base features was selected. information gain was performed to select features. TW-CON and TW-RAND datasets were used as test dataset while TW-PRO used as training dataset. Classification results show that AdaBoost performs very well with 100% accuracy than both NB and SVM.

(Magdy et al.) [12] collected a huge number of Arabic tweets depending on how the terrorist group name was used in the tweets and divided them into two classes. pro-ISIS when the user used the full name of ISIS and the description as "state" is associated to refer to the organization and anti-ISIS when the abbreviated version was used. By analyzing pro-ISIS's historic timelines, they found the support for ISIS stems from frustration with the missteps of the Arab Spring. Also, they gained 87% accuracy by building an

SVM classifier to predict future support or opposition of the ISIS. authors also showed some of the interesting geographical and temporal trends for both pro- and anti-ISIS tweets.

Frequency of using nouns in the terrorist blogs was used also by (Park et al) [13] to analyze 6 Islamic forum posts on the dark web to find people who have radical tendencies. Radical users were extracted by using PoS tagger to select the top 100 most frequent nouns in each post. Then SentiStrength keyword analysis was used to determine polarity and score of each post. Sentiment scores for posts were divided into monthly radical scores to map each user's opinion change over time. Comparison was done to determine possible relationship or connection between users.

(Gatti et al.) [14] used extremist and benign contents on terrorist groups web sites. The approach uses ML methods to build and evaluate a text classifier that can distinguish Sunni extremist propaganda on the internet, Darknet and social media. Data collected from anonymous postings on “paste” sites frequently visited by terrorists is manually classified and labelled as to whether there is presence of Sunni extremism to form a training set. This training dataset was used to train a predictive classifier to perform binary classification of documents which were represented as a doc2vec vector. Class “1” was assigned to “extremist document” and class “0” was assigned to “benign document”. The classifier is capable of taking in text in any language and classifies it as being related to Sunni extremist propaganda or not.

Hashtags associated with ISIS can be analyzed and capture the sentiment of the tweets. (Mirani and Sasi) [15] used hashtags referring to ISIS such as #DAESH, #ISIS, #ISIL, #IS, #ISLAMICSTATE to collect dataset from Twitter. Initially, a lexical dictionary was used to define the polarity of dataset. Then, five different algorithms were trained on this dataset. The results showed that Maximum Entropy achieved the best result with 99%, while the other algorithms performed with an average accuracy of more than 90%.

(Ali) [16] employed data mining tools to analyze ISIS-related tweets both in English and in Arabic. KNN clustering algorithm was used to find out the frequently appearing words in the tweets. Network graph was used also to verify three ISIS-sympathizing accounts that contain ISIS supporting tweets.

User behavior on social media has also been used for sentiment analysis to detecting a sentiment that leads to terrorism on Twitter. (Azizan and Aziz)[6] conducted a study for the detection of extremist affiliations using machine learning techniques. They used historical tweets of particular users based on specific keywords related to the terrorism issue. Previous tweets sentiment scores of these particular users compared with the sentiment score of the latest statement detected. They found that the machine learning approach is more accurate as compared to the lexicon-based approach.

3. PROPOSED TECHNIQUE:

The proposed model system consists of three main steps as follow: pre-processing, lexicon-based approach and ML-based approach. To extract sentiment from new tweet, we only used pre-processing and ML-based approach as illustrated in Figure 1.

Pre-processing is an essential step before analyzing the data. Any data collected from primary sources including Twitter, contains significant amounts of noise. For example, twitter data contains symbols, URLs, emoticons, etc. There is need to transform these phrases into normal text. We automatically removed Retweets (RT), hashtags (#), URL’s and emoticons. duplicate tweets also removed in order to reduce tweets that may be produced by bot accounts.

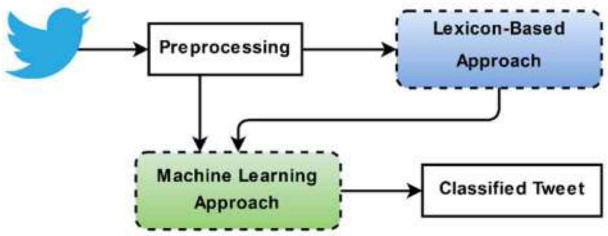

Figure 1 Main steps of the proposed Model

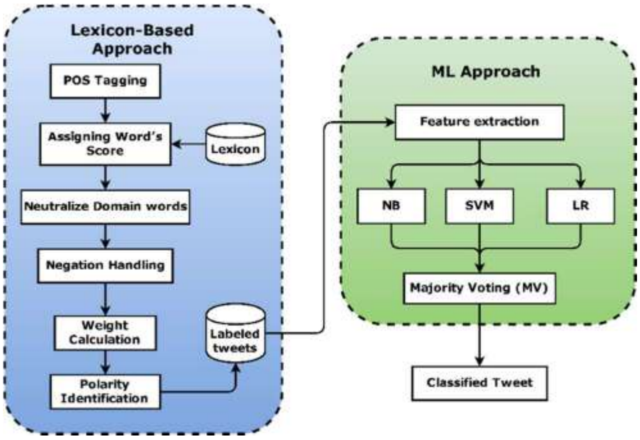

Figure 2 Lexicon and ML approaches processes in details

Second step is lexicon-based approach. In this step we build a training dataset using the following process as seen in Figure 2. Firstly, we employed python Natural Language Toolkit (NLTK) tokenize package to tokenize tweets into PoS which covers nouns, verbs, adjectives and adverbs. Then, SentiWords lexicon was used to determine polarity of the words. SentiWords contains approximately 155,000 English words that categorize words into nouns (N), verbs (V), adjectives (A) and adverbs (R) in alignment with WordNet lists. SentiWords assigns each word a sentiment score between -1 and 1 by learning from SentiWordNet [17],[18].

In the reviews of terrorist attacks domain, some words such as bomb, attack, kill, injured, explosion, etc. occur frequently and automatically reveal negative feelings.

According to SentiWords, these words have high negative scores. These high negative scores affect the final polarity of tweets making the sentiment of the tweet appear to be negative. To avoid this effect, we selected these words that automatically reveal negative feelings related to our domain and assigned them a score of zero, i.e. we neutralized them. These neutralized words are shown in the Table 1.

Example the review tweet of Wera Hobhouse (Figure 3); Member of Parliament for Bath in UK, after the Finsbury mosque attack in London.

My heart goes out to the victims of the vicious terror attack #finsburymosque, an attack on all of us and our shared values

6:56 PM - 19 Jun 2017

Figure 3 Wera Hobhouse tweet

Table 1
Neutralized domain lemmas

Lemma	PoS	Score	Lemma	PoS	Score
Arrest	V	-0.668	Gun	N	-0.335
Attack	V	-0.750	Gun	V	-0.335
Attack	N	-0.75	Gunman	N	-0.500
Attacker	N	-0.694	Incident	N	-0.200
Attacking	A	0.158	Incident	A	-0.2
Blood	N	-0.380	Injured	A	-0.389
Blood	V	-0.380	Kill	N	-0.798
Bloody	R	-0.535	Kill	V	-0.798
Bloody	A	-0.535	Killer	N	-0.815
Bloody	V	-0.535	Killing	A	-0.763
Bomb	N	-0.633	Killing	N	-0.763
Bomb	V	-0.633	Murder	N	-0.880
Bomber	N	-0.540	Murder	V	-0.880
Bombing	N	-0.725	Murderer	N	-0.770
Broken	A	-0.563	Murderous	A	-0.738
Casualty	N	-0.418	Shoot	V	-0.375
Dead	A	-0.745	Shoot	N	-0.375
Dead	R	-0.745	Shooter	N	-0.325
Dead	N	-0.745	Suicidal	A	-0.713
Deadliest	A	-0.745	Suicide	N	-0.855
Deadly	A	-0.775	Terror	N	-0.563
Deadly	R	-0.775	Terrorism	N	-0.850
Deadly	R	-0.775	Terrorist	N	-0.663
Death	N	-0.778	Terrorize	V	-0.625
Die	N	-0.833	Victim	N	-0.738
Die	V	-0.833	Weapon	N	-0.263
Died	V	-0.833	Weaponry	N	-0.323
Explosion	N	-0.458	Wound	V	-0.440
Explosive	N	-0.215	Wounded	A	-0.420
Explosive	A	-0.215			

On the lookout, this tweet gives positive sentiment. When we flat this tweet using PoS tagger to give scores from SentiWords to each word Table 2. Before neutralizing the domain words (victims, terror, and attack) the total score is negative implying negative sentiment. After neutralizing the domain words, the sentiment of the tweet changes from the negative to positive.

Negation Handling is a major issue while analyzing a given sentiment, which can be attributed to the fact that sentences contain a negation word such as not, don't, shouldn't etc.

These words shift the polarity of the sentence. For example, “I don’t like the movie”. The word “Like” carries a positive meaning, but “don’t” reverse the sentence meaning. We applied the window sizes approach to invert the polarity of the word following the negation word [19]. We used size =1 because we think the influence of the negation word mostly affects the meaning of the word that precedes it.

To deal with this problem we multiply the score of the word that precedes the negation word by (-1).

Then, we calculate tweet score by summing up all the scores of words in the tweet. We finally assign each tweet a polarity as follows:

$$polarity = \begin{cases} pos\ \ if\ Score >= \ \ 1 \\ neg\ \ if\ Score =< \ -1 \\ nat\ \ else \end{cases} \qquad (1)$$

Each tweet in the dataset passes through this processing to produce labelled tweets.

Table 2
Wera Hobhouse tweet’s neutralization

Token	**Tag**	**Description**	**Before**	**After**
my	PRP$	Pronoun	NA	NA
heart	NN	Noun	0.488	0.488
goes	VBZ	Verb	0.330	0.330
out	RP	Particle	NA	NA
to	TO	To	NA	NA
The	DT	Determiner	NA	NA
Victims	NNS	Noun	-0.738	0
of	IN	Preposition	NA	NA
the	DT	Determiner	NA	NA
vicious	JJ	Adjective	-0.593	-0.593
terror	NN	Noun	-0.563	0
attack	NN	Noun	-0.75	0
an	DT	Determiner	NA	NA
attack	NN	Noun	-0.75	0
on	IN	Preposition	NA	NA
all	DT	Determiner	NA	NA
of	IN	Preposition	NA	NA
us	PRP	Pronoun	NA	NA
and	CC	Conjunction	NA	NA
our	PRP$	Pronoun	NA	NA
shared	VBN	Verb	0.305	0.305
Values	NNS	Noun	0.545	0.545
Total:			-1.725	1.075
Sentiment:			**Negative**	**Positive**

Last step is ML approach, in this step the collection of assigned positive and negative polarities (labelled tweets) is used as training dataset to build the model. The major task during this step is feature extraction. There are different types of features extraction techniques that been applied in state-of-art such as Bag-of-Words models, n-grams models, lexicons-based models, and PoS based models.

In this work we used PoS models. PoS is a group of words or phrases that have similar grammatical properties, adjectives, adverbs, nouns, and verbs.

These phrases are extracted and used for classification of sentiments [20].

To obtain the final sentiment polarity, we used Logistic regression (LR), NB, and SVM.

We use NB, which is one of simplest and commonly used classifier in text categorization problem and sentiment analysis. It basically uses ‘Bayes theorem’ to describe the probability P for an event (class) to occur that is based on the conditions (features) that are thought be related to the event occurring. Given a class c and a dependent feature vector f_1 through f_n Bayes’ theorem states the following relationship:

$$P(c|f_1, \dots, f_n) = \frac{P(c)P(f_1, \dots, f_n|C)}{P(f_1, \dots, f_n)} \qquad (2)$$

SVM is widely regarded as one of the best text classification algorithms and it is robust when the problem is separate linearly. In SVM a few samples of data are used in classification, that make it very useful for the large data sets [21]. The main concept of SVM is to determine linear separators between a set of objects having different class memberships.

LR also known as Maximum Entropy is a probabilistic statistical method for classifying data into discrete outcomes. It is named as ‘Logistic Regression’, because it’s underlying technique is quite the same as Linear Regression. But the biggest difference lies in what they are used for. This model is not only used for regression but also the classification task [22]. It is one of the machine learning algorithms that provide low variance and great efficiency.

Then, voting between classification algorithm was used to determine the final decision of polarity. Our model determines the final decision depending on majority voting (MV) between the three classifiers (LR, NB and SVM). We define this MV as follows:

$$MV(x) = mode\,\{LR(x), NB(x), SVM(x)\} \quad (3)$$

That means, we predict the class of the voting classifier (MV(x)) via majority voting of each classifier (LR(x), NB(x), SVM(x)). Assuming that the prediction of the classifiers LR, NB and SVM are positive, negative and positive respectively, then.

$$MV(x) = mode\,\{pos, neg, pos\} = pos \quad (4)$$

4. EXPERIMENT & RESULTS

In this Section we present an experiment performed in order to evaluate the sentiment analysis process described in the proposed technique section. The proposed model is implemented using Python and R Language. R used for collection and cleaning the dataset while python used in the others process. The running environment for our experiment used was R studio and Python 3.6 running on PC (Intel Core i5 2.5 GHz / 8 GB DDR3). with Windows 10 operating system.

The dataset we used in this experiment contains 96,679 user review tweets after terrorist incidents that took place in different countries between 22 May 2017 to 31 October 2017.All these tweets were in English. Table 3 shows the places of these attacks, data collection date and number of tweets collected and the hashtags used. The data was collected based on the hashtags used.

The collected tweets were pre-processed followed by lexicon-based stage. At this stage as we explained above in the section 2; the result of this stage is labelling the dataset in 3 sentiment polarities: Positive if the total score of the tweet is equal or more than one, negative is the total score was equal or less than -1, otherwise is neutral.

From the total 96,679 tweets, result show that 21,140 tweets were positive sentiment, 9,838 tweets were negative, while the majority 65,701 of the tweets was neutral Figure 4.

Table 3
Collected tweets for each terrorist incident

Attack Date	Target place	Data collection dates	#Hashtags	Number of Tweets
22/05/2017	Manchester Arena, UK	22-30/05/2017	#manchesterattack, #manchesterbombing, #manchesterarena	12,472
03/06/2017	London Bridge, UK	03-06/06/2017	#Londonattacks, #Londonbridge	9,527
07/06/2017	Parliament building, Tehran, Iran	07-15/06/2017	#Tehranattacks, #Iranattacks, #Tehranunderattack, #Iranparliamentattack	7,898
19/06/2017	Finsbury Park mosque, London, UK	19-21/06/2017	#finsburyparkmosque, #Finsburymosque #finsburyparkterrorattack, #finsburypark	10,554
17/08/2017	La Rambla, Barcelona, Spain	17-22/08/2017	#Barcelonaattack, #barcelonaterrorattack, #Barcelona, #Prayforbarcelona	13,767
14/10/2017	center of Mogadishu, Somalia	15-18/10/2017	#Prayformogadishu, #Mogadishu, #Somalia, #Somaliaattack, #Mogadishutruckbomb	9,693
19/10/2017	Kandahar, Afghanistan	19-20/10/2017	#Taliban, #Kandahar, #Afghanistan	7,408
28/10/2017	Hotel- Mogadishu, Somalia	28-29/10/2017	#Prayformogadishu, #mogadishu, #somaliaattack, #mogadishutruckbomb	8,216
31/10/2017	Manhattan - New York, USA	31/10-01/11/2017	#NYTerrorAttack, #NYCStrong, #PrayForNYC, #Manhattan	17,144
TOTAL				**96,679**

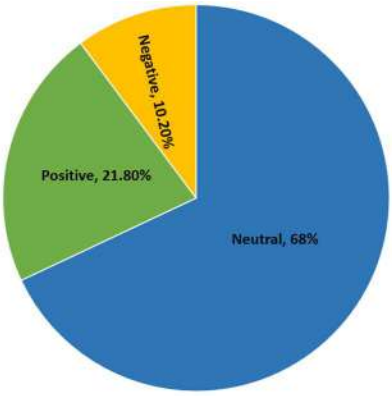

Figure 3 Lexicon-based labeled tweets

In the ML stage; only positive and negative labelled tweets were run. The labelled dataset was split into 3/4 training and 1/4 test. In this experiment, we examine three features types such as verb (VER), adjective (ADJ), and a combination of verb and adjective (VER+ADJ). Each feature type is classified using LR, NB, SVM, and MV classification algorithms

We applied the confusion matrix (Table 4) to evaluate the classification performance in terms of accuracy and F1-score for the both sentiment classes (Positive pos and Negative neg).

Accuracy *Ac* is used to calculate the proportion of the total number of predictions that were correct. While F1-scorei *F1* is used to calculate the weighted average of Recall *R* (proportion of actual pos/neg cases which are correctly identified) and Precision *P* (proportion of *pos*/*neg* cases that were correctly identified).

Table 4
Confusion matrix

	Predicted Positive	Predicted Negative
Actual Positive	True Positive (TP)	False Positive (FP)
Actual Negative	True Negative (TN)	False Negative (FN)

These measures are calculated as follows.

$$\mathrm{Ac} = \frac{\mathrm{TP+TN}}{\mathrm{TP+FP+TN+FN}} \tag{5}$$

$$\mathrm{P_{pos}} = \frac{\mathrm{TP}}{\mathrm{TP+FP}}\ ,\ \mathrm{P_{neg}} = \frac{\mathrm{TN}}{\mathrm{TN+FN}} \tag{6}$$

$$\mathrm{R_{pos}} = \frac{\mathrm{TP}}{\mathrm{TP+FN}}\ ,\ \mathrm{R_{neg}} = \frac{\mathrm{TN}}{\mathrm{TN+FP}} \tag{7}$$

$$F1_{pos} = \frac{2.P_{pos}.R_{pos}}{P_{pos}+R_{pos}}\ ,\ \mathrm{F1_{neg}} = \frac{\mathrm{2.P_{neg}.R_{neg}}}{\mathrm{P_{neg}+R_{neg}}} \tag{8}$$

We extract the result of these performance measure and compare it based on the classifier algorithm and the feature type to find out which roads are better.

The result show that MV classifier achieve best result with high *Ac,* and *F1* performance on all features in both *neg* and *pos* documents.

LR classifier achieved the second-best results in the most performance measures, but the result of $F1_{neg}$ of ADJ comes slightly lower than SVM result. SVM was third-best in performance results, while the worst performing approach in the all measure is NB. See Table 5.

According to the features the combination of the two features VER+ADJ achieve the high performance followed by VER while ADJ achieve the worst performance. That means the combination of features produces best results than a single type feature.

In General, all the classifications algorithms achieve pretty good accuracy with lowest being 90% achieved by NB with ADJ feature and highest 94.8% achieved by MV with VER+ADJ features. *F1* for *pos* documents achieves better performance than the *neg* documents. *pos* documents achieve score between 92.8% - 96.2% while the *neg* document was 83.8% - 91.6%.

Table 5
Classification measures result

Classifier	ADJ			VER			VER+ADJ		
	Ac	$F1_{pos}$	$F1_{neg}$	Ac	$F1_{pos}$	$F1_{neg}$	Ac	$F1_{pos}$	$F1_{neg}$
NB	90%	92.8%	83.8%	91.3%	93.7%	85.9%	90.8%	93.3%	85.6%
SVM	90.7%	93.2%	85.4%	92.4%	94.4%	87.9%	92.5%	94.5%	88.1%
LR	90.8%	93.4%	85.2%*	92.5%	94.6%	87.9%	93%	94.9%	88.6%
MV	93.1%	95%	88.7%	94.3%	95.9%	90.8%	94.8%	96.2%	91.6%

5. CONCLUSION

In this study we combine ML and lexicon approaches to build a model that automatically detects terrorist supporters on twitter from their comments using tweets after 9 terrorist attacks in different countries across the globe. The lexicon-based approach stage involved building a training dataset of labelled tweets as being positive, negative or neutral. In the ML stage, only positive and negative labelled tweets were used to build a classification model for feature extraction. Negative polarity tweets are regarded as terrorist supporters while positive polarity was regarded as non-supporters. PoS types such as VER, ADJ, and a combination of both VER+ADJ were used on selection features. Our model achieved high performance up to 94.8% accuracy and 95.9% F1 score. Accordingly, the combination of features produces better results than a single type feature. This study will be helpful for Law enforcement and intelligence agencies in their quest to develop effective deterrent strategies to prevent future terrorist attacks. In the future work, features will be extracted based on N-gram, and the obtained results will compare with PoS based features.

Funding

The authors received no financial support for the research, authorship or publication of this study.

The Declaration of Conflict of Interest/ Common Interest

No conflict of interest or common interest has been declared by the authors.

Authors' Contribution

İ.F: Constructing the idea of the article, planning the methodology to reach the conclusion, collecting the dataset, data management, execution of the experiments and reporting. logical interpretation and presentation of the results, writing of the body of the article, reviewing the article before submission.

C.Ö: Supervising the course of the article, Reviewing the article before submission.

The Declaration of Ethics Committee Approval

This work does not require ethics committee permission or any special permission.

The Declaration of Research and Publication Ethics

The authors of the paper declare that they comply with the scientific, ethical and quotation rules of SAUJS in all processes of the paper and that they do not make any falsification on the data collected. In addition, they declare that Sakarya University Journal of Science and its editorial board have no responsibility for any ethical violations that may be encountered, and that this study has not been evaluated in any academic publication environment other than Sakarya University Journal of Science.

REFERENCES

[1] J. Klausen, “Tweeting the Jihad: Social media networks of Western foreign fighters in Syria and Iraq,” Stud. Confl. Terror., vol. 38, no. 1, pp. 1–22, 2015.

[2] Council of Europe, “Cyberterrorism: The Use of the Internet for Terrorist Purposes,” United Nations Off. Drugs Crime, vol. 12, no. 1, p. 497, 2007.

[3] P. Choudhary and U. Singh, “A Survey on Social Network Analysis for Counter-Terrorism,” Int. J. Comput. Appl., vol. 112, no. 9, pp. 24-29, 2015.

[4] P. Burnap et al., “Tweeting the terror: modelling the social media reaction to the Woolwich terrorist attack,” Soc. Netw. Anal. Min., vol. 4, no. 1, pp. 1–14, 2014.

[5] T. Chalothorn and J. Ellman, “Using SentiWordNet and Sentiment Analysis for Detecting Radical Content on Web Forums,” Nrl.Northumbria. Ac. Uk, no. 1.

[6] A. Azizan, Sofea, Aziz, “Terrorism Detection Based on Sentiment Analysis

Using Machine Learning.pdf," J. Eng. Appl. Sci., vol. 12, no. 3, pp. 691–698, 2017.

[7] B. Liu, "Sentiment Analysis and Opinion Mining," Synth. Lect. Hum. Lang. Technol., vol. 5, no. 1, pp. 1–167, 2012.

[8] B. Pang, L. Lee, and S. Vaithyanathan, "Thumbs up?: sentiment classification using machine learning techniques," in The Conference on Empirical Methods in Natural Language Processing (EMNLP), 2002, vol. 10, pp. 79–86.

[9] N. A. S. Abdullah, N. I. Shaari, and A. R. A. Rahman, "Review on sentiment analysis approaches for social media data," Journal of Engineering and Applied Sciences, vol. 12, no. 3. pp. 462–467, 2017.

[10] W. Medhat, A. Hassan, and H. Korashy, "Sentiment analysis algorithms and applications: A survey," Ain Shams Eng. J., vol. 5, no. 4, pp. 1093–1113, 2014.

[11] M. Ashcroft, A. Fisher, L. Kaati, E. Omer, and N. Prucha, "Detecting Jihadist Messages on Twitter," Eur. Intell. Secur. Informatics Conf. EISIC 2015, pp. 161–164, 2016.

[12] W. Magdy, K. Darwish, and I. Weber, "#FailedRevolutions: Using Twitter to study the antecedents of ISIS support," First Monday, vol. 21, no. 2, 2016.

[13] A. J. Park, B. Beck, D. Fletche, P. Lam, and H. H. Tsang, "Temporal analysis of radical dark web forum users," Proc. 2016 IEEE/ACM Int. Conf. Adv. Soc. Networks Anal. Mining, ASONAM 2016, pp. 880–883, 2016.

[14] A. H. Johnston and G. M. Weiss, "Identifying sunni extremist propaganda with deep learning," 2017 IEEE Symp. Ser. Comput. Intell., no. December 2015, pp. 1–6, 2017.

[15] T. B. Mirani and S. Sasi, "Sentiment analysis of ISIS related Tweets using Absolute location," in International Conference on Computational Science and Computational Intelligence Sentiment, pp. 1140–1145, 2016.

[16] G. A. Ali, "Identifying Terrorist Affiliations through Social Network Analysis Using Data Mining Techniques," Valparaiso University, 2016.

[17] L. Gatti, M. Guerini, and M. Turchi, "SentiWords: Deriving a High Precision and High Coverage Lexicon for Sentiment Analysis," IEEE Trans. Affect. Comput., vol. 7, no. 4, pp. 409–421, 2016.

[18] Natural Language Processing, "SentiWords | HLT-NLP." [Online]. Available: https://hlt-nlp.fbk.eu/technologies/sentiwords. [Accessed: 19-Mar-2018].

[19] A. Hogenboom, P. Van Iterson, B. Heerschop, F. Frasincar, and U. Kaymak, "Determining negation scope and strength in sentiment analysis," in Conference Proceedings - IEEE International Conference on Systems, Man and Cybernetics, pp. 2589–2594, 2011.

[20] C. Bhadane, H. Dalal, and H. Doshi, "Sentiment analysis: Measuring opinions," Procedia Comput. Sci., vol. 45, no. C, pp. 808–814, 2015.

[21] J. M. Moguerza and A. Muñoz, "Support Vector Machines with Applications," Stat. Sci., vol. 21, no. 3, pp. 322–336, 2006.

[22] J. Feng, H. Xu, S. Mannor, and S. Yan, "Robust Logistic Regression and Classification," Neural Inf. Process. Syst., pp. 1–9, 2014.

SAKARYA ÜNİVERSİTESİ
FEN BİLİMLERİ ENSTİTÜSÜ
DERGİSİ

Sakarya University Journal of Science
SAUJS

e-ISSN 2147-835X | Period Bimonthly | Founded: 1997 | Publisher Sakarya University |
http://www.saujs.sakarya.edu.tr/en/

Title: On the Loci of Relaxation Time and Magnetic Dispersion Maxima in the Mean-Field Ising Model

Authors: Songül ÖZÜM

Recieved: 2020-08-13 14:48:26

Accepted: 2020-09-25 13:30:21

Article Type: Research Article

Volume: 24
Issue: 6
Month: December
Year: 2020
Pages: 1303-1313

How to cite
Songül ÖZÜM; (2020), On the Loci of Relaxation Time and Magnetic Dispersion Maxima in the Mean-Field Ising Model. Sakarya University Journal of Science, 24(6), 1303-1313, DOI: https://doi.org/10.16984/saufenbilder.780082
Access link
http://www.saujs.sakarya.edu.tr/en/pub/issue/57766/780082

Sakarya University Journal of Science 24(6), 1303-1313, 2020

On the Loci of Relaxation Time and Magnetic Dispersion Maxima in the Mean-Field Ising Model

Songül ÖZÜM*[1]

Abstract

Based on the phenomenological approach, loci of relaxation time and magnetic dispersion maxima near the critical regime in a spin-1/2 mean-field Ising model were performed. The shift in temperature (T) of relaxation time (τ) maximum was detected and its behavior near the second-order transition points are presented at different magnetic field values (h) and different lattice coordination numbers (q). An expression for the dynamic (or complex) susceptibility ($\chi = \chi_1 - i\chi_2$) is also derived. The temperature dependence of the magnetic dispersion (χ_1) and magnetic absorption (χ_2) factors have been studied near the critical regime. It is found that the maximum of χ_1 as a function of frequency (ω) and kinetic coefficient (L) obeying an approximately exponential increases and decreases in T- ω and T-L planes near the critical region.

Keywords: Ising model, mean-field approximation, phenomenological approach, relaxation time, magnetic dispersion maxima

1. INTRODUCTION

The study of relaxation phenomena (RP) has attracted much attention in many areas of condensed matter and statistical physics. Recent efforts on the RP in many different systems are devoted to either experimental [1-5] or theoretical [6-9] basis. Besides above works, it is mostly known that the RP in different Ising systems are one of the most actively studied problems in statistical physics and encountered in different areas of physics [10-29]. Similarly, the magnetic responses of Ising systems have long time been a subject of interest because of their potential applications as: spin glasses [30], cobalt-based alloys [31], magneto-optical devices [32], magnetic properties of magnetic fluids [33]. To achieve this aim, the authors constructed different types of Ising systems such as spin-1/2 Ising ferromagnet [34], Ising antiferromagnet [35], kinetic Ising model [36], spin-1/2 Ising system by using Monte Carlo simulations [37], an Ising system using the Glauber dynamics [38]. The static and dynamic properties of the magnetic responses of Ising systems have been investigated so far using a variety of techniques such as mean field approximation [27, 39, 40], Onsager's theory of irreversible thermodynamics [41]. However, the dynamical magnetic response properties have not been studied in detail, e.g., the loci of relaxation time and magnetic dispersion maxima in a spin-1/2 mean-field Ising model.

---

* Corresponding Author: songulozum@hitit.edu.tr

[1] Hitit University, Turkey, ORCID: https://orcid.org/0000-0003-2123-5856

In this paper, we would like to investigate the loci of relaxation time and magnetic dispersion maxima near the critical point in a spin-1/2 mean-field Ising model in the presence of oscillating external magnetic field. Since then, we describe the model and give static properties in Section 2. Then, in Section 3, we derived the kinetic (or rate) equations and relaxation time under the phenomenological approach. The complex (magnetic) susceptibility is obtain and magnetic dispersion and absorption factors are calculated with the solution of rate equations in same section. In Sec. 4, we present and discuss the calculated results. Section 5 includes the summary and some concluding remarks related with the topic.

2. THE MODEL AND ANALYSIS FOR EQUILIBRIUM STATE UNDER THE MEAN-FIELD APPROXIMATION

The spin-1/2 Ising model can be described through the Hamiltonian (in the presence of an external magnetic field h)

$$\mathrm{H} = -J\sum_{<ij>} S_i S_j - h\sum_i S_i , \tag{1}$$

where J is the bilinear coupling between the spins at sites i and j. q is the coordination number of the lattice (i.e. the number of nearest neighbours). Letting m and N be magnetization and the total number of Ising spins, Gibbs function $G(G = E - TS - hm)$ may be written in the Curie-Weiss approximation

$$G(m,h,T) = -\frac{1}{2}NJqm^2 + NkT\left[\left(\frac{1+m}{2}\right)\ln\left(\frac{1+m}{2}\right) + \left(\frac{1-m}{2}\right)\ln\left(\frac{1-m}{2}\right)\right] - hm, \tag{2}$$

where k and T are the Boltzmann factor and temperature, respectively. Also, the second derivative of G is

$$\frac{\partial^2 G}{\partial m^2} = -NJq + \frac{NkT}{1-m^2}, \tag{3}$$

and we write the critical temperature (T_C) by $T_C = Jq$. The magnetic field h is given by

$$h = \frac{\partial G}{\partial m} = -NJqm + \frac{1}{2}NkT\ln\frac{1+m}{1-m}. \tag{4}$$

The self-consistent equation has been obtained using Eq. (4) as

$$m = \tanh(\beta(Jqm + h)). \tag{5}$$

Thermal variations of m for different lattice coordination numbers ($q = 4, 6$) in the case of $L = 0.01$ and $J = 1$ are plotted for the system which undergoes a second-order phase transition (SOPT) in Figure 1. The dotted lines in the figure show T_C. From this figure one can see that m decrease to zero continuously from their values at $T_C = 4$ for $q = 4$ and $T_C = 6$ for $q = 6$ as the temperature increases; hence a SOPT occurs.

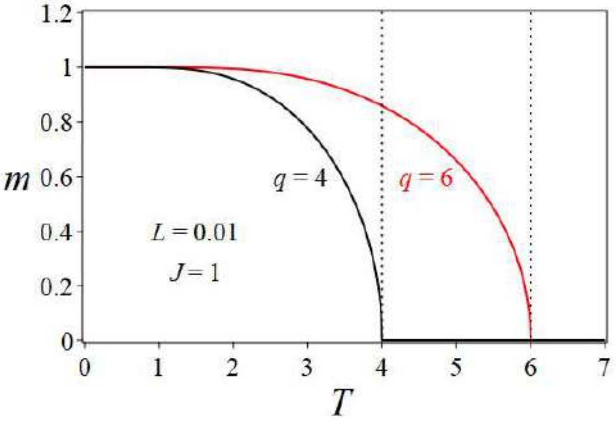

Figure 1 Temperature (T) dependence of m at various lattice coordination numbers (q) for $L = 0.01$ and $J = 1$

3. DERIVATIONS OF KINETIC EQUATION, RELAXATION TIME AND DYNAMIC SUSCEPTIBILITY

In this section, a mean-field approximation is used for the magnetic Gibbs free-energy production and a force and a current are defined. Then, the rate equation for the long-range order parameter (LROP or magnetization, m) is obtained within linear response theory. By solving these equations relaxation time (τ) is calculated for temperatures near the SOPT. A good reference for the description of relaxation properties of the Ising model is [27], whose notation is used here.

For a kinetic spin-1/2 Ising system, we define the $m(t)$ and for a nonequilibrium state, the τ towards equilibrium is written

$$\dot{m} = -\frac{m-m_0}{\tau}. \tag{6}$$

Where τ characterizes the rate at which the LROP m approaches the equilibrium (m_0). Eq. (6) is the simplest equation of irreversible thermodynamics [42] and can also be written as follows

$$\dot{m} = LX, \tag{7}$$

where L is the rate constant (or kinetic coefficient) and X is the generalized force conjugate to the current $\dot{m}$ by differentiating ΔG with respect to $m-m_0$:

$$X = \frac{d(\Delta G)}{d(m-m_0)}, \tag{8}$$

with

$$\Delta G = \frac{1}{2}\begin{bmatrix} \phi_{mm}(m-m_0)^2 + 2\phi_{mh}(m-m_0)(h-h_0) \\ +\phi_{hh}(h-h_0)^2 + \phi_h(h-h_0) \end{bmatrix}. \tag{9}$$

In Eq. (9), the coefficients are expressed:

$$\phi_{mm} = \left(\frac{\partial^2 G}{\partial m^2}\right)_{eq}, \quad \phi_{mh} = \left(\frac{\partial^2 G}{\partial m \partial h}\right)_{eq}, \quad \phi_{hh} = \left(\frac{\partial^2 G}{\partial h^2}\right)_{eq}$$

$$\phi_h = \left(\frac{\partial G}{\partial h}\right)_{eq}. \tag{10}$$

The kinetic equation is found using Eqs. (8)-(10) in the Eq. (7):

$$\dot{m} = L\phi_{mm}(m-m_0) + L\phi_{mh}(h-h_0). \tag{11}$$

One can introduce the rate equation when $h=0$, i.e., $h-h_0$ to find the τ for the single RP. Eq. (11) can be written

$$\dot{m} = L\phi_{mm}(m-m_0). \tag{12}$$

If we had assumed a solution form with $m-m_0 = \exp(-t/\tau)$ for Eq. (12), we find

$$\frac{1}{\tau} = L\phi_{mm}. \tag{13}$$

Using Eq. (10), one obtaines the relaxation time

$$\tau = -\frac{1-m_0{}^2}{NL(-Jq + Jqm_0{}^2 + kT)}. \tag{14}$$

The spin system is stimulated by a time dependent small external magnetic field $h(t) = h_1 e^{i\omega t}$ oscillating at an angular frequency ω. The quantities will oscillate at the same ω in the steady-state: therefore

$$m(t) - m_0 = m_1 e^{i\omega t}. \tag{15}$$

Substituting Eq. (9) into the rate equation Eq. (7) we obtain as following equation:

$$i\omega m_1 e^{i\omega t} = L\phi_{mm} m_1 e^{i\omega t} + L\phi_{mh} h_1 e^{i\omega t}. \tag{16}$$

Solving Eq. (16) for m_1 / h_1 yields as follows

$$\frac{m_1}{h_1} = \frac{L\phi_{mh}}{i\omega - L\phi_{mm}}. \tag{17}$$

We will use Eq. (17) to obtain the complex (magnetic) susceptibility $\chi(\omega)$. The Ising system induced magnetization is written as

$$m(t) - m_\infty = \mathrm{Re}(m_1 e^{i\omega t}). \tag{18}$$

m_∞ is the magnetization induced by a h oscillating at ω. In addition, $\chi(\omega)$ is given

$$m(t) - m_\infty = \mathrm{Re}\left[\chi(\omega) h_1 e^{i\omega t}\right], \tag{19}$$

in which $\chi(\omega) = \chi_1(\omega) - i\chi_2(\omega)$ is the dynamic susceptibility. Real $\chi_1(\omega)$ and imaginary $\chi_2(\omega)$ parts of $\chi(\omega)$ are magnetic dispersion and absorption factors, respectively. Eq. (16) can be given

$$\chi(\omega) = \frac{m_1}{h_1}. \tag{20}$$

The magnetic dispersion and absorption factors become

$$\chi_1(\omega) = \frac{\phi_{mm} L^2}{\phi_{mm}{}^2 L^2 + \omega^2} = L\phi_{mh} \frac{\tau}{1 + \omega^2 \tau^2}. \tag{21}$$

$$\chi_2(\omega) = \frac{L\omega}{\phi_{mm}{}^2 L^2 + \omega^2} = L\phi_{mh} \frac{\tau^2 \omega}{1 + \omega^2 \tau^2}. \tag{22}$$

4. NUMERICAL RESULTS AND DISCUSSION

Firstly, we plot the relaxation time τ as a function of T at using different lattice structures (with $q = 4, 6$ corresponding to the square and simple cubic lattice structures, respectively) for the case $L = 0.01$ and $J = 1$ in Figure 2. In this figure, τ grows rapidly with increasing T and diverges as the T approaches the SOPT temperature. The curves shift towards higher temperatures with increasing q.

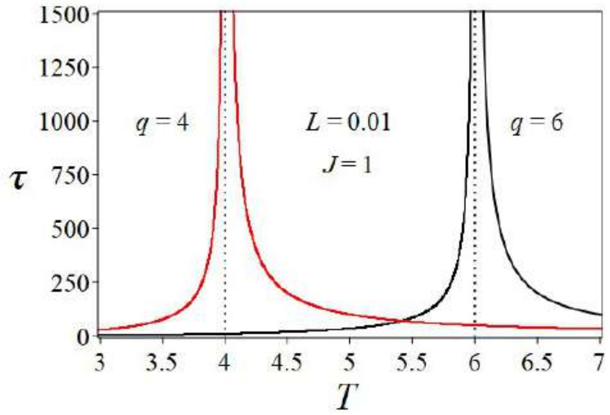

Figure 2 T dependence of τ at various q for $L = 0.01$ and $J = 1$

Thermal behaviours of τ are performed for four values of the external fields ($h = 0,\ 0.03, 0.05,\ 0.1$) for $L = 0.01$ and $q = 6$ and for two lattice coordination numbers $q = 4, 6$ with $h = 0.05$, $L = 0.01$. The results are displayed in Figures 3(a) and 3(b), respectively. Figure 3(a) shows that τ (black-colored curve) grows rapidly with increasing T and diverges to infinity around T_C (as seen dotted line) when $h = 0$. This result is a very good overall agreement with the relaxation phenomena around the Curie temperature belonging to the Bethe approximation in Barry's works [34]. On the other hand, for $h \neq 0$, maxima of the curves (or peaks) are observed in Figure 3(a). In particular, the maxima of these curves depend on the external field. One can see that with the increase of h ($h = 0.03,\ 0.05$ and 0.1) the maxima become smaller and shift towards higher T. In Figure 3(b), for the sake of comparison in the case of different lattice structures ($q = 4$, square lattice and $q = 6$, simple cubic lattice), we have also calculated τ vs. T for this system with $h = 0.05$. The peaks become smaller and shift towards higher T with increasing q. Also, we construct the plots of the maxima of τ that obtained from Figure 3(a) predicted for Ising model with $L = 0.01$ and $J = 1$ on the $h - T$ plane in Figure 3(c).

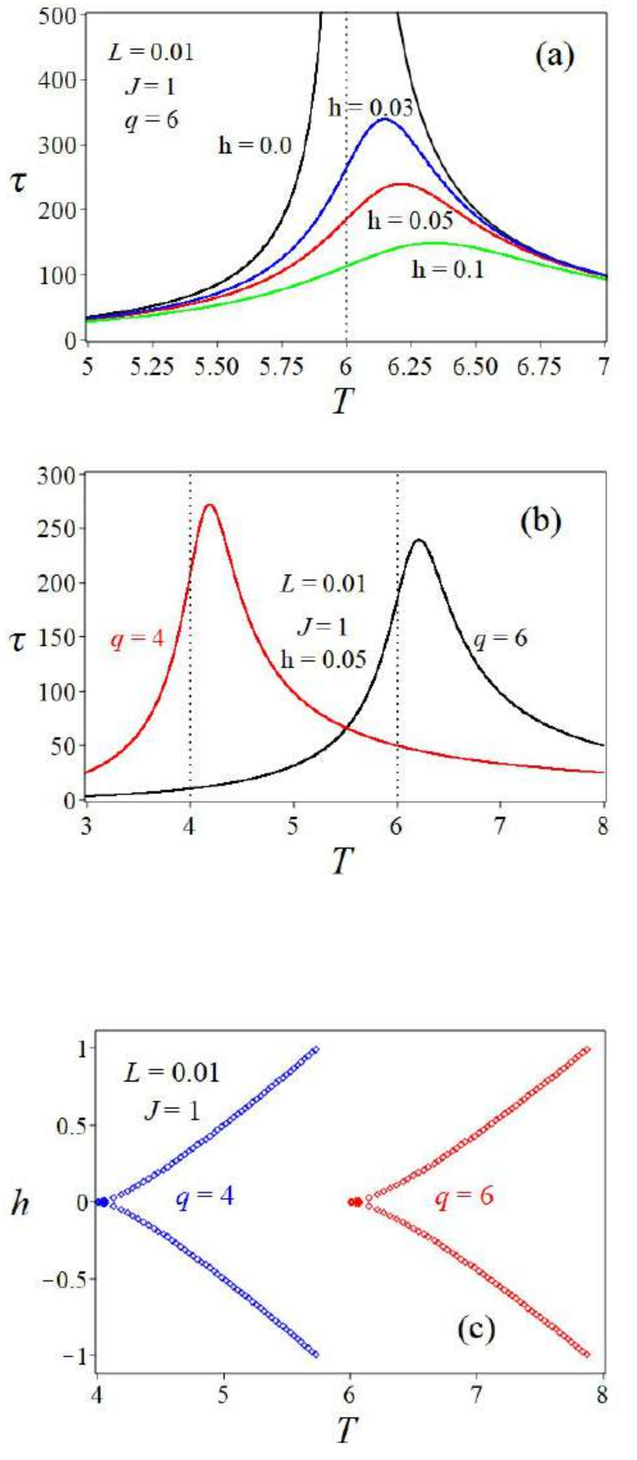

Figure 3 (a) T dependence of τ at various h for $L=0.01$, $J=1$ and $q=6$. (b) T dependence of τ for various q with $L=0.01$, $J=1$ and $h=0.05$. (c) Loci of maxima of τ (blue-colored square for $q=4$) and (red-colored square for $q=6$) with $L=0.01$ and $J=1$ on the $h-T$ plane

Figure 4 shows that the temperature behaviors of the χ_1 and χ_2 for the lower frequency regime $\omega\tau \ll 1$ for the case $L=0.01$ and $J=1$. Figures 4(a) and 4(b) show χ_1 and χ_2 increase with T and tend to infinity around the phase transition point. The χ_1 is independent of the ω, whereas χ_2 depends on ω. In these figures, dotted lines illustrate the T_C and the black-, blue- and red-colored curves are for $\omega = 2\times10^{-5}$, 4×10^{-5}, 6×10^{-5}, respectively. These results are in qualitative agreement with the obtained calculations by Barry and Harrington [34, 35, 41] and Gülpınar and co-workers [39, 40].

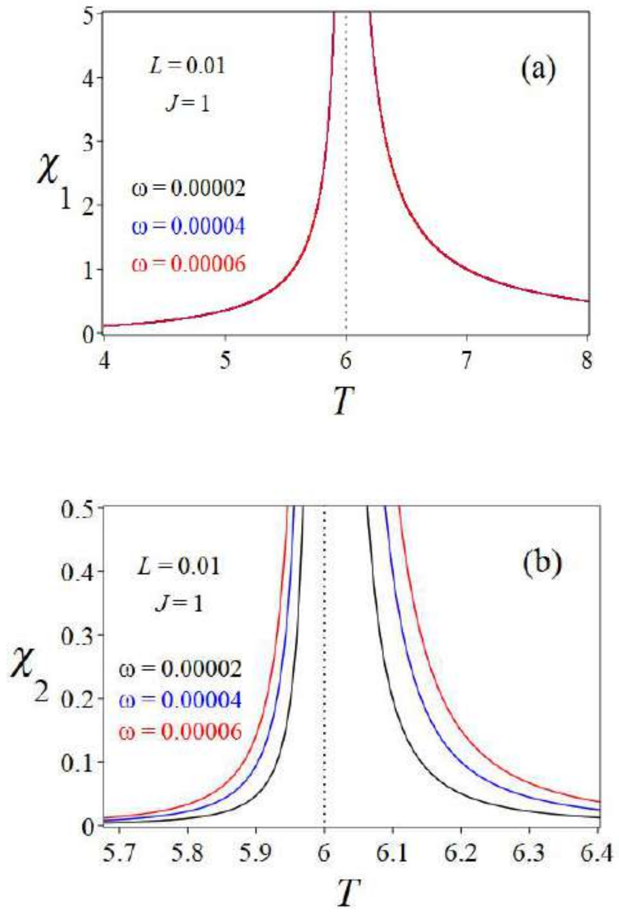

Figure 4 (a) χ_1 and (b) χ_2 as a function of the T for the low-frequency region $(\omega\tau \ll 1)$ when $L=0.01$ and $J=1$

The temperature behaviors of χ_1 and χ_2 are shown in the $\omega\tau \gg 1$ for the case of $L=0.01$ and $J=1$ in Figures 5(a) and 5(b). In both figures, dotted lines represent the T_C. χ_1 has two local maxima in the FM and paramagnetic (PM) phase regions, as shown in Figure 5(a). In this figure, one can see that these maxima are ω - dependent. The maximum observed at a temperature in the FM phase decreases and shifts to lower T when ω increases. The peak found at a T in the PM phase decreases but shifts towards higher T. A local minimum or a sharp dip is seen at the T_C for magnetic dispersion χ_1. These results are also in coherent with other theoretical studies of dynamic susceptibility for well-known spin systems [34, 35, 39-47].

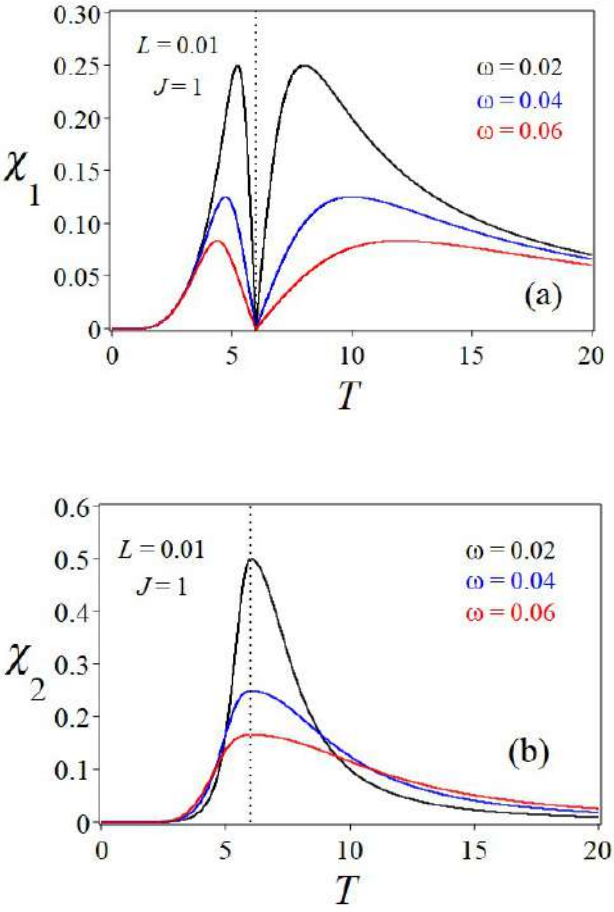

Figure 5 Same as Figure 4 but for the high-frequency region ($\omega\tau >> 1$)

To observe the effect of rate constant (or kinetic coefficient) L on χ_1 and χ_2 vs T curves, we have drawn, in Figure 6, for different values of L with $J = 1$ and $\omega = 2 \times 10^{-5}$ obeying the $\omega\tau << 1$ condition. The red-, blue- and green-colored curves in Figures 6(a) and 6(b) correspond to the cases $L = 0.03$, 0.02, 0.01, respectively. χ_1 in the FM and PM regions does not depend on the statistical rate parameter while χ_2 inversely proportional to L (Figure 6(b)). Although χ_1 is very similar to that in Figure 4(a), χ_2 is different from the case in Figure 4(b).

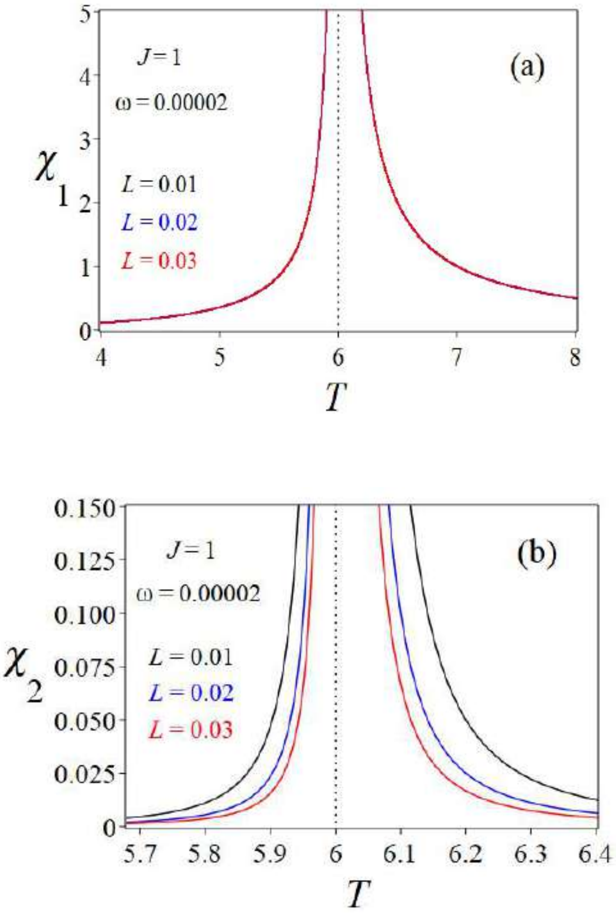

Figure 6 (a) χ_1 and (b) χ_2 as a function of the T for various values of L when $J = 1$ and $\omega = 2 \times 10^{-5}$

Figure 7 shows χ_1 and χ_2 vs T curves using $J = 1$ and different L values for $\omega\tau >> 1$. In these figures, the dotted lines refer to the T_C. Also, we have found that increasing values of L raises the peaks for χ_1 and χ_2. One can see in Figure 7(a), the heights and loci of the peaks obtained for χ_1 in the FM and PM phases depend on the L.

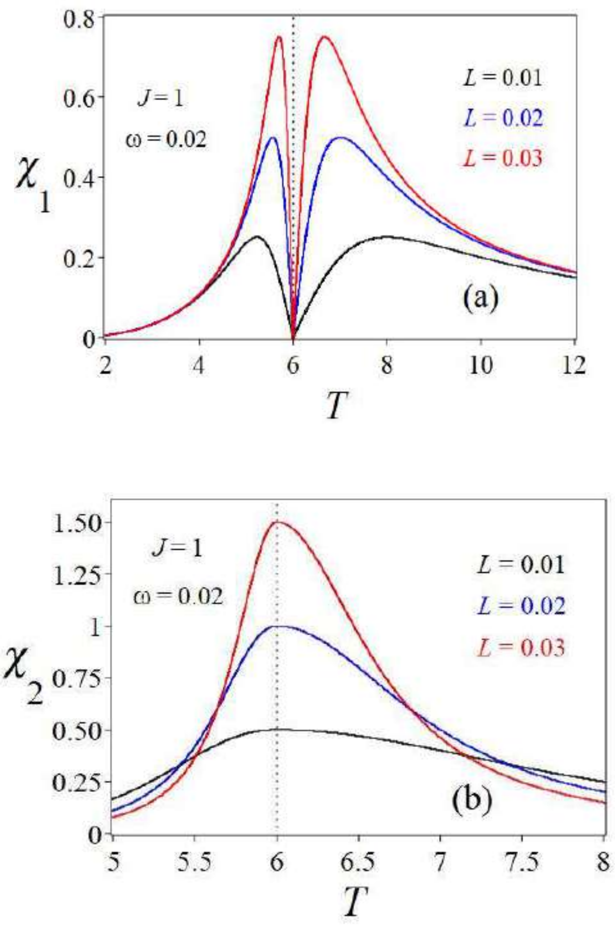

Figure 7 Same as Figure 6 but for $\omega = 0.02$

As the last figures, we represent the loci of magnetic dispersion maxima in T - ω and T - L planes in Figures 8(a) and 8(b). As seen in Figure 8(a), the temperatures of maxima observed in the PM phase (T_P^m) exponentialy increase (red-colored open diamonds) whereas the peak temperature in FM phase (T_F^m) exponentialy decrease (blue-colored open diamonds) with increasing frequency from 0 to 1. We also described, the exponential variation of the T with the L for $\omega = 0.02$ and $J = 1$ in Figure 8(b). It could be emphasized that the functional behaviours of $T_{F,P}^m$ obey second-order exponential form as $T_{F,P}^m = \pm A_1 \exp(\mp\omega / a_1) \pm A_2 \exp(\mp\omega / a_2) \pm B$. In Figure 8(a), for the blue-colored open diamonds we have determined the constants as $A_1 = 2.13$, $a_1 = 0.04$, $A_2 = -1.42$, $a_2 = 30.1$ and $B = 5.35$ while for the red-colored open diamonds these are obtained to be $A_1 = 36.9$, $a_1 = -0.27$, $A_2 = -34.9$, $a_2 = -1.80$, $B = -7.9$. Also, we can present the exponential variation of the temperatures $T_{F,P}^m$ with the L by $T_{F,P}^m = \pm A_1 \exp(\mp L / a_1) \pm A_2 \exp(\mp L / a_2) \pm B$ in Figure 8(b). As a result of our calculations, the fit to second-order exponential function gave values equal to $A_1 = 3.4$, $a_1 = 0.014$, $A_2 = 0.9$, $a_2 = 2.2$, $B = -5.35$ for the red diamonds and $A_1 = 1.0$, $a_1 = -0.02$, $A_2 = -0.01$, $a_2 = -0.02$, $B = 5.9$ for the blue diamonds in Figure 8(b). For Figures 8(a) and 8(b), converging to $T \approx 6$ (horizontal dotted lines) of both peak temperatures presents that χ_1 diverges to infinity is the continuous phase transition temperature. This result is the expected behaviour for Ising systems.

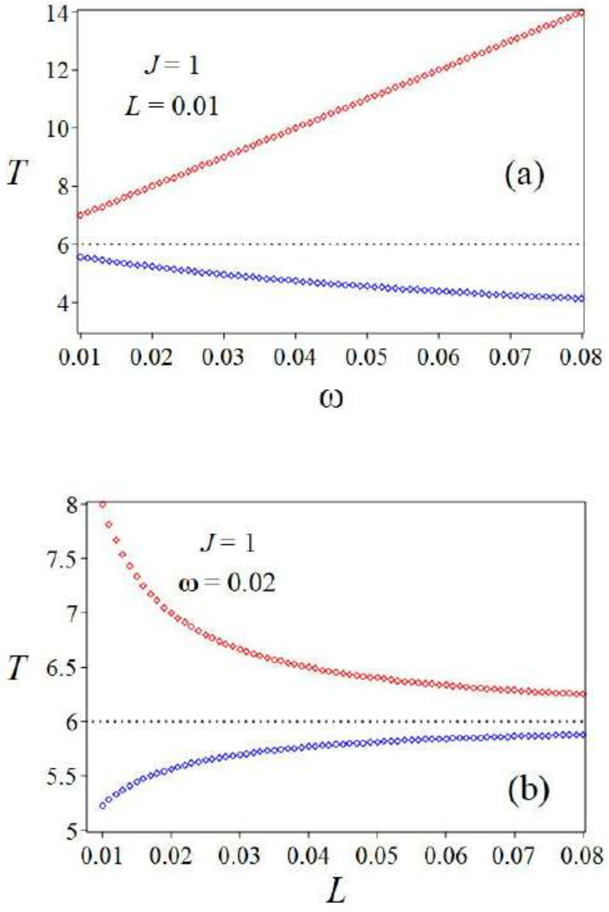

Figure 8 Loci of maxima of χ_1 (a) for $L = 0.01$ on the $T - \omega$ plane and (b) for $\omega = 0.02$ on the $T - L$ plane. $J = 1$

5. CONCLUSION

In this paper, we have investigated the loci of relaxation time and magnetic dispersion maxima in the mean-field spin-1/2 Ising model near the critical region. Firstly, having used LROP (magnetization) description, we obtained the simplest relaxation time (τ) based on phenomenological theory. Using different lattice coordination numbers (q) and magnetic field (h) values, temperature vs τ has been discussed. τ tends to infinity at $h = 0$ near the phase transitions while it shows a peak in the presence of h. The plots of the maxima of τ for different q values have been also investigated. The temperature dependence of the magnetic dispersion (χ_1) and absorption (χ_2) factors have been analyzed and illustrated in the case of $L = 0.01$ and $J = 1$ for low- and high-frequency regimes. χ_1 and χ_2 diverges to infinity at low-frequency regime as χ_1 has two frequency-dependent local maxima (or peaks) in the FM and PM phases. In order to observe the effect of rate constant L on the temperature dependence of χ_1 and χ_2, we have plotted the magnetic dispersion and absorption factors in the low- and high-frequency regimes. As a result of frequency and kinetic coefficient dependence of χ_1, we have shown loci of maxima of χ_1 with interesting features in T - ω and T - L planes. The study of dynamic response of a spin system in the presence of sinusoidally varying magnetic field is an important subject for all magnetic systems and their potential applications. It shoul be mentioned that the knowledge of dynamic susceptibility reveal the technological importance of a variety of physical phenomena such as nanocomposite particles for the design of magneto-optical devices.

Funding

The author received no financial support for the research, authorship, and/or publication of this paper.

The Declaration of Conflict of Interest/ Common Interest

No conflict of interest or common interest has been declared by the author.

The Declaration of Ethics Committee Approval

The author declares that this document does not require an ethics committee approval or any special permission.

The Declaration of Research and Publication Ethics

The author of the paper declares that she complies with the scientific, ethical and quotation rules of SAUJS in all processes of the paper and that she does not make any falsification on the data collected. In addition, she declares that Sakarya University Journal of Science and its editorial board have no responsibility for any ethical violations that may be encountered, and that this study has not been evaluated in any academic publication environment other than Sakarya University Journal of Science.

REFERENCES

[1] G. Lucas and M. J. Stephen, “Relaxing of the superconducting order parameter,” Physical Review, vol. 154, no. 2, pp. 349, 1967.

[2] I. Schuller and K. E. Gray, “Experimental observation of the relaxation time of the order parameter in superconductors,” Physical Review Letters, vol. 36, no.8, pp. 429-432, 1976.

[3] V. A. Atsarkin, V. V. Demidov, G. A.Vasneva and K. Conder, “Critical slowing down of longitudinal spin relaxation in $La_{1-x}Ca_xMnO_3$,” Physical Review B, vol. 63, no.9, pp. 092405, 2001.

[4] S. J. Etzkorn, W. Hibbs, J. S. Miller and A. J. Epstein, “Anomalous relaxation in a

quasi- one-dimensional fractal cluster glass," Physical Review B, vol. 70, no.13, pp. 134419, 2004.

[5] M. Ahart, A. Hushur, Y. Bing, Z. G. Ye, R. J. Hemley and S. Kojima, "Critical slowing down of relaxation dynamics near the Curie temperature in the relaxor Pb $(Sc_{0.5}Nb_{0.5})O_3$,"Applied Physics Letters, vol. 94, no.14, pp. 142906-1-142906-3, 2009.

[6] T. Nogawa and K. Nemoto, "Nonequilibrium relaxation analysis of a quasi-one-dimensional frustrated XY model for charge- density waves in ring-shaped crystals,"Physical Review B, vol. 73, no. 18, pp. 184504-1-184504-6, 2006.

[7] X. W. Lei and B. Zheng, "Short-time critical dynamics and aging phenomena in the two- dimensional XY model," Physical Review E, vol. 75, no.4, pp. 040104-1-040104-4, 2007.

[8] R. N. Bhowmik and R. Ranganathan, "Unconventional relaxation in antiferromagnetic $CoRh_2O_4$ nanoparticles," Physical Review B, vol. 75, no. 1, pp. 012410, 2007.

[9] C. Bonati, A. Cannizzo, D. Tonti, A. Tortschanoff, F. van Mourik and M. Chergui, "Subpicosecond near-infrared fluorescence upconversion study of relaxation processes in PbSe quantum dots," Physical Review B, vol. 76, no.3, pp. 033304-1-033304-4, 2007.

[10] L. Onsager, "Reciprocal relations in irreversible processes I," Physical Review, vol. 37, no.4, pp. 405-426, 1931, L. Onsager, "Reciprocal Relations in Irreversible Processes. II," Physical Review, vol. 38, no.12, pp. 2265-2279, 1931.

[11] T. Tanaka, P. H. E. Meijer and J. H. Barry, "Theory of Relaxation Phenomena near the Second-Order Phase-Transition Point," Journal of Chemical Physics, vol. 37, no.7, pp. 1397, 1962.

[12] R. J. Glauber, "Time-Dependent Statistics of the Ising Model," Journal of Mathematical Physics, vol. 4, no. 2, pp. 294-307, 1963.

[13] R. Kikuchi, "The Path Probability Method," vol. 35, pp. 1-64, 1966.

[14] T. Obokata, "Time-Dependent One-Dimensional Ising Model with Spin S=1," Journal of the Physical Society of Japan, vol. 26, no.4, pp. 895-900, 1969.

[15] M. Tanaka and K. Takahashi, "Kinetic Ising Model with the Bilinear and Biquadratic Interactions," Journal of the Physical Society of Japan, vol. 43, no. 6, pp. 1832-1838, 1977.

[16] G. L. Batten Jr. and H. L. Lemberg, "Dynamics of the spin-1 Ising mean field model," The Journal of Chemical Physics, vol. 70, no. 6, pp. 2934, 1979.

[17] Y. Saito and H. Müller-Krumbhaar, "Antiferromagnetic spin-1 Ising model. II. Interface structure and kinetic phase transition," The Journal of Chemical Physics, vol. 74, no. 1, pp. 721-727, 1981.

[18] M. Keskin and P. H. E. Meijer, "A model for quenching via hidden variables; Non-equilibrium behaviour of a system with two long range order parameters," Physica A, vol. 122, no. 1-2, pp. 1-12, 1983.

[19] Y. Achiam, "Critical relaxation of the one dimensional Blume-Emery-Griffiths model, "Physical Review B, vol. 31, no.1, pp. 260, 1985.

[20] M. Keskin, "A model for quenching via hidden variables; Non-equilibrium behavior of a system with two long range order parameters II: Influence of a magnetic field," Physica A, vol. 135, no. 1, pp. 226-236, 1986.

[21] M. Keskin and P. H. E. Meijer, “Dynamics of a spin-1 model with the pair correlation,”The Journal of Chemical Physics, vol. 85, no. 12, pp. 7324-7333, 1986.

[22] M. Keskin, M. Arı and P. H. E. Meijer, “Stable, metastable and unstable solutions of a spin-1 Ising system obtained by the molecular-field approximation and the path probability method,” Physica A: Statistical Mechanics and its Applications, vol. 157, no. 2, pp. 1000-1017, 1989.

[23] M. Keskin and R. Erdem, “Dynamic Behavior of a Spin- 1 Ising Model. I. Relaxation of Order Parameters and the “Flatness” Property of Metastable States,”Journal of Statistical Physics, vol. 89, no. 5/6, pp. 1035-1046, 1997.

[24] M. Keskin and P. H. E. Meijer, “Time-dependent one-dimensional spin-1 Ising system with weak coupling,” Physical Review E, vol. 55, no. 5, pp. 5343, 1997.

[25] M. Keskin and A. Solak,, “Dynamics of the spin-1 Ising Blume-Emery-Griffiths model by the path probability method,” The Journal of Chemical Physics, vol. 112, no.14, pp. 6396-6403, 2000.

[26] R. Erdem and M. Keskin, “Dynamics of a spin-1 Ising system in the neighborhood of equilibrium states,” Physical Review E, vol. 64, no. 2, pp. 026102-1-026102-9, 2001.

[27] R. Erdem and G. Gülpınar, “Nonequilibrium Thermodynamics of Ising Magnets,” Juan Carlos Moreno-Piraján (Ed.), IntechOpen, pp. 255-276, 2011.

[28] G. Gulpinar and F. Iyikanat, “Dynamics of the Blume-Capel model with quenched diluted single-ion anisotropy in the neighbourhood of the equilibrium states,” Physical Review E, vol. 83, no. 4, pp. 041101-1-041101-9, 2011.

[29] R. Erdem and S. Özüm, “Relaxation times obtained from the rate equations using path probability method for the spin-1 Ising model,” Modern Physics Letters B, vol. 33, no. 22, pp. 1950258-1-1950258-12, 2019.

[30] J. Kötzler and G. Eiselt, “Observation of spin-cluster freezing in dilute (EuxSr1-x)S by low-frequency magnetic absorption,” Journal of Physics C: Solid State Physics, vol. 12, no. 12, pp. L469-474, 1979.

[31] G. Durin, M. Bonaldi, M. Cerdonio, R. Tommasini and S. Vitale, “Magnetic viscosity of Co-based amorphous alloys between 0.02 and 4.2 K,” Journal of Magnetism and Magnetic Materials, vol. 101, no.1-3, pp. 89- 91, 1991.

[32] M. B. F. van Raap, F. H. Sánchez, C. E. R. Torres, L. Casas, A. Roig and E. Molins,“Detailed magnetic dynamic behaviour of nanocomposite iron oxide aerogels,” Journal of Physics: Condensed Matter, vol. 17, pp. 6519-6531, 2005.

[33] P. C. Fannin, C. N. Marin, I. Malaescu and A. T. Giannitsis, “Microwave absorption of composite magnetic fluids,” Journal of Magnetism and Magnetic Materials, vol. 289, pp. 78-80, 2005.

[34] J. H. Barry, “Magnetic Relaxation near a Second-Order Phase-Transition Point,” The Journal of Chemical Physics, vol. 45, no.11, pp. 4172-4177, 1966.

[35] J. H. Barry and D. A. Harrington, “Theory of Relaxation Phenomena in Ising Antiferromagnets,” Physical Review B, vol. 4, no. 9, pp. 3068-3077, 1971.

[36] M. Suzuki and R. Kubo, “Dynamics of the Ising Model near the Critical Point. I,” Journal of the Physical Society of Japan, vol. 24, no. 1, pp. 5160, 1968.

[37] M. Acharyya and B. K. Chakrabarti,“Response of Ising systems to oscillating and pulsed fields: Hysteresis, ac,

and pulse susceptibility," Physical Review B, vol. 52, no. 9, pp. 6550-6568, 1995.

[38] G. Ismail and A. Salem, "Dynamics of Ising spins with antiferromagnetic bonds on a triangular lattice," Physica Status Solidi (B), vol. 237, no. 2, pp. 530-539, 2003.

[39] G. Gulpinar and E. Vatansever, "Critical behavior of AC antiferromagnetic and ferromagnetic susceptibilities of a spin-1/2 metamagnetic Ising system," Journal of Magnetism and Magnetic Materials, vol. 324, pp. 983-990, 2012.

[40] G. Gulpinar, R. Erdem and M. Ağartıoğlu, "Critical and multicritical behaviors of static and complex magnetic susceptibilities for the mean-field Blume-Capel model with a random crystal field," Journal of Magnetism and Magnetic Materials, vol. 439, pp. 44-52, 2017.

[41] R. Erdem, "Magnetic relaxation in a spin-1 Ising model near the second-order phase transition point," Journal of Magnetism and Magnetic Materials, vol. 320, no. 18, pp. 2273-2278, 2008.

[42] S. R. De Groot and P. Mazur, "Non-equilibrium Thermodynamics," North-Holland Publishing Company, Amsterdam, pp. 263-273, 1962.

[43] A. Pawlak and R. Erdem, "Dynamic response function in Ising systems below T_c," Physical Review B, vol. 83, no. 9, pp. 094415-1- 094415-8, 2011.

[44] A. Pawlak and R. Erdem, "Effect of magnet fields on dynamic response function in Ising systems," Physics Letters A, vol. 377, no. 38, pp. 2487-2493, 2013.

[45] E. Vatansever and H. Polat, "Nonequilibrium dynamics of a spin-3/2 Blume-Capel model with quenched random crystal field," Journal of Magnetism and Magnetic Materials, vol. 332, pp. 28-37, 2013.

[46] G. Gulpinar and R. Erdem, "High-frequency magnetic field on crystal field diluted S = 1 Ising system: magnetic relaxation near continuous phase transition points," Canadian Journal of Physics, vol. 96, no.12, pp. 1321-1332, 2018.

[47] A. Pawlak, R. Erdem and G. Gulpinar, "Dynamic dipolar and quadrupolar susceptibilities for the spin-1 Blume-Emery-Griffiths model based on Onsager theory of Irreversible thermodynamics," Journal of Magnetism and Magnetic Materials, vol. 472, pp. 86-95, 2019.

SAKARYA ÜNİVERSİTESİ
FEN BİLİMLERİ ENSTİTÜSÜ
DERGİSİ

Sakarya University Journal of Science
SAUJS

e-ISSN 2147-835X | Period Bimonthly | Founded: 1997 | Publisher Sakarya University |
http://www.saujs.sakarya.edu.tr/en/

Title: The Role of Vertical Tool Load on the Joint Properties of Friction Stir Spot Welded Brass Alloy

Authors: Zafer BARLAS, Uğur ÖZSARAÇ

Recieved: 2020-08-18 16:00:08

Accepted: 2020-09-29 19:28:57

Article Type: Research Article

Volume: 24
Issue: 6
Month: December
Year: 2020
Pages: 1314-1320

How to cite
Zafer BARLAS, Uğur ÖZSARAÇ; (2020), The Role of Vertical Tool Load on the Joint Properties of Friction Stir Spot Welded Brass Alloy. Sakarya University Journal of Science, 24(6), 1314-1320, DOI: https://doi.org/10.16984/saufenbilder.781600

Sakarya University Journal of Science 24(6), 1314-1320, 2020

SAKARYA
ÜNİVERSİTESİ

The Role of Vertical Tool Load on the Joint Properties of Friction Stir Spot Welded Brass Alloy

Zafer BARLAS*[1], Uğur ÖZSARAÇ[2]

Abstract

This study consisted of the effects of vertical tool load on failure value in FSSW of CuZn30. Tensile-shear test, microstructural examination, microhardness, vertical tool load, and temperature measurements were utilized to reveal the influence of FSSW process. According to the results, the tool load plays a key role on the features of joint. Not only low tool load, but also excessive load used leads to drop in the tensile-shear values. The spot weld region was characterized by stir and heat-affected zones and these have various microhardness values ranging from 108.2 HV to 150.2 HV. The temperature measurements show that the peak temperature increased with increasing tool load value.

Keywords: FSSW, brass alloy, vertical tool load, tensile-shear failure load

1. INTRODUCTION

Friction stir spot welding (FSSW), which is a solid-state joining method firstly adapted to joints in hood and rear door in Mazda RX-8 car in 2003. FSSW process eliminates the certain problems such as electrode overheating, electrode sticking to work-piece and short electrode life associated with the conventional resistance spot welding process. FSSW also presents significant advantages such as excellent mechanical properties, low distortion, ease of handling, 40 % saving in equipment costs, 90 % saving in energy and clean working environment comparing to resistance spot welding [1-4]. Although it has had the benefits mentioned above, the experimental studies have been commonly focused on tool rotation speed (TRS), tool geometry, and plunge depth for aluminum and steel materials [3-8]. Jonckheere et al. [5] examined the influence of the tool size, tool rotation speed (TRS), and plunge depth on the properties of friction stir spot welded (FSSWed) Al-6063-T6 alloy. The authors reported that using a larger tool leads to a larger weld region and resulted in a higher lap-shear force. Tozaki et al. [6] studied the influence of pin

---

* Corresponding Author: barlas@subu.edu.tr

[1] Sakarya University of Applied Sciences, Faculty of Technology
ORCID: https://orcid.org/0000-0001-9063-6501

[2] Sakarya University of Applied Sciences, Faculty of Technology, E-Mail: ozsarac@subu.edu.tr
ORCID: https://orcid.org/0000-0002-4806-1609

length, TRS, and dwell time on static strength in 6061 aluminum alloy. According to researchers, the tensile-shear load increased with increasing TRS, dwell time and pin length. The using of advanced tool materials such as polycrystalline boron nitride, WC-Co for FSSW has paved the way to apply FSSW for steels, especially for DP and TRIP steels commonly used in automotive industry. A minimum nugget size should be obtained by the optimum combination of TRS and plunge speed in FSSW of DP590 dual phase steel sheets, according to the report by Sarkar et al. [7]. Mazzaferro et al. [8] investigated TRS and dwell time on the microstructures and mechanical properties of galvanized TRIP800 steel. They found that the highest lap-shear strength could be produced under the lowest TRS with highest dwell time condition. Lakshminarayanan et al. [9] looked at the effects of TRS, plunge depth and dwell time in FSSW of low carbon automotive steels and according to them, dwell time have a great influence on tensile-shear fracture load. Barlas [10] studied on the weldability of DP600 steel to CuZn30 brass by using different axial load and dwell time of the tool by FSSW. According to the researcher, tensile-strength failure load (TSFL) increased with the increasing of the tool load and dwell time, in addition the tool load has a great role in obtaining a favorable joint. Also Barlas [11] focused on the effect of TRS, dwell time and to be welded sheets position on the quality of FSSWed copper / brass bimetal sheets. The author revealed that the failure load increased with increasing TRS and / or dwell time, as the brass sheet was in upper position during the process. Recently, Garcia-Castillo et al. [12] aimed to understand the role of TRS, axial feed rate in the joints of thin Ti6Al4V sheets by experimental study and finite element modelling. According to authors, TRS and feed rate determined the temperature distribution during the process and using a higher axial feed rate lead to reduce the peak temperature and heat input, whereas the temperature increased with increment the TRS. Obtained temperatures affected the microstructural features such as α-β phase transformation, evolution of microstructural zones and hardness values of the titanium alloy joints. Shen et al. [3] reviewed the advances about FSSW. They pointed out that there is a lack of experimental results about the brass materials joined by FSSW. Therefore, the present study interested in the role of vertical tool load (VTL) on joint properties of CuZn30 brass sheet in FSSW process.

2. EXPERIMENTAL DETAILS

CuZn30 (30.5 Zn and 69.1 Cu) brass with dimensions of 110 (length) × 25 (width) × 1 (thickness) was used in FSSW process in overlap joint form, in this study (chemical composition in wt. % and dimensions in mm). All spot joint trials were done with tool made by EN X40CrMoV5 steel due to its high strength at elevated temperatures consisted of a shoulder diameter of 15 mm with concave shaped with a pin length of 0.6 mm (Fig. 1). Table 1 displays the FSSW conditions. The VTL values were simultaneously collected equipped with two load-cells and data acquisition system fixed bottom the backing plate during the FSSW. The temperatures were simultaneously measured by using K-type thermocouple having a diameter of 1 mm. Measurement from lap joint was done between the upper and lower sheets at mid-width. Tensile-shear tests were performed by a Shimadzu Tester at a cross-head speed of 2.5 $mm \cdot min^{-1}$ and an average value of three specimens presented as the result. The cross-sectional samples for microstructure observation and microhardness measurement were polished and etched by a solution consisted of 100 ml of H_2O, 4 ml of saturated NaCl, 2 g of $Cr_2K_2O_7$, and 5 ml of H_2SO_4. Optical microscope (OM) inspection in weld zones was made by a Nikon Eclipse L150A equipped with an image analysis software and a JEOL JSM 6060LV scanning electron microscope (SEM) equipped with energy dispersive X-ray spectroscopy (EDS) apparatus was used to characterize fracture surface of the failed tensile test specimens. Vickers microhardness (HV) test was utilized on etched cross-sectional sample applying a load of 100 g and a dwell time of 10 s by using a 402 MVD Model Wilson Hardness Tester. OM and SEM observations and microhardness test were carried out on the FSSWed joint having the best performance.

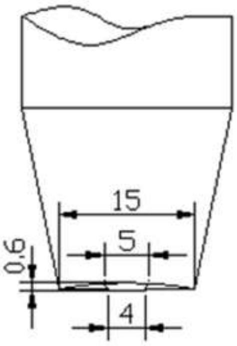

Figure 1 Tool used in FSSW processes (dimensions in mm)

Table 1
The FSSW parameters used in the process

VTL (kgf)	tool rotation speed (rpm)	tool tilt angle (°)	tool dwell time (s)	tool rotation direction
520	1100	0	7	Clockwise
590				
660				
730				
800				
870				

3. RESULTS and DISCUSSION

Surfaces of FSSWed trials are presented in Fig. 2. All of them have some weld flash and keyholes. Moreover, the brownish color change because of oxidation around the outer periphery shoulder is pointed out, especially in the joints at VTLs of 730 - 870 kgf. Tool load in the process affects the temperature distribution [10, 11]. Therefore, to attain the temperatures is important during FSSW, since it plays a key role in generation of mechanical properties and material flow [3]. As can be seen in Figure 3, the temperature measurements show that the frictional heat generation between the shoulder and the upper work-piece increased with increasing the VTL. The peak temperature reached to 835 °C at VTL of 870 kgf. Increment in the peak temperature led to produce more weld flash due to increasing the deformation, so this is more distinctive for the trials at 730 - 870 kgf. All obtained values are lower than the melting point (900 - 920 °C) and zinc evaporation temperature (907 °C) of the brass alloy. Consequently, suitable FSSW parameters were carried out in order to make a solid-state welding.

Figure 2 Joint surfaces after the FSSW process (kgf): (a) 520, (b) 590, (c) 660, (d) 730, (e) 800 and (f) 870

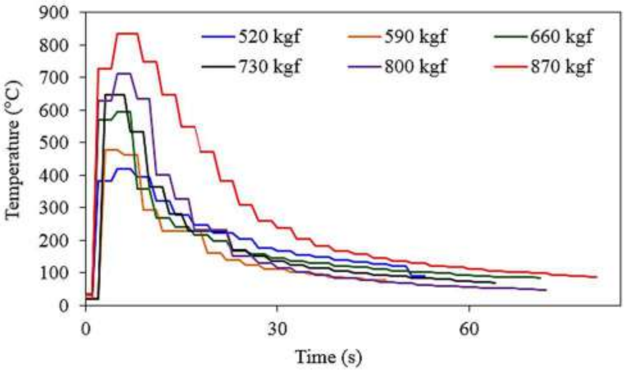

Figure 3 Temperature distributions dependence on VTL values

TSFL and images of the failed samples are given in Figures 4 and 5, respectively. TSFL increased with the increasing the VTL from 520 kgf to 800 kgf and decreased in the highest TL of 870 kgf. The highest TSFL value of approximately 6.5 kN was achieved when VTL of 800 kgf was applied and then it dropped to 4.5 kN which close to that of VTLs of 660 kgf and 730 kgf. In addition, a satisfying metallurgical bonding not occurred between the upper and lower sheets for the trials at 520-660 kgf, as can be obviously seen in Figures 5a-c. Even if just a bit deformation on the surface of the lower sheets clarified with increasing VTL, it did not adequate to bonding in the used conditions. Therefore, it might be said that deformation amount on the lower material is characteristic reagent to an acceptable bonding. On the other hand, a suitable bonding could be produced beginning from 730 to 870 kgf (Fig. 5d). Figure 5 also depicts that the metallurgical bonding mainly happened between bottom and around of the pin and it might probably be developed to the outwards. It is believed that the joints at 730, 800 and 870 kgf confirm this assessment, since they failed away from the pin around. The best joint failed with button pull out mode and a button with diameter of almost 5 mm from the lower sheet remained after completed the tearing by the test machine (Fig. 5e), whereas the sheets at 730 kgf separated with interfacial fracture mode (Fig. 5d). Furthermore, the joint at 870 kgf fractured at the outer periphery shoulder on the upper sheet. It was revealed in the OM observation that the thickness of the upper sheet after used the highest VTL of 870 kgf lower than that of 800 kgf, as obviously seen in the presented measurements in Fig. 6. The upper sheet in the weld region was thinned down to approximately 50 % according to its beginning due to excessive heat input and mechanical deformation. Therefore, the dropping in the TSFL value of the joint at 870 kgf can be attributed to the thinning of upper sheet. From this point of view, it should be noticed that not only insufficient VTL, but also excessive load leads to reducing of the weld performance due to excessive deformation on the upper material. SEM image denoting the presence of elongated dimples (Fig. 7) on the fracture surface for 800 kgf indicates the typical tensile-shear fracture mode. In addition, it is exhibited that there is no remarkably altering in the composition in the bonded zone for the best joint with regard to EDS analysis result.

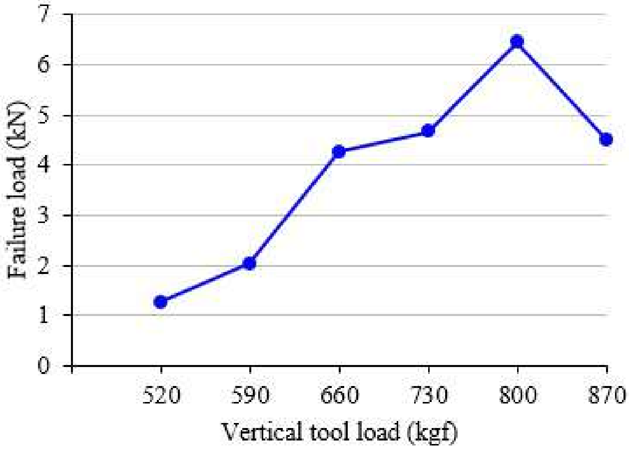

Figure 4 TSFL variation of the test samples according to VTL

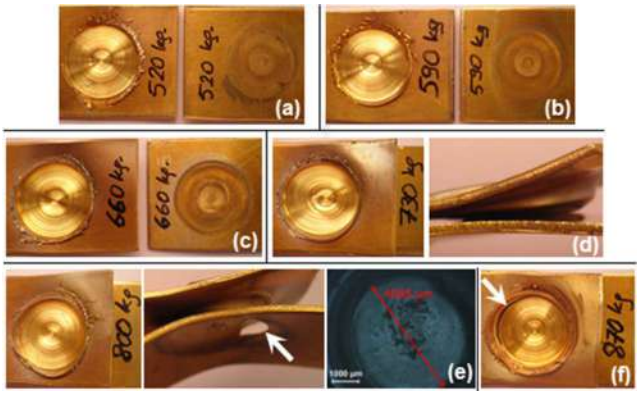

Figure 5 Images of failed FSSW samples (a) 520 kgf, (b) 590 kgf, (c) 660 kgf, (d) 730 kgf, (e) 800 kgf, (f) 870 kgf

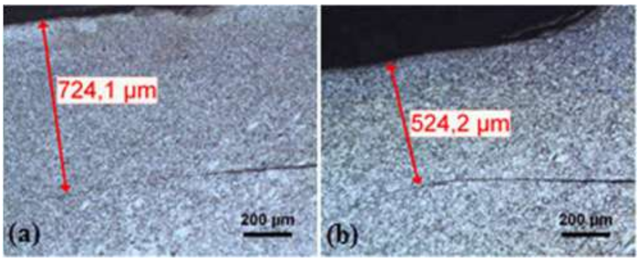

Figure 6 Cross-sectional measurements of the shorter area at the upper sheets (a) 800 kgf and (b) 870 kgf

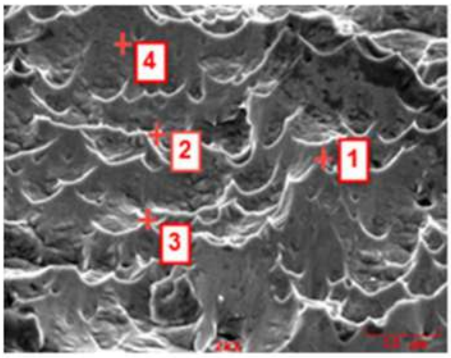

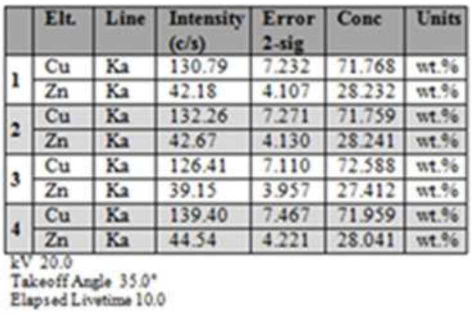

	Elt.	Line	Intensity (c/s)	Error 2-sig	Conc	Units
1	Cu	Ka	130.79	7.232	71.768	wt.%
	Zn	Ka	42.18	4.107	28.232	wt.%
2	Cu	Ka	132.26	7.271	71.759	wt.%
	Zn	Ka	42.67	4.130	28.241	wt.%
3	Cu	Ka	126.41	7.110	72.588	wt.%
	Zn	Ka	39.15	3.957	27.412	wt.%
4	Cu	Ka	139.40	7.467	71.959	wt.%
	Zn	Ka	44.54	4.221	28.041	wt.%

kV 20.0
Takeoff Angle 35.0°
Elapsed Livetime 10.0

Figure 7 SEM image and EDS analysis results on the fractured surface of the best joints

Figure 8 displays the macro-image of FSSWed joint at 800 kgf. Weld defect such as porosity, crack etc. could not be determined in the weld region and also the cross-section comprised of the shoulder and pin geometry is distinctive. Moreover, the keyhole depth is considerably less than that of common applications, since a very short pin was used in this study. Nevertheless, a keyholeless weld region could be nearly accomplished by the used tool geometry. It is believed that suchlike keyhole formation or keyholeless zone contributes to TSFL value, if a sufficient bonding is produced. As presented in Figure 9, a stir zone (SZ) and the heat-affected zone (HAZ) as well as the base metal (BM) have been developed in the weld region. The grains in the BM contain large deformation twins. The HAZ consisted of increased grains with less twins in comparison with that of the BM. However, a thermo-mechanically affected zone which characterized with elongated and / or rotated grains was not clearly stated in the FSSW process, alike in the result of previous study [10]. The reached temperatures in this joint are enough to recrystallization. Hence, recrystallized fine brass grains formed in the SZ were caused by the combination of intense plastic deformation and raised temperature. Furthermore, the grain size from the top to the bottom within SZ slightly decreased around the pin center, since the bottom side of weld region exposed to a shorter cycle. It was also recognized that the grains within both area where the bottom of periphery of the shoulder is relatively finer than that of the other areas in the SZ. It is considered that the circumference of shoulder with concave shaped brought about a more forging effect rather than heat dissipation for the areas.

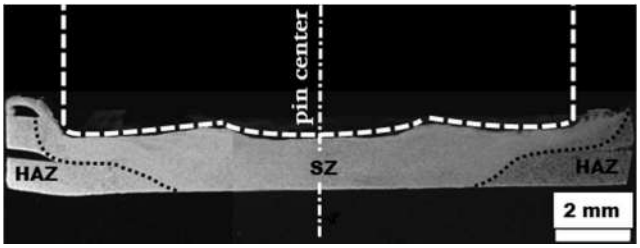

Figure 8 Cross-sectional macro-view of the FSSWed joint at VTL of 800 kgf

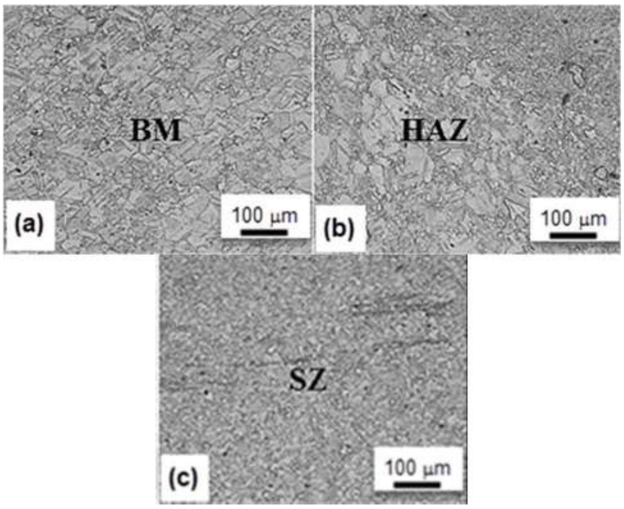

Figure 9 Microstructure zones of the best joint (a) CuZn30 BM, (b) HAZ, and (c) SZ

The hardness values in the weld region were affected by the change in the microstructures. It is understood that the hardness in the weld region was governed by three factors in the FSSW study of CuZn30; softening of annealing effect, grain refinement and deformation twins. On the other hand, it is supposed that there is no influence of zinc content on the hardness, since it is similar to the beginning material condition, taken account of the temperature measurement together with EDS analysis. The CuZn30 BM and the SZ have average hardness of 144.5 HV ± 4.6 and 114.2 HV ± 6.1, respectively, in addition an inhomogeneous distribution was seen in the hardness values in the SZ, viz., the SZ softened according to BM even though decreasing in its grains, since the dominant mechanism was the annealing effect. Besides, the hardness increased from the top (108.2 HV) to bottom (116.5 HV) around the centerline of the SZ due to the presence of slightly finer grains at the bottom side. However, the different hardness values from 135.8 to 150.2 HV were measured on the areas where around the bottom of the shoulder peripheries (namely, almost around the weld flashes) due to presence of the finest grains in the weld region. It might be ascribed to a rapid cooling in the area after the squeeze by the shoulder. As for the HAZ, it has between hardness of 121.3 HV and 127.7 HV (average value 124.8 HV ± 2.6), even though its larger grains according to the SZ. It can be said that the hardness in here was affected by together the deformation twins and coarse grains. As well known, dislocation movement is difficult in fine grained and twinned microstructures. Eventually, it has taken into account the overall changing of the hardness values in the weld region, it is believed that the grain refinement in this study has a little bit decisive effect than the others. On the other hand, the fracture zone for this type overlap joint was affected by the combination of the hardness distribution and the thinning of the upper sheet. Briefly, the cross-section of the SZ will be thickened due to a good metallurgical bonding, thus required failure load in order to fracture will increase by properly chosen the FSSW parameters. All in all, the fracture experienced relatively weaker section where between the SZ and HAZ in the present work.

4. CONCLUSIONS

The influences of vertical tool load on the features of FSSWed CuZn30 brass joint were investigated and the following conclusions were drawn: VTL level has important role to provide a metallurgical bonding between the work-pieces, as the other parameters were constant. The peak temperature induced by friction between the tool and sheets increased with increasing the vertical tool load and it reached to 835 °C at the highest VTL of 870 kgf. TSFL also increased with increasing VTL from 520 kgf to 800 kgf and then dropped in the highest VTL of 870 kgf due to the material loss in the upper sheet. A defect-free weld could be done in VTL of 800 kgf and it has the highest TSFL of almost 6.5 kN. The weld region comprised of the stir and the heat-affected zones with the brass base metal. Annealing, grain refining and twinning mechanisms affected the microhardness properties of these zones.

Funding

The authors received no financial support for the research, authorship, and/or publication of this paper.

The Declaration of Conflict of Interest/ Common Interest

No conflict of interest or common interest has been declared by the authors.

Authors' Contribution

Z.B: Making of the experimental study plan including determining of the materials, parameters and etc., Literature survey, Conducting of the tests, Data collection, Evaluation of the test results, Writing of the paper.

U.O: Literature survey, Conducting of the tests, Data collection, Evaluation of the test results, Writing of the paper.

The Declaration of Ethics Committee Approval

The authors declare that this document does not require an ethics committee approval or any special permission.

The Declaration of Research and Publication Ethics

The authors of the paper declare that they comply with the scientific, ethical and quotation rules of SAUJS in all processes of the paper and that they do not make any falsification on the data collected. In addition, they declare that Sakarya University Journal of Science and its editorial board have no responsibility for any ethical violations that may be encountered, and that this study has not been evaluated in any academic publication environment other than Sakarya University Journal of Science.

REFERENCES

[1] Z. Zhang, X. Yang, J. Zhang, G. Zhou, X. Xu, B. Zou, “Effect of welding parameters on microstructure and mechanical properties of friction stir spot welded 5052 aluminum alloy”, Materials and Design, vol. 32, no. 8–9, pp. 4461–4470, 2011.

[2] S. F Tebyani, K. Dehghani, “Effects of SiC nanopowders on the mechanical properties and microstructure of interstitial free steel joined via friction stir spot welding”, Materials and Design, vol. 90, pp. 660–668, 2016.

[3] Z. Shen, Y. Ding & A. P. Gerlich, “Advances in friction stir spot welding”, Critical Reviews in Solid State and Material Sciences, pp. 1–79, 2019.

[4] M. Li, C. Zhang, D. Wang, L. Zhou, D. Wellmann and Y. Tian, “Friction Stir Spot Welding of Aluminum and Copper: A Review”, Materials, vol. 13, no. 156, pp. 1–23, 2020.

[5] C. Jonckheere, B. D. Meester, C. Cassiers, M. Delhate, A. Simar, “Fracture and mechanical properties of friction stir spot welds in 6063-T6 aluminum alloy”, International Journal of Advanced Manufacturing Technology, vol. 62, pp. 569–575, 2012.

[6] Y. Tozaki, Y. Uematsu, K. Tokaji, “Effect of tool geometry on microstructure and static strength in friction stir spot welded aluminium alloys”, International Journal of Machine Tools and Manufacture, vol. 47, no. 15, pp. 2230–2236, 2007.

[7] R. Sarkar, T. K. Pal, and M. Shome, “Microstructures and properties of friction stir spot welded DP590 dual phase steel sheets”, Science and Technology of Welding and Joining, vol. 19, pp. 436–442, 2014.

[8] C .C. P Mazzaferro, T. S. Rosendo, M. A. D Tier, J. A. E. Mazzaferro, J. F. Dos Santos, T. R. Strohaecker, “Microstructural and Mechanical Observations of Galvanized TRIP Steel after Friction Stir Spot Welding”, Materials and Manufacturing Processes, vol. 30, pp. 1090–1103, 2015.

[9] A. K. Lakshminarayanan, V. E. Annamalai, K. Elangovan, “Identification of optimum friction stir spot welding process parameters controlling the properties of low carbon automotive steel joints”, Journal of Materials Research and Technology, vol. 4, no. 3, pp. 262–272, 2015.

[10] Z. Barlas, “Weldability of CuZn30 Brass/DP600 Steel Couple by Friction Stir Spot Welding” Acta Physica Polonica A, vol. 132, pp. 991–993, 2017.

[11] Z. Barlas, “Effect of friction stir spot weld parameters on Cu/CuZn30 bimetal joints”, International Journal of Advanced Manufacturing Technology, vol. 80, pp. 161–170, 2015.

[12] F. A. Garcia-Castillo, L. A. Reyes, C. Garza, O. E. Lopez-Botello, G. M. Hernandez-Munoz, and P. Zambrano-Robledo, “Investigation of Microstructure, Mechanical Properties, and Numerical Modeling of Ti6Al4V Joints Produced by Friction Stir Spot Welding”, Journal of Materials Engineering and Performance, vol. 29, no. 6, pp. 4105–4116, 2020.

SAKARYA ÜNİVERSİTESİ
FEN BİLİMLERİ ENSTİTÜSÜ
DERGİSİ

Sakarya University Journal of Science
SAUJS

e-ISSN 2147-835X | Period Bimonthly | Founded: 1997 | Publisher Sakarya University |
http://www.saujs.sakarya.edu.tr/en/

Title: Semi-Analytical and Finite Element Investigations of the Vibration of a Stepped Beam on an Elastic Foundation

Authors: Hakan ERDOĞAN, Safa Bozkurt COŞKUN

Recieved: 2020-03-23 02:16:08

Accepted: 2020-10-07 14:01:49

Article Type: Research Article

Volume: 24
Issue: 6
Month: December
Year: 2020
Pages: 1321-1328

How to cite
Hakan ERDOĞAN, Safa Bozkurt COŞKUN; (2020), Semi-Analytical and Finite Element Investigations of the Vibration of a Stepped Beam on an Elastic Foundation. Sakarya University Journal of Science, 24(6), 1321-1328, DOI: https://doi.org/10.16984/saufenbilder.707631
Access link
http://www.saujs.sakarya.edu.tr/en/pub/issue/57766/707631

Sakarya University Journal of Science 24(6), 1321-1328, 2020

Semi-Analytical and Finite Element Investigations of the Vibration of a Stepped Beam on an Elastic Foundation

Hakan ERDOĞAN*1, Safa Bozkurt COŞKUN2

Abstract

In this study free vibration behavior of a stepped beam on an elastic foundation is considered. The vibration of uniform beams on an elastic foundation has been previously studied extensively and various solutions are available in the literature. However, the problem considered in current study appears not to have been widely covered in the literature and analytical solutions are strictly limited. To this aim, semi-analytical solutions are obtained first by using Adomian decomposition method, then finite element solutions are computed via structural finite element analysis software (SAP 2000). The free vibration analysis of stepped beam considering the combinations of different support conditions at each end are performed employing semi-analytical and finite element methods. The findings of the analysis are compared and discussed in detail.

Keywords: segmented beam, elastic foundation, vibration, Adomian decomposition method

1. INTRODUCTION

Beam on elastic foundation problems are of great interest for researchers in the fields of civil, mechanical and aeronautical engineering related to the design of structural members of buildings, aircrafts, pipes, railroads, etc.

In the literature, numerous studies were conducted on the vibration analysis of beams [1-3]. Researchers also focused on the special cases such as stepped beams [4] and beams on elastic foundations [5]. Wang [6], Kukla [7] and Belles *et al.* [8] are three interesting contributions to the technical studies about the subject. Thambiratnam and Zhuge [9] developed a simple finite element method and applied to treat the free vibration of

---

* Corresponding Author: hakan.erdogan@kocaeli.edu.tr
1 Kocaeli University, ORCID: https://orcid.org/0000-0002-7241-7652
2 Kocaeli University, E-Mail: sb.coskun@kocaeli.edu.tr
ORCID: https://orcid.org/0000-0002-1962-7722

analysis of Euler-Bernoulli beams on elastic foundations for different cases. Durgun [10] also conducted a study on the analysis of stepped beams on elastic foundation by employing Homotopy Perturbation Method (HPM). Durgun [8] solved the same numerical example with Wang [6] and obtained exactly the same results up to four decimals. The solution proposed by Wang [6] was tedious and is only valid for specific cases and he reported the results only for the beams having free-free and simply supported end conditions. In addition to Wang's work, Durgun [10] also presented the results for fixed-fixed and fixed-hinged end condition cases. However, Durgun [10] has not verified his findings regarding the fixed-fixed and fixed-hinged end conditions with other reliable methods in the literature.

The main aim of this study is to provide semi-analytical and finite element solutions to the same problem in order to verify the results obtained by using HPM [10] and fulfill the lack of analytical solutions provided in the work by Wang [6].

2. VIBRATION OF STEPPED BEAM ON ELASTIC FOUNDATION

In this section, vibration of an Euler beam on Winkler foundation is considered that are the most widely used models for the beams on elastic foundations. Such a beam is shown in Figure 1.

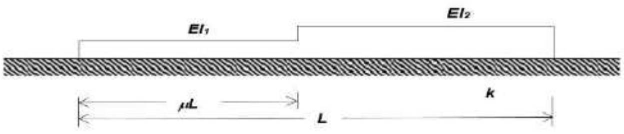

Figure 1 Stepped beam on elastic foundation

Equation of motion for a uniform Euler beam on Winkler foundation is given as:

$$EI\frac{\partial^4 y(x,t)}{\partial x^4}+\rho A\frac{\partial^2 y(x,t)}{\partial t^2}+ky(x,t)=0 \qquad (1)$$

where *EI* is the flexural rigidity of the beam, ρ is the density per unit volume, *A* is the cross-sectional area, k is the stiffness of Winkler foundation and *y* is the transverse displacement.

In order to find the eigenfrequencies ω of the beam one may assume

$$y(x,t)=w(x)\,e^{i\omega t} \qquad (2)$$

Substituting Eq.(2) in Eq.(1) yields

$$EI\frac{d^4w(x)}{dx^4}-\rho A\omega^2 w(x)+kw(x)=0 \qquad (3)$$

Eq.(3) can be rearranged as

$$\frac{d^4w(x)}{dx^4}-\left(\lambda^4-\frac{k}{EI}\right)w(x)=0 \qquad (4)$$

where $\lambda^4=\omega^2\rho A/EI$. Introducing the parameter β, such that, $\beta^4=\lambda^4-\frac{k}{EI}$ solution to Eq.(4) is

$$w(x)=C_1\sin(\beta x)+C_2\cos(\beta x)$$
$$+C_3\sinh(\beta x)+C_4\cosh(\beta x) \quad (5)$$

when $\beta^4\geq 0$ which describes that foundation stiffnes has no effect in the solution. However, if the vibration frequency of the beam is relatively low, *i.e.*, $\beta^4<0$ the solution of Eq.(4) becomes

$$w(x)=C_1\sin\left(\frac{\beta x}{\sqrt{2}}\right)\sinh\left(\frac{\beta x}{\sqrt{2}}\right)+$$
$$C_2\sin\left(\frac{\beta x}{\sqrt{2}}\right)\cosh\left(\frac{\beta x}{\sqrt{2}}\right)+C_3\cos\left(\frac{\beta x}{\sqrt{2}}\right)\sinh\left(\frac{\beta x}{\sqrt{2}}\right)+$$
$$C_4\cos\left(\frac{\beta x}{\sqrt{2}}\right)\cosh\left(\frac{\beta x}{\sqrt{2}}\right)$$
(6)

which is a different solution when compared to Eq.(5). The coefficients C_1, C_2, C_3, and C_4 in both solutions can be evaluated according to boundary conditions at the supports. These conditions are given as follows:

- For free end $w''(x)=0$ and $w'''(x)=0$
- For hinged end $w(x)=0$ and $w''(x)=0$
- For clamped end $w(x)=0$ and $w'(x)=0$

There are also four boundary conditions due to continuity at the junction of two segments of the stepped beam. These conditions impose the equality of the displacement, the slope, the moment and the shear force at the junction and given as follows:

- $w_1(x)=w_2(x)$

- $w_1'(x) = w_2'(x)$
- $w_1''(x) = \alpha\, w_2''(x)$
- $w_1'''(x) = \alpha\, w_2'''(x)$

where $\alpha = I_2/I_1$.

3. ADOMIAN DECOMPOSITION METHOD

In Adomian decomposition method (ADM) a general form of the following differential equation is assumed.

$$Lu + Nu + Ru = g(x) \tag{7}$$

where $u(x)$ is the unknown solution, $g(x)$ is the source term, L is the linear operator, N is the nonlinear operator and R is the operator for remainder terms. The solution to Eq.(7) is

$$u(x) = f(x) - L^{-1}(Nu) - L^{-1}(Ru) \tag{8}$$

where L^{-1} is the inverse linear operator and $f(x) = L^{-1}(g(x))$. The solution is constructed with an infinite series in the following form

$$u(x) = \sum_{n=0}^{\infty} u_n(x) \tag{9}$$

The nonlinear term *Nu* is represented by so-called Adomian polynomials given below.

$$Nu = \sum_{n=0}^{\infty} A_n(u_0, u_1, \cdots, u_n) \tag{10}$$

where A_n is the n^{th} Adomian polynomial defined as the following term.

$$A_n = \frac{1}{n!}\frac{d^n}{d\lambda^n} N\left(\sum_{n=0}^{\infty} \lambda^k u_k\right) \tag{11}$$

The method leads to successive approximations as follows:

$$u_0(x) = f(x) \tag{12}$$

$$u_n(x) = -L^{-1}(Ru_{n-1} - A_{n-1}) \tag{13}$$

Finally, the solution is calculated by adding the successive approximations given in Eqs.(12-13). An N^{th} order analytical approximation includes the terms up to u_N as given below

$$u(x) = \sum_{n=0}^{N} u_n(x) \tag{14}$$

For further details of the method, the reader may refer to [11].

4. ADM SOLUTION OF THE PROBLEM

An initial approximation based on Eq.(12) may be obtained as

$$w_0(x) = Ax^3 + Bx^2 + Cx + D \tag{15}$$

where $A = y'''(0)/6$, $B = y''(0)/2$, $C = y'(0)$ and $D = y(0)$. Successive approximations for an N^{th} order solution may be computed according to Eq.(13) as

$$w_n(x) = L^{-1}(\beta^4 y_{n-1}) \ , \ n > 0 \tag{16}$$

Since there are two segments in the stepped beam, an initial approximation of the form given in Eq.(15) is assumed for both segments of the beam.

$$w_0^{(1)}(x) = A_1x^3 + B_1x^2 + C_1x + D_1 \tag{17}$$

$$w_0^{(2)}(x) = A_2x^3 + B_2x^2 + C_2x + D_2 \tag{18}$$

Eight boundary conditions are required to determine eight unknowns introduced in Eqs.(17) and (18). These conditions are four boundary conditions at the supports and four continuity conditions. Hence eight equations in eight unknowns are produced can be represented in the following matrix form.

$$[K]_{8\times 8}\{\Lambda\}_{8\times 1} = \{0\}_{8\times 1} \tag{19}$$

where $[K]$ includes the term β which is the function of vibration frequency ω and the unknown vector $\{\Lambda\}$ includes unknown coefficients in the initial approximations in Eqs.(17) and (18). The trivial solution of Eq.(19) corresponds the undeformed beam. Hence, a nontrivial solution to the problem can be obtained by equating the determinant of coefficient matrix to zero that lead to free vibration frequencies of the stepped beam on elastic foundation considered.

5. NUMERICAL APPLICATION

Wang [6] calculated analytical solutions for natural frequencies of two stepped beams on elastic foundation, one simply supported and one with free ends. There are no available analytical solutions for the beam with both ends clamped, the beam with one end clamped and one end simply supported and the beam with one end clamped and one end free. For simplicity following abbreviations are used for different combinations of end conditions.

FF	Free – Free
SS	Both ends simply supported
CC	Clamped – Clamped
CS	Clamped – Simply supported

Wang [6] performed the analysis for the following data: $E = 6.50 \times 10^{11}$ Pa, $\rho = 213.60$ kg/m^2, $H_1 = 0.10$ m, $H_2 = 0.15$ m, $B = 0.08$ m, $L = 5.00$ m. Two different foundation modulus were used in the calculations, $\nu = 1/100$ and $\nu = 1/200$ where ν is defined as k/EI. μ denotes the ratio of the length of thinner segment having depth of H1 to total length L.

SAP2000 [12] was employed for obtaining finite element (FE) solutions. Line springs that can be assigned in any of the local axes direction of a frame object is defined in vertical direction to simulate the elastic foundation. SAP2000 [12] distributes the springs associated with the frame object to all of the nodes (Figure 2).

Figure 2 FE model for simply supported stepped beam on elastic foundation (50 beam elements)

Table 1 compares the previous results (analytical [6], HPM [10]) with the results of present study (ADM, FE solution) for natural frequencies of stepped FF beam on elastic foundation. ADM solutions are conducted to 12th order and computations are identical to the analytical [6] and HPM [10] solutions. FE solutions are also in excellent agreement for the first two frequency values.

In Table 2 only first two natural frequencies are available for SS beams [6, 10] and used for comparison. However, first three frequencies are computed for stepped SS beam on elastic foundation using ADM and FEM. ADM results are in excellent agreement with previous results while FE solutions are in very good agreement with the same results for which first two frequencies have the same accuracy of analytical solution.

Analytical solutions for the first three frequencies for stepped CC and CS beams on elastic foundation are not available in the literature. Only HPM solutions [10] exist and the results of this study for these cases are compared with only HPM results.

In Table 3 and Table 4 it seems that ADM solutions are in excellent agreement with HPM results [10]. FE solutions are in very good agreement with both results as in previous cases.

Table 1
Natural frequencies of FF stepped beam on elastic foundation

	v = 1 /100											
	Wang [6], Durgun [10]			ADM			FE (50 Elements)			FE (100 Elements)		
μ	f_1 (Hz)	f_2 (Hz)	f_3 (Hz)	f_1 (Hz)	f_2 (Hz)	f_3 (Hz)	f_1 (Hz)	f_2 (Hz)	f_3 (Hz)	f_1 (Hz)	f_2 (Hz)	f_3 (Hz)
0	5.8531	5.8531	96.4081	5.8531	5.8531	96.4081	5.8531	5.8531	96.2888	5.8531	5.8531	96.3783
0.1	5.8534	6.2201	101.0194	5.8534	6.2201	101.0194	5.8534	6.2199	100.8885	5.8534	6.2201	100.9867
0.2	5.8557	6.5291	100.7912	5.8557	6.5291	100.7912	5.8558	6.5287	100.6555	5.8557	6.5290	100.7573
0.3	5.8635	6.7692	93.4247	5.8635	6.7692	93.4247	5.8636	6.7688	93.2962	5.8636	6.7691	93.3926
0.4	5.8821	6.9403	82.2168	5.8821	6.9403	82.2168	5.8822	6.9399	82.1076	5.8821	6.9402	82.1895
0.5	5.9194	7.0513	72.8477	5.9194	7.0513	72.8477	5.9196	7.0509	72.7549	5.9195	7.0512	72.8245
0.6	5.9876	7.1161	66.7402	5.9876	7.1161	66.7402	5.9876	7.1161	66.6565	5.9876	7.1160	66.7193
0.7	6.1046	7.1494	63.2525	6.1046	7.1494	63.2525	6.1048	7.1492	63.1733	6.1047	7.1494	63.2327
0.8	6.2993	7.1637	61.5574	6.2993	7.1637	61.5574	6.2996	7.1636	61.4814	6.2994	7.1637	61.5384
0.9	6.6214	7.1680	61.4321	6.6214	7.1680	61.4321	6.6216	7.1679	61.3585	6.6214	7.1680	61.4137
1.0	7.1685	7.1685	64.5528	7.1685	7.1685	64.5528	7.1685	7.1685	64.4735	7.1685	7.1685	64.5330

	v = 1 /200											
	Wang [6], Durgun [10]			ADM			FE (50 Elements)			FE (100 Elements)		
μ	f_1 (Hz)	f_2 (Hz)	f_3 (Hz)	f_1 (Hz)	f_2 (Hz)	f_3 (Hz)	f_1 (Hz)	f_2 (Hz)	f_3 (Hz)	f_1 (Hz)	f_2 (Hz)	f_3 (Hz)
0	4.1388	4.1388	96.3192	4.1388	4.1388	96.3192	4.1387	4.1387	96.1998	4.1388	4.1388	96.2893
0.1	4.1390	4.3983	100.9251	4.1390	4.3983	100.9251	4.1390	4.3982	100.7942	4.1390	4.3983	100.8924
0.2	4.1406	4.6169	100.6918	4.1406	4.6169	100.6918	4.1407	4.6166	100.556	4.1406	4.6168	100.6579
0.3	4.1462	4.7867	93.3148	4.1462	4.7867	93.3148	4.1462	4.7864	93.1862	4.1462	4.7866	93.2827
0.4	4.1593	4.9076	82.0879	4.1593	4.9076	82.0879	4.1594	4.9074	81.9785	4.1593	4.9076	82.0606
0.5	4.1857	4.9861	72.6959	4.1857	4.9861	72.6959	4.1858	4.9858	72.6029	4.1857	4.9860	72.6727
0.6	4.2340	5.0319	66.5679	4.2340	5.0319	66.5679	4.2341	5.0317	66.4841	4.2340	5.0318	66.5470
0.7	4.3168	5.0554	63.0664	4.3168	5.0554	63.0664	4.3170	5.0553	62.9870	4.3169	5.0554	63.0465
0.8	4.4546	5.0655	61.3656	4.4546	5.0655	61.3656	4.4548	5.0654	61.2893	4.4547	5.0655	61.3465
0.9	4.6823	5.0686	61.2398	4.6823	5.0686	61.2398	4.6824	5.0685	61.1660	4.6823	5.0685	61.2214
1.0	5.0689	5.0689	64.3534	5.0689	5.0689	64.3534	5.0689	5.0689	64.2740	5.0689	5.0689	64.3336

Table 2
Natural frequencies of SS stepped beam on elastic foundation

	v = 1 /100										
	Wang [6], Durgun [10]		ADM			FE (50 Elements)			FE (100 Elements)		
μ	f_1 (Hz)	f_2 (Hz)	f_1 (Hz)	f_2 (Hz)	f_3 (Hz)	f_1 (Hz)	f_2 (Hz)	f_3 (Hz)	f_1 (Hz)	f_2 (Hz)	f_3 (Hz)
0	42.8519	169.9023	42.8519	169.9023	382.0982	42.8518	169.9015	382.0961	42.8519	169.9022	382.0979
0.1	42.5839	166.0556	42.5839	166.0556	366.1519	42.5846	166.0658	366.1715	42.5841	166.0583	366.1570
0.2	41.0205	152.2872	41.0205	152.2872	341.8899	41.0216	152.2827	341.8246	41.0207	152.2861	341.8737
0.3	38.1581	143.7692	38.1581	143.7692	342.1057	38.1587	143.7517	342.0941	38.1583	143.7649	342.1030
0.4	35.0630	143.4669	35.0630	143.4669	323.7582	35.0600	143.4542	323.7748	35.0629	143.4638	323.7625
0.5	32.5477	142.6401	32.5477	142.6401	300.8846	32.5466	142.6422	300.8384	32.5475	142.6407	300.8732
0.6	30.8291	134.7613	30.8291	134.7613	299.4122	30.8275	134.7667	299.3834	30.8287	134.7627	299.4052
0.7	29.8260	124.2508	29.8260	124.2508	291.5502	29.8243	124.2480	291.5687	29.8256	124.2501	291.5550
0.8	29.3576	116.7971	29.3576	116.7971	270.3553	29.3560	116.7862	270.3455	29.3572	116.7945	270.3530
0.9	29.2113	113.7982	29.2113	113.7982	256.8519	29.2102	113.7865	256.8102	29.2110	113.7953	256.8416
1.0	29.1940	113.4278	29.1940	113.4278	254.8031	29.1939	113.4272	254.8017	29.1940	113.4277	254.8029

	v = 1 /200										
	Wang [6], Durgun [10]		ADM			FE (50 Elements)			FE (100 Elements)		
μ	f_1 (Hz)	f_2 (Hz)	f_1 (Hz)	f_2 (Hz)	f_3 (Hz)	f_1 (Hz)	f_2 (Hz)	f_3 (Hz)	f_1 (Hz)	f_2 (Hz)	f_3 (Hz)
0	42.6517	169.8519	42.6517	169.8519	382.0758	42.6515	169.8511	382.0737	42.6516	169.8518	382.0755
0.1	42.3838	166.0034	42.3838	166.0034	366.1278	42.3825	166.0136	366.1473	42.3820	166.0060	366.1329
0.2	40.8063	152.2257	40.8063	152.2257	341.8616	40.8074	152.2212	341.7964	40.8066	152.2246	341.8455
0.3	37.9155	143.6983	37.9155	143.6983	342.0765	37.9161	143.6809	342.0649	37.9156	143.6940	342.0738
0.4	34.7788	143.3927	34.7788	143.3927	323.7259	34.7785	143.3800	323.7425	34.7787	143.3896	323.7302
0.5	32.2173	142.5639	32.2173	142.5639	300.8481	32.2161	142.5659	300.8019	32.2170	142.5645	300.8367
0.6	30.4553	134.6785	30.4553	134.6785	299.3743	30.4537	134.6839	299.3454	30.4549	134.6799	299.3672
0.7	29.4174	124.1574	29.4174	124.1574	291.5103	29.4157	124.1546	291.5288	29.4170	124.1567	291.5151
0.8	28.9261	116.6927	28.9261	116.6927	270.3108	28.9245	116.6818	270.3010	28.9257	116.6900	270.3084
0.9	28.7695	113.6864	28.7695	113.6864	256.8028	28.7685	113.6747	256.7611	28.7692	113.6835	256.7925
1.0	28.7506	113.3144	28.7506	113.3144	254.7527	28.7505	113.3139	254.7513	28.7506	113.3143	254.7525

Table 3
Natural frequencies of CC stepped beam on elastic foundation

	v = 1 /100											
	Durgun [10]			ADM			FE (50 Elements)			FE (100 Elements)		
μ	f_1 (Hz)	f_2 (Hz)	f_3 (Hz)	f_1 (Hz)	f_2 (Hz)	f_3 (Hz)	f_1 (Hz)	f_2 (Hz)	f_3 (Hz)	f_1 (Hz)	f_2 (Hz)	f_3 (Hz)
0	96.4081	265.3269	520.0532	96.4081	265.3269	520.0532	96.4080	265.3266	520.0519	96.4080	265.3267	520.0528
0.1	83.6134	244.1429	489.1152	83.6134	244.1429	489.1152	83.6146	244.1571	489.1690	83.6136	244.1464	489.1286
0.2	83.6454	237.3657	463.9575	83.6454	237.3657	463.9575	83.6489	237.3735	463.8752	83.6462	237.3675	463.9367
0.3	82.1239	224.3318	461.3383	82.1239	224.3318	461.3383	82.1273	224.3007	461.2855	82.1247	224.3239	461.3249
0.4	78.6631	222.7447	442.1322	78.6631	222.7447	442.1322	78.6628	222.7168	442.1659	78.663	222.7376	442.1406
0.5	76.2090	221.3049	410.8338	76.2090	221.3049	410.8338	76.2048	221.3131	410.7568	76.2079	221.3068	410.8143
0.6	76.4158	208.0189	409.6846	76.4158	208.0189	409.6846	76.4094	208.0273	409.6691	76.4141	208.0210	409.6806
0.7	78.2691	196.9283	391.5603	78.2691	196.9283	391.5603	78.2638	196.9116	391.5853	78.2677	196.9240	391.5664
0.8	77.9781	198.5024	373.5053	77.9781	198.5024	373.5053	77.9761	198.479	373.4486	77.9775	198.4964	373.4910
0.9	72.8548	196.4500	377.8571	72.8548	196.4500	377.8571	72.8546	196.4459	377.8291	72.8547	196.4489	377.8500
1.0	64.5528	176.9868	346.7543	64.5528	176.9868	346.7543	64.5527	176.9866	346.7534	64.5527	176.9867	346.7540

	v = 1 /200											
	Durgun [10]			ADM			FE (50 Elements)			FE (100 Elements)		
μ	f_1 (Hz)	f_2 (Hz)	f_3 (Hz)	f_1 (Hz)	f_2 (Hz)	f_3 (Hz)	f_1 (Hz)	f_2 (Hz)	f_3 (Hz)	f_1 (Hz)	f_2 (Hz)	f_3 (Hz)
0	96.3192	265.2946	520.0368	96.3192	265.2946	520.0368	96.311	265.2943	520.0355	96.3191	265.2944	520.0363

0.1	83.5108	244.1077	489.0976	83.5108	244.1077	489.0976	83.512	244.1219	489.1513	83.5110	244.1110	489.1110
0.2	83.5418	237.3276	463.9370	83.5418	237.3276	463.9370	83.5453	237.3354	463.8548	83.5426	237.3294	463.9162
0.3	82.0136	224.2872	461.3165	82.0136	224.2872	461.3165	82.017	224.2562	461.2638	82.0144	224.2794	461.3032
0.4	78.5377	222.6973	442.1082	78.5377	222.6973	442.1082	78.5374	222.6694	442.1422	78.5375	222.6902	442.1169
0.5	76.0668	221.2558	410.8071	76.0668	221.2558	410.8071	76.0625	221.2640	410.7300	76.0657	221.2578	410.7876
0.6	76.2617	207.9649	409.6571	76.2617	207.9649	409.6571	76.2553	207.9734	409.6416	76.2601	207.9669	409.6531
0.7	78.1095	196.8683	391.5305	78.1095	196.8683	391.5305	78.1042	196.8517	391.5555	78.1081	196.8641	391.5367
0.8	77.8138	198.4392	373.4726	77.8138	198.4392	373.4726	77.8118	198.4158	373.4159	77.8133	198.4332	373.4582
0.9	72.6783	196.3846	377.8232	72.6783	196.3846	377.8232	72.6780	196.3805	377.7952	72.6782	196.3835	377.8162
1.0	64.3534	176.9142	346.7173	64.3534	176.9142	346.7173	64.3534	176.9140	346.7164	64.3534	176.9141	346.7169

Table 4

Natural frequencies of CS stepped beam on elastic foundation

	v = 1 /100											
	Durgun [10]			ADM			FE (50 Elements)			FE (100 Elements)		
μ	f_1 (Hz)	f_2 (Hz)	f_3 (Hz)	f_1 (Hz)	f_2 (Hz)	f_3 (Hz)	f_1 (Hz)	f_2 (Hz)	f_3 (Hz)	f_1 (Hz)	f_2 (Hz)	f_3 (Hz)
0	66.5734	214.9847	448.4203	66.5734	214.9847	448.4203	66.5731	214.9836	448.4177	66.5731	214.9837	448.4182
0.1	56.5047	195.8623	420.3049	56.5047	195.8623	420.3049	56.5049	195.8703	420.3450	56.5046	195.8636	420.3136
0.2	56.2305	192.4146	399.6111	56.2305	192.4146	399.6111	56.2318	192.4243	399.5628	56.2307	192.4164	399.5977
0.3	55.8497	181.3330	393.1700	55.8497	181.3330	393.1700	55.8516	181.3177	393.1022	55.8500	181.3286	393.1518
0.4	53.7662	176.7855	386.3098	53.7662	176.7855	386.3098	53.7671	176.7596	386.3394	53.7662	176.7784	386.3160
0.5	50.7342	177.9354	355.5730	50.7342	177.9354	355.5730	50.7338	177.9263	335.5419	50.7338	177.9325	355.5641
0.6	47.9739	172.5648	346.3939	47.9739	172.5648	346.3939	47.9714	172.5730	346.3369	47.9731	172.5662	346.3785
0.7	46.0879	159.7651	342.7486	46.0879	159.7651	342.7486	46.0845	159.7659	342.7674	46.0869	159.7647	342.7522
0.8	45.1264	148.8735	319.4041	45.1264	148.8735	319.4041	45.1230	148.8606	319.4003	45.1254	148.8697	319.4021
0.9	44.8212	144.0672	301.8586	44.8212	144.0672	301.8586	44.8188	144.0499	301.8069	44.8204	144.0624	301.8447
1.0	44.7878	143.4492	299.0073	44.7878	143.4492	299.0073	44.7876	143.4485	299.0056	44.7876	143.4486	299.0059
	v = 1 /200											
	Durgun [10]			ADM			FE (50 Elements)			FE (100 Elements)		
μ	f_1 (Hz)	f_2 (Hz)	f_3 (Hz)	f_1 (Hz)	f_2 (Hz)	f_3 (Hz)	f_1 (Hz)	f_2 (Hz)	f_3 (Hz)	f_1 (Hz)	f_2 (Hz)	f_3 (Hz)
0	66.4446	214.9448	448.4012	66.4446	214.9448	448.4012	66.4443	214.9438	448.3986	66.4443	214.9438	448.3991
0.1	56.3529	195.8184	420.2844	56.3529	195.8184	420.2844	56.3530	195.8264	420.3245	56.3527	195.8198	420.2931
0.2	56.0771	192.3682	399.5875	56.0771	192.3682	399.5875	56.0784	192.3779	399.5392	56.0773	192.3700	399.5741
0.3	55.6914	181.2788	393.1444	55.6914	181.2788	393.1444	55.6932	181.2634	393.0766	55.6917	181.2744	393.1262
0.4	53.5919	176.7255	386.2827	53.5919	176.7255	386.2827	53.5928	176.6997	386.3124	53.5919	176.7185	386.2889
0.5	50.5341	177.8737	355.5421	50.5341	177.8737	355.5421	50.5333	177.8646	355.5111	50.5337	177.8708	355.5332
0.6	47.7443	172.4997	346.3611	47.7443	172.4997	346.3611	47.7419	172.5079	346.3041	47.7435	172.5011	346.3457
0.7	45.8312	159.6924	342.7145	45.8312	159.6924	342.7145	45.8279	159.6932	342.7333	45.8302	159.6921	342.7181
0.8	44.8500	148.7919	319.3664	44.8500	148.7919	319.3664	44.8466	148.7790	319.3626	44.8490	148.7882	319.3644
0.9	44.5350	143.9791	301.8169	44.5350	143.9791	301.8169	44.5327	143.9618	301.7652	44.5343	143.9743	301.8030
1.0	44.5000	143.3596	298.9644	44.5000	143.3596	298.9644	44.4998	143.3589	298.9626	44.4998	143.3590	298.9630

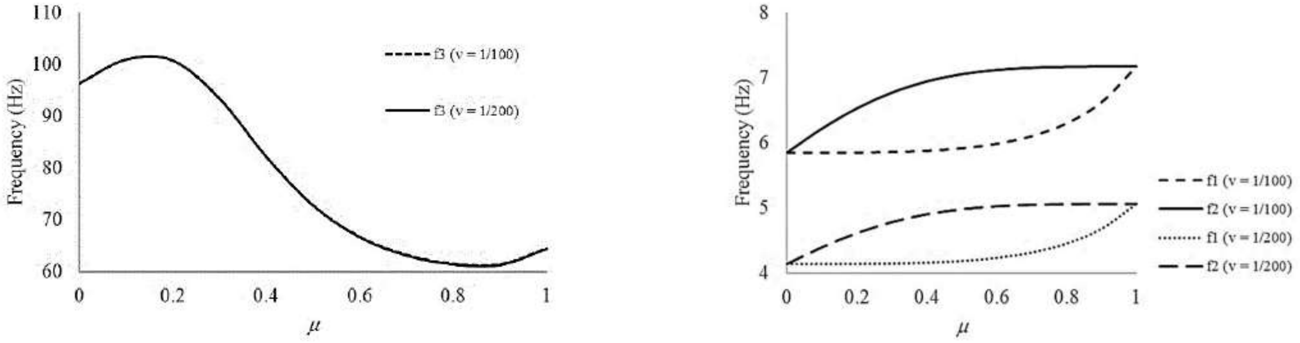

Figure 3 Effect of foundation stiffness on natural frequencies of stepped FF beam

Effect of foundation stiffness on first two frequencies is clearly illustrated in Fig.3 However, foundation effect for the third natural frequency is indistinguishable.

For stepped SS, CC and CS beams there are no significant difference in the natural frequencies for $\nu = 1/100$ and $\nu = 1/200$. Hence, between Figs. 4 and 6 only the variation of first three frequencies is plotted for $\nu = 1/100$.

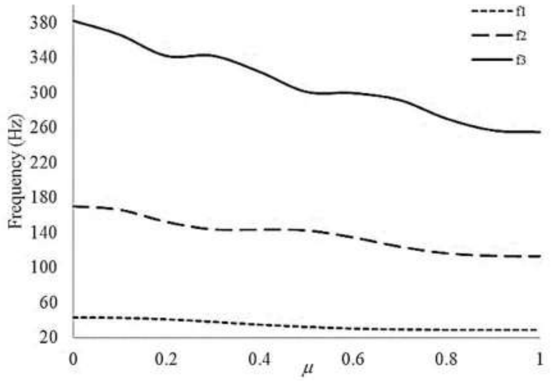

Figure 4 Variation of natural frequencies of stepped SS beam

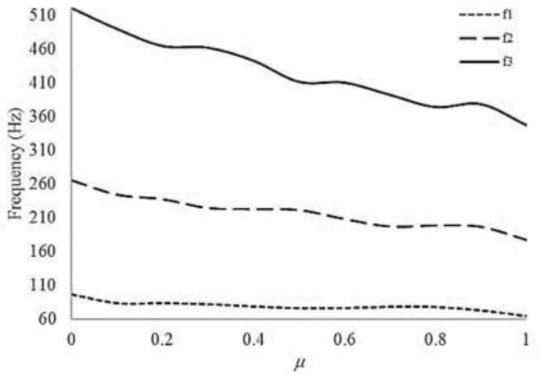

Figure 5 Variation of natural frequencies of stepped CC beam

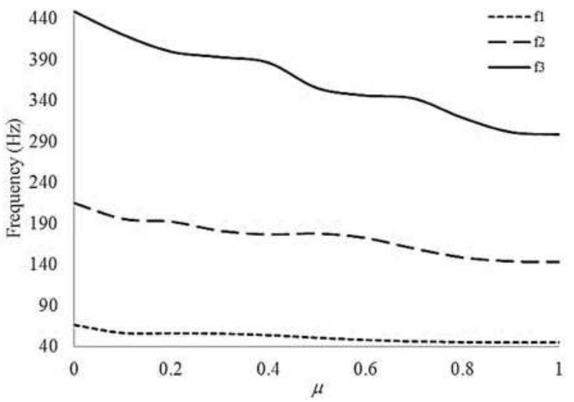

Figure 6 Variation of natural frequencies of stepped CS beam

It can be mentioned that natural frequencies of the stepped SS, CC and SS beams decreases with increasing μ values considering the variations shown in figures 4-6.

6. CONCLUSIONS

In this study, natural frequencies of stepped beams on elastic foundations are investigated via ADM and FEM. Analytical solutions for this problem are available for the beam with free ends and for simply supported beam. There are no other available analytical solutions for the beam with both ends clamped and for the beam with one end clamped and one end simply supported. All four cases previously were solved using HPM. ADM solutions of this study are in perfect agreement with analytical and HPM solutions. FE solutions are computed employing SAP 2000 software by using 50-element and 100-element models. Both FE models produced reliable results when compared ADM and previously available solutions.

Effect of foundation modulus is found to be distinguishable only for stepped FF beam considering the two different foundation modulus investigated in the scope of study. Variation of frequencies with the position of the intersection point of the two segments is also depicted graphically for stepped SS, CC and CS beams for which it is observed that natural frequencies decreases while μ increases. This result makes sense; As μ value increases, the frequency is mostly dominated with segment one that is having relatively low moment of inertia.

Funding

The authors received no financial support for this work.

The Declaration of Conflict of Interest/ Common Interest

No conflict of interest or common interest has been declared by the authors.

Authors' Contribution

In this study, the contributions of the authors during the research, analysis, submission, review and editing stages are equal.

The Declaration of Ethics Committee Approval

The authors declare that this document does not require an ethics committee approval or any special permission.

The Declaration of Research and Publication Ethics

The authors of the paper declare that they comply with the scientific, ethical and quotation rules of SAUJS in all processes of the paper and that they do not make any falsification on the data collected. In addition, they declare that Sakarya University Journal of Science and its editorial board have no responsibility for any ethical violations that may be encountered, and that this study has not been evaluated in any academic publication environment other than Sakarya University Journal of Science.

REFERENCES

[1] J.P. Den Hartog, Advanced Strength of Materials, Dover Publications Inc., New York, pp. 286–290, 1952.

[2] S.P. Timoshenko D.H. Young and W. Weaver, Vibration Problems in Engineering, John Wiley, New York, 1974.

[3] R.D. Blevins, Formulas for Natural Frequency and Mode Shape, New York, 1979.

[4] S.K. Jang and C.W. Bert, “Free Vibration of Stepped Beams: Exact and Numerical Solutions”, Journal of Sound and Vibration, vol. 130, pp. 342-346, 1989.

[5] Y.C. Lai, B.Y. Ting, W.S. Lee and W.R. Becker, “Dynamic Response of Beams on Elastic Foundations”, J. Struct. Engng. ASCE, vol. 118, pp. 853-858, 1992.

[6] J. Wang, “Vibration of Stepped Beams on Elastic Foundations”, Journal of Sound and Vibration, vol. 149, no. 2, pp. 315-322, 1991.

[7] S. Kukla, “Free vibration of a beam supported on a stepped elastic foundation”, Journal of Sound and Vibration, vol. 149, no. 2, pp. 259-265, 1991.

[8] P.M. Belles, M.J. Maurizi, and D.H. Di Luca, “Vibration of stepped beams on non-uniform elastic foundations”, Journal of Sound and Vibration, vol. 169, no. 1, pp. 127-128, 1994.

[8] D. Thambiratnam and Y.Zhuge, “Free vibration analysis of beams on elastic foundation”, Computers and Structures, vol. 60, pp. 971-980, 1996.

[10] O.F. Durgun, “Elastik Zemin Uzerindeki Kademeli Kirişin Homotopi Pertürbasyon Yönetimi ile Serbest Titreşim Analizi”, M.Sc.Thesis, in Turkish, 2015.

[11] G. Adomian, Solving Frontier Problems of Physics: The Decomposition Method, Springer, Netherlands, 1994.

[12] CSI, SAP 2000, Ver. 21.02, integrated software for structural analysis and design. Computers and Structures Inc., Berkeley, CA, USA, 2019.

SAKARYA ÜNİVERSİTESİ
FEN BİLİMLERİ ENSTİTÜSÜ
DERGİSİ

Sakarya University Journal of Science
SAUJS
e-ISSN 2147-835X | Period Bimonthly | Founded: 1997 | Publisher Sakarya University |
http://www.saujs.sakarya.edu.tr/en/

Title: The Method to Predict First Critical Core Loading for Nuclear Reactors

Authors: Senem ŞENTÜRK LÜLE

Recieved: 2020-01-20 15:28:43

Accepted: 2020-10-08 23:38:58

Article Type: Research Article

Volume: 24
Issue: 6
Month: December
Year: 2020
Pages: 1329-1336

How to cite
Senem ŞENTÜRK LÜLE; (2020), The Method to Predict First Critical Core Loading for Nuclear Reactors. Sakarya University Journal of Science, 24(6), 1329-1336,
DOI: https://doi.org/10.16984/saufenbilder.677487

Sakarya University Journal of Science 24(6), 1329-1336, 2020

The Method to Predict First Critical Core Loading for Nuclear Reactors

Senem ŞENTÜRK LÜLE*[1]

Abstract

Nuclear power plants have an important role in carbon free electricity production in the world. One of the important steps of commissioning a nuclear power plant is the first core loading. This is also called approaching the criticality. Since the number of fuel elements for the criticality is not known, precautions must be taken to prevent safety incidents. Although the procedure is performed on-line such that the neutron counts are measured at each loading of fuel elements to calculate sub-critical multiplication and the number of fuel element to reach criticality were predicted, computer simulations can also be used. In this study, inverse sub-critical multiplication method was applied to Istanbul Technical University TRIGA Mark II research reactor first criticality in 1979 by using Monte Carlo simulation code MCNP6.2. Full 3-D model of the reactor was generated for calculations. Both results, experimental and simulation, showed that reactor became critical with 62 fuel elements. The core excess reactivity of 23.1 cents was predicted as 21.7 with the code. The simulation results are in good agreement with experimental results. The methodology and simulations can be used for power reactor analysis as well.

Keywords: Criticality approach, Monte Carlo method, sub-critical multiplication, reactor start-up

1. INTRODUCTION

Currently, 450 operable nuclear power plants with 399 GW_e total installed capacity are producing 2563 TWh carbon free electricity [1]. In addition, 55 GW_e net installed capacity is going to be utilized when 53 nuclear power plants under construction start commercial operation [2]. One of those 53 plants is the one that is being constructed in Akkuyu site in Turkey. Akkuyu project involves the construction of four 1200 MWe VVER-1200 type power plants [3]. The first unit is expected to be online in 2023 [4]. A successful commissioning of a nuclear power plant requires successful initial reactor start-up which involves hydraulic tests, pressure tests, plant heat-up, start-up to minimum load, etc… As a matter of fact, it may take several months. It is very important at the initial reactor start-up that the approach to criticality be performed very slowly and carefully since the actual fuel mass or number of fuel elements required for criticality is unknown. In addition, throughout its lifetime, a nuclear reactor can be started up for various reasons such as start-up after normal shutdown or after refueling. All these start-ups include the step of approaching criticality or start-up to minimum load. This step requires the final effective multiplication factor (k_{eff}) of the reactor becoming one at the end of the start-up [5]. Therefore, it is important to estimate critical conditions such as critical rod positions, critical core inlet temperature, and critical boron

---

*Corresponding Author: senturklule@itu.edu.tr

[1] Istanbul Technical University, ORCID: https://orcid.org/0000-0002-6632-5831

concentration if power plant is a pressurized water reactor (PWR). Approach to criticality can be measured with subcritical multiplication (M) which reflects the effect of reactivity change on neutron flux [6]. It can simply be defined as the inverse of $(1 - k_{eff})$.

The knowledge of the degree of subcriticality is important not only to understand the reactor response but also to satisfy criticality safety control. If obtained in a timely manner during the operation of nuclear facilities, it could lead to the application of advanced control methods such as more positive usage of neutron absorbers [7].

In general, power plant data are not available to researchers. Therefore, the general practice is to utilize experimental facilities for research and development on criticality safety. There are several experimental facilities in the United States, Japan, Russian Federation, and Europe that are used for criticality safety [7]. On the other hand, research reactors are used to acquire data for research and development activities for many years in nuclear field. In fact, research reactors play an important role in nuclear industry not only for research and development but also human resource development with their flexibility at core designs, powers, flux levels, fuel element types, fuel element shapes, and experimental facilities. The criticality approach can also be experimented in research reactors. There are also computational methods for criticality predictions.

The first criticality prediction and experiment for the Jordan Research and Training Reactor owned by Jordan Atomic Energy Commission (JAEC) was performed and reported in [8]. The Monte Carlo code for Advanced Reactor Design and Analysis (McCARD) with ENDF/B-VII.0 cross section libraries was used for the prediction calculations. The simulation results for the critical control rod position showed good agreement with the experimental data. Least square inverse kinetics method was employed to measure reactivity with source term for the HANARO Research Reactor [9]. This method is widely used for power reactors at high power level when there is no neutron source at the core. But, at subcriticality, the effect of neutron source must be taken into account. The method is proved to be successful to predict reactivity worth. The validation of reactor physics and criticality safety code SCALE 5.1 KENO V.a for seven weight percent ^{235}U fuel was performed with benchmark data from the seven percent critical experiment [10]. The experiment involved the criticality approach procedure. The results of the number of fuel elements for criticality from the experiments and simulations showed a large difference. The first fuel loading of HANARO research reactor was performed both experimentally and analytically in [11]. The fuel elements inserted in the core batch wise and subcritical multiplication versus number of fuel elements graph was drawn. The reactor became critical when four 18-element assemblies and thirteen 36-element assemblies were inserted in the core which required the critical control rod position as 600.8 mm with excess reactivity of 0.71$. WIMS-VENTURE and MCNP codes were used for the simulations. The predicted criticality overestimated the experimental value for both codes.

In this study, the first criticality approach experiment of Istanbul Technical University (ITU) TRIGA Mark II Research Reactor in 1979 was described and then used to develop and verify a Monte Carlo model with MCNP6.2 code [12]. The verified model can be used for future start-up procedures of ITU TRIGA reactor in case there is a new core configuration. In addition, this study can be beneficial if calculations are required for Akkuyu nuclear power plant.

2. ITU TRIGA MARK II RESEARCH REACTOR

The construction of ITU TRIGA Mark II research reactor started in 1977 and first criticality was achieved in 1979. The reactor is designed by General Atomics. It has a 250 kW nominal power and 1200 MW pulse capacity. The light water cooled and graphite reflected reactor core is placed aboveground Aluminum tank of approximately 2 m diameter and 6.4 m height which is centered in a hexagonal reactor structure of heavy concrete for radiation protection and structural integrity [13]. Top and side view of ITU TRIGA Mark II research reactor are shown in Figure 1. Currently, there are 69 fuel elements, which are composed of 19.75% low enriched Uranium Zirconium Hydride ($UZrH_{1.6}$) fuel meat surrounded by stainless steel clad, in the reactor core. The reactivity control is achieved with three control rods: Safety, Regulating, and Transient. There are several irradiation facilities in the core for research and development studies. The central thimble and pneumatic transfer system provide in-core whereas radial, piercing, and tangential beam ports provide out-core irradiation opportunities. Since reactor power is relatively low, natural cooling is enough to remove the heat that is generated by fuel elements from the core [14].

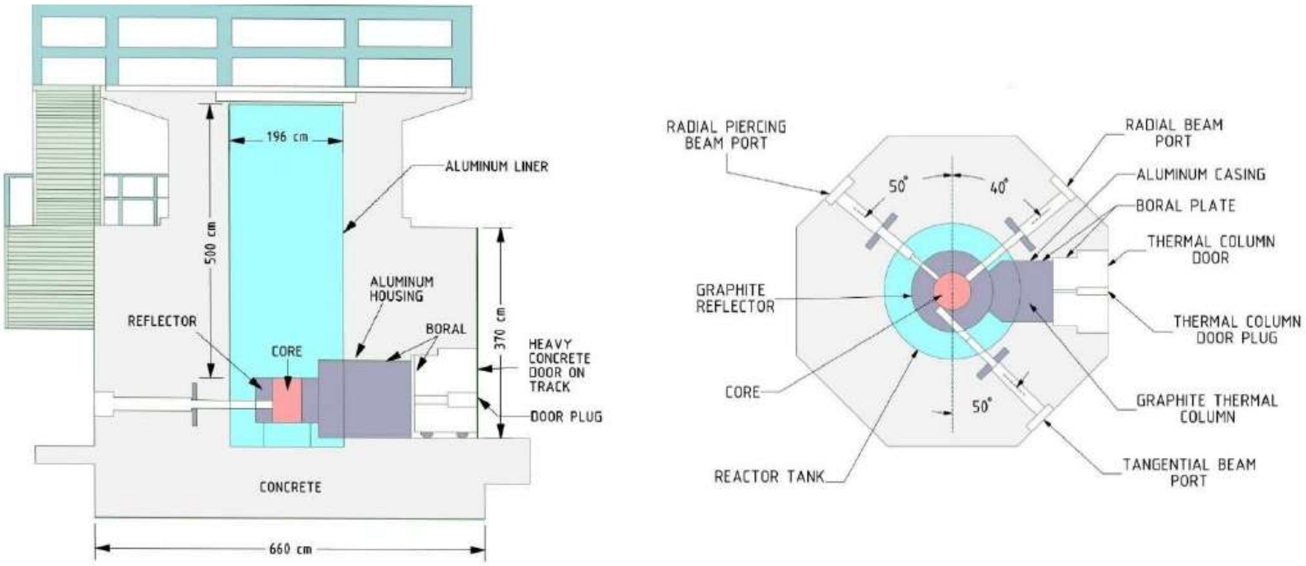

Figure 1 Side and top view of ITU TRIGA Mark II research reactor

3. METHODOLOGY

The multiplication factor of a reactor is defined as in Eq.1 and indicates that the neutrons from one fission reaction induce yet another reaction [15]. If the number of neutrons in one generation is greater than the number of neutrons in preceding generation, k_{eff} becomes greater than one and the reactor is called "*super-critical*". On the contrary, if the number of neutrons are decreasing between two generations, k_{eff} becomes less than one and the reactor is called "*sub-critical*". The ideal condition is where there is balance between the number of neutrons in each generation that results in "*critical*" reactor with k_{eff} equals to one.

$$k_{eff} = \frac{Number\ of\ neutrons\ in\ one\ generation}{Number\ of\ neutrons\ in\ preceding\ generation} \qquad (1)$$

Under normal circumstances, a sub-critical reactor will never be self-sustaining since the number of neutrons decreasing in time (with the mean generation time). On the other hand, if there is an external neutron source in the core, neutron population reaches an equilibrium level that is determined by the neutron source strength S such that it can be measured by neutron detectors to provide information to reactor operator. The number of neutrons at any generation for a sub-critical reactor with an external source can be calculated by using Eq.2 [16].

$$\frac{n}{S} = M = \frac{1 - k_{eff}^{m+1}}{1 - k_{eff}} \qquad (2)$$

where n is the neutron density level at the m^{th} iteration, S is external source strength, and M is sub-critical multiplication of the reactor. After sufficiently long time, the number of neutrons in the core takes the form defined in Eq.3.

$$n = S \times M = S\frac{1}{1 - k_{eff}} \qquad (3)$$

It is not practical to use M to follow criticality approach since as reactor approaches criticality when k_{eff} approaches to one, M becomes infinitely large. Instead, the inverse of sub-criticality multiplication $(1/M)$ can be used since its value will be zero at the point of criticality. Therefore, the approach to criticality is performed by loading fuel elements in the core in batches, measuring the count rates on the detectors after each batch was loaded, and plotting $1/M$ as a function of number of elements loaded. The critical mass then can be predicted by extrapolating the $1/M$ versus the number of fuel elements curve to the horizontal axis. When approach to criticality is performed, long time lapses between the batches are required in order to permit the equilibrium state to be reached. This is particularly important when the reactor gets close to critical. After the last fuel is loaded, the reactor will become slightly super-critical. The core excess reactivity then can be measured by determination of doubling time.

4. RESULTS AND DISCUSSIONS

In this study, criticality approach experiment of the first core loading of ITU TRIGA Mark II research reactor in 1979 was simulated with MCNP6.2 Monte Carlo code. The detailed 3D model of the research reactor was generated for this purpose and can be seen in Figure 2. The Monte Carlo calculations were performed with 45000 initial number of neutrons to complete 2200 active cycles skipping 200 of them to allow Shannon entropy to converge to achieve steady-state value for fission source distribution. ENDF/B-VII.1 cross section library was used. With these arrangements, the standard deviation of the calculated k_{eff} was guaranteed to be below 10^{-3}. The values of active and skipped cycles define not only the magnitude of the error in the results but also the computational time. An increase in active cycles reduces the error but increases the computational time. The value for the skipped cycles must be arranged in a way to allow Shannon entropy to converge. The combination used in this study provided the optimum in terms of accuracy and computational time.

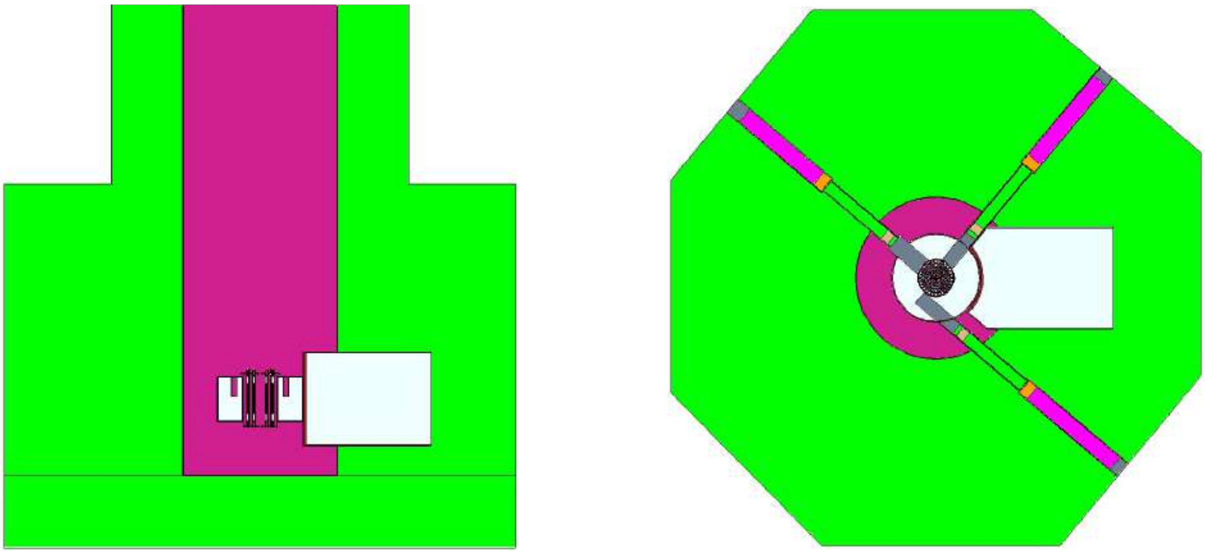

Figure 2 Side and top view from the MCNP model of ITU TRIGA Mark II research reactor

The experiment in 1979 started with withdrawal of all control rods out of the core. Then, 3 Ci Am-Be neutron source providing 3 x 10^6 neutrons/s was placed into the core and count rate was recorded. According to experimental data, 24 fuel assemblies were loaded into the reactor core as a first step. Later, 10, 6, 3, 3, 2, 2, 1, 1, 1, and 1 additional fuel assemblies were loaded into the core. After each step, enough time lapse was given to system to reach steady-state before recording the counted data. The inverse subcritical multiplication was calculated by division of count rates between two steps. Whenever a new data point was obtained, that point and the previous point was used to predict the critical mass by linear extrapolation [17]. When the last fuel was added, the reactor became super-critical with a period of 29.3 s.

The same core loading pattern described above was applied to MCNP simulations. On the contrary to experiments, the sub-critical multiplication was determined by using calculated k_{eff} values. The sample core configurations for 24, 46, 56, and 62 elements that are used for the simulations are shown in Figure 3.

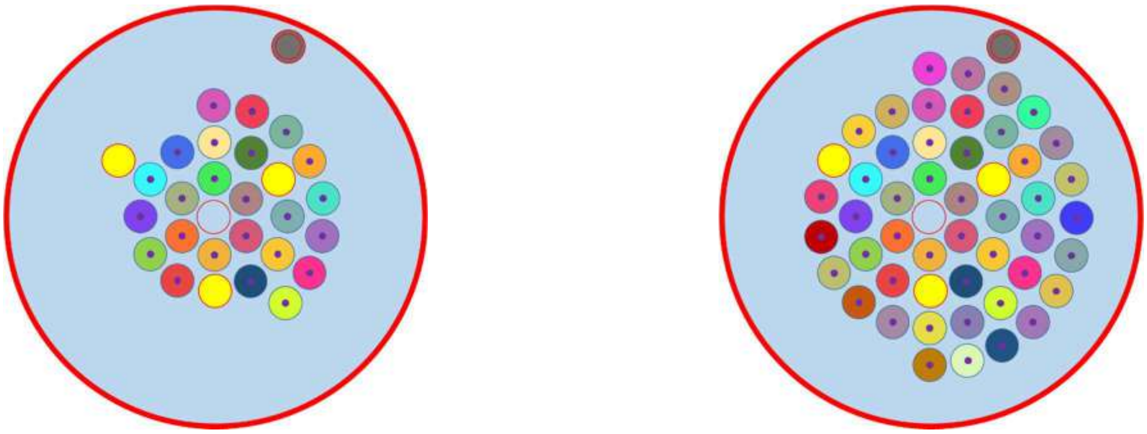

24 fuel elements loaded

46 fuel elements loaded

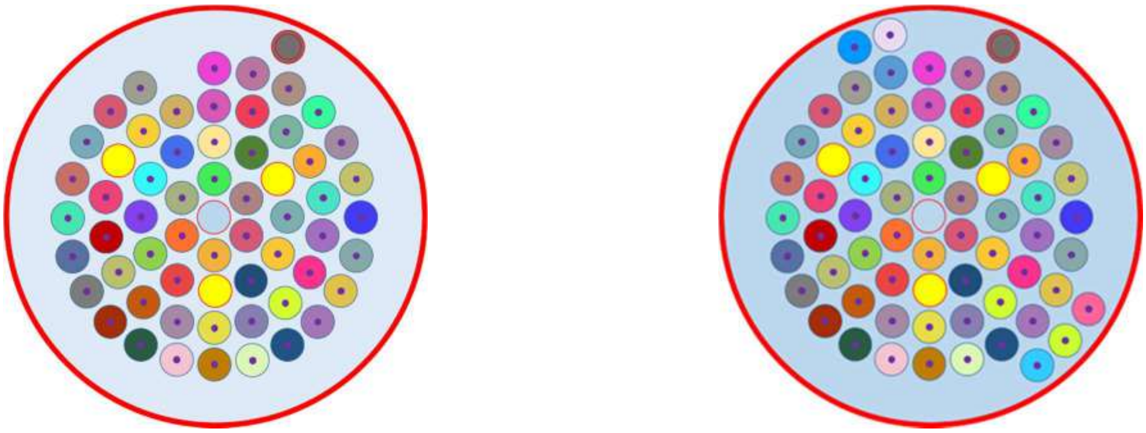

56 fuel elements loaded

62 fuel elements loaded

● Control Rod ○ Central Thimble ● Fuel Element ◉ Pneumatic System

Figure 3 Core loading pattern with various number of fuel elements

The graph of inverse sub-critical multiplication versus the number of fuel elements including both experimental and simulation results is shown in Figure 4. As seen in Figure 4, addition of fuel elements decreases inverse sub-critical multiplication indicating that the core multiplication factor increases therefore it approaches to criticality. It is clear that at the beginning MCNP over predicts core criticality. It is because of the fact that in reality there is not enough fission in the core but MCNP simulates the core as if all materials including fissile isotopes fission while performing criticality calculation. As a result, it over predicts the core multiplication factor. As number of fissions increases with the addition of fuel elements, the results of MCNP and experiment agrees quite well. The error bars on MCNP curve in Figure 4 shows this agreement clearly.

As mentioned above, the prediction of the number of fuel elements that makes the core critical is performed by using the results of two consecutive fuel loading steps. The curves in Figure 4 were used to predict the number of fuel elements required for criticality after each core loading step. Table 1 shows that at first, the prediction is far from the actual value since there is not enough fission in the core. Later, with the addition of new fuel elements the result converges to the actual value. Table 1 indicates that the experimental results are comparable with the simulation results therefore concludes that the simulations and methodology used in this study are appropriate.

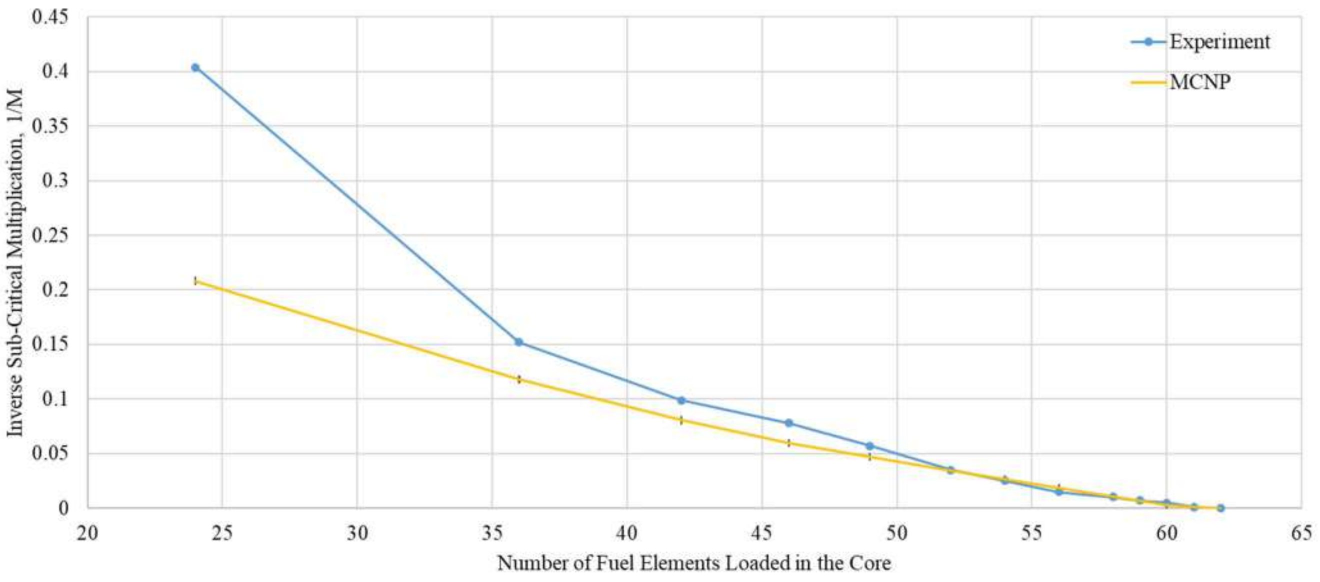

Figure 4 The variation of inverse subcritical multiplication factor with core fuel loading

Table 1
The predictions of experiment and MCNP simulation for the number of fuel elements for criticality

The number of fuel elements loaded	Prediction for the number of fuel elements for criticality	
	Experiment	MCNP
24	-	-
36	43	52
42	53	55
46	61	57
49	57	60
52	57	61
54	59	61
56	59	60
58	62	61
59	61	61
60	62	61
61	61	61

The reactor period at super-criticality state can be used to determine the excess reactivity of the core by using in-hour equation shown in Eq. 4 [16].

$$\rho = \frac{l}{l+T} + \frac{T}{T+l}\sum_{i=1}^{6}\frac{\beta_i}{1+\lambda_i T} \qquad (4)$$

where l is prompt-neutron lifetime, T is reactor period, β_i is the i^{th} group delayed neutron fraction, and $\lambda_i$is the i^{th} delayed neutron group decay constant.

By using the 29.3 s period reported in the experiment, the reactor excess reactivity was calculates as 23.1 cents. The MCNP simulations predicted the excess reactivity as 21.7 cents. It is clear that the result of the simulation agrees well with the experimental result.

5. CONCLUSIONS

The detailed 3D model of the ITU TRIGA Mark II research reactor was generated with MCNP6.2 Monte Carlo code geometry modelling feature to perform calculations to predict the number of fuel elements required to achieve first criticality. The approach to criticality is an important step for the commissioning of nuclear reactors either power or research. The precautions must be taken to prevent safety incidents. Therefore, it is important to have accurate predictions. The inverse sub-criticality method was employed in this study and the experimental results were compared with the simulation results. The simulation results predicted well the number of fuel elements required for the first criticality. The results deviated from the experimental results when there is not enough fission reaction at the reactor core due to small amount of fuel elements loaded in the core. Since MCNP performs criticality simulations assuming all fissile materials fission, which is not the case in reality, it overestimates the core multiplication factor at the beginning of the core loading. On the other hand, this is not a problem when there are great number of fission reactions in the core. The calculated core excess reactivity also agrees well with the experimental result indicating that MCNP6.2 with ENDF/B-VII.1cross section library is capable of accurate simulation. The method of approaching the first criticality can be used for the power reactors as well.

Funding

The author received no financial support for the research, authorship, and/or publication of this paper.

The Declaration of Conflict of Interest/ Common Interest

No conflict of interest or common interest has been declared by the author.

The Declaration of Ethics Committee Approval

The author declares that this document does not require an ethics committee approval or any special permission.

The Declaration of Research and Publication Ethics

The author of the paper declares that she complies with the scientific, ethical and quotation rules of SAUJS in all processes of the paper and that she does not make any falsification on the data collected. In addition, she declares that Sakarya University Journal of Science and its editorial board have no responsibility for any ethical violations that may be encountered, and that this study has not been evaluated in any academic publication environment other than Sakarya University Journal of Science.

REFERENCES

[1] A. Rising, “World Nuclear Performance Report,” 2019.

[2] International Atomic Energy Agency, “Nuclear Power Reactors in the World,” 2019.

[3] IAEA, “The Database on Nuclear Power Reactors,” 2019..

[4] Akkuyu Nükleer, “Akkuyu Nükleer Güç Santrali’nin temeli Rusya Federasyonu Devlet Başkanı ve Türkiye Cumhuriyeti Cumhurbaşkanı’nın tatıldığı törenle atıldı,” 2018.

[5] J. R. Lamarsh, Introduction to Nuclear Engineering. Addison-Wesley Company, 1977.

[6] G. Gedeon, “Reactor Kinetics and Operation,” 1993.

[7] M. Yoshinori and S. Takenori, “Review of Criticality Experiment Facilities In Japan,” in Experts Meeting on Experimental Needs in Criticality Safety, 1995.

[8] K. O. Kim, B. J. Jun, B. Lee, S. J. Park, and

G. Roh, “Comparison of first criticality prediction and experiment of the Jordan research and training reactor (JRTR),” Nucl. Eng. Technol., vol. 52, no.1, pp. 14-18, 2020.

[9] N. Jahan, M. M. Rahman, M. Q. Huda, and S. M. Seo, “Sub-Criticality Measurement with Source Term for Research Reactor in Inverse Kinetics Method,” World J. Nucl. Sci. Technol., vol. 07, no. 03, pp. 129–135, 2017.

[10] A. D. Barber and G. A. Harms, “Results for the First Approach-to-Critical for the Seven Percent Critical Experiment at the Sandia Pulse Reactor Facility,” 2009.

[11] C. S. Lee, C. G. Seo, and B. Jun, “The Initial Criticality and Nuclear Commissioning Test Program at HANARO,” 1995.

[12] C. J. Werner, “MCNP Users Manual - Code Version 6.2,” 2017.

[13] E. H. Özkul and A. Durmayaz, “A Parametric Thermal-Hydraulic Analysis Of I.T.U. Triga Mark-II Reactor,” in TRIGA users conference, p. 366., 2008.

[14] M. Türkmen, “Design of Piercing Beam Port of ITU TRIGA Mark II Research Reactor for BNCT Application,” 2015.

[15] J. Duderstadt and L. Hamilton, Nuclear Reactor Analysis. John Wiley & Sons Inc., 1976.

[16] D. D. Glover, Experimental Reactor Analysis and Radiation Measurements. McGraw-Hill Book Company, 1965.

[17] G. Csom, Laboratory Training Manual on the Use of Research Reactors. International Atomic Energy Agency, 1979.

SAKARYA ÜNİVERSİTESİ

FEN BİLİMLERİ ENSTİTÜSÜ
DERGİSİ

Sakarya University Journal of Science
SAUJS

e-ISSN 2147-835X | Period Bimonthly | Founded: 1997 | Publisher Sakarya University |
http://www.saujs.sakarya.edu.tr/en/

Title: Investigation of Neuregulin-1 Gen rs6994992 Polymorphism in Gifted Students in Turkish Population

Authors: Fikriye POLAT, Tuğba Büşra BAYRAM, Burcu YÜKSEL

Recieved: 2020-08-14 13:00:11

Accepted: 2020-10-13 12:31:15

Article Type: Research Article

Volume: 24
Issue: 6
Month: December
Year: 2020
Pages: 1337-1343

How to cite
Fikriye POLAT, Tuğba Büşra BAYRAM, Burcu YÜKSEL; (2020), Investigation of Neuregulin-1 Gen rs6994992 Polymorphism in Gifted Students in Turkish Population. Sakarya University Journal of Science, 24(6), 1337-1343, DOI: https://doi.org/10.16984/saufenbilder.780155
Access link
http://www.saujs.sakarya.edu.tr/en/pub/issue/57766/780155

Sakarya University Journal of Science 24(6), 1337-1343, 2020

Investigation of Neuregulin-1 Gen rs6994992 Polymorphism in Gifted Students in Turkish Population

Fikriye POLAT*[1], Tuğba Büşra BAYRAM[2], Burcu YÜKSEL[3]

Abstract

***Aim**: The aim of this study is to investigate whether neuregulin-1 gene (NRG1) rs6994992 polymorphism has any role in gifted students in Turkish population.*

***Methods**: During the 2017-2018 academic year, 97 gifted students (experiment group) and 99 students with normal development (control group) attending 5th grade of different public schools participated in the research. Genomic DNA was extracted from the oral epithelial cells. Genotyping of the molecular variant was performed by Polymerase Chain Reaction- Agarose gel electrophoresis-DNA sequencing techniques.*

***Results**: Genotype difference in gifted students was estimated as odds ratio and 95% confidence interval using binary logistic regression models. While the frequencies of CC (wild type), CT (heterozygous), TT (polymorphic type) genotypes were 33.0, 53.6 and 13.4%for the experimental group, respectively, they were observed as 33.0, 60.0 and 7.0% in the control group. In the Turkish population, no association could be detected for both genotype and allele distribution for NRG1 rs6994992 C/T polymorphism between gifted and control group (OR: 0.538, CI: 0.190-1.525, p = 0.244).*

***Conclusion:** According to the results of our study, there was no relationship between NRG1 rs6994992 polymorphism and gifted students in the Turkish population.*

Keywords: NRG1, rs6994992, SNP, gifted, intelligence, Turkish population

---

* Corresponding Author: fikriyepolat@gmail.com

[1] Kocaeli University, Turkey, ORCID: https://orcid.org/0000-0002-5414-2501

[2] Kocaeli University, Turkey, E-Mail: tugbabusrabayram@gmail.com
ORCID: https://orcid.org/0000-0003-2850-6938

[3] Kocaeli University, Vocational School of Health Services, E-Mail: burcu.yuksel@yahoo.com
ORCID: https://orcid.org/0000-0001-8691-6447

1. INTRODUCTION

Neuregulins are ligands that bind to ErbB receptors, enable activation, but also mediate cell-to-cell interactions. They are paracrine, autocrine, and juxtrachrin signal peptides linked to the Epidermal Growth Factor (EGF) family. They are encoded with four different genes: NRG1, NRG2, NRG3 and NRG4 [1, 2, 3]. Neuregulin-1 (NRG1) is a gene with more than 20 exons and large introns located in the 8p13 region on the chromosome. It belongs to the Epidermal Growth Factor Receptor (EGFR) family, and encodes an endogenous glycoprotein of 44 kD. These proteins are mostly secreted from the nervous system, cardiovascular system, intestines, and kidneys, and operate signal pathways that will cause stimulation or inhibition of functions such as proliferation, apoptosis, migration, differentiation, and adhesion in the cell. NRG1 is effective in many physiological and pathophysiological mechanisms, and in the nervous system. By providing endothelial barrier function, it plays a role in protecting blood brain barrier and brain microvascular structures and increasing permeability [4, 5]. Neuregulin protein, also known as the glial growth factor encoded by the NRG1 gene, is an endogenous protein that plays a critical role in the intercellular communication and signaling system. It is also expressed on motor axons in the nerve and is required for Schwann cell development. NRG1 is also a ligand for the NEU/ERBB2 protooncogene. It has been shown that NEU/ ERBB2 is closely related to EGFR. NRG1 produces at least fifteen developmentally regulated proteins [3]. Functionally, various products of this gene have been implicated in various biological processes such as embryogenesis, angiogenesis, breast cancer, nervous system development, myogenesis and gonadogenesis [6]. Neuregulins interact with the transmembrane tyrosine kinase receptors of the ErbB family and send signals to target cells. Receptor-ligand interactions stimulate heterodimerization of receptor monomers, thereby stimulating proliferation, migration and differentiation in cells. NRG1 can acquire specificity by affecting the biological functions of the signal path as well as its specific interest in the receptor types [7]. Transcription factors that bind to these regions of ERBB4 and NRG1 genes predispose to schizophrenia or have a protective effect on the disease [8]. As a result of oxygen-glucose deficiency cytotoxicity and expression of ErbB4, the NRG1 gene has been shown to protect the brain against cerebral ischemia disease [9]. Significant results have been found in the rs35753505 polymorphism genotypes of the NRG1 gene in patients with hepatocellular carcinoma [10]. Another study has discovered that NRG1 gene helps in functional recovery after spinal cord injury [11].

The aim of this study is to investigate whether NRG1 gene rs6994992 polymorphism has any role on intelligence in gifted students attending the 5th grade. This study is the first study that explores the relationship between intelligence and genetics among the Turkish population.

2. MATERIALS AND METHODS

2.1. Subjects

The current study has been carried out in the city of Kocaeli, Turkey, between the years 2017-2019 with the gifted (n= 97) students and students with normal development (n= 99), whose age ranged from 10 to13 and who attended the 5th grade. The experimental group was made up of students who had previously taken Wisc-r and group intelligence test and were diagnosed as gifted. The control group consisted of students attending different public school. No intelligence test was applied to the control group. This can be listed as a limitation of our study.

Prior to data collection research, KOU GOKAEK Non-Interventional Ethics Committee permission numbered 2017/375 was granted and MoNE and Governorship approvals dated 10.05.2018 and numbered 99332089/605.01/9238429 were obtained. All participants provided voluntary consent forms before participating in the study.

2.2. DNA Isolation

Students who participated in the study were asked to clean their teeth and mouths with disposable toothbrushes before saliva samples were collected. After waiting for 30 minutes, 200 µl saliva samples were taken from each student. The samples were kept in cool containers until they were taken to the laboratory for DNA isolation.

DNA isolation was performed using the EURx GeneMATRIX Tissue & Bacterial DNA Purification Kit (Gdansk Poland, Cat no. E3551) following the procedures recommended by the company.

2.3. Polymerase Chain Reaction (PCR)

Primers were designed using Primer3web version 4.1.0 program [12]. PCR was performed using primers of the NRG1 gene from the isolated DNA. The primers and PCR conditions used in the study can be seen in Table 1 and Table 2. 5x FIREPol Master Mix (Solis BioDyne) was used to prepare the PCR reaction mixture. PCR reaction mix 5x Master Mix: 6µl, 10 µM primer (sense): 0.5 µl, 10 µM primer (antisense): 0.5 µl Mold DNA: 2 µl were used. Bidistillated water was added to 30 µl for the PCR mixture of each gene region. PCR products were run for 30 minutes at 100 volts in agarose gel electrophoresis and visualized with a UV transluminator.

Table 1
Forward and reverse primers of the NRG1 gene

Gene Name	SNP number	Primer sequence
NRG1	rs6994992	Forward- 5’-CCTCCCAAAAAGTCGAGTCA-3’ Reverse-5’-CGCTTCAGGAGAAGATCACC-3’

Table 2
PCR conditions for NRG1 gene rs6994992 polymorphism

	Temperature (°C)	Time (second)	Cycle
Predenaturation	94	240	1
Denaturation	95	30	35
Annealing	55	30	
Elongation	72	30	
Final Elongation	72	350	1

2.4. DNA Sequence Analysis

PCR products were purified by the BM Lab in accordance with the kit procedures used with the ExoSAP-ITTM PCR Product Cleanup Reagent (Thermo Fisher Scientific, USA) purification enzyme. Sequence analysis was performed using forward and reverse primers of the purified PCR products NRG1 gene. For the Sanger sequencing, the ABI 3730XL Sanger sequencing device (Applied Biosystems, Foster City, CA) and the BigDye Terminator v3.1 Cycle Sequencing Kit were used in the Macrogen Netherlands laboratory. DNA sequence analysis was performed on DNA samples that were amplified in agarose gel electrophoresis. Genotypes were identified.

Genotypes of NRG1 gene rs6994992 polymorphism were revealed by imaging with Chromas 2.6.6 program. The DNA sequence that includes the NRG1 gene rs6994992 polymorphism (C/T) is shown in Figure 1. The sections underlined show forward and reverse primers.

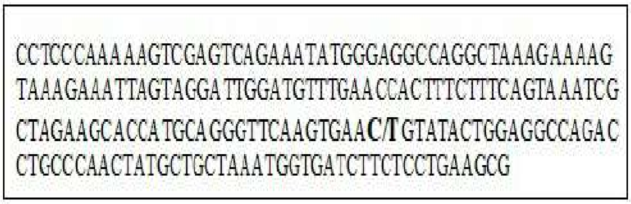

CCTCCCAAAAAGTCGAGTCAGAAATATGGGAGGCCAGGCTAAAGAAAAG
TAAAGAAATTAGTAGGATTGGATGTTTGAACCACTTTCTTTCAGTAAATCG
CTAGAAGCACCATGCAGGGTTCAAGTGAA**C/T**GTATACTGGAGGCCAGAC
CTGCCCAACTATGCTGCTAAATGGTGATCTTCTCCTGAAGCG

Figure 1 NRG1 gene sequence including rs6994992 polymorphism

2.5. Statistical Analysis

SPSS 22 statistical software was used for statistical analysis. Homozygous and heterozygous genotype frequencies and allelic mutation frequencies between experiment and control groups were compared using Chi-square analysis. Odds ratio (OR) and binary logistic regression analysis were performed to calculate 95% confidence intervals for each polymorphism. $p<0.05$ was considered for statistical significance. Michael H. Court's (2005-2008) online calculation engine was used because of any deviations from the Hardy-Weinberg equation

[13]. On the result of power analysis which was performed for detecting an association between gifted children and the studied polymorphisms, sample size was found to be sufficient for experiment and control groups consisting of 97 and 99 individuals (α: 0,05 and 1-β: 0,98).

3. RESULTS

While 35% of gifted students (i.e., the experimental group) were female students and 65% were male students, these values were 55% for girls and 45% for boys in the control group. Since the numbers in girls and boys were not equal between groups, p = 0.003 was found statistically significant. The difference between two groups were not statistically significant either in terms of height, weight and waist circumference (Table 3).

Hardy-Weinberg equation was calculated as $\chi2$ = 1.281, p = 0.257 in the gifted group and $\chi2$= 8,596, p = 0.0003 in the group with normal development. The reason for the deviation from HWE may be that the group with normal development in this study was formed from five different schools.

Table 3
Demographic characteristics of gifted students and students with normal development

	Gifted group N=97 (%)	**Normal Development group N=99 (%)**	**p value**	**OR (95% CI)**
Gender				
Girl	34 (35)	55 (55)		
Male	63 (65)	44 (45)	**0.003***	2.3 (1.337-4.179)
Size	143.9±7.15	143.3±7.67	0.809	0.801-0.901
Weight	38.39±9.00	37±7.86	0.840	0.789-0.891
Waist circumference	65.67±11.14	64.31±7.83	0.535	0.466-0.604

Genotype and allele frequencies of NRG1 gene C/T rs6994992 single nucleotide polymorphism in gifted students and students with normal development are shown in Table 4.

Table 4
Genotype and allel distributions of NRG1 gene rs6994992 polymorphism in students with Special Ability and Normal development

NRG1 rs6994992	**Gifted group N=97 (%)**	**Normal Development Group** N=99 (%)	**p value**	**OR (95% CI)**
Genotype				
CC	32 (33.0)	32 (33.0)		
CT	52 (53.6)	60 (60.0)	0.244	0.538 (0.190-1.525)
TT	13 (13.4)	7 (7.0)	0.132	0.467 (0.173-1.257)
Allel				
C	116 (59.8)	124 (62.6)		
T	78 (40.2)	74 (37.4)	0.565	0.888 (0.591-1.333)

*When compared to the control group, it is significantly different at p <0.05 level.

When Table 4 is analyzed, it can be seen that for the NRG1 gene rs6994992 single nucleotide genotype frequencies for gifted students, CC (wild type) is 33.0%, CT (heterozygous) is 53.6%, and TT (polymorphic type) is 13.4%, while these values were found 33.0%, 60.0% and 7.0% for students with normal development, respectively. Allel frequencies were C 59.8% and T 40.2% in gifted students, and C 62.6% and T 37.4% in students with normal development. No statistically significant difference was found in genotype and allele distributions between gifted students and students with normal development (p> 0.05).

Genotypes were determined by investigating electropherograms of NRG1 gene rs6994992 single nucleotide polymorphism separately for both experimental and control groups. Figure 2 shows the CC, CT and TT genotypes, respectively.

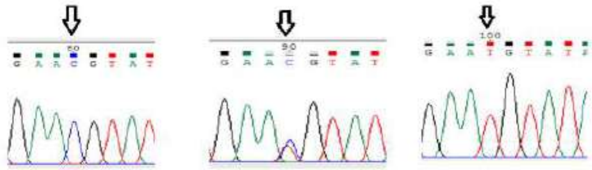

Figure 2 Arrows show CC, CT and TT genotypes of NRG1 gene rs6994992 SNP, respectively from left to right

4. DISCUSSION

NRG1 gene, which has been proposed as a potential gene for psychosis, plays a role in neuronal development, synaptic plasticity, glutameric neurotransmission and glial function. In particular, the TT genotype of rs6994992 of functional promoter polymorphism; NRG1 has been associated with increased gene expression, an increased risk of psychosis and other psychological and neurological phenotypes. NRG1 gene, which has an extremely important effect on brain development, can also cause individual differences [6]. NRG1 gene rs6994992 has been found to be related with creativity in intellectually successful individuals with high promoter polymorphism. According to the study by Kéri (2009), the NRG1 gene, which is regarded as a potential gene for glial functions that help nerve cells, has been examined to determine the role it plays in neural development. To this end, creativity tests were carried out, in which the IQ scores of the participants were measured together with the schizotypic features. Among these, healthy participants with high intellectual and academic performance were identified and the study investigated whether there was a relationship between creativity and NRG1 promoter polymorphism. The results of this study has revealed that NRG1 gene has an effect on functions that impact both creativity and some psychopathology [14].

The prefrontal cortex of the brain is important in cognitive inhibition and creativity, and the rs6994992 promoter polymorphism of the NRG1 gene affects the function of this region of the brain [15, 16]. In 2012, a study conducted Yokley et al., which investigated the effects of NRG1 gene, has found that it may have an impact on psychopathology and intelligence, thus arguing for a relationship between variants in NRG1 and cognitive domains [17]. In the literature on the relationship between genetics and gifted people, Durdiakova et al. (2013) and Celec et al. (2013) have two studies that focus on that, apart from NRG1, androgen receptor repeat polymorphism, ESR1, ESR2, SRD5A2 and SHBG variants [18, 19]. Both Kéri (2009) and Yokley et al. (2012) found significant results for NRG1 gene rs6994992 polymorphism in their studies in terms of creativity and / or psychopathology [14, 17]. In our study, we investigated the same gene polymorphism and, unlike them, included gifted children in our research. Unfortunately, as mentioned earlier, there were some limitations of our study such as the disclosure of IQ scores by the institutions and not being able to giving IQ tests to students that show normal development.

As a result, no statistically significant differences were found between the gifted students and the students with normal development in terms of NRG1 rs6994992 promoter polymorphism. In the Turkish population, there was no other study, to our best knowledge, that focused on the genetic polymorphism that had the sample of gifted students This study is one of the pioneering genetic studies conducted with gifted individuals in our country. In a larger sample, we recommend researchers interested in intelligence and genetics to study genes that are thought to be related to intelligence such as NRG1, APO E, ESR1, ESR2, SRD5A2 and SHBG.

Funding

The authors would like to thank to Scientific Research Project Unit of Kocaeli University (Project number: 2019-047-BAP-HD).

The Declaration Conflict of Interests/Common Interest

The authors declared no potential conflicts of interest with respect to the research, authorship, and/or publication of this paper.

Authors' Contribution

All authors have contributed in experimental study and writing of the manuscript equally.

Research and Publication Ethics

All applicable international, national, and/ or institutional guidelines for non-invasive clinical studies were followed.

Ethics Committee Approval

Prior to data collection research, KOU GOKAEK Non-Interventional Ethics Committee permission numbered 2017/375 was granted and MoNE and Governorship approvals dated 10.05.2018 and numbered 99332089/605.01/9238429 were obtained.

REFERENCES

[1] Y. Yarden and M. X Sliwkowski, "Untangling the ErbB signalling network," Nat. Rev. Mol. Cell Biol., vol. 2, pp. 127-137, 2001.

[2] M. A. Olayioye, R. M. Neve, and H.A. Lane, "The ErbB signaling network: receptor heterodimerization in development and cancer," EMBO J., vol. 19, pp. 3159-3167, 2000.

[3] D. L. Falls, "Neuregulins: functions, forms and signaling strategies," Exp. Cell Res., vol. 284, pp.14-30, 2003.

[4] M. Xu, X. Wu, B. Jie et al., "Neuregulin-1 protects myocardial cells against H_2O_2-induced apoptosis by regulating endoplasmic reticulum stress," Cell Biochem. Funct., vol. 32, pp. 464-469, 2014.

[5] T. Cvetkovic, J. Stankovic, S. Najman et al., "Oxidant and antioxidant status in experimental rat testis after testicular torsion/detorsion," Int. J. Fertil. Steril., vol. 9, pp. 121-128, 2015.

[6] S.A. Crone and K. F. Lee, "Gene targeting reveals multiple essential functions of the neuregulin signaling system during development of the neuroendocrine and nervous systems," Ann. N. Y. Acad Sci. vol. 971, pp. 547-553, 2002.

[7] S. Britsch, "The neuregulin-I/ErbB signaling system in development and disease," Springer Science & Business Media, vol. 190, 2002.

[8] S. Ağım, "Schizophrenia: another emphasis Of Erbb4 And NRG1 impact on disease development". Graduate Program in Molecular Biology and Genetics, Boğaziçi University, 2012.

[9] J. Yoo, H. Kim, S. Yoo, et al., "Neuregulin 1/ErbB4 signaling attenuates neuronal cell damage under oxygen-glucose deprivation in primary hippocampal neurons," Anat. Cell Biol., vol. 52, pp. 462-468, 2019.

[10] L. Luo, L. Li, M. Guo et al., "Genetic variation in NRG 1 gene and risk of post-traumatic stress disorders in patients with hepatocellular carcinoma," J. Clin. Lab. Anal., vol. 34, no. 5, e23187, 2020.

[11] X. Yin, Y. Chen, and G. Tu, Neuregulin-1 impacting bone marrow mesenchymal stem cell migration is conducive to functional recovery following spinal cord injury," Mol. Med. Rep., vol. 20, pp. 41-48, 2019.

[12] URL-1: http://www.primer3.ut.ee/, Visit date: 09.10.2018.

[13] URL-2: http://www.tufts.edu/~mcourt01/Documents/Court%20lab%20%20HW%20calculato r.xls., Visit date: 08.09.2019.

[14] S. Kéri, "Genes for psychosis and creativity: a promoter polymorphism of the neuregulin 1 gene is related to creativity in people with high intellectual achievement," Psychol. Sci. vol. 20, pp.1070-1073, 2009.

[15] S.H. Carson, J.B. Peterson, and D.M. Higgins, “Reliability, validity, and factor structure of the creative achievement questionnaire,” Creativ. Res. J, vol. 17, no. 1, pp. 37-50, 2005.

[16] A. Dietrich, “The cognitive neuroscience of creativity,” Psychonomic Bulletin & Review, vol.11, pp.1011–1026, 2004.

[17] J.L. Yokley, K.M. Prasad, K.V. Chowdari et al., “Genetic associations between neuregulin-1 SNPs and neurocognitive function in multi generational, multiplex schizophrenia families,” Psychiatr. Gene., vol. 22, pp. 70-81, 2012.

[18] J. Durdiakova, S. Lakatosova, A. Kubranska et al., “Mental rotation in intellectually gifted boys is affected by the androgen receptor CAG repeat polymorphism,” Neuropsychologia., vol. 51, pp. 1693–1698, 2013.

[19] P. Celec, D. Tretinarova, G. Minarik et al., “Genetic polymorphisms related to testosterone metabolism in intellectually gifted boys,” PLoS ONE, vol. 8, no. 1, e54751, 2013.

SAKARYA ÜNİVERSİTESİ

FEN BİLİMLERİ ENSTİTÜSÜ
DERGİSİ

Sakarya University Journal of Science
SAUJS

e-ISSN 2147-835X | Period Bimonthly | Founded: 1997 | Publisher Sakarya University |
http://www.saujs.sakarya.edu.tr/en/

Title: An in Vivo Study for the Use of Lupinus Albus (Fabaceae) in Drosophila Melanogaster Diet

Authors: Eda GÜNEŞ, Hatice Ferhan NİZAMLIOĞLU, Zafer BULUT, Mehmet NİZAMLIOĞLU

Recieved: 2020-03-02 17:00:09

Accepted: 2020-10-15 13:58:40

Article Type: Research Article

Volume: 24
Issue: 6
Month: December
Year: 2020
Pages: 1344-1351

How to cite
Eda GÜNEŞ, Hatice Ferhan NİZAMLIOĞLU, Zafer BULUT, Mehmet NİZAMLIOĞLU; (2020), An in Vivo Study for the Use of Lupinus Albus (Fabaceae) in Drosophila Melanogaster Diet. Sakarya University Journal of Science, 24(6), 1344-1351, DOI: https://doi.org/10.16984/saufenbilder.696047
Access link
http://www.saujs.sakarya.edu.tr/en/pub/issue/57766/696047

Sakarya University Journal of Science 24(6), 1344-1351, 2020

An in Vivo Study for the Use of *Lupinus Albus* (Fabaceae) in *Drosophila Melanogaster* Diet

Eda GÜNEŞ*[1], Hatice Ferhan NİZAMLIOĞLU[1], Zafer BULUT[2], Mehmet NİZAMLIOĞLU[2]

Abstract

Based on the oral chronic toxicity studies in humans, the daily intake of *Lupinus albus* L. (termiye, white lupine) with diet is recommended to be about 0.02%. The study was designed to investigate the use of lupine shells in nutrition. Dried *L. albus* shell was added to the artificial diet of the model organism (*Drosophila melanogaster*) and then lipid peroxidation, antioxidant enzyme activity, total oxidation, and total antioxidant activity were determined in the tissues obtained from the third larval phase. Changes that occurred in the larval midgut cells were examined microscopically. As the amount of shell consumption increased, malondialdehyde concentration (0.33 - 0.09 ± 0.71 nmol/ mg protein) and glutathione S transferase activity (19.91 - 14.06 ± 0.04 nmol/ mg protein/ dk) decreased statistically compared to the control. In addition to this, larval total oxidation level and total antioxidant activity also decreased ($P < 0.05$). No damage was detected in the larval midgut epithelial cells.

Keywords: *Drosophila melanogaster*, Lipid peroxidation, *Lupinus albus*, Oxidative status, Total antioxidant activity

---

*Corresponding Author: egunes@erbakan.edu.tr

[1] Department of Gastronomy and Culinary Arts, Faculty of Tourism, Necmettin Erbakan University, Konya, Turkey
ORCID: https://orcid.org/0000-0001-7422-9375, ORCID: https://orcid.org/0000-0002-5042-0172
E-Mail: hfnizamlioglu@erbakan.edu.tr

[2] Department of Basic Veterinary Sciences Biochemistry, Faculty of Veterinary Medicine, Selçuk University, Konya, Turkey
ORCID: https://orcid.org/0000-0003-1794-1651, ORCID: https://orcid.org/0000-0002-7747-519X
E-Mail: zbulut@selcuk.edu.tr E-Mail: mnzmoglu@selcuk.edu.tr

1. INTRODUCTION

In recent years, many researchers have tried to develop environmentally friendly technologies by using herbal sustainable resources and the safety of the herbal applications used in the traditional treatments of humans and animals has been evaluated[1,2]. According to the free radical theory, plant components are also highly toxic like environmental pollutants and chemicals because they cause oxidative damage in cells, lipids, nucleic acids, and proteins by providing reactive oxygen species (ROS)[3]. For this reason, researchers have focused on plant products that suppress ROS, have low toxicity, environmentally friendly, biodegradable, but do not cause resistance in the organisms.

In Turkey, known as termica in many regions and simply consumed, Lupin (*Lupinus albus* L., Fabaceae: Leguminosae) is used as gluten-free raw material in the food industry and feed stuff in animal nutrition (monogastric animals, poultry and pigs)[4]. Moreover, Lupin is a functional food with high sugar (5.82%), protein (32.2%), fiber (16.2%), and fat (5.95%) content. Its fat content contains saturated (13.5%), monounsaturated (55.4%), and polyunsaturated (31.1%) fatty acids as oil[5]. Toxic secondary metabolites such as alkaloids found in Lupin species have antifungal and insect deterrent activity. However, the total amount of alkaloid in *L. albus* is just 0.186 g which is eliminated to remove the bitter taste for commercial sale, therefore it is known to be safe for use as feed stuff[4-6].

Model organisms are vital for making successful predictions about the living organisms and the environment[7]. Although the digestive system in humans has similarities with digestive system of the model organisms, it is much more complex. However, *Drosophila* intestine is similar to the human gastrointestinal system in both structure and function[8]. The digestion in *Drosophila* larva stage starts in the mouth and continues throughpharynx, esophagus, anterior midgut, middle midgut, posterior midgut end hindgut, and ampulla. In addition, *Drosophila melanogaster* has great advantages such as high reproducibility and no ethical concern, and therefore is frequently used in research as a model organism for nutrition. The effect of ROS on the metabolism can be explained by the balance of oxidant-antioxidant mechanisms. Oxidative stress in tissues can be estimated by the amount of lipid peroxidation products such as malondialdehyde (MDA) and total oxidation level (TOS). One of the antioxidant enzymes, Glutathione S transferase (GST) and total antioxidant activity (TAS) is, are used for explaining the antioxidant balance against oxidation.

In recent years, shells, fats, and extracts of plants have been usedas performance enhancer in animal nutrition[9]. This study aimed to investigate the possible use of lupin shell (LK) in nutrition. Larvae of *D. melanogaster* were fed with a diet containing dried *L. albus* shell and the oxidative stress levels of tisses and changes in the intestinal epithelial cells were observed

2. MATERIALS AND METHODS

D. melanogaster (Oregon) were housed (60-70% humidity and 25 ± 2°C) at the culture laboratory in the Department of Gastronomy, Necmettin Erbakan University and fed with an artificial diet[10]). Commercially available *L. albus* shells were removed, dried in the oven at 60°C for 24 hours, and ground to the powder. In oral chronic toxicity studies performed in humans, it is recommended to use a daily average consumption of 0.02% per day[11], therefore the dried-ground LK at a ratio of 0.02-0.1% was added to the diet of the larvae. After the preliminary feeding studies of the consumed shell ratio, the experimental setup was established. The hatched new larvae were transferred to flasks (100 pcs) using a fine-tipped brush. The larvae were monitored daily until reaching the third stage, and the larvae were collected by washing in 20% isotonic solution. For biochemical analysis, larval tissues (100 pcs) were extracted in homogenization buffer (pH 7.4, + 4°C) by ultrasonic homogenizer.

2.1. Biochemical analysis

MDA, TOS level and GST and TAS activity were determined in order to detect total oxidative stress level. In addition, for each concentration, the larval midgut dissections (Olympus SZ61) were stained with orsein, the changes in the epithelial cells were visualized under the microscopic examination and were photographed with the Cameram program (Olympus C3 X 33; at least 25 times). The amount of MDA was determined by the method of Jain and Levine[12] and Glutathione S transferase (EC 2.5.1.18) by Habig et al.[13]. By using the kits (Rel Assay Diagnostics), TOS (μmol H_2O_2 E/L) and TAS (mmol Trolox Eq/L) were measured in Biochrom Libra S22 and oxidative stress index (OSI = TOS / TAS) was determined according to the standard formula[14].

2.2. Statistic analysis

The experiments were repeated four times. In the evaluation of the data, one-way analysis of variance (ANOVA, F test) was performed by statistical package program and LSD test was performed to determine the significance of the difference between means. The significance of the means was evaluated at the 0.05 probability level and the degrees of freedom were given. All chemicals were also purchased from Sigma Chemical Co (St. Louis, MO).

3. RESULTS

In the diet fed with LK (0.02%), the amount of MDA increased by 0.33 ± 1.25 nmol/mg protein, and the increased concentration of feeding caused statistically similar results (0.1 and 0.09 ± 1.12 nmol/mg protein). Figure 1 shows GST activities of insect that antioxidant resistance to lipid peroxidation occurs in those fed with 0.02% LK. It was determined that GST activity decreased against low peroxidation in insects fed with high concentration LK (14.06 ± 0.02; $P < 0.05$). When TOS values formed in larval stage of insect were examined, the change observed in the amount of MDAwas similar to that of the larva fed with 0.02% LK and while the TOS level was 60.00 ± 1.08, its level in the control group and at the highest feeding concentration was 20.00 ± 1.65 (Figure 2, F_{11} = 67.007 μmol/L; $P < 0.05$). The activity of Larval TAS was determined to decrease from 0.5 to 0.25 ± 0.173 (F_{11} = 1.186 mmol/L; $P = 0.349$). While the OSI index of the individuals fed with control food was in the 40 s, the reduction in the LK-fed from 120 (0.02%) to 80 (0.1%) indicates that increase in the stress level can be reduced, but not to the minimum level ($P = 0.456$). Deformations were not observed in the epithelial tissues of larval midgut under microscopic examination (Figure 3).

4. DISCUSSION

Each species has to meet its energy needs in order to survive, which makes it necessary to consume foods / nutrients necessary for the living. It is essential to know that the organism is not damaged when using substitute products in nutrition. For example, the addition of Lupin to the chicken diets for five weeks (20%) did not change the growth performance[15]; it was digested by sheep[16], it can be used up to 30% in rainbow trout diet[17]; it was used for feeding chicken and ducks; it did not significantly affect[18] the blood parameters (50 and 100%); it did not cause a significant change in monocytes[19]; the addition of up to 20% of the diet to the chicken health did not have any negative effects[20]. In human studies, it is known that Lupin meals taken daily with 12 mg (0.02%) oral diet as a food are digestible and did not cause a significant change in blood parameters[11].

Although the diet content used in nutrition is important for living, nondigestible nutrients are either directly excreted from the body or increase oxidation, adversely affecting survival. Especially in larvae, it has to be fed continuously for pupulation to occur, but there is no feeding during the pupal period[21] which shows that food consumed in the body accumulates. For example, the use of Lupin in feeds at 15-30% level in different organisms reduced the intake of feed although it increased feed intake with the use of Lupin in the feeding of *Helip aspersa*, a lung snail[22]. In birds, Lupin digestibility decreases when given at 300 g/kg[23]. The small amount of

LK used in this study accumulated in the midgut of the larva, increasing the amount of MDA and TOS, and the intact epithelial tissue in the feeding with increasing concentration suggests that the non-digestible LK was discarded or taken into the body. Lupin added to the chick diet lowered the intestinal viscosity[24]. Digestive system of *D. melanogaster*[25], which is a valid model for research of mammalian digestion has a strong barrier role to respond directly to environmental pathogens such as pathogenic infections, toxic substances, and pro-oxidants that pollute food[26]. This barrier limits contact with potentially harmful substances such as toxins and pathogens, thus giving them selective properties. This selectivity is supported by a strong mucosal immune system. *Drosophila* immune defense, which is devoid of an adaptive immune system, is based only on the natural immune system[26]. In addition, the peritrophic membrane around the intestine helps the antioxidant system[27]. The fact that fruit flies have a unique antioxidant system similar to that of mammals is preferred by researchers[28]. There are many enzymes that detoxify toxins in *Drosophila*. The increase in superoxide dismutase, catalase, GSTactivities against the increase in larval MDA is seen as the natural defense mechanism of the body[29]. Foods such as green tea and broccoli added to the diet in *Drosophila* reduce total lipid peroxidation and increase the antioxidant activity[30]. In the study, the feeding of larvae with 0.02% LK was thought to be related to increased oxidation (MDA and TOS) balance between antioxidant defense by increasing GST and TAS activity. The absence of deformation in the midgut epithelium also suggests that antioxidant concentration can be increased in tissues[31]. It is stated that Lupin added at 35% level or above to the diet has been shown to have a negative effect on various parts of the gastrointestinal tract[32]. Oxidative stress occurs due to increased free radicals and antioxidants with a scavenging effect against them, and degradation of oxidative balance[33]. Although the use of LK caused stress at low concentration, it was determined that the stress was reduced by an antioxidant mechanism. Similarly, in diabetic rats, it is known that Lupin reduces the amount of MDA[34]. Up to 30% Lupin can be used in the diet of rainbow trout; It is said to reduce triglyceride, cholesterol, alkaline phosphatase and lactate dehydrogenase[17]. However, flies gain resistance to free radical stimulants, thus attenuating the toxic effects of ROS[35]. Although there is the idea that insect has gained resistance in feeding with increased LK, low MDA and TOS amount and deformation are not observed. Lupeol [36], the most prominent minor component in the lipid portion of the lecane, is a triterpene alcohol that plays a role in the regeneration of the epidermal tissue[37]. This information is thought to be renewable midgut epithelium with the use of 0.1% LK.

It can be asserted that the OSI index obtained by using 0.1% LK reduces lipid peroxidation levels and the oxidation is tried to be balanced with the antioxidant system. It is stated that Lupin (50% of food), which is consumed together with the other nutrients, has a high feed potential in the feeding of poultry with its macro and micro element content, and it will affect the health of the intestine positively[38,39].

L. albus (100 g) contains 1.42 phytic acid, 0.9 saponin, 0.01 tannin, 0.01 trypsin inhibitors, 0.8 raffinose[6]. It is known that the amount of alkaloits of Lupin, which is cooked at 100 ° C or kept at 30 ° C for 45 hours, decreases by 43%, some of the proteins are degraded and the bitterness is reduced by 50%[40]. Although Lupin shows toxic effects on poultry, they stated that Lupin 150 g/kg can be used for the removal of the bitterness[20]. Lupin can be used upto 150 g/kg of diet in order to reduce the bitterness of diet. Saponin and tannins have a lethal effect on insects. However, the reduction by cooking explains why oxidation is reduced in insects feeding with 0.1%. It was determined that the amount of alkaloids in LK mixed with food and the thermal drying process did not cause any oxidation in the insect and did not adversely affect the model organism morphologically and biochemically.

5. CONCLUSION

It is thought that the use of *L. albus* shell in the model organism, an insect, in the amount of 0.02 or 0.1%, does not cause any damage to the tissue in terms of biochemical oxidation. It can be used as feed additive as a functional product after further research investigate its potential benefits or disadvantages. This will also contribute to the elucidation of the mechanism of action of natural products in the nutritional oxidative stress. We plan to determine the effect of the rate of Lupine accumulation in the adipose tissue of *D. melanogaster* fed with lupine and how this accumulation causes the saturated and unsaturated fatty acid reserves in future studies.

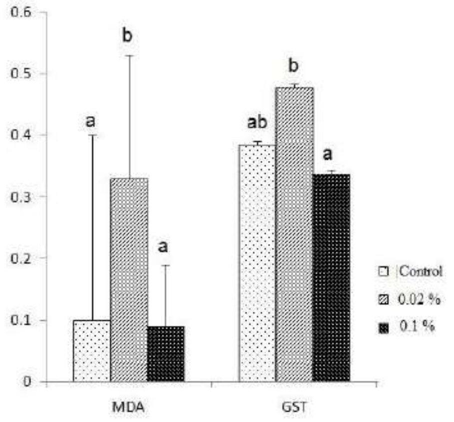

Figure 1 The amount of MDA and the change in GST activity in the feeding of the *Drosophila melanogaster* larvae with Lupin shell (0.02% and 0.1% LK). The average of four replicates, 100 larvae per replicate was used

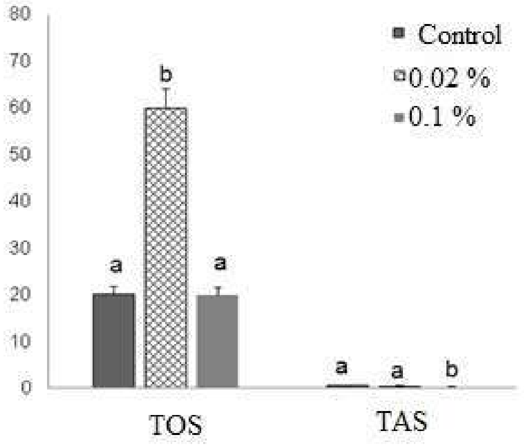

Figure 2 Total oxidation (TOS) and total antioxidant capacity (TAS) changes in feeding of *Drosophila melanogaster* larvae with Lupin shell (0.02% and 0.1% LK). The average of four replicates, 100 larvae per replicate was used

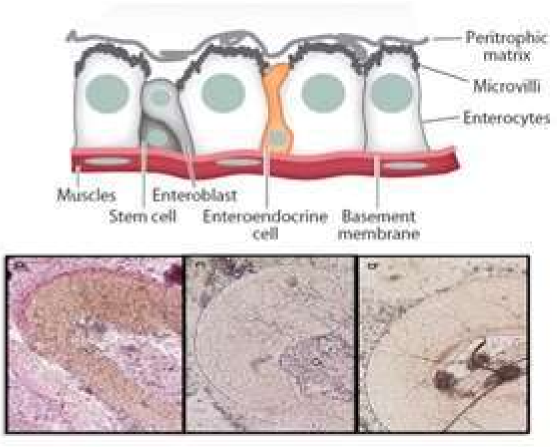

Figure 3 *Drosophila melanogaster* larvae in the digestive system a. midgut epithelial structure (Lemaitre & Miguel-Aliaga, 2013), b. The control group of the midgut epithelium, c. The group midgut epithelium fed with 0.02% Lupin shell (LK), d. The group midgut epithelium (X 100) fed with 0.1% LK

Note: This study was presented as an oral presentation at First International Veterinary Biochemistry And Clinical Biochemistry Congress (2018) and published as an abstract in the abstracts book.

Funding

The authors received no financial support for the research, authorship or publication of this work.

The Declaration of Conflict of Interest/ Common Interest

No conflict of interest or common interest has been declared by the authors.

Authors' Contribution

E.G: designing the study, performing the analyses and writing the first draft of the manuscript.

H.F.N: managing the analyses of the study.

M.N and Z.B: writing the first and final draft of the manuscript.

The Declaration of Ethics Committee Approval

The authors declare that this document does not require an ethics committee approval or any special permission.

The Declaration of Research and Publication Ethics

The authors of the paper declare that they comply with the scientific, ethical and quotation rules of SAUJS in all processes of the paper and that they do not make any falsification on the data collected. In addition, they declare that Sakarya University Journal of Science and its editorial board have no responsibility for any ethical violations that may be encountered, and that this study has not been evaluated in any academic publication environment other than Sakarya University Journal of Science.

REFERENCES

[1] Y.S. Jang, M.K. Kim, Y.J. Ahn and H.S. Lee, “Larvicidal activity of Brazilian plants against Aedes aegypti and Culex pipiens pallens (Diptera: Culicidae)” Journal of Applied Biological Chemistry, vol. 45, no. 3, pp. 131–134, 2002.

[2] MB. Isman, “Botanical insecticides, deterrents, and repellents in modern agriculture and an increasingly regulated world”, Annual Review of Entomology, vol. 51, pp. 45–66, 2006.

[3] N. Akhtar and B. Mirza, “Phytochemical analysis and comprehensive evaluation of antimicrobial and antioxidant properties of 61 medicinal plant species”, Arabian Journal of Chemistry, vol. 11, no. 8, pp. 1223–1235, 2015.

[4] B.R. Okuyucu and F. Okuyucu, “Chemical composition and feed value of lupines and the possible uses in animal feeding”, Animal Production, vol. 49, pp. 60–62, 2008.

[5] M. Erbaş, M. Certel and M.K. Uslu, “Some chemical properties of white lupin seeds (Lupinus albus L.)”, Food Chemistry, vol. 89, no. 3, pp. 341–345, 2005.

[6] F.E. Carvajal-Larenas, A.R. Linnemann, M.J.R Nout, M. Koziol and M.A.J.S. Van Boekel, “Lupinus mutabilis: composition, uses, toxicology, and debittering”, Critical Reviews in Food Science and Nutrition, vol. 56, no. 9, pp. 1454–1487, 2016.

[7] O. Riabinina and C.J. Potter, “The Q-system: a versatile expression system for Drosophila. In: Dahmann C. (eds) Drosophila”, Methods in Molecular Biology, pp. 1478 53–78, Humana Press, New York, NY, USA, 2016.

[8] A. Casali and E. Batlle, “Intestinal stem cells in mammals and Drosophila”, Cell Stem Cell, vol. 4, no. 2, pp. 124–127, 2009.

[9] R. Gümüş and H. İmik, “Use of Saponins as Feed Additive in Animal Nutrition”, Ataturk University Journal of Veterinary Sciences, vol. 7, no. 3, pp. 221–229, 2012.

[10] B. Rogina and S.L. Helfand, “Cu, Zn superoxide dismutase deficiency accelerates the time course of an age-related marker in Drosophila melanogaster”, Biogerontology, vol. 1, no. 2, pp. 163–169, 2000.

[11] J.M. Aguilera and A. Trier, “The revival of the lupin”, Food Techology, vol. 32, pp. 70–76, 1978.

[12] S.K. Jain and S.N. Levine, “Elevated lipid peroxidation and vitamin Equinone levels in heart ventricles of streptozotocin-treated diabetic rats”, Free Radical Biology and Medicine, vol. 18, no. 2, pp. 337–341, 1995.

[13] W. Habig, M.J. Pabst and W.B. Jakoby, “The first enzymatic step in mercapturic acid formation. Glutathione-S-transferase”, Journal of Biological Chemistry, vol. 249, 7130–7139, 1974.

[14] O. Erel, “A new automated colorimetric method for measuring total oxidant status”, Clinical Biochemistry, vol. 38, no. 12, pp. 1103–1111, 2005.

[15] D.A. Roth-Maier and B.R. Paulicks, “Feeding and nutritional value of sweet blue and yellow lupin seed (Lupinus angustifolius L., Lupinus luteus L.) for broiler chicks”, Archiv fur Geflugelkunde, vol. 67, no. 4, pp. 175–178, 2003.

[16] Z.H. Miao, J.A. Fortune and J. Gallagher, “Anatomical structure and nutritive value of lupin seed coats”, Australian Journal of Agricultural Research, vol. 52, no. 10, pp. 985–993, 2001.

[17] Ü. Acar, O.S. Kesbiç, S. Yılmaz and A. Karabayır, “Growth performance, haematological and serum biochemical profiles in rainbow trout (Oncorhynchus mykiss) fed diets with varying levels of lupin (Lupinus albus) meal”, Aquaculture Research, vol. 49, no. 7, pp. 2579–2586, 2018.

[18] M. Geigerová, R. Švejstil, E. Skřivanová, E. Straková and P. Suchý, “Effect of dietary lupin (Lupinus albus) on the gastrointestinal microbiota composition in broiler chickens and ducks”, Czech Journal of Animal Science, vol. 62, no. 9, pp. 369–376, 2017.

[19] D. Zapletal, L. Kudělková, V. Šimek, P. Jakešová, M. Macháček, E. Straková and P. Suchý, “Haematological indicators in hybrid mallard ducks (Anas platyrhynchos) with regard to the use of meal from whole white lupin seeds in their diet”, Acta Veterinaria Brunensis, vol. 86, no. 3, pp. 309–315, 2017.

[20] M.R. Lee, S. Parkinson, H.R. Fleming, V.J. Theobald, D.K. Leemans and T. Burgess, “The potential of blue lupins as a protein source, in the diets of laying hens”, Journal of Veterinary and Animal Sciences, vol. 1, pp. 29–35, 2016.

[21] V. Lushchak, B.M. Rovenko, D.V. Gospodaryov and VI. Lushchak, “Drosophila melanogaster larvae fed by glucose and fructose demonstrate difference in oxidative stress markers and antioxidant enzymes of adult flies”, Comparative Biochemistry and Physiology Part A: Molecular and Integrative Physiology, vol. 160, no. 1, pp. 27–34, 2011.

[22] L. Chevalier, C. Desbuquois, J. Papineau and M. Charrier, “Influence of the quinolizidine alkaloid content of Lupinus albus (Fabaceae) on the feeding choice of Helix aspersa (Gastropoda: Pulmonata)”, Journal of Molluscan Studies, vol. 66, no. 1, pp. 61–68, 2000.

[23] M. Kubiś, S.A. Kaczmarek, S. Nowaczewski, M. Adamski, M. Hejdysz and A. Rutkowski, “Influence of graded inclusion of white lupin (Lupinus albus) meal on performance, nutrient digestibility and ileal viscosity of laying hens”, British Poultry Science, vol. 59, no. 4, pp. 477–484, 2018.

[24] S. Kaczmarek, M. Hejdysz, M. Kubiś and A. Rutkowski, “Influence of graded inclusion of white lupin (Lupinus albus) meal on performance, nutrient digestibility and intestinal morphology of broiler chickens”, British Poultry Science, vol. 57, no. 3, pp. 364–374, 2016.

[25] Y. Apidianakis and L.G. Rahme, “Drosophila melanogaster as a model for human intestinal infection and pathology”, Disease Models and Mechanisms, vol. 4, no. 1, pp. 21–30, 2011.

[26] N. Buchon, N.A. Broderick, S. Chakrabarti and B. Lemaitre, “Invasive and indigenous microbiota impact intestinal stem cell activity through multiple pathways in Drosophila”, Genes and Development, vol. 23, no. 19, pp. 2333–2344, 2009.

[27] T. Kuraishi, A. Hori and S. Kurata, "Host-microbe interactions in the gut of Drosophila melanogaster", Frontiers in Physiology, vol. 4, pp. 375–376, 2013.

[28] E.M. Ha, C.T. Oh, J.H. Ryu, Y.S. Bae, S.W. Kang and W.J. Lee, "An antioxidant system required for host protection against gut infection in Drosophila", Developmental Cell, vol. 8, no. 1, pp. 125–132, 2005.

[29] H. Ataş, F. Hacınecipoğlu, M. Gönül, Y. Öztürk and M. Kavutçu, "Antioksidan Enzim ve Oksidatif Biyobelirteçlerin Psöriasiste Klinik Değeri", Journal of Okmeydanı J Training and Research, vol. 33, pp. 270–280, 2017.

[30] Y.M. Li, H.Y.E Chan, X.Q .Yao, Y. Huang and Z.Y. Chen, "Green tea catechins and broccoli reduce fat-induced mortality in Drosophila melanogaster", Journal of Nutritional Biochemistry, vol. 19, no. 6, pp. 376–383, 2008.

[31] R.S. Vijayakumar, D. Surya and N. Nalini, "Antioxidant efficacy of black pepper (Piper nigrum L.) and piperine in rats with high fat diet induced oxidative stress", Redox Report, vol. 9, no. 2, pp. 105–110, 2004.

[32] A. Brenes, R.R. Marquardt, W. Guenter and A. Viveros, "Effect of enzyme addition on the performance and gastrointestinal tract size of chicks fed lupin seed and their fractions", Poultry Science , vol. 81, no. 5, pp. 670–678, 2002.

[33] O. Özcan, H. Erdal, G. Çakırca and Z. Yönden, "Oksidatif stres ve hücre içi lipit, protein ve DNA yapıları üzerine etkileri", Journal of Clinical and Experimental Investigations, vol. 6, no. 3, pp. 331–336, 2015.

[34] F. Erman, T. Kaya, O. Yilmaz and O. Erman, A.D. Ozsahin, "Influences of Physalis peruviana L. and Lupinus albus L. Extracts on the levels of some biochemical parameters in erythrocytes and serum of streptozotocin induced diabetic rats", Fresenius Environmental Bulletin, vol. 48, pp. 76–4882, 2017.

[35] M.C. Wang, D. Bohmann and H. Jasper, "JNK signaling confers tolerance to oxidative stress and extends lifespan in Drosophila", Developmental Cell , vol. 5, no. 5, pp. 811–816, 2003.

[36] A.A. Hamama and H.L. Bhardwaj, "Phytosterols, triterpene alcohols, and phospholipids in seed oil from white lupin", Journal of the American Oil Chemists' Society, vol. 81, no. 11, pp. 1039-1044, 2004.

[37] Msi Msika P., A. Piccirilli and N. U.S. Piccardi, Patent No. 8,747,815. Washington, DC: U.S. Patent and Trademark Office, 2014.

[38] S.K. Johnson, V. Chua, R.S. Hall and AL. Baxter, "Lupin kernel fibre foods improve bowel function and beneficially modify some putative faecal risk factors for colon cancer in men", British Journal of Nutrition, vol. 95, no. 2, pp. 372–378, 2006.

[39] S.C. Smith, R. Choy, S.K. Johnson, R.S. Hall, A.C.M. Wildeboer-Veloo and G.W. Welling, "Lupin kernel fibre consumption modifies fecal microbiota in healthy men as determined by rRNA gene fluorescent in situ hybridization", European Journal of Nutrition, vol. 45, no. 6, pp. 335–341, 2006.

[40] E. Agosin, D. Diaz, R. Aravena and E. Yañez, "Chemical and nutritional characterization of lupine tempeh", Journal of Food Science, vol. 54, no. 1, pp. 102–104, 1989.